University of Southampton

Faculty of Engineering and Physical Sciences

Civil, Maritime & Environmental Engineering

Single Acting Uniflow Condensing Engine System for Low Grade Heat Recovery

by

Curtis Howell

ORCID ID 0000-0003-0494-8766

Doctoral Thesis

May 2023

University of Southampton

Abstract

Faculty of Engineering and Physical Sciences

Civil, Maritime & Environmental Engineering

Single Acting Uniflow Condensing Engine System for Low Grade Heat Recovery

by

Curtis Howell

Low grade heat with temperatures of 50°C - 150°C from renewable or industrial sources (eg. waste heat) constitutes a substantial and unused energy resource. Several barriers to low grade heat recovery exist, but rising energy costs are increasing the importance of its development. The most common technology currently used for low grade heat recovery is the Organic Rankine Cycle. This is a heat engine which uses organic refrigerants at high pressures for recovery of low temperature heat with high energy density. The atmospheric condensing steam engine has been proposed as a potential alternative technology for low grade heat recovery with safety and sustainability benefits arising from its use of water as a working fluid and operation at atmospheric pressure and below. This technology has reduced energy density but offers advantages for applications on smaller power scales (1kW – 200kW) where simplicity is favoured, such as in domestic systems or in remote and rural communities.

This thesis has continued the development of the condensing engine technology by building on previous work conducted at the University of Southampton. Specifically, this research has built and tested a novel single acting uniflow design for improved performance. This allows increased steam evacuation through ports on the cylinder wall resulting in a larger pressure driving force for power production. With an effective temperature difference of around 30^{o}C and without steam expansion the engine reached a maximum power output of 5.4W, assuming 10% mechanical losses, and thermal efficiency of 2.5%. Assuming no losses between boiler and cylinder, this equated to a second law efficiency of around 40%. This constitutes comparable power output to the previous model under similar operating conditions and an increase of 25% in maximum efficiencies. Second law efficiencies were also comparable to Organic Rankine Cycle systems of a similar scale. Future condensing engine thermal efficiencies as high as 9% were predicted through analysis of the data.

A novel heat recovery and re-use concept within the condensing engine system itself was also investigated theoretically and experimentally in this thesis with the aim of improving efficiency. Theoretical modelling confirmed that as much as 75% of thermal energy input would be available for recovery during condensation, assuming dry steam. Modelling showed that if this heat was re-used within the engine system, to drive a second sub-atmospheric stage, it could operate at reduced steam expansion without compromising efficiency. This would allow improved power output and stability. Experimental testing demonstrated suitable proof of concept of heat recovery on the condensing engine using a two-stage condenser arrangement with intermediate flat plate heat exchanger for latent heat recovery. A maximum heat recovery efficiency around 60% was achieved empirically with cooling water outlet temperatures of 65^{o}C - 90^{o}C without affecting the system pressure required for engine operation, maintained around 0.2bar.

Table of Contents

List of Tables

List of Tables

List of Figures

List of Figures

List of Figures

List of Figures

Declaration of Authorship

Print name: Curtis Howell

Title of thesis: Single Acting Uniflow Condensing Engine System for Low Grade Heat Recovery

I declare that this thesis and the work presented in it are my own and has been generated by me as the result of my own original research.

I confirm that:

1. This work was done wholly or mainly while in candidature for a research degree at this University;
2. Where any part of this thesis has previously been submitted for a degree or any other qualification at this University or any other institution, this has been clearly stated;
3. Where I have consulted the published work of others, this is always clearly attributed;
4. Where I have quoted from the work of others, the source is always given. With the exception of such quotations, this thesis is entirely my own work;
5. I have acknowledged all main sources of help;
6. Where the thesis is based on work done by myself jointly with others, I have made clear exactly what was done by others and what I have contributed myself;
7. Parts of this work have been published as:-

Muller, G. & Howell, C., 2021. Comparative analysis of recent and historic low power heat engines for low grade waste heat recovery. *Applied Engineering*. Volume 5, pp 7-13

Signature: Curtis Howell ..... Date: 06/05/2023 .....

Acknowledgements

I firstly wish to thank the funders of this project, without whom the project could not have been realised. These included an EPSRC Doctoral Training Grant Research Studentship (Funding Code: F2J7NG. Sub Project Number: 5179791025656), a Global Challenges Research Fund (GCRF) grant (Grant Number: 519016142), and a Southampton Marine & Maritime Institute (SMMI) EPSRC Institutional Sponsorship funded by the GCRF (Grant Title: Enhanced heat engine for low-temperature thermal energy re-use). I also thank the journal bodies which gave me permission to re-use material from their papers, specifically *Elsevier* and *Springer Nature*.

Next, I would like to thank my supervisors, Dr Gerald Muller and Professor Andrew Cruden, for their continued support and guidance. Their insights were critical to the success of the project and allowed me to become a more well-rounded engineer as a result. I also owe a huge debt of gratitude to several technicians and engineers from the University of Southampton who helped in the design, manufacture, and assembly of the prototype condensing engines and heat recovery experiment. Namely, I would like to thank Peter Russell, Karl Scammell, and Hannah Williams for their help in the lab. I would also like to thank David Thurley and Michael Street from the 'Engineering Design and Manufacturing Centre' (EDMC) for their technical expertise. I would also like to thank the EDMC for the production of the Mk.IV engine technical drawings, funded by GCRF grant 519016142, available in the data repository for this project. I also extend thanks to the Electrical Engineering Workshop who provided patient guidance as I developed a new skill. Furthermore, I thank the authors of the unpublished Masters thesis (Mk.II engine) produced previously at the university upon which I have built my research, as well as Dr Gerald Muller for giving me permission as supervisor of the work to re-use pertinent material in this thesis.

I also thank the external collaborators for their roles in the completion of this project. I would like to thank Peter Hanley (Hanley Design) for the production of technical drawings for the Mk.III engine, funded by the SMMI EPSRC grant acknowledged above, available in the data repository for this project. I would also like to thank Quayside Engineering Ltd for the manufacture of the components for the Mk.III engine. I also thank Dr Michael Owen and Cobus Van Zyl from the University of Stellenbosch for the continued collaboration integrating the condensing engine with solar thermal panels in South Africa and for giving me permission to use their photographs of the system for use in this thesis.

Finally, I would especially like to extend thanks to my friends and family who have supported me through the difficult times of this project and are a greater part of this success than they will ever know.

List of Abbreviations, Symbols & Subscripts

Abbreviations

BDC	Bottom Dead Centre
CA	Cross Section Area
CE	Condensing Engine
CHP	Combined Heat & Power Engine
CO	Condenser
CW	Cooling Water
EDMC	Engineering Design and Manufacturing Centre
ER (also *n*)	Expansion Ratio
FPHE	Flat Plate Heat Exchanger
LCOE	Levelised Cost of Electricity
LGWH	Low-Grade Waste Heat
LTDH	Low Temperature District Heating
Mk.II	2nd iteration of condensing engine
Mk.III	3rd iteration of condensing engine
Mk.IV	4th iteration of condensing engine
NRV	Non-Return Valve
NTU	Number of Transfer Units
ORC	Organic Rankine Cycle
PD	Probability Density
PTFE	Polytetrafluoroethylene
PV	Photovoltaic (solar panel)
SC	Solar Collector
SMMI	Southampton Marine & Maritime Institute
STERG	Solar Thermal Energy Research Group

SV	Solenoid Valve
TDC	Top Dead Centre
TDS	Total Dissolved Solids
TES	Thermal Energy Storage
UHMWPE	Ultra-High Molecular Weight Polyethylene
UoS	University of Southampton
XCPC	External Compound Parabolic Concentrator

Symbols

A_{ht}	Heat transfer surface area	m^2
C_{max}	Maximum mass heat capacity	J/K
C_{min}	Minimum mass heat capacity	J/K
C_p	Specific heat capacity at constant pressure	kJ/kg.K
C_r	Mass specific heat capacity ratio	-
C_v	Specific heat capacity at constant volume	kJ/kg.K
d	Diameter	m
E_a	Thermal energy available for recovery	J
E_r	Thermal energy recovered	J
F	Change in load cell reading on friction brake	N
g	Acceleration due to gravity	m/s^2
h_t	Local heat transfer coefficient	$W/m^2.K$
h	Enthalpy	kJ/kg
I	Moment of inertia	kg/m^2
KE	Kinetic energy	J
K_i	Minor head loss coefficient	-
k	Thermal conductivity	W/m.K
L	Length	m

m	Mass	kg
$\dot{m}$	Mass flow rate	kg/s
N	Engine speed	rpm
N_{fly}	Flywheel speed	rpm
n	Expansion ratio	-
n_H	Number of horizontal tubes	-
P	Pressure	Pa or bar
$\dot{Q}$	Thermal power	kW
Q	Thermal energy	kJ
R_w	Thermal resistance of heat transfer plate	m^2K/W
r	Radius	m
s	Specific entropy	J/kg.K
T	Temperature	^oC or K
T_{LM}	Log mean temperature difference	^oC
t	Time	s
U	Overall heat transfer coefficient	W/m^2K
u	Fluid heat exchanger channel velocity	m/s
V	Volume	m^3
v	Velocity	m/s
$\dot{W}$	Mechanical power	kW
W	Mechanical energy	J
x	Dryness fraction	-

Greek Symbols

α	Heat transfer coefficient	W/m^2K
α_{te}	Thermal expansion coefficient	m/m.K
γ	Adiabatic Coefficient of Expansion	-

ε	Heat exchanger effectiveness	-
η	Efficiency	%
φ	Angle	Rad / degrees
θ	Angular distance	rad
λ	Thermal conductivity	W/m.K
μ	Viscosity	Pa.s
ρ	Density	kg/m^3
ω	Angular velocity	rad/s

Subscripts

0	Point 0
1	Point 1
2	Point 2
3	Point 3
II	Second law
atm	Atmospheric
avg	Average
b	Boiler
bdy	Boundary
bottom	Bottom
c	Cold
Carnot	Carnot efficiency
con	Condenser
cyl	Cylinder
d	Downstroke
exp	Expansion
fb	Friction brake

fly	Flywheel
FPHE	Flat plate heat exchanger
g	Gaseous state
gl	Vaporisation
h	Hot
i	Iteration number
in	Input
isen	Isentropic
isot	Isothermal
l	Liquid state
loss	System loss
MKIII	3rd iteration of condensing engine
MKIV	4th iteration of condensing engine
max	Maximum
min	Minimum
pis	Piston
pump	Pump
rev	Revolution
s	Steam
sat	Saturated
sj	Steam jacket
slot	Evacuation slot
th	Thermal
top	Top
u	Upstroke
ws	Working steam

Chapter 1 Introduction

1.1 Background

Due to process inefficiencies and limits set by the laws of thermodynamics, as much as 20% - 50% of all energy put into the industrial sector is lost in the form of waste heat (US DOE, 2017). This presents a significant energy resource and, if recovered, can offset the financial and environmental cost of energy production. As a result, waste heat recovery has received considerable research in literature. This research typically categorises waste heat into three temperature ranges: High-grade (> 650°C), medium-grade (230 °C - 650°C), and low-grade (< 230°C), eg. (Su, et al., 2021). High and medium grade waste heat's higher temperatures makes recovery relatively simple and as a result it is adopted widely in industry. However, low-grade waste heat (LGWH) is more difficult to recover. Barriers to LGWH recovery suggested in literature include its weak potential, difficult utilisation, lack of suitable heat sink, and typical poor economic payback period (Su, et al., 2021; Xu, et al., 2019).

However, energy related economics, effected by external factors such as the war in Ukraine and security of supply, mean that the recovery of LGWH is becoming more financially viable. For example, non-domestic sectors in the UK experienced 124% and 63% increases in their gas and electricity bills for the period of July to September in 2022 compared to the same period in 2021 (BEIS, 2022). Subsequently, as much as 33% - 66% of all unrecovered waste heat is now considered to be LGWH (Haddad, et al., 2014; Langhan & O'Toole, 2017; Xu, et al., 2019). This amounts to an estimated 100TWh of LGWH below a temperature of 200°C in Europe available for recovery each year (Papapetrou, et al., 2018). For context, taking the average UK household electricity consumption as 3760 kWh/yr in 2017 (OVO Energy, nd), 100TWh would be enough to power 27 million homes for a full year.

The most common technology observed in literature for the recovery of LGWH is currently the Organic Rankine Cycle (ORC). An advancement of the traditional *Rankine* cycle, the ORC uses waste heat to evaporate a thermal fluid which can be expanded to produce mechanical work before being condensed and returned to the evaporator. Typical working fluids include organic refrigerants which allow the favourable thermodynamics required to effectively target the low temperature range exhibited by LGWH. It is noted that these working fluids require consideration of safety and environmental concerns, including global warming and ozone depletion potential as well as flammability amongst others (Kumar & Dibakar, 2021; Rahbar, et al., 2017; Mahmoudi, et

al., 2018). However, these working fluids have ideal thermal properties, specifically low boiling points, allowing the ORC system to operate at higher pressures. For example, evaporator pressures of 1.3bar - 16bar have been observed in recent low temperature ORC literature, with 10+bar being typical (Rahbar, et al., 2017; Muller & Howell, 2021). Operation at higher pressure is advantageous as it increases energy density and reduces required footprint for a given power output (Semmens & Goldfinch, 2000). Whilst this makes the ORC system ideal for higher power ratings, the use of organic refrigerants at high pressures increases the cost associated with the working fluid as well as equipment design which must meet pressure related safety regulations. As a result, it is suggested in literature that small-scale ORC systems may not be economically viable (Frate, et al., 2019; Quoilin, et al., 2013; Tocci, et al., 2017).

As a result, the development of the atmospheric condensing engine (CE) has begun at the University of Southampton (UoS) as an alternative LGWH recovery technology, eg. (Muller, et al., 2018). The CE is a historic technology, originally developed by Thomas Newcomen and James Watt, dating back to the 18th Century. It uses the principle that condensation of atmospheric steam inside a sealed vessel or system creates a sub-atmospheric pressure. This creates a pressure driving force which can be used to move a piston and produce mechanical work. The condensing engine can also be run using sub-atmospheric boiler pressures, reducing the boiling point of the water and allowing waste heat of a temperature below 100^{o}C to be recovered, increasing the range of applications the CE can be used for. The benefits that made the engine appealing in the 18th Century are of interest again today. Namely, the engine uses water as a safe and sustainable working fluid and operates at low temperature and pressure.

These characteristics make the condensing engine an ideal choice for small power scale applications where safety, sustainability, and cost effectiveness are of increased concern. Examples include domestic systems or systems installed in remote and rural locations, investigated further in this thesis. The condensing engine can also make direct use of LGWH in the form of steam, commonly vented directly from industry (Armitage, 2017) or available from renewable technologies such as bio-steam (TCE, 2019) and solar thermal collectors (Chu, 2018). The latter is of specific interest, as a combined system made up of solar collectors and the condensing engine can provide both water purification and electricity production. This is possible due to the thermal distillation process that occurs when evaporating the feed water. Such a system could be employed in rural communities in developing countries who have no access to the grid or clean water. The simplicity of the condensing engine lends itself well to this scenario with expected reductions in installation cost, required maintenance and repair, and risk associated with the leakage of working fluid when compared against the ORC. This specific application has been explored further in this

thesis through collaboration with the University of Stellenbosch, where a combined system of solar collectors and condensing engine is under construction.

Literature investigating the modernised condensing engine has suggested potential future target heat source temperature and power scale ranges of around 50°C – 150°C and 1kW – 200kW respectively (Muller, et al., 2018). ORC systems operating at the same temperature and power scale demonstrate electrical efficiencies around 5% - 15% and second law efficiencies of 20% - 40% (Landelle, et al., 2017; Muller & Howell, 2021). The second law efficiency is defined as the ratio between achieved efficiency and the maximum possible for a given operating temperature range, an important thermodynamic principle that will be discussed in more detail in the main body of this thesis. In comparison, recent work published as part of this research found that *Davey's* engine, built in 1885 and the last known commercial use of the condensing engine, achieved estimated second law efficiencies in the range of 18% - 25% (Muller & Howell, 2021). This is comparable with the lower end of current small-scale ORC systems, justifying the potential of the condensing engine to match the efficiencies of current technologies once optimised. This is supported by recent research, estimating theoretical thermal efficiencies as high as 17.7% when employing steam expansion (Bortolin, et al., 2021). Steam expansion was first proposed by James Watt and involves shutting the steam inlet valve part way through the condensing engine's stroke to allow cylinder steam to expand against the piston. This removes a greater portion of work from the same steam mass thus increasing efficiency.

Research into the condensing engine at the University of Southampton has begun to develop modernised practical models of the technology. The latest iteration, built and tested by Muller, et al. (2018) and called the Mk.II engine, has been reviewed in detail as part of this thesis' literature review. Operating between a boiler temperature of 100°C and condenser temperature of 55°C - 70°C, the Mk.II engine successfully demonstrated steam expansion to achieve power outputs of 3.6W - 27W and a maximum thermal efficiency of 5.5% (Muller, et al., 2018). Whilst a promising development, this engine achieved just 30% - 40% of theoretical maximum for the given operation (Muller, et al., 2018). This highlighted that there existed further development potential, giving rise to this research project. Specifically, the two key sources of inefficiency on the Mk.II engine were insufficiently low cylinder pressures, which reduced pressure driving force, and excessive mechanical losses due to friction. Cylinder pressure was negatively affected by restrictions to the evacuation of steam from the cylinder to the condenser. Mechanical friction was caused by the complex crank shaft system required as a result of the double acting cylinder.

The research in this thesis has undertaken further development of the condensing engine technology by building and testing the next iteration, the Mk.III CE, for improved performance by

implementing a single acting uniflow configuration. This had not before been tested on the atmospheric condensing engine and constituted a novel advancement in the technology's design. The uniflow engine incorporates evacuation ports on the cylinder wall to maximise the channel area available for steam evacuation. This allows for improved reduction in cylinder pressure and in turn a maximised driving force for power production. Additionally, a single acting engine with traditional crank shaft simplifies the design and reduces the number of mechanisms allowing a minimisation of mechanical losses. It also allows for multiple cylinders to be attached to the same crank shaft more easily, giving flexibility to scale the technology.

Previous work on the Mk.II engine also proposed the concept of heat recovery within the condensing engine system itself. This can be achieved by recovering the latent heat released during steam condensation, constituting as much as 2258kJ per kilogram of steam at 1bar (Rogers & Mayhew, 1995). This was attempted using a condenser with two sections of coil, allowing heat recovery to be performed in the top condenser section and total condensation of residual steam in the bottom. However, during testing this setup was unable to recover latent heat without negatively affecting the sub-atmospheric pressure achieved during the condensation which in turn worsened engine performance (Ho Chan, et al., 2017). The research in this thesis has therefore also undertaken theoretical modelling and experimental proof of concept testing to demonstrate successful heat recovery on the atmospheric condensing engine, another novel advancement of the technology.

1.2 Research Aims & Objectives

Background to this thesis has been given in Section 1.1. Based on this, two aims were identified for this research project:

1. To investigate the potential of the single acting uniflow condensing engine through development and testing.
2. To show proof of concept of heat recovery on the condensing engine without negatively affecting engine performance and to quantify the potential effect.

To meet the above aims, the research objectives were:

- Investigate theory of single acting uniflow stroke and quantify expected efficiency.
- Design, build, and test a prototype single acting uniflow condensing engine.
- Compare prototype single acting uniflow engine results with previous condensing engine models and current ORC systems seen in literature.
- Propose design improvements following lessons learned during prototype testing.

- Investigate the integration of the condensing engine with solar thermal collectors.
- Conduct theoretical analysis to predict energy available for recovery during steam condensation.
- Perform practical experiments to show proof of concept of heat recovery on the condensing engine without negatively affecting engine performance.
- Develop a theoretical model to simulate expected performance improvements through re-use of the recovered energy, justifying implementation of heat recovery on future condensing engine iterations.

1.3 Research Novelties

This research is considered to have three novelties, as required for a Doctoral degree. To be novel, research must both be original and not clear or obvious to an expert in the art. In this case, this research investigated prototypes or concepts that were the first of their kind with quantification of efficiency/performance not being obvious without the conducted testing and analysis. This included:

1. Testing of a single acting uniflow atmospheric condensing engine for improved efficiency.
2. Demonstrating proof of concept of successful heat recovery on the condensing engine during steam condensation, without negatively affecting engine performance.
3. The proposal and theoretical assessment of a novel re-use of latent heat recovered during steam condensation and assessment of the potential performance.

1.4 Thesis Overview

An overview of the remainder of the thesis is given in Figure 1-1. The literature review, reported in Chapter 2, follows this introduction. This systematically reviews literature pertaining to the availability of low-grade heat, both as waste and from renewables, as well as the available technologies for its recovery with a focus on the ORC. The literature review then investigates the atmospheric condensing engine as an alternative technology and critically reviews the most recent practical example, the Mk.II engine. A summary then outlines the research methodology defined by the reviewed literature.

The first aim of this research, the testing of a single acting uniflow atmospheric condensing engine (the Mk.III), is addressed in Chapter 3 to Chapter 5. The theoretical potential of the engine arrangement is investigated in Chapter 3 using a mathematical model. Chapter 4 details the design, assembly, and testing of the prototype Mk.III engine. Chapter 5 builds upon the Mk.III

development, outlining the design improvements made on the improved Mk.IV engine built in collaboration with the University of Stellenbosch in South Africa for integration with solar thermal panels.

The second aim of this research, proof of concept of heat recovery on the condensing engine, is addressed in Chapter 6. This work involves the theoretical assessment of both the potential energy available for recovery as well as the improvements to engine performance heat re-use could yield. It also includes experimental testing of a new heat recovery setup, using two condensation stages including a flat plate heat exchanger, to successfully show demonstration of the concept for use on future engine iterations.

Finally, Chapter 7 draws relevant conclusions from the conducted research, linking back to the aims and objectives, and makes recommendations for future work. Chapter 8 lists the referenced works. Chapter 9 comprises the appendices which provide additional background information, list the data associated with the project, and present any calculations performed.

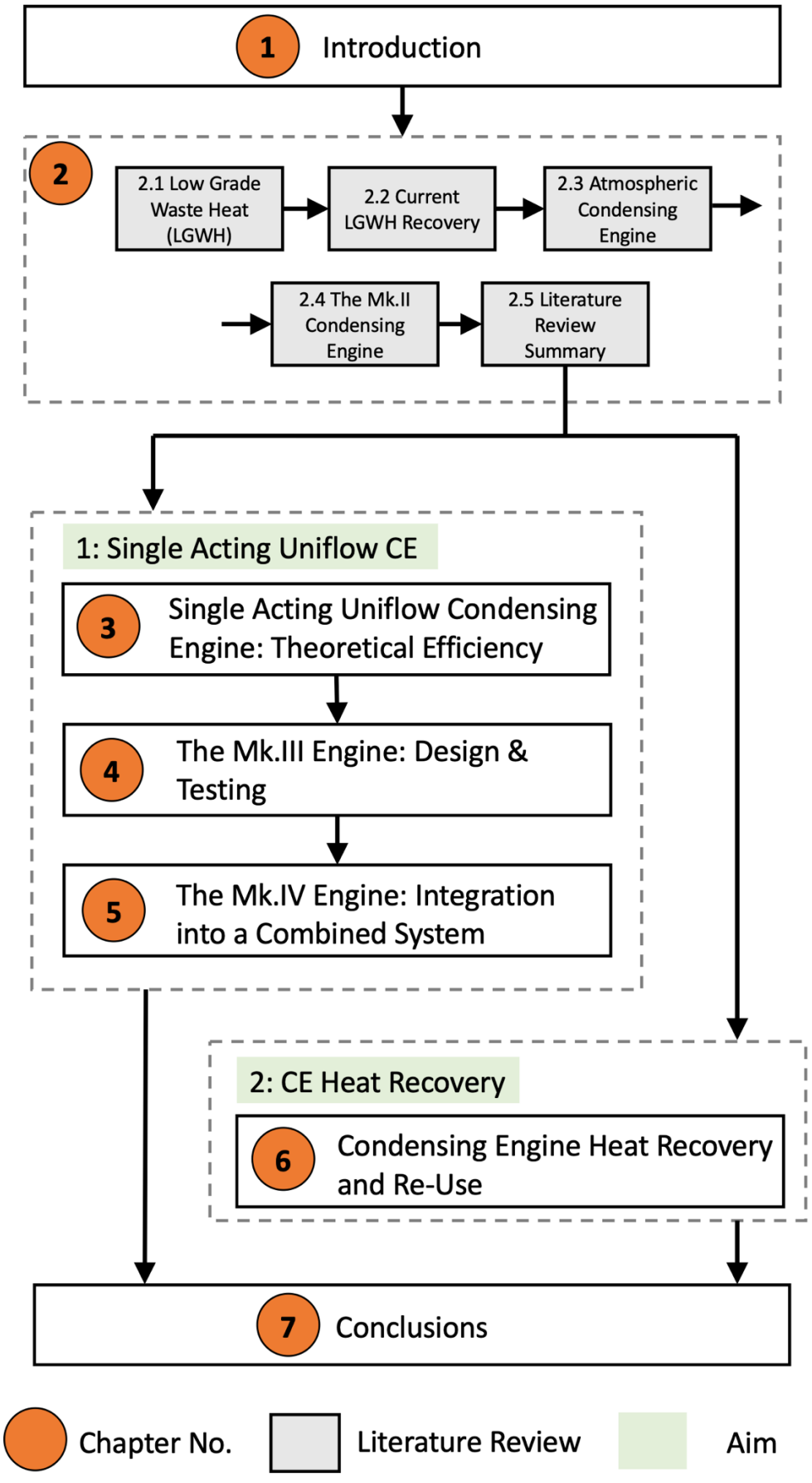

Figure 1-1 Thesis overview flow chart

Chapter 2 Literature Review

2.1 Low Grade Waste Heat

It is important to justify the potential of low-grade heat available for recovery before investigating the available recovery technologies for comparison against the condensing engine. Low grade heat is available both as waste from industry and from renewables, and on both large and small scales. The relevant literature is explored in this section.

2.1.1 Low Grade Waste Heat Potential in Industry

2.1.1.1 Industrial Waste Heat Terminology in Literature and the Effect of Recent Energy Economics

Before the amounts of low-grade waste heat reported in literature are investigated, the different terminology surrounding the quoted values should be understood. The categorisation of waste heat as high grade (> 650°C), medium grade (230°C - 650°C), or low grade (< 230°C) (Su, et al., 2021) has already been outlined in the introduction, with low-grade heat of interest to this research project due to its increased complexity of recovery and large amounts of available energy. Literature also describes waste heat as a 'total' value, a value 'technically' viable for recovery, and/or a value that is 'economically' viable for recovery. Technical viability is based on the efficiencies of current technologies, and what energy could be physically harnessed. Economic viability describes the fraction of waste heat recovery that is financially feasible with the chosen technology.

The total low-grade waste heat available for recovery is of most interest to this review, to understand the overall potential of the untapped energy reserve. Whilst technically and economically recoverable low-grade waste heat are also of interest, these values are dependent on the effectiveness of available recovery technologies and the state of energy economics at the time the research was conducted. The war in Ukraine has led to reduced gas exports from Russia and therefore a limited global supply. This has created an energy crisis in Europe and resulted in an increase in energy prices. According to the UK Government Department for Business, Energy, & Industrial Strategy, average non-domestic sector gas and electricity prices were 6.53 pence per kWh and 21.56 pence per kWh respectively between July and September in 2022 (BEIS, 2022). For context, this represented increases of 124% and 63% compared to the same period in 2021 (BEIS,

2022). Domestic customers saw their gas and electricity bills increase by 85% and 46% respectively over the same time frame (BEIS, 2022). Therefore, it can be observed that the economics of heat recovery, either for re-use in heating applications to reduce gas consumption or for conversion to electricity, can be drastically improved by global situations. This is directly relevant to the economic feasibility of the condensing engine, a heat to power technology, being researched in this thesis. With the price of fossil fuels continually trending upwards, the prospect of heat recovery becomes more financially viable over time.

2.1.1.2 Accuracy of Estimation

When reporting the low-grade waste heat potential in industry it is first important to understand the accuracy of methods used to estimate the energy potential. Ammar, et al. (2012) claim that specific data for waste heat from industrial processes is typically confidential, and therefore quoted values are estimations only. Ammar, et al. (2012) suggest that estimations are usually made using CO_2 emissions data, however some more sophisticated estimation methods are used in more recent literature. For example, the study performed by Element Energy (2014) utilised "innovative" databases which include heat sources and sinks at 73 of the largest UK industrial sites supported by literature, expert review, and site visits where possible. The study by Brueckner, et al. (2017) found the waste heat present for a 58% market share of industrial energy use in Germany and extrapolated for a 100% share. Whilst this introduces uncertainty it allows useful insight into what a total sector value might look like. Additionally, the study performed by Papapetrou, et al (2018) used a unique method which takes historical data from 2003 for the UK industry and adjusts it to the year 2015 for each European country based on industries present, energy intensity per industry, and energy efficiency changes. However, Papapetrou, et al (2018) acknowledge that the waste heat values used in their analysis still only have an accuracy of +/- 33%. It is important to consider the uncertainty in quoted values when making comparison in the sub-sections which follow.

2.1.1.3 Estimated Available Low-Grade Waste Heat in Literature

Inaccuracies in waste heat estimations can lead to differences in values quoted in literature. However, whilst studies might disagree in the actual value, they all agree that the amount of low-grade waste heat available for recovery is substantial. Examining the UK first, around 40-48 TWh/yr of total waste heat is expected to exist in industry, with as much as 11-24 TWh/yr being technically viable for recovery (Ammar, et al., 2012; Element Energy, 2014; Papapetrou, et al., 2018). Literature suggests that 1/3rd - 2/3^{rds} of all total waste heat in the industrial sector is now of low grade (Haddad, et al., 2014; Langhan & O'Toole, 2017; Xu, et al., 2019). Therefore, the above values would suggest that there exists anywhere between 13-32TWh/yr of total LGWH in the UK's

industrial sector. To give this context, taking the average UK household electricity consumption as 3760 kWh/yr in 2017 (OVO Energy, nd), 10TWh would be enough to power 2.7 million homes for a full year.

The data presented by Papapetrou, et al (2018) also allows for a useful understanding of low-grade waste heat across Europe, offering a breakdown of waste heat potential by country; see Figure 2-1. Papapetrou, et al (2018) find that there exists as much as 100TWh/yr of waste heat potential below the temperature of 200°C in Europe. Whilst this study found there to be little waste heat available below 100°C, this is attributed to the use of 'technically recoverable' energy. This value could therefore increase with improvement to recovery technologies. According to this study, the countries with the most waste heat available in Europe are France, Germany, Italy, Spain, and the UK (Papapetrou, et al., 2018). These countries therefore offer potential markets for the condensing engine once commercialised.

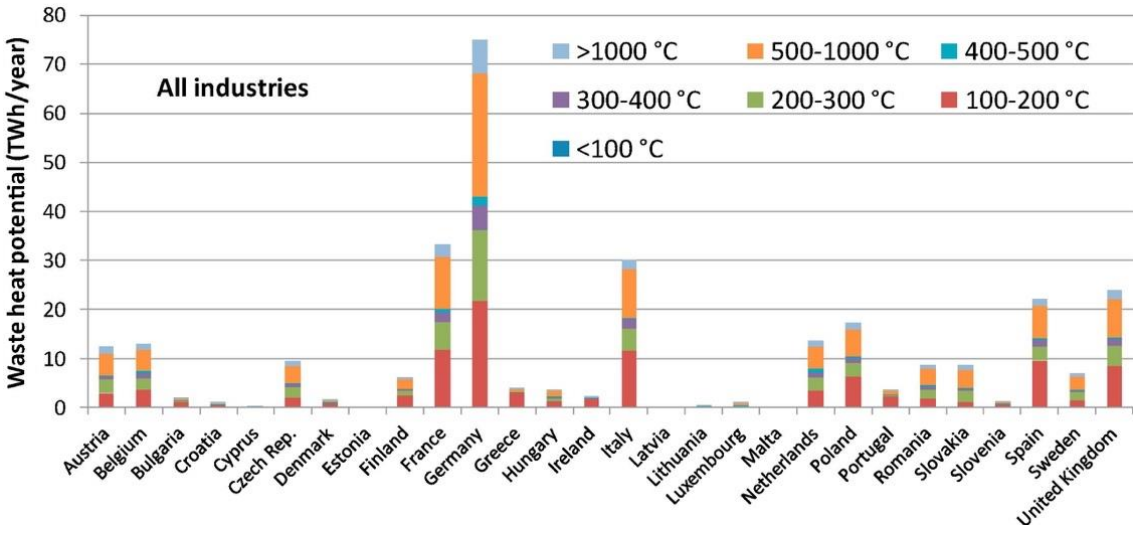

Figure 2-1 Technically recoverable waste heat (TWh/yr) across all industries for European countries, categorised by temperature. Reproduced from (Papapetrou, et al., 2018) under CC BY-NC-ND 4.0.

Further values for the waste heat in Europe can be found in literature for comparison. A recent study (Brueckner, et al., 2017) also estimates that approximately 60TWh/yr of total waste heat is available in Germany, close to the estimation made by Papapetrou, et al (2018). The study by Brueckner, et al. (2017) is of particular use as it uses a cumulative analysis for waste heat availability based on the temperature of the source; see Figure 2-2. This allows for an understanding of the energy available in the chosen scope for this project; approximately 16 TWh/yr of waste heat between 50°C - 150°C in Germany alone (Brueckner, et al., 2017). Figure 2-2 also shows cumulative energy available significantly increases at low temperature supporting previous arguments made in this section.

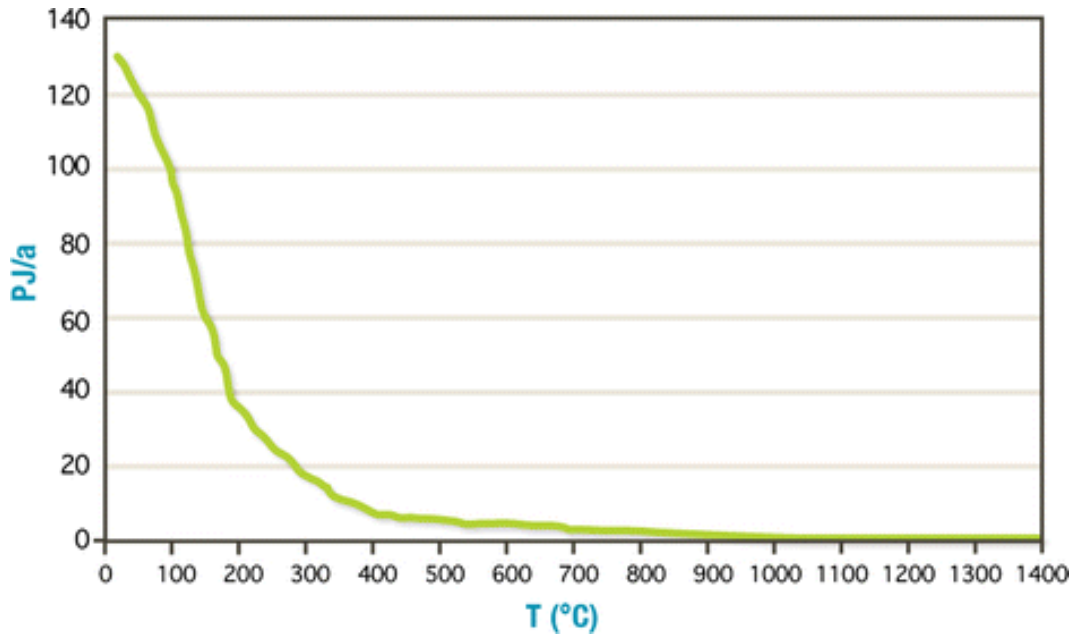

Figure 2-2 A cumulative plot of waste heat availability in Germany, presented as waste heat in PJ/a vs source temperature. 1PJ = 0.28 TWh. Reproduced from (Brueckner, et al., 2017) with permission from Springer Nature.

A breakdown of technically available waste heat in Europe available from a range of industries at different temperatures is found by Papapetrou, et al (2018) and given in Figure 2-3. This graph suggests that several major industries will have LGWH available for recovery. This is supported by Jouhara, et al (2018) and Ammar, et al (2012) who find the most energy consuming industries in the UK to include the production of cement, iron and steel, chemicals, glass, ceramics, food & drink, and paper.

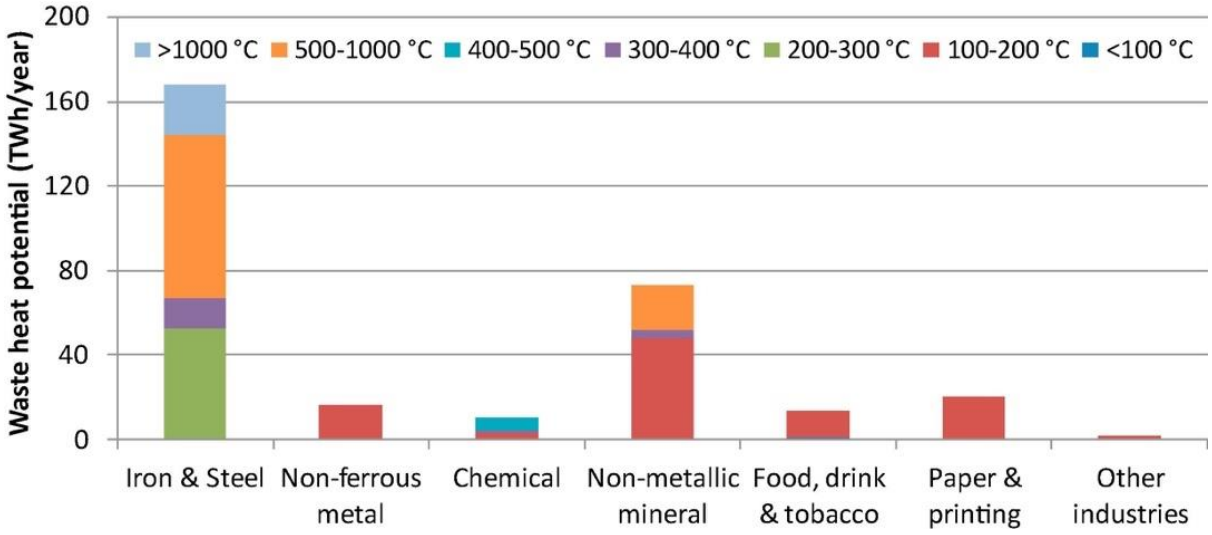

Figure 2-3 Technically recoverable waste heat (TWh/yr) for Europe as a whole, categorized by industry and temperature. Reproduced from (Papapetrou, et al., 2018) under CC BY-NC-ND 4.0.

Whilst these industries may not always be present in Europe and could move to geographical locations where more cost-effective services can be provided, these industries are considered to be robust against a global minimisation supporting that worldwide low-grade waste heat potential will be resilient and require long term recovery solutions. To support this, low-grade waste heat opportunities outside of Europe are already substantial. A recent review of LGWH availability found there to be approximately 0.9EJ of waste heat dissipated below 230°C from the US glass, cement, iron/steel, aluminium, metal casting and ethylene industries each year (Xu, et al., 2019). An assumption of steady energy output across the year allows this to be estimated as 28.5GW of available thermal power. The same review also found there to be 20GW, 1.9GW, and 0.8GW of waste heat below 150°C in China from the cement, iron/steel, and glass industries respectively (Xu, et al., 2019). Furthermore, other sources of low-grade waste heat exist, including renewable sources, providing resilience for the future. These are discussed later in this section. Table 2-1 gives examples of specific LGWH streams available from industry between 50°C - 150°C, according to the reviewed literature.

Table 2-1 Example LGWH sources from industry with a temperature between 50°C - 150°C. Credit: various sources.

LGWH Waste Stream	Industries	Temperature (°C)	References
Cooling and process water	Textiles, Paper, Steel, Chemical	50-90	(Chin, et al., 2018) (Ammar, et al., 2012) (Su, et al., 2021)
Flue and exhaust gases	Iron/Steel, Aluminium, Food & Drink	70-150	(Chin, et al., 2018) (Zhang, et al., 2019) (Su, et al., 2021)
Hot and warm air	Food & Drink, Cement	90-150	(Chin, et al., 2018) (Zhang, et al., 2019) (Su, et al., 2021)
Steam and condensate	Food & Drink, Paper	90-100	(Chin, et al., 2018) (Su, et al., 2021)

2.1.1.4 Steam as a Direct Emission of Low-Grade Waste Heat

Table 2-1 offers waste steam as a direct source of low-grade heat. Waste steam and water vapour can be emitted from boilers, vent pipes, and condensate collection tanks found in industrial processes (TLV, 2019); see Figure 2-4. This is of specific interest to this research as it can be used

directly as the working fluid in the atmospheric condensing engine. This removes the heat exchange step required by most heat engines to evaporate the working fluid, simplifying the integration of the recovery technology and increasing efficiency by eliminating the heat losses associated with the heat transfer step. Specifically, heat exchange typically has an approach temperature, representing the minimum difference between hot and cold side fluids. In this case, this would result in an evaporation temperature lower than the temperature of the heat source medium. This is eliminated if the heat source medium is used directly as the working fluid.

Figure 2-4 Photograph of a paper and packaging factory emitting water vapour in Germany. Reproduced from (Muller & Howell, 2021) under CC BY 4.0.

Waste steam is a form of low-grade heat not typically considered in literature (Muhammad, et al., 2015). However, steam is a high value source of energy, containing significant latent heat. If the steam in the photograph is assumed to be saturated at atmospheric pressure, then it contains 2258kJ/kg of energy as latent heat alone (Rogers & Mayhew, 1995). It also has around 300kJ/kg of energy as sensible heat if cooled down to 20^{o}C (Rogers & Mayhew, 1995). There is expected to be around 40TWh emitted as waste steam globally each year (Armitage, 2017).

2.1.2 Renewable Sources of Low-Grade Waste Heat: Solar Thermal

Section 2.1 has thus far introduced the substantial resource of LGWH in industry. However, low-grade heat between 50^{o}C - 150^{o}C can also be produced by renewable energies. As more sustainable primary fuels are integrated into everyday lives the ability to convert low-temperature heat into additional electricity can contribute to the achievement of a circular economy. Renewable sources of low-grade heat include geothermal (US EPA, 2017), bio-steam production (TCE, 2019), and solar thermal technologies.

Due to its synergy with the condensing engine, allowing production of both electricity and purified water, only solar thermal is considered in this report. Both large and small scale solar thermal installations are on the rise across the globe, attributed predominantly to improvement in cost competitiveness (IEA-SHC, 2020). There was a reported cumulated solar thermal capacity of 479 GWth at the end of 2019, covering 684 million square meters and producing 389 TWh of thermal energy in 2019 alone (IEA-SHC, 2020). Of relevance to this project are the small-scale installations which provide hot water and heating in residential and public spaces. This is a result of the expected applications of the condensing engine, addressed in the introduction and further in Section 2.2.3. These collectors are suitable for combination with the condensing engine at low power scales, and now represent 60% of all new systems being installed (IEA-SHC, 2020). It was also reported that 53% of total solar thermal capacity is attributed to domestic heating systems (IEA-SHC, 2020). As discussed in Section 2.1.1, global factors have resulted in a recent increase in gas prices, typically used for domestic systems, and therefore a further increase in use of solar thermal for domestic heating could be expected.

Solar energy is an abundant form of renewable energy. Solar thermal technologies harness this energy to heat a working fluid, commonly water. Various types of solar thermal collector exist, with a typical parabolic trough type design shown in Figure 2-5. This type is of relevance as it was chosen for use by the University of Stellenbosch Solar Thermal Energy Research Group (STERG) in the collaboration presented in Chapter 5 to integrate with the condensing engine. The radiation emitted from the sun can be concentrated using the reflective parabola and is collected by a metal 'receiver' tube covered by glass to reduce thermal losses. The energy is transferred to the fluid inside the receiver tube (Kalogirou, 2004).

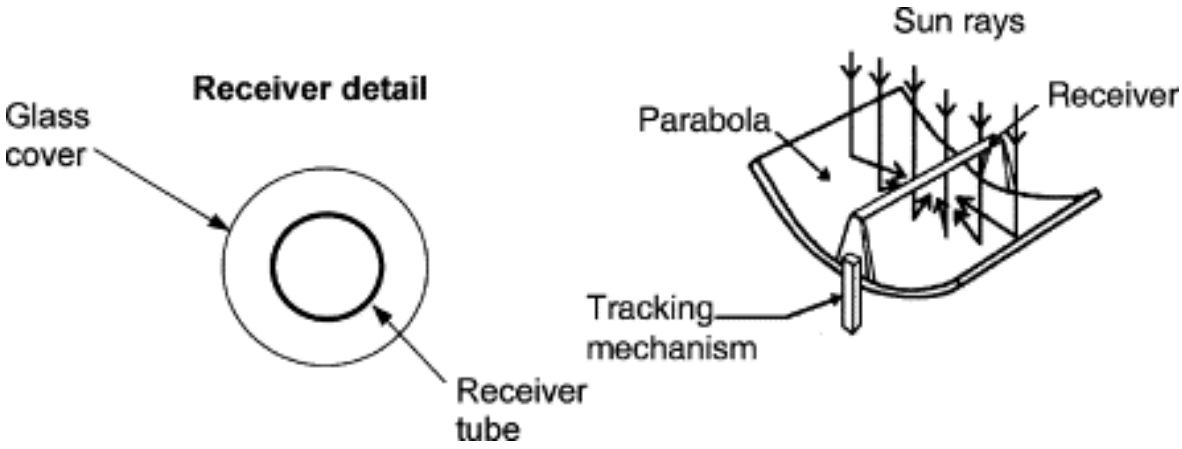

Figure 2-5 Schematic of a parabolic trough solar thermal collector. Reproduced from (Kalogirou, 2004) with permission from Elsevier.

Solar collectors can easily achieve temperatures of 50°C - 150°C required for this project (Mauthner, 2014). Also capable of producing steam directly (Chu, 2018), solar thermal collectors

could be used to drive the condensing engine for renewable electricity production. The development of solar steam generation projects has grown significantly, with over 300 plants in different stages of development all over the world (Dellicompagni, et al., 2018).

An important point for investigation at this juncture is a comparison between solar thermal and photovoltaics (PV). PV panels harness the Sun's radiation to produce electricity, and therefore offer a competing option to the combined system of solar thermal collector and condensing engine. Mauthner (2014) suggests that to meet the scope of this project a range of technologies could be used, including evacuated tube collectors, advanced flat plate collectors, small parabolic trough collectors or advanced evacuated tube collectors. Figure 2-6 shows that the maximum efficiencies of these types of solar thermal panels range between 69% - 85%. However, the panel's efficiency is closely linked to its temperature (Cooper & Wallace, 2008). The water is to be heated from ambient, assumed to be 20°C, to 100°C to power the engine under atmospheric conditions. Taking the mean collector temperature, the average of the inlet and outlet temperatures, as 60°C and ambient temperature as 20°C results in an estimated efficiency of around 60% - 70%. This is higher than the energy efficiency achieved by PV panels, which typically operate around 17% - 18% currently (IRENA, 2019). In addition to this, solar thermal panels are less complex than PV, cost less, and require less space (Renewable Energy Hub UK, 2019). This goes some way to explaining the expanding use of solar thermal technology.

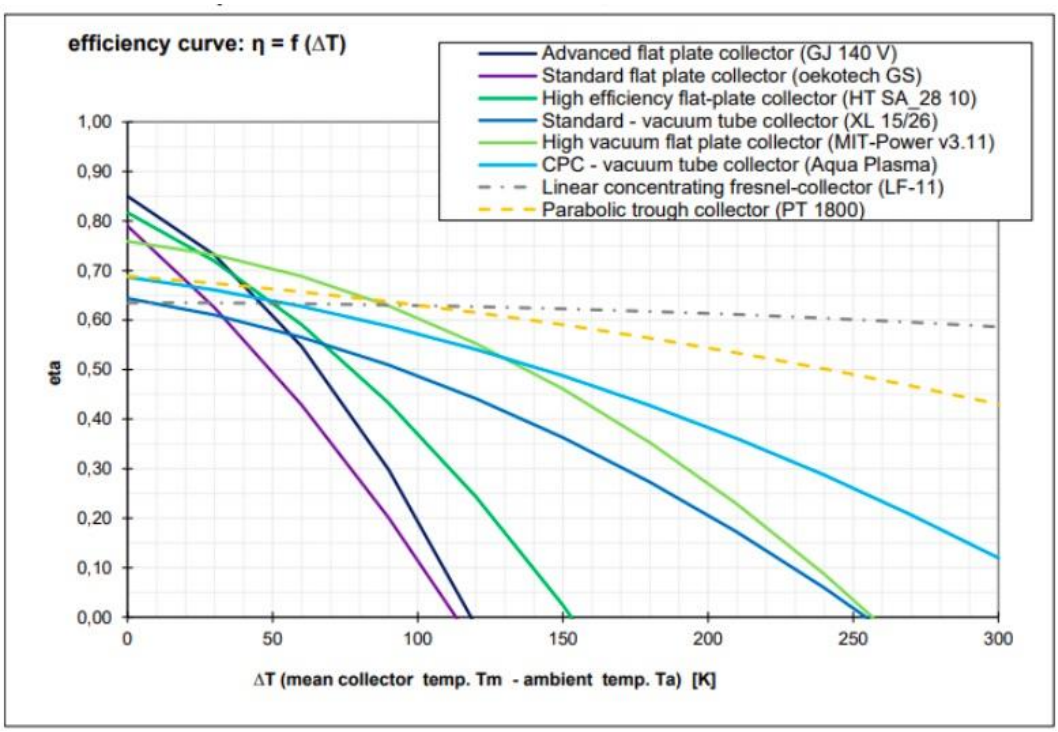

Figure 2-6 Efficiency of different types of solar thermal panels as a function of panel temperature. Credit: (Mauthner, 2014).

However, combining the solar thermal collector with a condensing engine, assumed to be operating at an electrical efficiency of 10% in this case, gives a total electrical efficiency of just 6% - 7%. Despite having lower electrical efficiency compared to PV panels, the combined system is still attractive. First, a small scale solar thermal power plant could control the destination of the heated fluid and provide both hot water and electricity to its community, increasing the technology's flexibility. Additionally, if running at 100^{o}C this system could utilise sensible heat thermal storage tanks to supply the engine and produce electricity during night-time hours. This is less complex and more cost effective than the battery setup that would be required if using PV panels in the same scenario (Kennedy, et al., 2022). However, it is noted that the combined solar thermal and condensing engine system would need to be competitive with the PV system economics. The cost of manufacturing solar panels has reduced significantly in recent years, with the cost of a solar module falling by up to 93% between 2010 and 2020 (IRENA, 2022). The Levelised Cost of Electricity (LCOE) associated with solar projects in a number of different countries in 2019 ranged from 0.04USD/kWh to 0.14USD/kWh (IRENA, 2022).

A potential standout use for the combined solar thermal system with condensing engine could be combined purification of water and renewable energy production for remote and rural communities. This is achieved through the evaporation of the contaminated water in the solar thermal system, passing the steam through the engine to produce electricity, and the condensation and collection of the thermally distilled water. The same outputs from a PV system would require a separate purification process, such as reverse osmosis, to be driven by the electricity produced by the PV, thus reducing electricity available to the user.

It is concluded that the use of solar thermal panels in combination with the condensing engine has promising applications in small scale domestic scenarios, especially rural areas of developing countries without access to clean water and/or electricity. The existence of such a market provides further justification for the need for a safe and sustainable low-grade heat recovery technology such as the condensing engine.

2.1.3 Small-Scale Low-Grade Waste Heat Case Studies

Whilst the condensing engine has the theoretical capability to recover low temperature heat on large scales, it was suggested in the introduction of this thesis that the condensing engine is more suited to low power applications because of the technology's energy density. It is therefore important to highlight the existence of suitable small-scale applications, in addition to the industrial applications already covered in Section 2.1.1. One example is small scale solar thermal collectors and their integration with the condensing engine, already discussed above. Further examples are

given by (Landelle, et al., 2017) in the context of use of Organic Rankine Cycle systems, including biomass, geothermal, waste heat recovery from industry, and waste heat recovery from internal combustion engines. Some additional examples are discussed below in Section 2.1.3 to further support the development of the condensing engine for small scale low temperature applications.

2.1.3.1 Off-Grid Electricity Production: Diesel Generators

This is relied upon in rural areas without grid connection (Kim & Jung, 2018) or when reliability of power is needed (Energy Solutions, 2018). South Africa is estimated to have 3500MW of back-up diesel generator capacity because of regular blackouts or "load shedding" by the country's electricity provider (Pretorius, et al., 2015). As much as 65% of input energy is wasted by a typical diesel generator (Ghoreishi-Madiseh, et al., 2019), with LGWH available at around 90^{o}C from the cooling water (Langhan & O'Toole, 2017). Use of a condensing engine could improve efficiency and reduce fuel requirement. The same is also true of the jacket water used to cool combined heat and power engines (CHP).

2.1.3.2 Marine & Maritime

This is of relevance to this project through the funding received by the Southampton Marine & Maritime Institute (SMMI). The cooling water onboard a typical cruise liner can reach temperatures of 30–95^{o}C with as much as 26,000kW of thermal energy requiring dissipation to protect the engines (Meyer, 2018). Stricter fuel regulations will result in economic incentive to recover this energy which is currently dumped into the sea in most cases. The condensing engine could be used to produce electricity, typically provided by generators using fossil fuels on board these ships (Sommer, 2018).

2.1.3.3 Low Temperature District Heating

Domestic heating and cooling accounts for one third of society's energy consumption (Schmidt, et al., 2017), with demands met by a centralised district heating network in some cases. Thermal energy from fossil fuels, renewables, and waste heat can be collected in one location and distributed to homes and office spaces as needed (Hartley, 2018). 17,000 systems of this nature exist in the UK, with almost 500,000 connections (Hartley, 2018). These typically operate at temperatures between 70^{o}C - 120^{o}C (Schmidt, et al., 2017). However, research in literature suggests a trend towards low-temperature district heating (LTDH) which instead operates at 50^{o}C - 55^{o}C (Schmidt, et al., 2017). This reduces fossil fuel consumption and minimises thermal losses. Therefore, a condensing engine could be used in existing systems to step down any source of higher-grade heat to be used in LTDH networks, producing power whilst doing so. The engine could be used on a large scale in a centralised hub or on small scales within the community itself.

However, it should be noted that most end user heating systems are designed to operate at the original higher temperature. For example, radiators will have been sized to provide sufficient space heating using the supply water temperature they were designed for. Reducing the water temperature in a radiator will reduce its effectiveness in heating the space. Therefore, LTDH will face challenges when trying to synergise with existing systems not designed for operation at lower temperatures. Future systems may instead employ a heat pump to upgrade lower temperature heat to that required by domestic heating. Nonetheless, this example is given in this thesis to demonstrate the type of opportunities for temperature step changes which the condensing engine could make use of in the future.

2.1.4 Summary of Low-Grade Heat Case Studies

This section has reviewed several different low-grade heat case studies. A summary of this information is given in Table 2-2. This section is deemed to have justified the substantial resource that low-grade heat offers and the resulting need for recovery technologies. The technologies that currently exist for low-grade heat recovery will be addressed next.

Table 2-2 Summary table of the LGWH case studies reviewed in Section 2.1.

Source Originator	Nature of Stream	Temperature (°C)	Comments	References
Industrial Thermal Processes	Cooling/process water	50-90	• Steam can be used directly as the working fluid in the CE. • 100TWh/yr of waste heat below 200°C in Europe. • 16 TWh/yr of waste heat between 50°C - 150°C in Germany alone.	(Chin, et al., 2018; Bruckner, et al., 2015; Ammar, et al., 2012; Brueckner, et al., 2017; Zhang, et al., 2019)
	Hot air (eg. from drying)	90-150		
	Flue/exhaust gases	70-150		
	Steam	95-100		
Renewables	Solar Thermal	65-130	• Standalone energy production with water purification. • 6.0% - 7.0% estimated electrical efficiency with integrated solar thermal collector and condensing engine.	(Li, 2019; Chu, 2018)
	Bio Steam	100		(TCE, 2019)
Marine and Maritime	Cooling Water	30-95	• At nominal load and full speed, a cruise ship can dissipate 26,000kW of heat into the cooling water	(Meyer, 2018)
Off Grid Diesel Generators	Cooling Water	90	• Waste 65% of thermal input as heat. • Small scale application.	(Langhan & O'Toole, 2017)
Domestic	Low Temperature District Heating	70-120	• Domestic heating and cooling accounts for 1/3 of society's energy consumption. • Small scale application.	(Schmidt, et al., 2017)

2.2 Current LGWH Recovery: The Organic Rankine Cycle

It is important to review current LGWH recovery technologies to understand the context of the condensing engine's characteristics in comparison to competing technologies. A review of the available technologies is given in section 2.2.1. Of these, the Organic Rankine Cycle (ORC) is the most common in literature and the most important to understand for comparison against the condensing engine. Therefore, the remainder of this section focusses only on the ORC.

2.2.1 LGWH Recovery Technology Review

Several technologies exist or are in development for the recovery of LGWH. These can generally be categorised into direct heat use technologies or heat to power technologies. Typical examples of direct heat use include heat exchange and thermal energy storage with the ability to upgrade heat using heat pumps. Heat exchange can often be the simplest way of achieving re-use of thermal energy, providing a suitable heat sink is available. For example, the food industry requires 25% of its process heat below 100^{o}C (Frate, et al., 2019). Thermal energy storage (TES) can be especially useful in balancing the supply from intermittent sources and can store energy in summer to be released in winter. When water is used as the storage medium in well insulated tanks energy densities up to 60-80kWh/m^{3} can be achieved (Dahash, et al., 2019). If LGWH is considered too low temperature for direct re-use this can be upgraded using a heat pump, capable of lifting LGWH by 50^{o}C - 100^{o}C (Mikielewicz & Wajs, 2018; Frate, et al., 2019). However, direct heat use is considered less flexible than heat to power as a local heat sink is required. It is therefore not in direct competition with the condensing engine, which instead produces power with the heat, and not considered any further in this research.

Typical heat to power examples of LGWH recovery include thermoelectric devices and the ORC. Thermoelectric devices produce a voltage from a temperature gradient by either using a shape memory alloy to lift a weight, known as solid-state thermoelectric devices, (Langhan & O'Toole, 2017) or by using the *Seebeck* effect, known as thermal electrochemical devices (Gao, et al., 2017). Thermoelectric devices are compact, low-maintenance, and reliable (Langhan & O'Toole, 2017; Konig, et al., 2018) making them suitable for applications with space restrictions and where no moving parts are desirable. However, thermoelectric devices are still considered developmental technologies in the application of recovering low-grade heat (Hyeongwook, et al., 2016) expected to reach electrical efficiencies of just 3% - 5% with optimisation (Konig, et al., 2018). As a result, these are not considered any further in this research. Instead, this review focusses on the Organic Rankine Cycle. It can achieve greater efficiencies than thermoelectric devices and is the more

common LGWH recovery technology currently being explored in literature, therefore providing the more appropriate benchmark for comparison against the condensing engine at this stage.

2.2.2 ORC Process Description and Background

ORCs are well established and were used commercially as early as 1980 (US DOE, 2008). The basic *Rankine* cycle involves evaporating a working fluid through heat exchange with the LGWH and then expanding it, for example through a turbine, to generate electrical power. The vapour is then condensed and pumped back to the evaporator. This process is shown in Figure 2-7. Traditionally, steam was adopted as the working fluid. However, this is best suited for very high temperature applications. For LGWH recovery an organic fluid, such as a refrigerant, with low boiling point is usually used (Tchanche, et al., 2011).

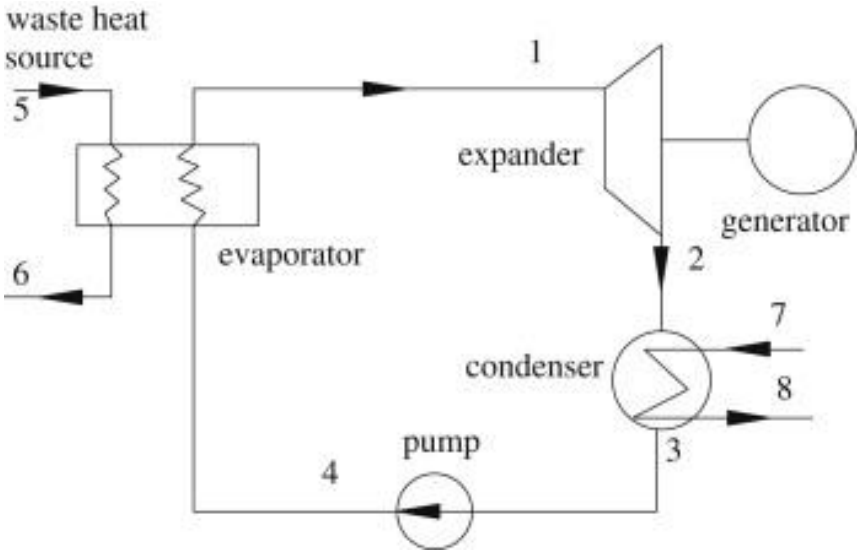

Figure 2-7 Schematic of the ORC process in application to waste heat recovery. Reproduced from (Liu, et al., 2013) with permission from Elsevier.

ORC systems are a mature technology when applied in the Mega-Watt range with high heat source temperatures, achieving electrical efficiencies of around 20% - 25% (CES Energy, 2019; Landelle, et al., 2017). For context, Landelle, et al. (2017) state that commercial ORC plants are available in the 10 kWe to 10 MWe range converting heat sources between 80°C - 300°C. The need for heat recovery technologies capable of operating at both low temperature and on small scales, identified in section 2.1, has also been recognised in ORC literature. Consequently, the development of 'micro ORCs' have recently become a topic of focus in recent research (Bianchi, et al., 2019). An experimental 16.3kW low-temperature heat recovery ORC tested in literature is shown photographed in Figure 2-8, giving context to the physical scale of the technology.

Figure 2-8 Example of a 16.3kW low temperature heat recovery ORC system tested in literature. Note, cooling water circuit not shown in image as it was located on the roof. Reproduced from (Li, et al., 2021) under CC BY.

2.2.3 ORC Operational Characteristics: Comparison Against the Condensing Engine

There are two main characteristics which separate the ORC from the condensing engine: working fluid choice and operating pressure. These are discussed simultaneously in Section 2.2.3 as they are intrinsically linked. Whilst the below review of the ORC is by no means exhaustive, given the depth of research available in literature, it is sufficient to allow comparison against the condensing engine and understand advantages and disadvantages of the respective technologies. This has allowed specific applications to be identified where the condensing engine could offer benefit over the ORC as well as ones where it is less suited, already discussed in the introduction of this thesis.

As discussed in Section 2.2.2, the ORC typically uses an organic refrigerant as the working fluid. As a result, review papers in literature identify safety and environmental impacts as key considerations when choosing an ORC working fluid (Kumar & Dibakar, 2021; Rahbar, et al., 2017). Review papers categorising optimum working fluids by heat source temperature find R245fa, R134a, R236fa, R236ea, R152a, R227ea, R143a, R23, R7146, R218, R124, Pentane, Isobutane, and Ammonia to be most appropriate for LGWH recovery (Rahbar, et al., 2017; Mahmoudi, et al., 2018). Typical concerns when choosing working fluid for an ORC system are the global warming potential, the ozone depletion potential, and/or the flammability or toxicity of the fluid (Kumar & Dibakar, 2021;

Rahbar, et al., 2017; Mahmoudi, et al., 2018). As a result, Velez (2014) suggests that there does not exist one working fluid which can satisfy all criteria for use in an ORC, and compromise must be made. For example, Wajs & Mikielewicz (2018) have developed an ORC using ethanol, which whilst not having a global warming potential it is flammable. Velez (2014) has studied R600, Toluene, R113, and R245a as commonly used working fluids. Whilst these might have desirable thermal properties; R600 is flammable, Toluene is toxic, and R113 & R245a contribute to global warming. Dependent on the chosen fluid, the relevant safety measures must be considered during design and operation of ORC systems. Leakage must also be minimised as far as possible, both during operation and decommissioning. An environmental study of ORCs suggested a typical annual leakage rate of working fluid from an ORC system of around 2% during operation, and typical loss of fluid around 20% at end of life (Li, 2019). For context, the research performed by Wang, et al. (2019) gives a generalised working fluid use of around 5.6 kg/kW for typical ORC systems.

However, the thermal properties of fluids used in ORC systems provide a significant benefit to heat recovery applications, especially for low temperature heat. They have a lower boiling point than water and therefore allow higher pressures to be used in the heat engine for a given heat source temperature. Quoilin, et al. (2013) state that pressure does not generally exceed 30 bar in ORC systems whilst providing results from ORC experimental studies where pressures between 6bar - 20bar were seen. Evaporator pressures seen in low-temperature small-scale ORC systems in recent review papers range from 1.3bar - 16bar, with 10+ bar being typical (Rahbar, et al., 2017; Muller & Howell, 2021). As is discussed later in the thesis, historic heat engines transitioned towards higher operating pressures due to the higher energy density provided. Greater power can be recovered from a given mass of fluid, meaning the engine requires a reduced footprint. Therefore, the atmospheric condensing engine will not be able to achieve comparable energy densities when compared to the ORC due to the lower operating pressure. As a result, the condensing engine is not as well suited to larger power applications where physical scale will become a limiting factor.

However, when analysing the operational characteristics of the two technologies for use on smaller scales, the condensing engine has beneficial properties. For example, water is a much more accessible working fluid that has reduced environmental and safety concerns. Additionally, the condensing engine operates at atmospheric pressure, reducing risk of leakage and explosion. This makes it ideal for use in renewable energy systems in remote and rural communities, investigated in Chapter 5 of this thesis, as well as domesticated small-scale systems. The use of water as a working fluid and the requirement for components rated only to atmospheric pressure should also enable a cost-effective system relative to the ORC.

It is noted that an economic analysis of the condensing engine is not included in the scope of this project, and this is recommended for future research once the technology is optimised. However, it is acknowledged in literature that economics could cause difficulties in ensuring small scale ORC plants are profitable (Frate, et al., 2019; Quoilin, et al., 2013). As a result, it is thought by some that small scale ORCs are unlikely to be widely adopted by the market without incentives or subsidies (Tocci, et al., 2017). For reference, the experimental 16.3kW ORC photographed in Figure 2-8 was built for recovery of low temperature heat between 90^{o}C - 150^{o}C and had a reported total investment of $113,040 US dollars. Approximately 61% of expenditure was attributed to the ORC system itself (expander, condenser, preheater, superheater, pumps, working fluid, etc) and the remainder was associated with the control system, software design, and cooling water system (Li, et al., 2021). Another 11kW system reported in literature had a total cost of $20,470 US Dollars. However, this system was recovering heat in the range of 33^{o}C - 450^{o}C and did not give as comprehensive a cost breakdown, not including software and control costs for example (Zhang, et al., 2019). This same research suggested theoretical predicted LCOE values of between 0.18 $/kWh to 0.27 $/kWh for ORC systems using R245fa and R123 as working fluids and evaporation temperatures of 75^{o}C - 150^{o}C (Zhang, et al., 2019). For reference, the cost of working fluid in this study was quoted as 17.97 $/kg for R245fa and 14.81 $/kg for R123 (Zhang, et al., 2019). This is higher than the cost of water would be for the condensing engine.

Section 2.2.3 has identified that the condensing engine should focus on low power scale applications for low temperature waste heat recovery. This is supported by previous literature which has already suggested potential power scales between 1kW - 200kW for the atmospheric condensing engine (Muller, et al., 2018; Muller & Howell, 2021). Further investigation into the scalability of the condensing engine is required to confirm this hypothesised range and an economic study to be performed on an optimised engine to demonstrate commercial viability. The economic values for ORC systems given above can be used for comparison.

2.2.4 Efficiencies of Small-Scale Low Temperature ORC Systems

The thermal efficiency of any heat engine is the useful work out as a ratio of the required energy input. In the case of both the ORC and condensing engine, this is the mechanical or electrical power production as a ratio of the waste heat supplied to the evaporator or boiler, see Equation (2.1). It is important to distinguish between these, as mechanical power output will give a higher efficiency as the conversion of mechanical to electrical energy suffers associated losses.

$$\eta_{th} = \frac{W_{out}}{Q_{in}} \tag{2.1}$$

Where:

- η_{th} is the thermal efficiency as a decimal fraction.
- W_{out} is useful power output (J).
- Q_{in} is required thermal enginery input (J).

Landelle, et al. (2017) have performed a comprehensive review of numerous experimental ORCs of different scales, heat source temperatures, and expander technologies. Importantly, Landelle, et al. (2017) have presented the data collectively, using log plots to account for the wide range in ORC operations in literature. This will allow comparison of small scale and low temperature ORCs versus the condensing engine during future comparison. Figure 2-9 shows that ORC plants with a heat source temperature between 50 °C - 150°C achieve, on average, electrical efficiencies of 5% - 10%. Figure 2-10 shows that ORCs rated between 1kWe to 200kWe will achieve average electrical efficiencies of around 5% - 15%. However, ORC systems of a similar power scale to the Mk.II condensing engine tested at the UoS have average electrical efficiencies around 2% - 3%.

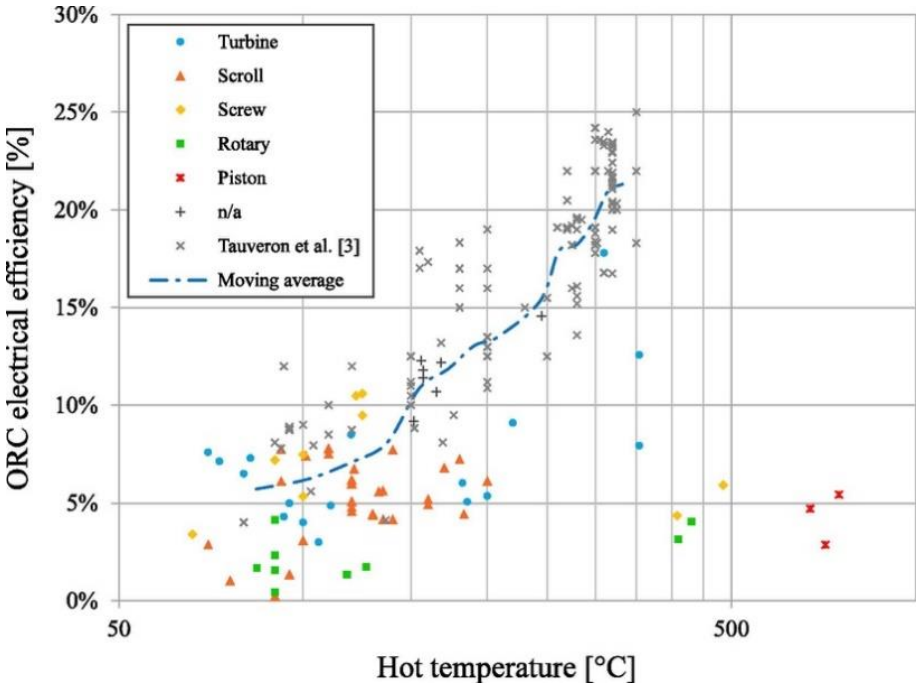

Figure 2-9 Plot showing typical heat source temperature vs resultant ORC electrical efficiency for different expander technologies. Each x-axis step is 50°C on the log scale. Reproduced from (Landelle, et al., 2017) with permission from Elsevier.

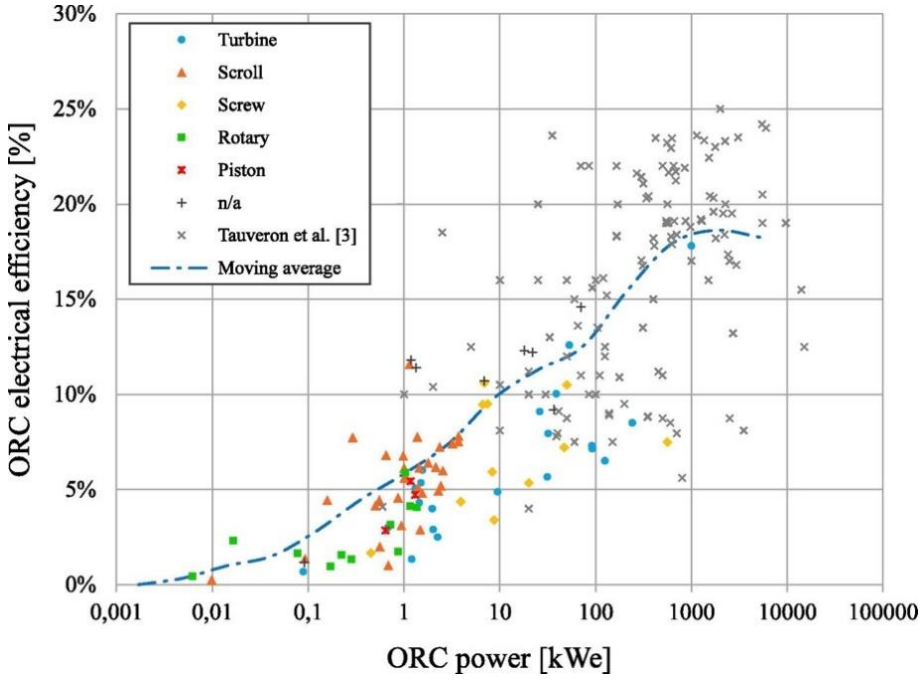

Figure 2-10 Plot showing typical ORC power vs electrical efficiency for different expander technologies. Reproduced from (Landelle, et al., 2017) with permission from Elsevier.

These values are supported by other sources in literature not included in the database created by Landelle, et al. (2017). Haddad, et al. (2014) give efficiency values of no higher than 8% for several small-scale ORCs studied for the recovery of LGWH. Rahbar, et al. (2017) reported results from small-scale ORC systems operating with heat source temperatures between 58°C - 170°C with a mixture of mechncial and electrical efficiencies ranging between 3.9% - 13.7% and power outputs between 0.15kW - 220kW. Kumar & Dibakar (2021) reported ORC systems with different configurations and working fluids, with heat source temperatures in the range of 90°C - 220°C and thermal efficiencies of 6% - 12.5%.

However, ORC experiments reported in literature use a variety of heat source and sink temperatures leading to difficulty in fairly comparing different technologies. The *Carnot* efficiency, see Equation (2.2), is the highest theoretical efficiency a heat engine can achieve between a given heat source and heat sink temperature. Equation (2.2) shows that when lower heat sink temperatures or increased heat source temperatures are used higher efficiencies can be achieved.

$$\eta_{carnot} = 1 - \frac{T_c}{T_h} \tag{2.2}$$

Where:

- T_c is the heat sink temperature (K).
- T_h is the heat source temperature (K).

Therefore, it is important to consider the operating conditions when comparing test results of different heat engine technologies. This can be done by using the second law efficiency, defined as the percentage of the maximum theoretical efficiency that is achieved in practice. As the maximum theoretical efficiency is defined by *Carnot*, the heat source and sink temperatures are accounted for in this analysis; see Equation (2.3).

$$\eta_{II} = \frac{\eta_{th}}{\eta_{carnot}} = \eta_{th} \times \frac{1}{\left(1 - \frac{T_c}{T_h}\right)} \tag{2.3}$$

The second law efficiency of ORC systems is not reported as commonly as the thermal efficiency. However, the review by Landelle, et al., (2017) has collated second law efficiency data for a series of experimentally tested ORCs with increasing power rating; see Figure 2-11. The average second law efficiency plateaus at around 40% for high, established power ratings. For systems with power rating of 1kW - 200kW the average second law efficiency ranges from 20% - 40%. A recent review by Muller & Howell (2021) has also calculated the second law efficiency for some recent low-temperature small-scale ORC tests for comparison against a historic condensing engine. Systems with heat source temperatures of 78 °C - 101°C, heat sink temperatures of 14 °C - 36°C, and power ratings of 0.5kW - 1.4kW were found to have second law efficiencies of 20% - 35%. These second law efficiencies provide a benchmark for the required efficiency of a modern condensing engine to be competitive with current ORC systems at low power scales.

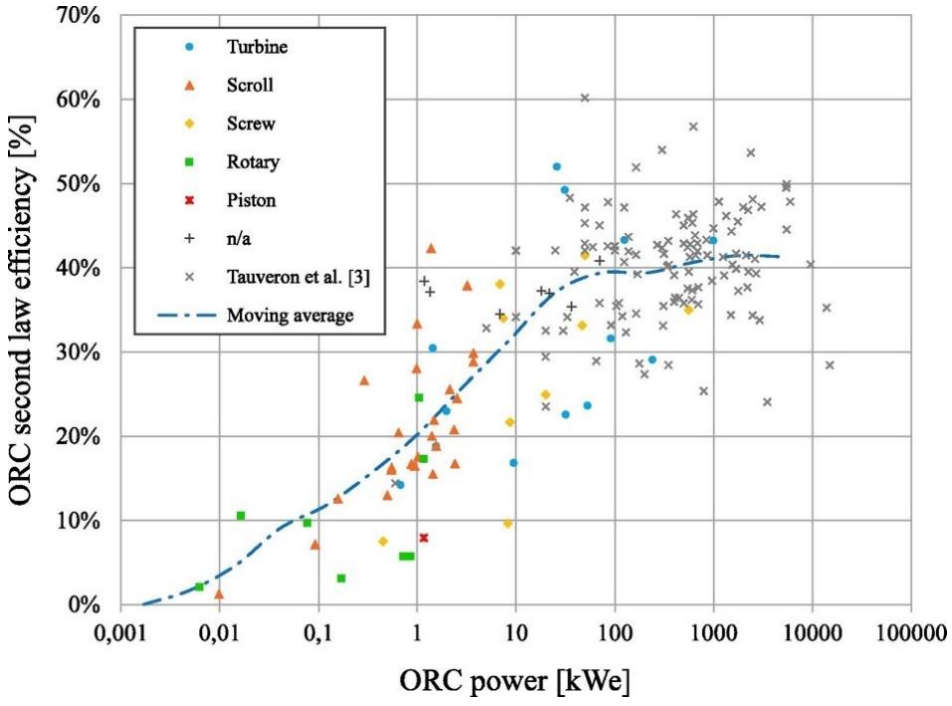

Figure 2-11 ORC Second law efficiency vs electrical power for a number of ORC's reviewed in literature, categorized by different expander technologies. Reproduced from (Landelle, et al., 2017) with permission from Elsevier.

It is acknowledged by the author of this research that the data from (Tauveron, et al., 2015) appears to suggest efficiency values above that of the moving average in Figure 2-9 and Figure 2-10. This data is from a separate database of commercial ORC systems and was merged with the database of experimental ORC systems created by Landelle, et al. (2017) to give a wider understanding of current systems. ORC data given by Tauveron, et al. (2015) suggests electrical efficiencies around 12.5% for a heat source temperature of 100^{o}C and around 10% - 25% for power scales between 1kW and 200kW.

However, the second law efficiency data given by Tauveron, et al. (2015) is more evenly spread around the moving average in Figure 2-11. This is created by a transition point at around 10kW, where lower power values are dominated by experimental systems and greater power values are dominated by commercial systems. This could be attributed to the suggestion in literature that small scale ORC systems may not be economically viable (Frate, et al., 2019; Quoilin, et al., 2013; Tocci, et al., 2017). As a result, the moving average value for powers greater than 10kW is set by the commercial data. Therefore, future comparison of the condensing engine against the ORC using the second law efficiency for power scales of 1kW - 200kW incorporates both experimental and commercial data.

2.2.5 Summary of Current Technologies for LGWH Recovery

This section has reviewed several current technologies for the recovery of LGWH. A summary is given in Table 2-3. Of the heat to power technologies in direct competition with the condensing engine the ORC is the most common and has been the focus of this review. This review identified that the ORC offers an increased energy density compared to the condensing engine but is less suited to smaller scale applications due to its choice of working fluid and operating pressure. Therefore, it was concluded that the condensing engine technology should focus on low power applications of low temperature heat recovery, around 1kW - 200kW.

Table 2-3 Summary of LGWH recovery technologies along with advantages and disadvantages and sources of information.

Technology Type	Technology	Operating Temperature	Advantages	Disadvantages	References
Heat to Power	Organic Rankine Cycle (ORC)	80°C - 300°C	• Mature technology at high temperature and large scale • More efficient at high temperature and large scale (20% - 25%) • Higher energy density	• Less efficient at low temperatures and small scale (5% - 15% max) • Uses organic refrigerant (toxic, flammable, etc) • Operates at high pressure	(Landelle, et al., 2017) (Rahbar, et al., 2017) (Kumar & Dibakar, 2021) (Mahmoudi, et al., 2018) (Frate, et al., 2019) (Haddad, et al., 2014) (Velez, 2014)
Heat to Power	Thermoelectric	60°C +	• Compact • No moving parts	• Inefficient at low temperatures (Approx. 3% - 5%)	(Konig, et al., 2018) (Langhan & O'Toole, 2017)
Direct Heat Use	Heat Exchange	35°C +	• Often uses simple technology • Can target lower temperature range	• Less flexible than power production • Requires a heat demand	(Frate, et al., 2019)

Technology Type	Technology	Operating Temperature	Advantages	Disadvantages	References
Direct Heat Use	Heat Pumps	< 130°C	• Can improve the low temperature range not otherwise usable	• Organic working fluid • High operating pressures • Still requires a downstream heat sink	(Frate, et al., 2019) (Mikielewicz & Wajs, 2018)
Direct Heat Use	Thermal Storage	35°C +	• Balances supply and demand of heat	• Expensive • Requires large volumes	(Dahash, et al., 2019)

2.3 The Atmospheric Condensing Engine: An Alternative Technology for Low Grade Heat Recovery

The literature review thus far has explored the potential of low-grade heat recovery as well as current technologies used in literature for small scale low temperature applications. Specifically, the benefits of the condensing engine when applied to low power applications in domestic or rural settings have been reported. Therefore, this research proposes the development of the condensing engine technology as an alternative option to current systems. Some background surrounding this technology is given here as well as some justification for its development and an assessment of the current state of the research into the technology.

2.3.1 Condensing Engine Background

The phenomenon of using vacuum generated by the condensation of steam is recorded in literature as far back as 1606, used to extract water from wells (Ewing, 1910). Thomas Newcomen developed an engine in 1705 using this principle, where atmospheric steam was condensed to create sub-atmospheric pressure allowing a piston to be acted upon and driven by the atmosphere, thus producing work. This was called an 'atmospheric engine' or 'condensing engine'. Newcomen condensing engines were used to drive water pumps in mines and were commonplace by 1725 (Ewing, 1910).

James Watt went on to further develop the Newcomen engine, making numerous improvements. He noted that the condensation of steam inside the cylinder of the Newcomen engine caused thermal losses in the cylinder wall, resulting in premature condensation of steam admitted to the cylinder in the next cycle and an associated reduction in efficiency; see Figure 2-12. Watt understood that the cylinder (B) needed to remain hot and introduced a separate condenser (C) to the system (Ewing, 1910). Watt also introduced an air pump to maintain sub-atmospheric pressure and evacuate condensate. Furthermore, Watt developed the double acting cylinder which allowed steam to be used as working fluid on both sides of the piston (P), increasing power output.

Watt's final improvement to the engine was that of steam expansion. By closing the cylinder steam inlet valve (V) to stop flow entering from the boiler before the end of the stroke the residual steam is allowed to expand, further driving the piston and removing additional work from the steam (Ewing, 1910). This results in an increase in engine efficiency because a greater amount of work is recovered from the same mass of steam. However, it is believed that steam expansion was never explored practically on atmospheric condensing engines in the 18th Century, likely because of

technical limitations. Nor could the full theoretical effect on efficiency be properly understood at this time, with key thermodynamic principles such as *Carnot* yet to be developed. As a result, along with the phase out of steam power, the use of steam expansion on the atmospheric condensing engine became something of historical interest only.

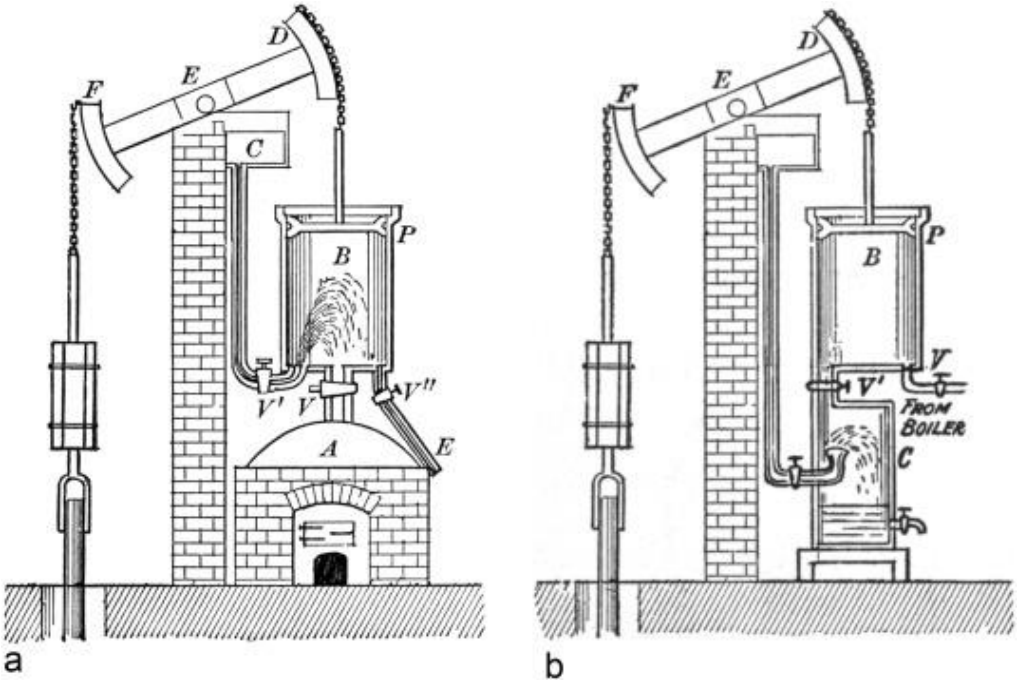

Figure 2-12 Diagrams of the Newcomen (a) and Watt (b) engines showing the improvements of the Watt engine, mainly the separate condenser and air pump. A = Boiler. B = Cylinder. C = Condenser. E, D, F = Beam. P = Piston. V = Boiler Valve. V' = Condenser Valve. Reproduced from (Muller & Parker, 2015) with permission from Elsevier. Original figures taken from (Black & Davis, 1913) and (Thurston, 1878).

However, through the benefits that made it popular in the 18th century, the condensing engine is of relevance again today, as explored in the introduction and Section 2.2.3. The engine uses water as a safe and sustainable working fluid at low temperature and pressure. This reduces the required complexity of the system, and with it, the cost. Synergy also exists with sources of low-grade heat emitted directly as steam, already examined in this literature review.

2.3.2 The Condensing Engine Cycle and Theoretical Efficiency

The condensing engine cycle, including use of steam expansion, is shown in Figure 2-13. Figure 2-13 depicts a 'double acting' engine, as developed by Watt, meaning the cylinder has two closed chambers separated by the piston. Each chamber is functional, and each will be charged with steam once per full engine revolution. In phase one of the cycle, steam is supplied from the boiler to the cylinder driving the piston against a partial vacuum thus producing work. In phase 2, the

inlet valve is closed part way through the stroke. This allows steam expansion to take place for the remainder of the stroke in phase 3, increasing engine efficiency. The expansion ratio ('ER' or '*n*') is defined as the ratio of the cylinder's swept volume to the volume of steam charged to the cylinder. An expansion ratio of *n* = 2 is used in this example. In phase 4, the working steam is released to the condenser. Rapid condensation of the steam creates a partial vacuum which is translated back to the cylinder through the open steam outlet valve. This provides the driving force for the next stroke, in this case by supplying steam to the opposite side of the piston.

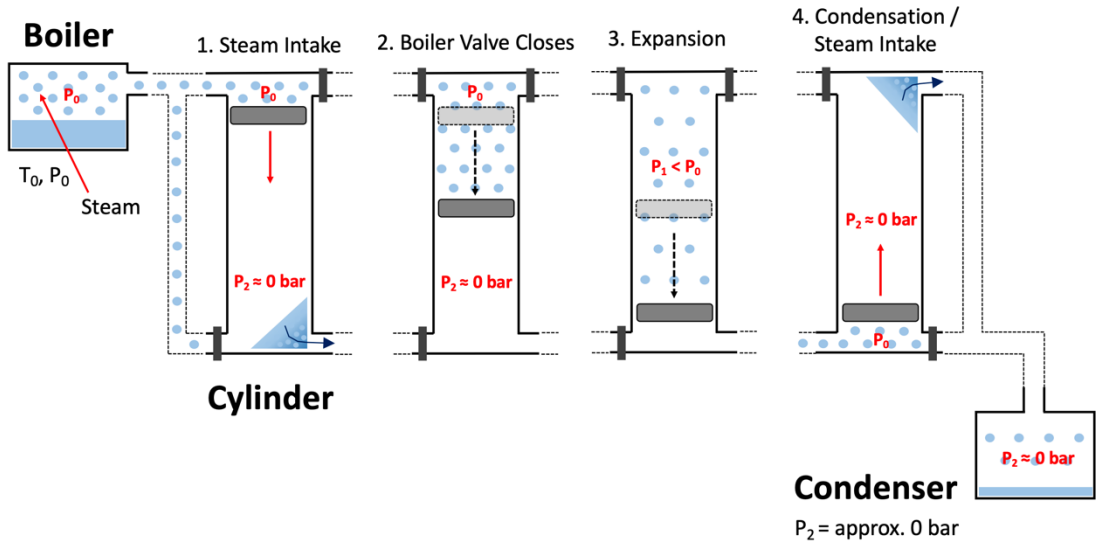

Figure 2-13 Diagram of the four stages of steam expansion in a condensing engine with double acting cylinder.

Bortolin, et al. (2021) have plotted the Pressure-Volume and Temperature-Entropy charts for the atmospheric condensing egnine with expansion ratio of *n* = 4, shown in Figure 2-14. Transition from phase (1) to (2) represents the heating of water and generation of steam in the boiler. Transition from phase (2) to (2)' represents the isentropic expansion of steam inside the cylinder. Transition from phase (2)' to (3)' represents a constant volume heat transfer during which the steam condenses and pressure inside the cylinder is reduced to equal the saturation pressure associated with condenser temperature. The transition from phase (3)' to (4) represents final condensation at constant pressure and transition from (4) to (1) represents compression of the condensate through pumping back to that start of the process cycle.

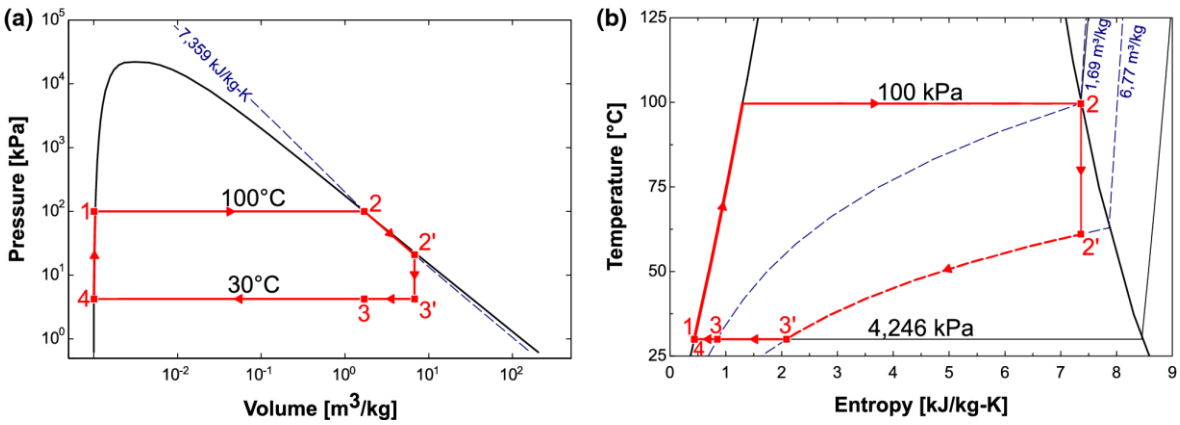

Figure 2-14 (a): P-v diagram of atmospheric CE with expansion. (b): T-s diagram of atmospheric CE with expansion. Reproduced from (Bortolin, et al., 2021) with permission from Springer Nature.

A theoretical analysis of steam expansion inside the condensing engine cylinder was performed at the UoS and detailed in the published paper (Muller, et al., 2018) and Group Design Project report (Ho Chan, et al., 2017). This calculated the work produced at each stage of the expansion cycle, defined as a function of pressure and volume. The pressure inside the cylinder will remain constant during steam charging and will subsequently reduce non-linearly during expansion; see Figure 2-15 for the case with an expansion ratio of n = 4.

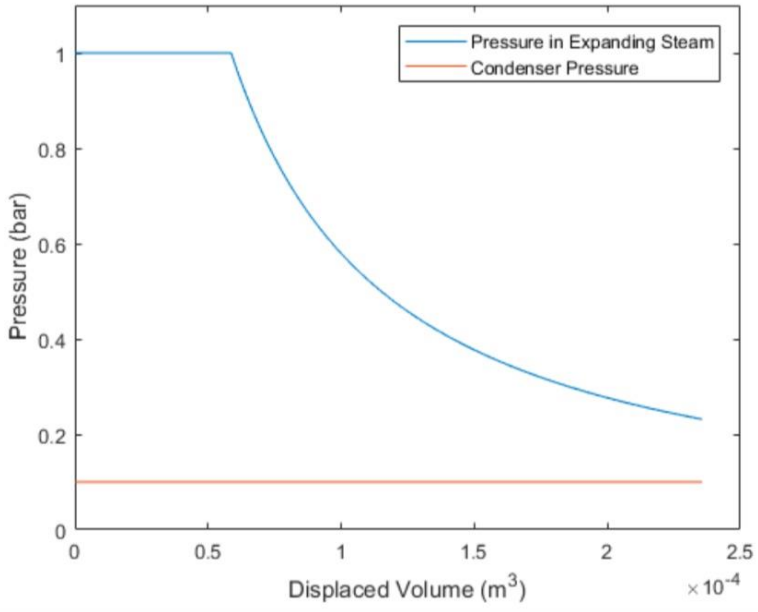

Figure 2-15 Theoretical pressure profile inside the cylinder during an expansion ratio of n = 4. Credit: (Ho Chan, et al., 2017).

The first work term, found during steam inlet, is treated as boundary work. This is work produced at constant pressure and is defined by Equation (2.4). The boundary volume is the volume of swept cylinder at constant pressure, related to the total cylinder volume by Equation (2.5).

$$W_{bdy} = P_b \times V_{bdy} \tag{2.4}$$

$$V_{bdy} = \frac{V_{cyl}}{n} \tag{2.5}$$

Where:

- W_{bdy} is boundary work (J).
- V_{bdy} is boundary volume (m^3).
- P_b is boiler pressure (Pa).
- V_{cyl} is total cylinder volume (m^3).
- n is the expansion ratio.

The next work term is produced during steam expansion, found by Muller, et al. (2017) for both the isentropic and isothermal cases. Isentropic expansion assumes that the process is (1) adiabatic, meaning no heat losses, and (2) reversible, meaning no losses due to friction (Cengel & Boles, 2011). In reality, no engine is reversible, and this represents the theoretical maximum work that can be expected from this particular engine (Cengel & Boles, 2011). However, the assumption of isentropic expansion is widely used for heat engine calculations to simplify the problem (Cengel & Boles, 2011).

The isentropic and isothermal expansion work equations used by Muller, et al. (2017) are defined by the ideal gas laws, given in Equations (2.6) and (2.8) respectively. These equations require knowledge of the final pressure after expansion, also conveniently defined by ideal gas laws through Equations (2.7) and (2.9) for the isentropic and isothermal cases respectively.

Isentropic

$$W_{isen} = \frac{1}{\gamma - 1}(P_0 \cdot V_0 - P_1 \cdot V_1) \tag{2.6}$$

$$P_{1,isen} = P_0 \times \left(\frac{V_0}{V_1}\right)^{\gamma} \tag{2.7}$$

Isothermal

$$W_{isot} = P_0 \cdot V_0 \cdot ln\left(\frac{P_0}{P_1}\right) \tag{2.8}$$

$$P_{1,isot} = P_0 \times \left(\frac{V_0}{V_1}\right) \tag{2.9}$$

Where:

- W_{isen} and W_{isot} are the isentropic and isothermal work terms produced during expansion (J).
- V_0 and P_0 are the volume (m^3) and pressure (Pa) at the start of expansion.
- V_1 and P_1 are the volume (m^3) and pressure (Pa) at the end of expansion.

- γ is the dimensionless adiabatic coefficient of expansion, defined as ratio of specific heat capacities at constant pressure and volume, see Equation (2.10). Values are given in literature for several gases and vapours. A value of 1.08 was used by Muller et al (2017).

$$\gamma = \frac{C_p}{C_v} \tag{2.10}$$

Thus far the calculated work terms have been positive in value, due to steam working in the same direction as the piston's stroke. However, there are negative work terms due to losses in the system to account for also. The largest of these is back pressure losses associated with the sub-atmospheric steam pressure acting against the piston stroke. This has already been described as a constant pressure process, and therefore the boundary work equation can again be used; see Equation (2.11).

$$W_{loss} = P_{con} \times V_{cyl} \tag{2.11}$$

Where:

- W_{loss} is the boundary work lost due to back pressure (J).
- P_{con} is the condenser pressure (Pa).

It is noted that additional losses result from driving the mechanical air pump. However, pumping losses are often ignored in heat engine theory due to their negligible size in comparison to all other terms (Cengel & Boles, 2011). The final steps are to calculate the thermal energy requirement of the engine, Equation (2.12), and the associated thermal efficiency, Equation (2.13).

$$Q_{in} = (h_g - h_l) \times m_s \tag{2.12}$$

$$\eta_{th} = \frac{W_{bdy} + W_{exp} - W_{loss}}{Q_{in}} \tag{2.13}$$

Where:

- η_{th} is the thermal efficiency given as a decimal fraction.
- h_g is the enthalpy of the vapour at boiler temperature (kJ/kg);
- h_l is the enthalpy of the feed water at associated temperature (kJ/kg);
- m_s is the mass of steam (kg).

The theoretical analysis described above was used by Muller et al (2018) to evaluate the theoretical efficiency of a double acting atmospheric condensing engine operating with different expansion ratios, a heat source of 100°C, and realistic heat sink of 30°C. Whilst it must be acknowledged that steam is not an ideal gas, as assumed in the above equations, the maximum

error associated with using ideal gas laws for steam at 1bar or below is just 1.6% as a percentage (Cengel & Boles, 2011). The analysis Muller et al (2018) found maximum theoretical thermal efficiencies as high as 17.8% for an expansion ratio of n = 8. This analysis has also been confirmed by more recent work by Bortolin, et al. (2021) using real gas data and heat source and sink temperatures of 100°C and 30°C respectively. This work found that the adiabatic cycle is more efficient than the isothermal, with a theoretical efficiency of 14% being calculated at an expansion ratio of n = 4 and a maximum theoretical efficiency of 17% calculated at an expansion ratio of n = 10, see Figure 2-16.

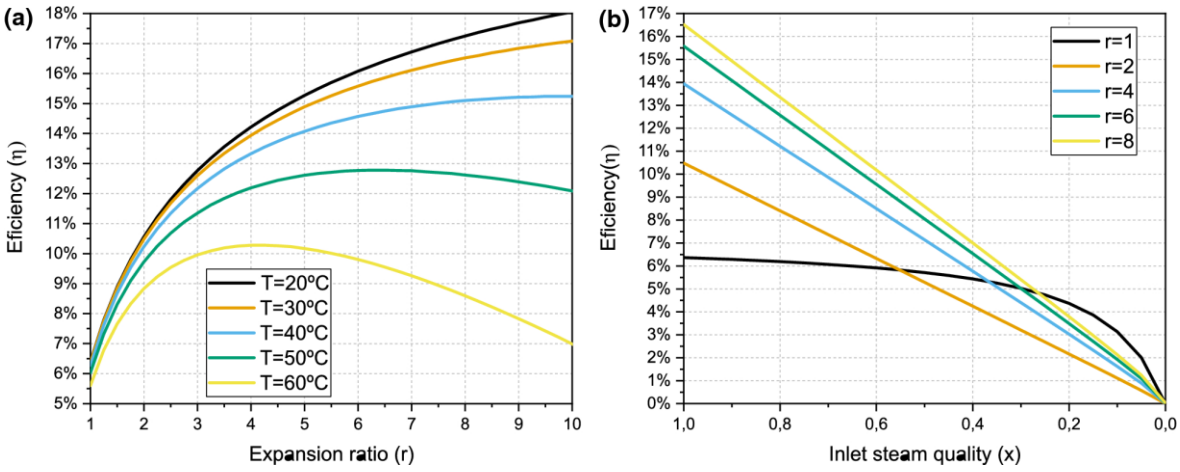

Figure 2-16 (a): Effect of condensation temperature on atmospheric condensing engine efficiency. (b): Effect of boiler steam dryness fraction on atmospheric condensing engine efficiency. Reproduced from (Bortolin, et al., 2021) with permission from Springer Nature.

The use of real gas data by Bortolin, et al. (2021) is more accurate than use of ideal gas laws. However, the research conducted by Muller, et al. (2018) extended its scope to practical assessment of the technology, and therefore simplified theoretical analysis methods were needed. This critical analysis identifies similar results for both methods, and suggests that the scope of this project could be aided by the simplified methodology presented by Muller, et al. (2018). These theoretical efficiencies, along with the already discussed operational benefits, provide justification for development of a modern condensing engine system for LGWH recovery and has resulted in recent research into the technology.

It is noted that Bortolin, et al. (2021) also analysed the effect of condensation temperature and boiler steam dryness fraction on the efficiency of the atmospheric condensing engine with expansion; see Figure 2-16. It was demonstrated theoretically that the ideal expansion ratio is reduced with increasing condensation temperature and reducing boiler steam dryness fraction. Whilst the impact of heat sink temperature is well covered in literature, the highlighted need for an

effective steam generator is of significance. A case of specific interest throughout this thesis is the expansion ratio of n = 4, identified as a potential optimum on a practical engine due to required valve timings and thermal losses at ratios higher than this. In this case, the maximum theoretical efficinecy can be reduced from around 14% to around 12%, a drop of approximately 15%, by reducing steam dryness fraction from x = 1 to x = 0.9.

2.3.3 The Current State of Condensing Engine Research

The last known commercial example of the condensing engine was Davey's engine of 1885 (Bortolin, et al., 2021). Davey's engine data was reported in (Josse, 1870) and more recently reviewed in comparison with modern ORC systems in (Muller & Howell, 2021). This engine achieved a maximum power output of 0.8kW, maximum thermal efficiency of 3.7%, and maximum second law efficiency of 25% when operating with a heat source temperature of 100^{o}C, heat sink of around 40^{o}C - 50^{o}C, and expansion ratio of n = 1. Only recently has practical optimisation of the technology been seen in literature. Thermodynamic modelling of the technology for both adiabatic and isothermal steam cycles has recently been performed using real gas data and ideal gas laws, already discussed above. This work led to physical models of a modern engine being developed.

Researchers at the University of Southampton are responsible for the extent of current testing of a physical prototype of the modern condensing engine (Muller & Parker, 2015; Muller, et al., 2018). The first piece of research involved an experiment designed to test the steam expansion cycle and show proof of concept (Muller & Parker, 2015). A cylinder with piston connected to boiler, condenser, and evacuation pump was set up and four strokes operated for each expansion ratio. The produced work was measured using a pulley system and used to calculate efficiency. This test achieved a thermal efficiency of 3.2% with expansion ratio of n = 1 and a reported maximum efficiency of 10.2% with expansion ratio n = 4, thus supporting the potential of the technology. The Mk.I engine built at the university was not successful. Anecdotal evidence at the university reports excessive friction in the parallelogram and loss of seal around the piston rod, demonstrating the difficulty in translating proof of concept to practical machine. However, the more recent Mk.II engine (Muller, et al., 2018; Ho Chan, et al., 2017) ran successfully, achieving speeds of 25–126 rpm and maximum measured piston powers of 26.7 W (n = 1) to 3.64 W (n = 4). Associated maximum thermal efficiencies ranged from 2.0% (n = 1) to 5.5% (n = 4) (Muller, et al., 2018). Mk.II engine results demonstrated proof of concept of steam expansion increasing engine efficiency but fell short of theoretical predictions, achieving 30% - 40% of the maximum achievable for the given operation (Muller, et al., 2018). Review of the Mk.II engine results highlights several shortcomings which resulted in significant power and efficiency losses. This review is presented next and was used to guide design of the next iteration of engine (the Mk.III) built as part of this research.

2.3.4 Summary: The Condensing Engine Technology for Low Heat Recovery

Section 2.3 has reviewed the atmospheric condensing engine from past to present. This review first highlighted the numerous benefits of the condensing engine, including theoretical efficiency. It also reviewed the current state of research pertaining to the condensing engine. The conclusions drawn from Section 2.3 are:

- The condensing engine is a historic technology with the last known commercial use being in 1885.
- The engine utilises the condensation of steam to create sub-atmospheric pressure, used as a pressure driving force to produce power using a piston in a cylinder.
- The engine uses water as a safe and sustainable working fluid and operates at low temperature and pressure, reducing complexity of design and safety concerns.
- High theoretical thermal efficiencies are estimated, up to 17% with realistic 30^{o}C heat sink when steam expansion is used.
- Recent practical engine models tested at the University of Southampton have achieved thermal efficiencies as high as 5.5%. The most recent practical model, the Mk.II engine, is reviewed in Section 2.4.

2.4 The MK.II Condensing Engine: A Review

The condensing engine technology has been introduced and its development as a low temperature heat recovery technology justified. The Mk.II CE built and tested at the University of Southampton has been highlighted as the most recent physical model seen in literature. Therefore, this section reviews the design and test results of this engine to provide critical discussion and identify areas for improvement on the next iteration of condensing engine to be built as part of this research (the Mk.III). This review is based on both the associated published paper (Muller, et al., 2018) as well as the unpublished Master's thesis (Ho Chan, et al., 2017) which provides additional background.

2.4.1 Mk.II Design and Dimensions

2.4.1.1 MK.II Engine Overall Design and Dimensions

It is important to understand the Mk.II engine design and intended operation in order to properly review the test results and establish recommendations for design improvement to implement as part of this research. The MK.II was a double acting, single cylinder engine. The CAD assembly is shown in Figure 2-17 and a photograph of the assembled engine is also given in Figure 2-18.

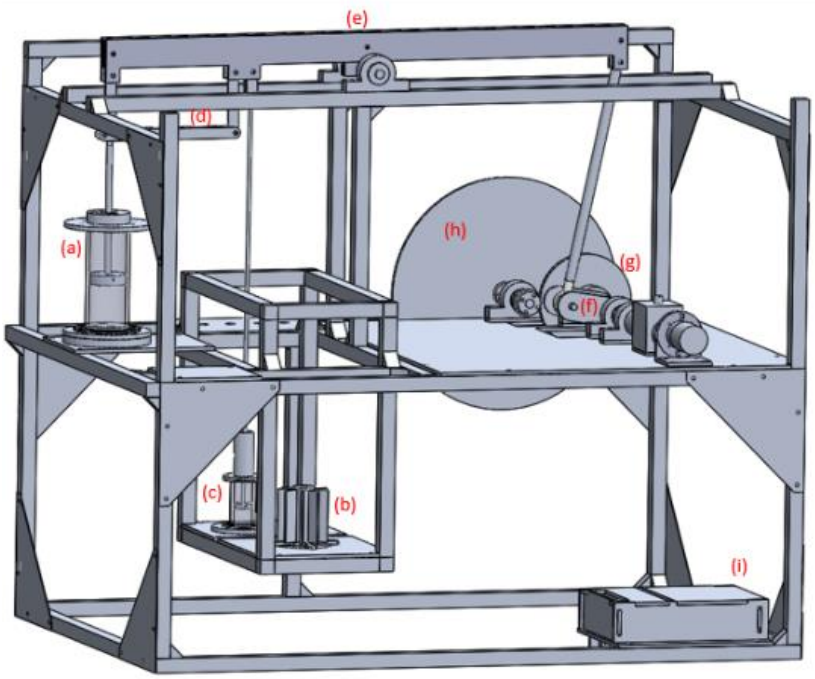

Figure 2-17 MK.II atmospheric condensing engine schematic and design CAD. (a) = cylinder. (b) = condenser. (c) = pump. (d) = parallelogram. (e) = beam. (f) = crankshaft. (g) = gearing. (h) = flywheel). (i) = electronics and control. Credit: (Ho Chan, et al., 2017)

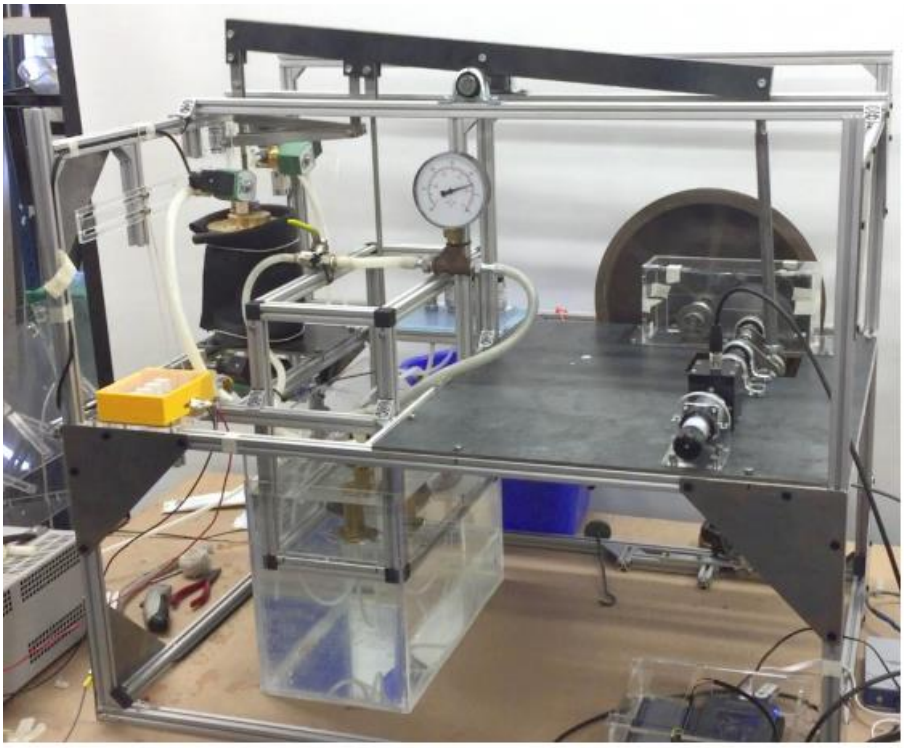

Figure 2-18 MK.II engine built to test expansion on the condensing engine. Credit: (Ho Chan, et al., 2017)

Atmospheric pressure steam is produced by the boiler and flow into the cylinder (a) is controlled by electronic solenoid valves. Solenoid valves also control steam evacuation from the cylinder to the condenser (b). Both a spray condenser and coiled copper pipe heat exchanger were tested on the

MK.II engine, with the former being shown in the figure below but omitted from this review due to inferior performance. Design of the coiled tube condenser is discussed in detail in Section 2.4.1.2. Laboratory mains water was used to supply the condenser and achieved a heat sink temperature, associated with condenser pressure, of around 50°C - 70°C (Muller, et al., 2018). The piston rod is connected to a power take off system comprising of: Parallelogram (d), beam (e), crankshaft (f), gearing (g), and flywheel (h).

This complex system is required as angular motion of the piston rod cannot be achieved on a double acting engine, as the piston rod must seal to the cylinder cap. The flywheel is required to balance power output. The air pump (c), a piston pump driven by the mechanical motion of the engine, evacuates condensate from the system. Electronic control (i) was implemented for the valves and sensors. Key engine dimensions were based on a historic engine, reported by an engineer called John Farey (Muller, et al., 2018; Farey, 1827). These are given in Table 2-4.

Table 2-4 MK.II engine dimensions taken from (Muller, et al., 2018).

Component	Parameter	Value / Unit
Cylinder	Diameter Stroke Length Material	50mm 120mm Brass
Condenser	See Figure 2-21.	
Air Pump	Diameter Height Material	25mm 50mm Brass
Beam	Length	500mm
Gear Ratio	1:3	-
Flywheel	Diameter Mass	320mm 3.2kg

2.4.1.2 Heat Recovery

As well as testing for the engine thermal efficiency, heat recovery during steam condensation was attempted on the MK.II engine. The condensing engine relies on the condensation of steam to create vacuum, achieved by bringing the steam to its relevant condensation temperature and removing its latent heat. In a condenser this is achieved through heat exchange with a cooling fluid, typically water. Latent heat can be a considerable source of energy, with 2257 kJ of thermal energy

removed from each kilogram of steam condensed at 100°C (Rogers & Mayhew, 1995). It was proposed by Ho Chan, et al (2017) that the recovered energy could be used for boiler pre-heat, reducing the thermal energy input requirement thus increasing energy efficiency. Such heat recovery had not before been tested on an atmospheric condensing engine. Heat recovery on the Mk.II engine was tested using two stages of copper coil inside the condenser, as shown schematically in Figure 2-19. The first stage attempted to recover latent heat during initial steam condensation. The second stage would then enable total condensation of the residual steam as required for operation of the engine. The first stage allowed for a slower water flow rate to maximise increase in water temperature, with the second stage using a faster cooling water flow rate to maximise heat transfer and therefore condensation. Design of the condenser is discussed next.

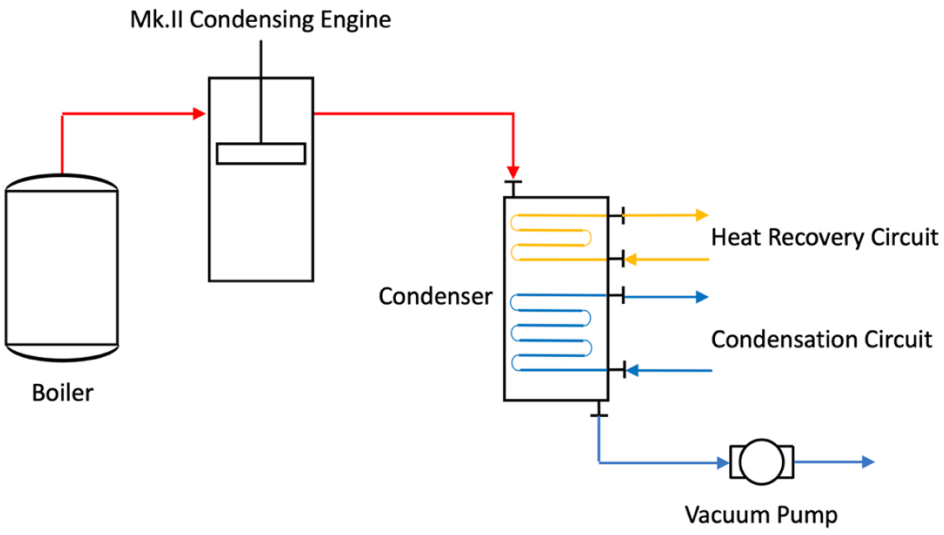

Figure 2-19 Visual illustration of the MK.II engine heat recovery concept.

2.4.1.3 MK.II Coiled Shell and Tube Condenser Design

The design process undertaken for the MK.II coiled condenser for heat recovery, as well as the final design dimensions, are important to this project as it was re-used during testing of the MK.III engine to save both time and money. This design was performed by Ho Chan, et al. (2017) and is repeated here and analysed.

The first step in the design of this condenser was to calculate the heat transfer coefficients on both the water and steam side of the coils. The mean heat transfer coefficient for steam condensing on tubes is given by Equation (2.14); (Ho Chan, et al., 2017). As tubes are coiled in this condenser, condensate will drip onto the tubes below increasing the film thickness and reducing heat transfer potential. This is accounted for by using Equation (2.15); (Ho Chan, et al., 2017).

$$\overline{\alpha_1} = 0.725 \left[\frac{{\lambda_L}^3 \rho_L (\rho_L - \rho_G) g h_{GL}}{\mu_L d_T (T_{sat} - T_W)} \right]^{\frac{1}{4}} \quad (2.14)$$

$$\overline{\alpha_{con}} = \overline{\alpha_1} {n_H}^{-\frac{1}{4}} \quad (2.15)$$

Where:

- α_1 is the mean heat transfer coefficient for condensation on tubes (W/m^{2}K)
- λ_L is the thermal conductivity of water (W/m.K)
- ρ_L is the density of water (kg/m^3)
- ρ_G is the density of water vapour (kg/m^3)
- g is acceleration due to gravity (m/s^2)
- h_{GL} is the enthalpy of vaporisation (kJ/kg)
- μ_L is the viscosity of water (Pa.s)
- d_T is the diameter of the tube (m)
- T_{sat} and T_W are the saturation and wall temperatures (^{o}C)
- α_n is the average heat transfer coefficient for 'n' number of tubes (W/m^{2}K).
- α_{con} is the condensation heat transfer coefficient (W/m^{2}K).
- n_H is the number of horizontal tubes.

The mean heat transfer coefficient for the cooling water, assumed to be a fully developed laminar velocity profile, is given by Equation (2.16); (Ho Chan, et al., 2017).

$$\alpha_{cw} = \frac{Nu \cdot \lambda_l}{L} \quad (2.16)$$

Where:

- α_{cw} is the mean water side heat transfer coefficient (W/m^{2}K)
- Nu is the dimensionless Nusselt number
- L is the characteristic length of the tube (m)

The heat transfer coefficients for the condensation side, the water side, as well as the conduction of heat through the copper tube walls are combined to give the overall heat transfer coefficient; see Equation (2.17); (Ho Chan, et al., 2017).

$$\frac{1}{U} = \frac{d_1}{2\lambda_W}\ln\frac{d_1}{d_2} + \frac{1}{\alpha_{cw}} + \frac{d_1}{\alpha_c d_2} \tag{2.17}$$

Where:

- U is the overall heat transfer coefficient (W/m^{2}K)
- λ_W is the thermal conductivity of the copper pipe (W/m.K)
- d_1 and d_2 are the outer and inner diameters of the tube (m).

The overall heat transfer coefficient represents the inverse of the resistance to heat transfer. It can be used in Equation (2.18) along with the average heat load and the log mean temperature difference, defined in Equation (2.19), to give the required heat transfer surface area; (Ho Chan, et al., 2017).

$$A_{ht} = \frac{\dot{Q}_{peak}}{U \times T_{LM}} \tag{2.18}$$

$$T_{LM} = \frac{\Delta T_{top} - \Delta T_{bottom}}{\ln \Delta T_{top} - \ln \Delta T_{bottom}} \tag{2.19}$$

Where:

- A_{ht} is the heat transfer surface area (m^2).
- $\dot{Q}_{peak}$ is the peak thermal power load (W). This is the average condenser thermal energy load divided by the number of seconds condensation must occur within to provide rapid pressure reduction, chosen to be 0.1 seconds during the Mk.II engine design.
- T_{LM} is the log mean temperature difference (^{o}C)
- ΔT_{top} and ΔT_{bottom} are the differences in temperature at the top and bottom of the heat exchanger respectively (^{o}C).

It is noted that the typical use of Equation (2.18) is to use a thermal energy term. However, the Mk.II design used a thermal power to represent the time restriction under which the energy was required to be condensed in order to create rapid reduction in cylinder pressure. This is unique to this analysis but deemed appropriate to sufficiently size the condenser. In this case the heat load expressed as a power term was greater than the energy load due to the required condensation time being <1 second.

This theory was used by Ho Chan, et al (2017) to specify the necessary dimensions of the coiled shell and tube condenser. This was performed in a MATLAB model. Some thermal property data for the final simulated condenser are given in Figure 2-20, and the resulting condenser dimensions are given in Figure 2-21. A photograph of the assembly of the condenser is given in Figure 2-22.

Parameter	Unit	Value
Average Cooling Power	kW	0.69
Peak Cooling Power	kW	3.45
Cooling Water Inlet Temp T_{CWin}	celsius	20
Cooling Water Outlet Temp T_{CWout}	celsius	50
Cooling Water Flow Rate	ml/s	5.5
Saturation Temperature T_{sat}	celsius	40
Saturation Pressure P_{sat}	bar	0.074
Copper Pipe Outer Diameter	mm	6
Number of vertical coils	-	15
Condensation heat transfer coefficient α_c	$\mathrm{W/(m^2K)}$	1593
Cooling water heat transfer coefficient α_{CW}	$\mathrm{W/(m^2K)}$	450
Overall Heat Transfer Coefficient U	$\mathrm{W/(m^2K)}$	303
Assumed Temperature Difference ΔT_{LM}	celsius	32.7
Required Surface area	$\mathrm{m^2}$	0.173
Equivalent Pipe Length	m	9.2
Number of Parallel Coils	-	2
Water Side Pressure Drop ΔP_{coil}	Pa	660
Pumping Power Loss $\dot{W}_{\mathrm{pump}}$	W	0.004

Figure 2-20 Final condenser thermal design parameters. Credit: (Ho Chan, et al., 2017).

Global Variable	Dimension,(mm)	Defined by
Hot & Cold Coil Outer Diameter	82.3	Stock brass tube <Outer Casing
Hot & Cold Coil Wall Thickness	0.5	Stock Copper pipe
Hot Coil Height	45	Heat exchanger calcs.
Hot Coil Turns	8	Heat exchanger calcs.
Hot Coil Pipe Internal Diameter	3	Suppliers and Calcs
Cold Coil Height	200	Heat exchanger calcs.
Cold Coil Turns	20	Heat exchanger calcs.
Cold Coil Pipe Diameter	6	Suppliers and Calcs.
Outer Casing Diameter	88.9	Stock brass tube <150mm
Outer Casing Wall Thickness	3.175	Stock Brass Tube
Core Diameter	19.05	Stock Brass tube
Core Wall Thickness	1.5	Stock Brass tube

Figure 2-21 Final condenser design dimensions. Credit: (Ho Chan, et al., 2017).

Figure 2-22 Assembly of MK.II coiled shell and tube condenser. Credit: (Ho Chan, et al., 2017).

2.4.2 Mk.II Test Results & Discussion

2.4.2.1 MK.II Engine Thermal and Second Law Efficiency

The MK.II engine was tested with expansion ratios ranging between n = 1, i.e. no expansion, to n = 4. The piston power was calculated using equations outlined in section 2.3.2 and recorded pressure data. This was shown by Muller, et al. (2018) to equal the sum of the recorded shaft power and pre-determined system friction, supporting the method of calculation. The resulting thermal efficiency is plotted in Figure 2-23. Thermal efficiency was analysed due to poor mechanical efficiencies, reviewed in more detail in a later discussion. Figure 2-23 shows that the maximum thermal efficiency achieved was 5.5% at an expansion ratio of n = 4 (Muller, et al., 2018). At an expansion ratio of n = 1, the Mk.II engine achieved thermal efficiencies ranging from 1% - 2%.

Muller, et al. (2018) suggest that during operation at an expansion ratio of n = 1, the top and bottom cylinder pressures remained 0.15bar and 0.20bar below boiler pressure respectively. Assuming an average boiler pressure of 1bar, this gives top and bottom cylinder pressures of 0.85bar and 0.80bar. This gives a cylinder temperature of 94^{o}C following steam admission (Rogers & Mayhew, 1995). For the purposes of analysing prototype condensing engines in this thesis, this has been assumed as the heat source temperature. This is an extension of the method commonly used in literature, eg. (Muller & Howell, 2021), of using the condenser pressure as the indicator of the heat sink. This analysis allows any inefficiency in the transfer of boiler pressure to the cylinder to be removed from the analysis of the engine to understand the technology's potential following

optimisation. It does however mean that a direct comparison cannot be made to existing ORC technologies, and this is considered in later discussion. The condenser pressure for testing at n = 1 was around 0.34 bar for the Mk.II engine (Muller, et al., 2018) giving a heat sink temperature of 72°C. This gives a *Carnot* efficiency of 6.0% and second law efficiency for the Mk.II engine of 17% - 34% with an expansion ratio of n = 1. Applying the same analysis to the engine results for an expansion ratio of n = 4 results in a maximum second law efficiency of 55%.

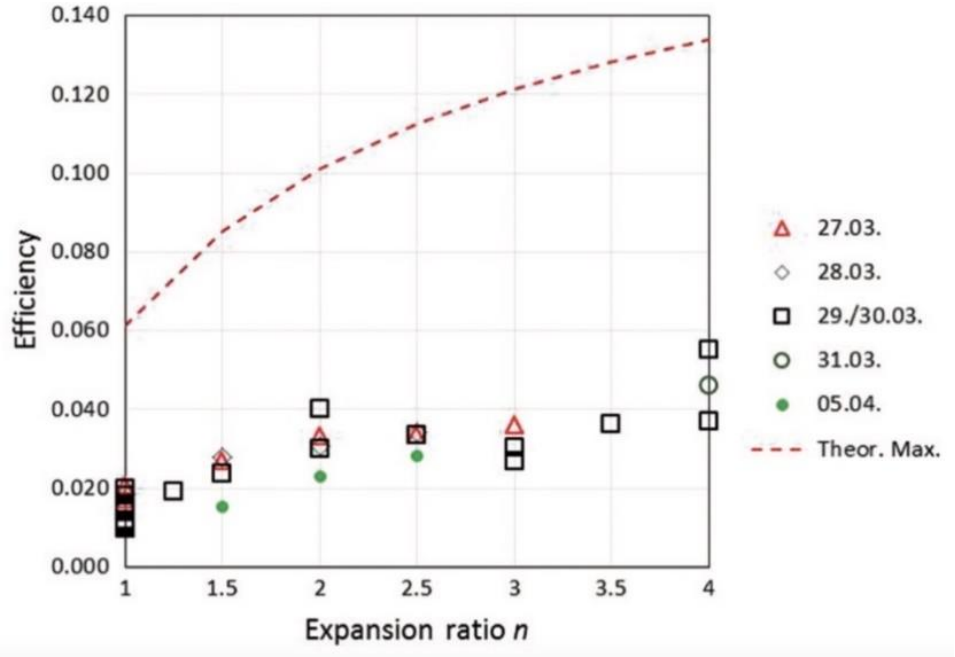

Figure 2-23 A plot of expansion ratio vs achieved thermal efficiency from the MK.II engine tests. Credit: (Muller, et al., 2018)

The reported maximum Mk.II thermal efficiency is comparable to the lower end of ORC efficiencies for LGWH recovery, observed as being around 5% in literature at similar operating temperature and power scale (Landelle, et al., 2017). Mk.II second law efficiencies were also comparable with values expected for a LGWH ORC system, observed as around 20% - 40% in literature (Landelle, et al., 2017; Muller & Howell, 2021).

However, it is noted that the efficiency was determined for the MK.II engine using piston power, therefore not accounting for mechanical losses and therefore not comparative with mechanical or electrical efficiencies reported in literature. Additionally, Mk.II engine efficiency was calculated using a theoretical thermal energy input calculated using the expected consumption of steam. Thermal losses and condensation of steam will result in a greater volume of steam being used and therefore a lower thermal efficiency. It was estimated by Muller, et al. (2018), using a comparison of cylinder displacement and weight of evaporated water in a study performed by Josse (1870), that this can lead to an overestimation in efficiency by as much as 30%. Whilst modern insulation

and materials would mean this value is likely an overestimation for a current engine, this would result in a new MK.II maximum thermal efficiency of 3.8% and second law efficiency of 38%. Whilst this second law efficiency is still comparable to current ORC systems it assumes a narrowed temperature range, as discussed above, and must achieve improved translation of boiler pressure to the cylinder to be truly comparable. Nevertheless, this shows promise from the technology and justifies further research as part of this work.

2.4.2.2 MK.II Engine Heat Recovery

Results from testing show that even at extremely low flow rates in the heat recovery coil, around 2 mL/s, a maximum outlet temperature of 40°C was seen; see Figure 2-24. This represents a 10°C - 20°C increase and is not sufficient to achieve any significant gains in engine performance. Therefore, the heat recovery coil in the MK.II condenser was unsuccessful. The tests shown here were performed with expansion ratios of n = 2 and n = 3 according to Ho Chan, et al. (2017).

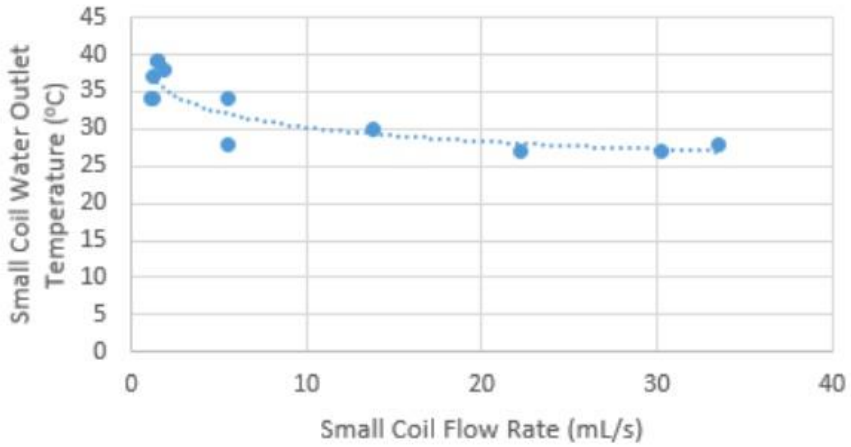

Figure 2-24 Heat recovery coil results from MK.II testing, showing water flow rate and outlet water temperature. Credit: (Ho Chan, et al., 2017).

The main condensation coil, however, was able to achieve outlet water temperatures of up to 70°C when the flow rate was reduced to around 8mL/s; see Figure 2-25. Therefore, the MK.II heat recovery tests essentially used a single stage performing both condensation and heat recovery, due to the first coil recovering little to no thermal energy. This is an ineffective way of operating the engine. Figure 2-25 shows that condensation coil water flow rates below approximately 25mL/s were required to increase water temperature significantly, but Figure 2-26 and Figure 2-27 show that at this flow rate average condenser pressure and engine power output were negatively affected. The minimum flow rate used, 8mL/s, achieved 1/3rd of the maximum achievable power output during testing according to Ho Chan, et al. (2017).

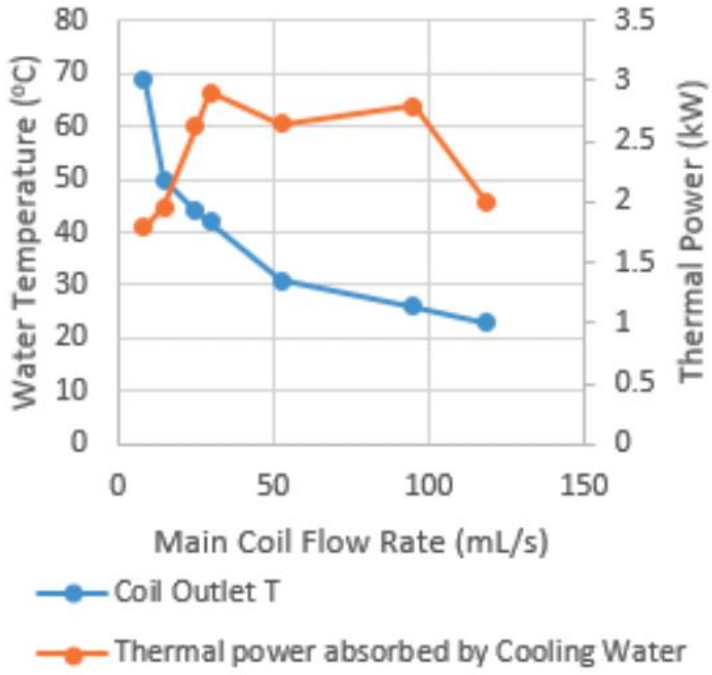

Figure 2-25 MK.II heat recovery tests results for the condensation coil, showing water flow rate and resultant outlet water temperature. Credit: (Ho Chan, et al., 2017).

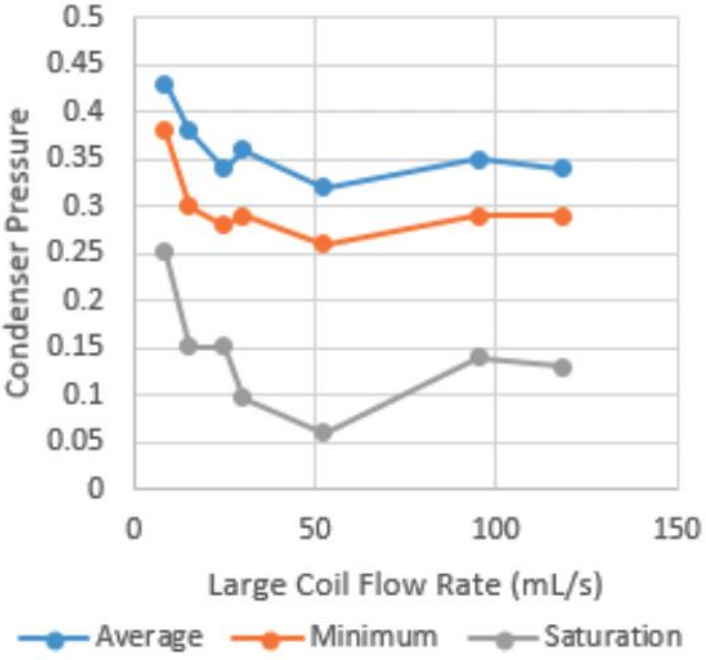

Figure 2-26 Mk.II heat recovery test results, showing effect of condensation coil flow rate on condenser pressure with an expansion ratio of n = 1.Credit: (Ho Chan, et al., 2017).

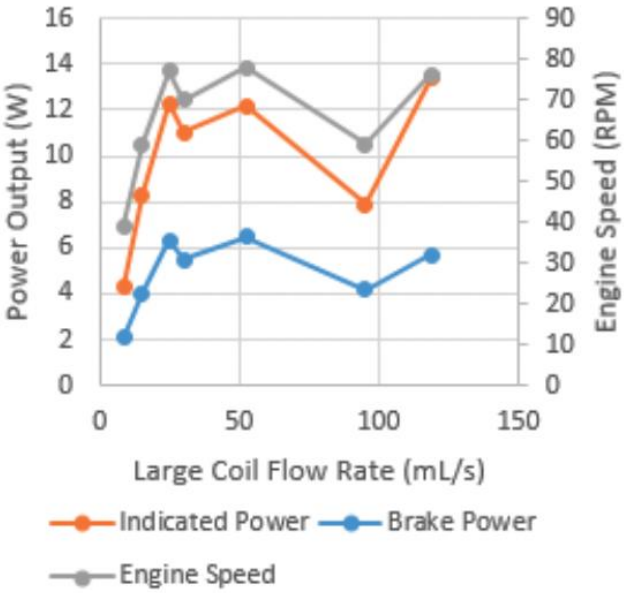

Figure 2-27 MK.II heat recovery tests results, showing achieved power output from the engine for different condensation coil cooling water flow rates. Credit: (Ho Chan, et al., 2017).

It was acknowledged in the Mk.II engine project report that the thermal energy available for recovery was in excess of the expected value based on the estimated steam flow rate (Ho Chan, et al., 2017). This was attributed to steam leakage across the valves during heat recovery tests. Therefore, as part of this literature review, the data reported in Figure 2-25 was checked through calculation to ensure confidence in the results before critically analysing. The water flow rate and water outlet temperature were manually read from the plot for each data point and a simple analysis performed using Equation (2.20). The inlet flow temperature was not given in the source material but cited as the mains water supply in the laboratory (Ho Chan, et al., 2017). Therefore, this analysis read the reported thermal power recovery from Figure 2-25 and calculated the required inlet water temperature to balance the equation. It was found that the required inlet water temperature ranged from 17°C - 19°C. Considering the uncertainty associated with the manual reading of temperature and power values, the estimated temperatures are within the expected range for the cooling water temperature and therefore corroborated the thermal power values reported in Figure 2-25.

$$\dot{Q} = \dot{m} \times C_p \times \Delta T \tag{2.20}$$

Where:

- $\dot{Q}$ is the thermal power (kW)
- $\dot{m}$ is the mass flow rate (kg/s)
- Cp is the specific heat capacity (kJ/kg.K)
- ΔT is the change in temperature (K)

2.4.2.3 MK.II Engine Sub-Atmospheric Operation

Testing on the MK.II engine found that during long runs the steam demand increased beyond the boiler's supply, creating a sub-atmospheric boiler pressure. Despite this, the MK.II engine continued to produce power. This is possible if the boiler pressure and temperature are higher than that of the condenser, creating driving force between the two. Following this observation, tests were performed on the MK.II engine with the boiler operating at a pressure of 0.75bar, giving a net power production of 5.78W and a thermal efficiency of 1.1% (Muller, et al., 2018). This has far reaching implications for the flexibility of the condensing engine. By reducing the operating pressure of the boiler this also reduces the associated boiling temperature of water. According to steam tables the saturation temperature of steam at 0.75 bar is 91.8°C. This means that in this operation, the MK.II engine could have been run from a LGWH source with a temperature of 91.8°C. This is a subtle difference in this case but demonstrates the effect that will allow the condensing engine to target a lower LGWH temperature range. However, operating sub-atmospherically does have consequences relating to efficiency, see Figure 2-28.

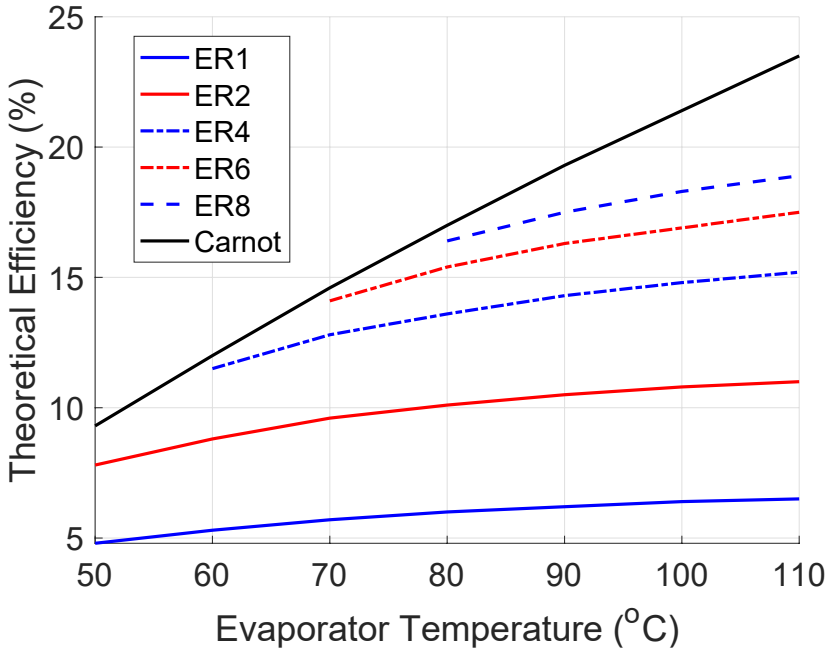

Figure 2-28 Condensing engine theoretical efficiency across a range of expansion ratios and evaporator temperatures. Heat sink temperature of 20°C. Reproduced from (Muller & Howell, 2021) under CC BY 4.0.

As per the *Carnot* theorem, the efficiency of a sub-atmospheric engine is reduced due to the reduced operating temperature range. For example, reducing the heat source temperature from 100°C to 50°C, whilst maintaining the same heat sink of 20°C, causes the maximum theoretical efficiency of the condensing engine to drop from 21.4% to just 9.3%. Figure 2-28 shows that

theoretical thermal efficiencies for heat source temperatures of below 100°C can drop as low as 5%. The reducing efficiency below a heat source temperature of around 50°C identifies that this should be the minimum target temperature for the condensing engine technology, as highlighted in previous literature (Muller, et al., 2018).

2.4.3 Identified Areas for Improvement and Proposed Solutions

The MK.II engine achieved a maximum thermal efficiency of 5.5%. Whilst commendable given the context of the current LGWH recovery technology space, the theoretical maximum efficiency of around 13.5% for this operation (expansion ratio of n = 4) suggests significant room for improvement. Areas of potential improvement over the Mk.II design are discussed below, guiding the design of the next iteration of engine to maximise performance.

2.4.3.1 Pressure Observations

For effective driving force to increase power output, and therefore efficiency, the condenser pressure needs to remain low and must be translated quickly to the cylinder during steam evacuation. The cylinder pressure must also reach boiler pressure quickly during the steam inlet phase. Condenser and cylinder pressures observed during Mk.II testing are shown in Figure 2-29 and reviewed below to identify areas for improvement on the next iteration of engine.

Condenser Pressure

Figure 2-29 shows that condenser pressure in the MK.II engine never dropped below 0.2 bar when running with an expansion ratio of n = 2. Whilst not plotted, Muller, et al. (2018) state that a minimum condenser pressure of 0.13bar was seen at an expansion ratio of n = 4. These pressures are higher than the saturation pressures of 0.02bar - 0.04bar associated with a heat sink temperature of 20°C - 30°C (Rogers & Mayhew, 1995). Reducing condenser pressure should be an area of further investigation to increase the pressure driving force on the piston and can be achieved through several improvements such as increased heat transfer area, improved heat rejection, and reducing air leaks. The Mk.II engine report also suggested that the solenoid valves could have been allowing steam to leak by, which would also inhibit vacuum generation. Whilst not quantified or proven in the report, it is important to consider any future valve selection for suitability with steam to ensure proper seals are created.

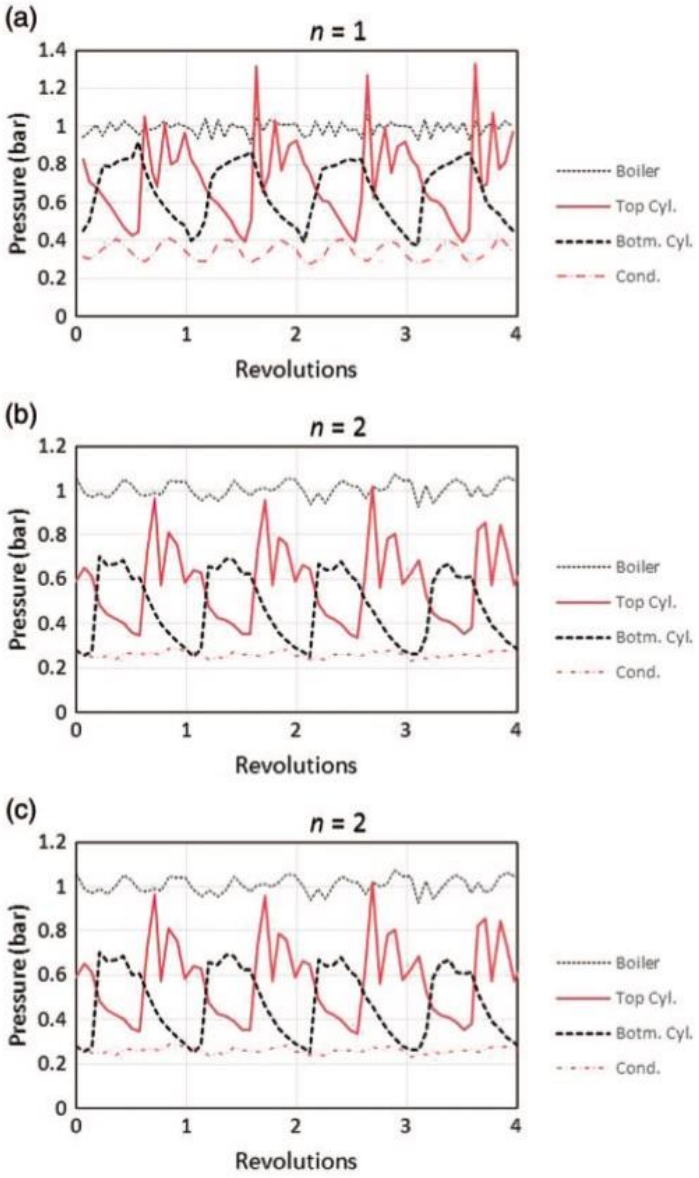

Figure 2-29 Pressure profiles recorded during MK.II Engine tests: (a) *n* (ER) =1 at 82.2rpm (b) *n* = 2 at 94.3rpm (c) *n* = 2 at 27rpm. Credit: (Muller, et al., 2018).

Cylinder Pressure

Figure 2-29 highlights that whilst the top cylinder pressure successfully reached that of the boiler during steam inlet, the bottom cylinder pressure did not. This effect became more exaggerated with increased expansion ratio, with maximum bottom cylinder pressures of just 0.7bar with an expansion ratio of *n* = 2. It is expected that the cooling effects of steam expansion caused additional condensation in the initial charging of the cylinder with steam. The condensate blocked the steam inlet port, located on the bottom cap of the cylinder, choking the steam flow into the cylinder and resulting in a pressure drop. This can be overcome by changing the arrangement of the engine and reducing heat losses. The former can be achieved by using a single acting engine arrangement removing the need for the bottom part of the cylinder. This would have additional

benefits, such as reduced friction through removal of the need for the beam and parallelogram as well as the ability to use multiple cylinders on the same crank shaft. The latter can be achieved through use of improved insulation, with a steam jacket providing an active method of maintaining cylinder temperature by passing steam around the outside of the cylinder. This has been shown in historic texts to reduce overall steam demand, and therefore increase thermal efficiency, by reducing steam condensation during steam inlet (Ewing, 1910). Figure 2-29 also shows that the top cylinder section did not reach condenser pressure, achieving a minimum pressure of just below 0.4bar. This indicates that steam was not evacuated rapidly enough. Potential improvements include changing the arrangement of the cylinder to maximise steam evacuation, for example using a uniflow cylinder which incorporates additional steam evacuation ports in the cylinder wall (Hills, 1989). Using the uniflow arrangement on the condensing engine is a large focus of this research and is reviewed in more detail in Section 2.4.4.1 and the theory applied in Chapter 3, Chapter 4, and Chapter 5.

2.4.3.2 Impact of Valve Channel Diameter and Path

Another solution for improved cylinder steam evacuation is improved outlet solenoid valve selection. During operation, normally closed solenoid valves use an electromagnet to activate a plunger, revealing a small orifice for the fluid to flow through, as shown in Figure 2-30. When the electromagnet is not energised a spring is typically used to return the plunger to its original position.

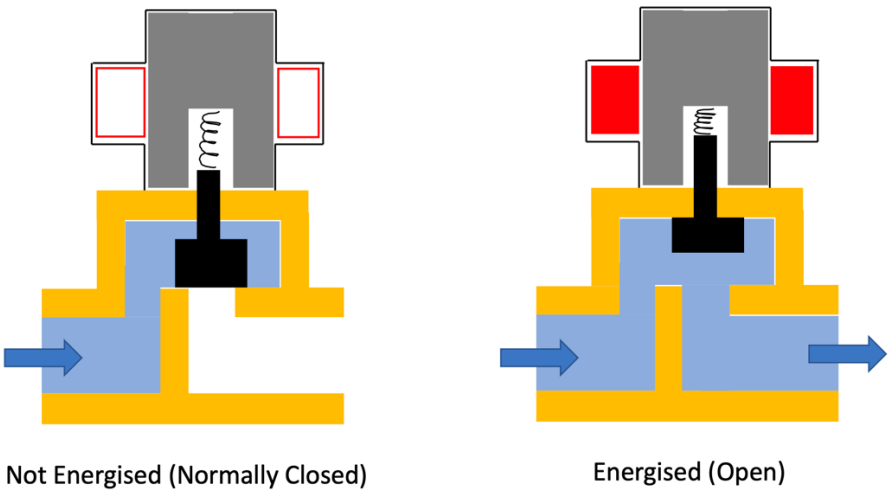

Figure 2-30 Cross section schematic of a normally closed solenoid valve.

The Bernoulli equation for flow in a pipe can be used to highlight the impact of valve selection, see Equation (2.21). This form of the Bernoulli equation accounts for minor head loss due to

restrictions in the flow. These are available in literature with some relevant examples given in Table 2-5 (Cengel & Cimbala, 2010).

$$v_2 = \sqrt{\frac{2(P_1 - P_2)}{(1 + \sum K_i)\rho}} \tag{2.21}$$

Where:

- Point *1* is inside the cylinder
- Point *2* is inside the condenser
- *v* is velocity (m/s)
- *P* is pressure (Pa)
- ρ is density, in this case the average density in the pipe (kg/m^3)
- K_i is the minor head loss coefficient for component i.

Table 2-5 Minor loss coefficients for steam flow from cylinder to condenser (Cengel & Cimbala, 2010)

Minor Loss Source	Minor Loss Value (K_i)
Exit from cylinder	0.5
Entry to condenser	1.0
Solenoid Valve	10

Equation (2.21) and Table 2-5 together highlight that the valve has a significant effect on the velocity of the steam due to pressure losses, especially in comparison to the effect of the cylinder and condenser exit and entry. Therefore, future valve selection should aim to reduce the pressure drop and resistance to flow through optimum arrangement. The already mentioned uniflow engine concept would allow for a reduction in minor head loss coefficient by using ports in the cylinder wall. The ports on the uniflow engine present the steam with a more direct flow path with fewer bends in comparison to a typical solenoid valve. This further justifies the selection of the uniflow concept as one for testing during this project.

Additionally, valve orifice area should be maximised to ensure that steam velocity is not choked, that is not limited by the maximum velocity governed by the speed of sound, and volume flow rate of steam is maximised for a given velocity. Further inspection of the specifications for the MK.II engine's chosen valves (ASCO E262K090S1N00H1) indicate that the orifice was 7.1mm in diameter (ASCO, 2012). A larger orifice diameter should be used in future testing. A slide valve is proposed as a potential solution, discussed in Section 2.4.4.2.

2.4.3.3 Engine Friction

The piston power from MK.II tests can be compared to the recorded shaft power to understand how much friction was present on the MK.II engine. The Mk.II engine achieved maximum power ratings of 3.6W (n = 4) to 27W (n = 1) (Muller, et al., 2018). Power output without expansion ranged from around 5W - 27W. Figure 2-31 shows a considerable difference between piston and shaft power, and internal friction accounted for approximately 60% of total power production according to Muller, et al (2018). The mechanical efficiency of the engine therefore also requires significant improvement, achieved by reducing the mechanical complexity of the system and the number of mechanisms which cause friction. An example is use of a single acting engine which removes need for the beam and parallelogram used on the Mk.II engine and allows the piston to attach directly to the crank shaft. Low friction materials should also be chosen where possible, such as PTFE.

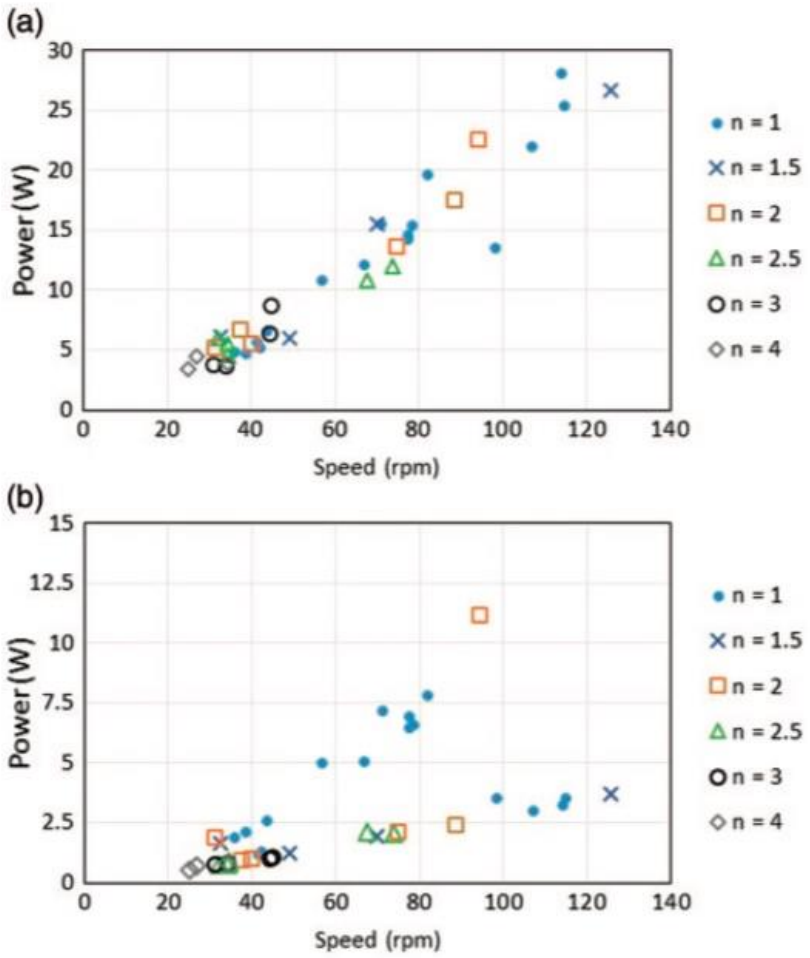

Figure 2-31 (a) Speed vs piston power data for the MK.II engine. (b) Speed vs shaft power for the MK.II engine. Credit: (Muller, et al., 2018)

2.4.3.4 Heat Recovery

The coil designed to recover heat in the condenser during MK.II engine testing was unsuccessful. However, the coil designed to ensure total condensation of steam achieved a temperature increase to 70°C when at a low water flow rate. This suggests that steam preferentially condensed on the second coil, drawn through by the lower pressure. This would suggest that steam condensation needs to be performed in two separate stages, with heat being recovered in the first stage before the second stage ensures total condensation. Additionally, it could have been possible for condensate to be collecting in a film on the heat exchanger pipes and re-evaporating at sub-atmospheric pressure between pulses of steam, removing heat from the water circuit. Therefore, any heat exchanger designed for future heat recovery on the condensing engine should maximise condensate removal wherever possible. For example, a flat plate heat exchanger with steam flow from the top to bottom of the plate could be used.

Furthermore, the heat recovery work performed as part of the Mk.II engine tests did not include any theoretical assessment of the energy available for recovery. In the case of the condensing engine with steam expansion, the pressure and temperature of the steam evacuated from the cylinder will be reduced. This in turn reduces the thermal energy available for recovery. Therefore, this research has assessed the available energy and potential for re-use to further the knowledge in this area. Part of this should be to suggest an alternative use for the recovered thermal energy. The Mk.II work proposed use as boiler feed pre-heat. However, in cases where steam is used as a direct waste heat emission input into the engine then this heat sink would not exist. Therefore, greater flexibility in the heat re-use is required.

2.4.4 Heat Engine Theory

Section 2.4.3 has critically analysed the Mk.II CE testing results and proposed some areas for improvement. These included the use of a uniflow arrangement and slide valve to reduce pressure losses, use of a steam jacket to reduce thermal losses, use of a single acting arrangement and traditional crank to reduce friction, and a multi-stage heat recovery and re-use system. Section 2.4.4 covers the uniflow engine arrangement and the slide valve in more detail. It also introduces further concepts from heat engine theory that could be used on future atmospheric condensing engines to improve performance or simplify design. These are based on historical advancements of the steam engine, concepts that have since been supplanted by more modern technologies. It is highlighted that the lower power scales that the condensing engine is identified to be targeting reduces the ability to power electronic valve and control systems, as these will draw a larger percentage of overall system power output. Therefore, modern versions of historic mechanical

systems, such as governors and slide valves, should be developed for the atmospheric condensing engine to reduce wasted power. These concepts are reviewed below.

2.4.4.1 Uniflow Engine

The uniflow engine concept incorporates steam evacuation ports in the cylinder wall (Hills, 1989). The ports are sealed by the piston during the downstroke and revealed at the bottom of the piston stroke. This allows additional area for steam evacuation, greater than that available with outlet valves only. This should improve steam evacuation rate and therefore allow for improved cylinder pressures and greater power production in the condensing engine. Compared to a counterflow arrangement, as used on the Mk.II engine, it also limits the steam passing back through the cylinder, which following steam expansion reduces thermal losses from the cylinder and prevents condensation of the next admission of steam (Hills, 1989). As a result, it is proposed that a uniflow arrangement could significantly improve the next iteration of modernised atmospheric condensing engine. A diagram of the uniflow concept is shown in Figure 2-32 below. A more detailed diagram showing each stage of the revolution is shown in a more detailed review in Figure 3-1.

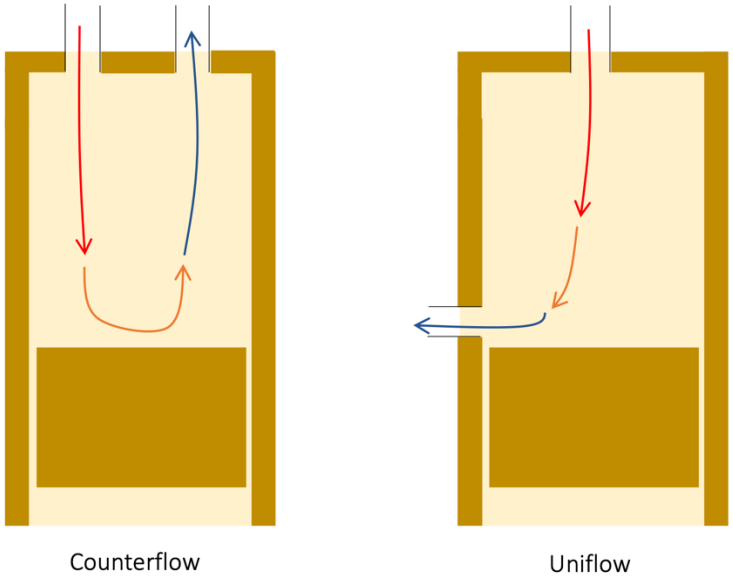

Figure 2-32 Uniflow versus counterflow concept diagram.

The most common modern-day use of the uniflow cylinder is on gasoline powered two-stroke engines to evacuate combustion gases, eg. (Wang & Zhao, 2019; Ma, et al., 2017). The most recent examples of current steam engines utilising the uniflow arrangement are those built by hobbyists which exclusively operate at high pressures and do not implement the condensing engine cycle to produce power, eg. an engine built by (Kimmel, 2012) which operates at 40bar. This literature review has found that, to the best of the author's knowledge, there is no previous or current

example of a modern atmospheric condensing engine in the uniflow configuration. Therefore, considering the advantages it offers, the design and testing of such an engine would be novel. Implementing the uniflow arrangement on the atmospheric condensing engine was a large focus of this research project, documented in Chapter 3 and Chapter 4 of this thesis.

2.4.4.2 Slide Valve

The slide valve has already been identified in Section 2.4.3 as having the potential to reduce the minor head loss coefficient associated with steam inlet and outlet. A diagram is shown in Figure 2-33. The slide valve piece sits on the face of the cylinder wall and moves along a linear path driven by the reciprocating motion of the engine. When the slide valve piece reaches one end of the cylinder it allows steam inlet to the relevant chamber of the double acting cylinder and evacuates steam from the other.

This is a mechanical valve mechanism that significantly reduces head loss. These are factors that will both be important for the development of the atmospheric condensing engine, the former because the engine power produced will not be sufficient to sustain use of electronic valves except at large engine scales and the latter to reduce pressure losses and improve performance. A key challenge is expected to be optimisation of slide valve timing for operation with different expansion ratios. Whilst a slide valve has been developed as part of this research, see Section 4.5.7, the mechanical linkage and timing of the valve was not considered part of the scope. This should be investigated in future work, drawing on lessons from historic steam engine design.

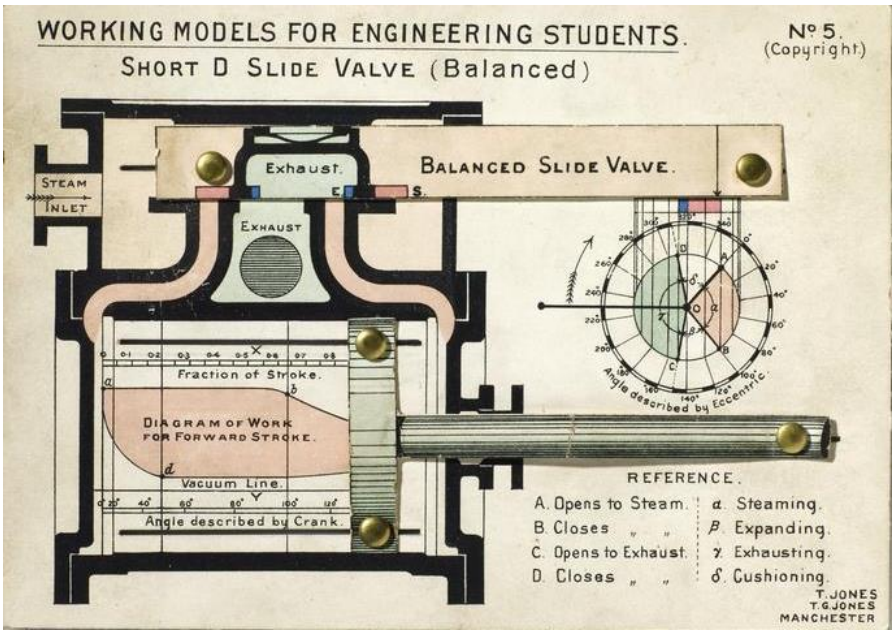

Figure 2-33 Diagram of 'Short D Slide Valve' designed by T and TG Jones. Reproduced from (Science Museum Group, nd) under CC BY-NC-SA 4.0.

2.4.4.3 Compound Expansion Engines

Compound expansion steam engines employ a staged expansion across two or more cylinders. This allows the ratio of inlet to outlet pressure to be reduced in each cylinder and therefore reduce the effect of cooling losses. Whilst this is more appropriate for high pressure engines, and the change in pressure experienced in the atmospheric condensing engine with expansion does not require a compounded engine design, the historical use of staged cylinders supports the proposal of re-using heat recovered during steam condensation in a lower pressure cylinder stage. The compounded engine designs of historical engines could be used in future work to guide design of an atmospheric engine with heat recovery and re-use, utilising multiple cylinder stages. This concept is discussed in Chapter 6 where the work in this thesis has investigated the theoretical potential of such a design.

2.4.4.4 Mechanical Governor

A centrifugal or flyball governor is a mechanical device used on historical steam engines to control engine speed through use of centrifugal forces (L.R. Ingersoll Physics Museum, 2023). As engine speed increases so does the angular velocity of the flywheel *(ω)*. As the angular velocity of the flywheel increases centrifugal forces cause rotating masses (*m*) to swing out to a circular motion of larger diameter, shown in Figure 2-34 as an increase in angle between the axis and the governor rods *(φ)*. As the masses, or flyballs, swing out they lift a sleeve which acts to adjust the steam inlet valve position thus controlling steam inflow into the engine (*Q*) and with-it engine speed.

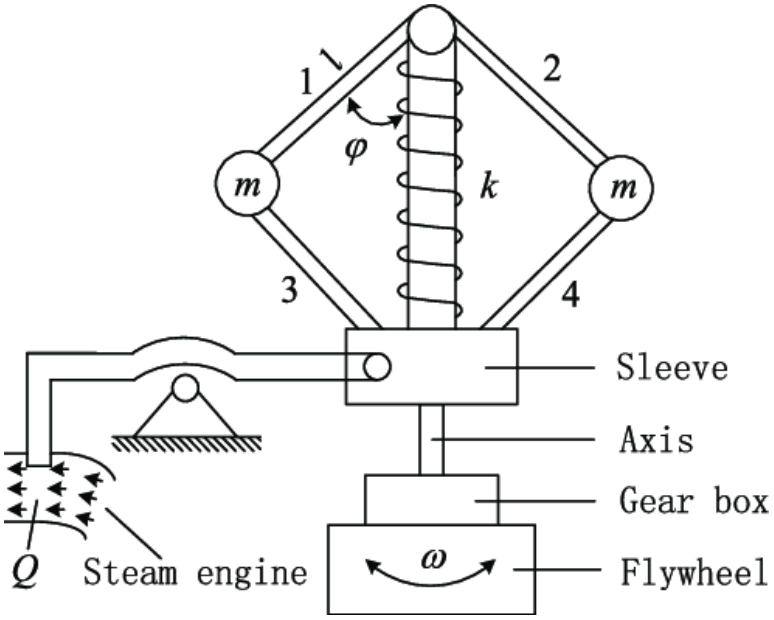

Figure 2-34 Diagram of centrifugal governor. *m* = mass. *ω* = angular velocity. l = rod length. *k* = spring stiffness. *Q* = steam flow into the engine. *φ* = angle between axis and rods. Reproduced from (Yan, et al., 2020) under CC BY 4.0.

This device could be used on future atmospheric engine condensing designs to control engine speed. It is noted that testing of the Mk.III engine, described in Chapter 4, identified that the atmospheric condensing engine regulates its own speed, increasing to a maximum point where evacuation of steam from the cylinder is no longer effective, resisting power production and causing a subsequent decrease in engine speed. Therefore, it is proposed here that a mechanical governor could be an effective method of ensuring atmospheric condensing engine speeds are maintained around an optimum set point on future iterations. Use of a mechanical device would remove the need for the electronic control employed on modern engines to date, simplifying the design.

2.4.4.5 High Pressure Engines

Steam engines began to transition to high pressure versions around the year 1800, otherwise known as 'strong steam' (Semmens & Goldfinch, 2000). The increased pressure created a greater driving force on the piston allowing more power to be produced and engines to become smaller as a result. However, this increased the risk of explosion, and it is suggested in literature that James Watt disapproved of high-pressure engines as a result (Semmens & Goldfinch, 2000). The impact of pressure on energy density is relevant to this project, as the atmospheric condensing engine has a lower energy density than alternative heat engines operating at high pressure, such as the ORC as discussed in Section 2.2.3.

Whilst the lower operating pressures of the atmospheric CE are beneficial to the applications being discussed for the technology in this thesis, such as domestic systems, there is the opportunity to increase the condensing engine boiler pressure above atmospheric to create a positive pressure difference across the piston when operating without expansion to help improve the stability of power output. Recent work by Muller & Howell (2021) investigated the theoretical thermal efficinecy of the condensing engine for evaporator temperatures up to 110^{o}C with increasing expansion ratios and a heat sink of 20^{o}C; see Figure 2-28.

Increasing boiler temperature from 100^{o}C to 110^{o}C increases the theoretical maximum thermal efficiency from 18.3% to 18.9% at an expanion ratio of n = 8 (Muller & Howell, 2021). Whilst this is a modest gain of just 3.3% it demonstrates an example case study, and would result in smoother power which is not accounted for in the theoretical data but would greatly benefit the operation of the engine. Investigating higher pressures was not included as part of the scope of this work, but is recommended to be investigated on future practical engines. Previous condensing engine literature suggests a targeted heat source temperature range up to 150^{o}C (Muller, et al., 2018). It is noted, however, that in order for the condensing engine to remain beneficial compared to the ORC

in domestic applications, relevant safety standards and their added complexity once triggered at higher pressures should be considered.

2.4.4.6 Minimising Thermal Energy Losses: Material Selection and Steam Jackets

Review of literature has already discussed the impact of cooling effects in the cylinder causing steam condensation. This results in a larger steam requirement, a larger thermal energy input, and a reduced efficiency. This effect is prevalent in engines with high expansion ratios and is exacerbated when the cylinder and piston are manufactured from thermally conductive materials. It is therefore identified that the modern-day condensing engine could have a cylinder and piston manufactured from thermally insulating materials. Modern advancement in material selection allows plastics such as PTFE to be investigated. PTFE would also offer the benefit of having a low friction coefficient reducing associated losses. The investigation of different material types for use on the modern condensing engine was not included in the scope of this project, but is a recommendation for future work.

The use of steam to drive the condensing engine means that an alternative method of reducing thermal losses also exists in the form of a steam jacket. The steam jacket is a steam filled space around the cylinder, as shown in Figure 2-35. As jacket steam condenses the latent heat is passed to the cylinder wall and maintains its temperature. This mitigates heat transfer from the working steam to the cylinder wall and minimises condensation inside the cylinder.

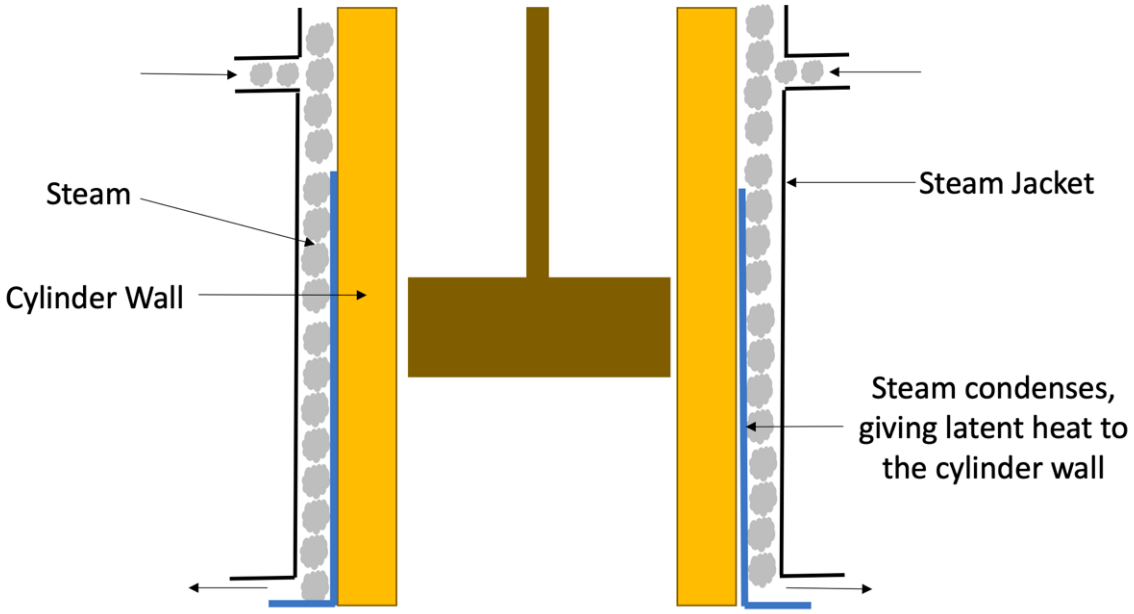

Figure 2-35 Diagram of steam jacket around steam engine cylinder.

Thermal energy input from the steam jacket also ensures that any condensate inside the cylinder re-evaporates early in the stroke. By re-evaporating condensate in the cylinder earlier in the stroke it has a higher pressure and therefore a greater enthalpy for energy production (Ewing, 1910). Whilst the steam jacket requires an increased thermal input, this is offset by the reduced steam requirement inside the cylinder, and the overall effect is for an increase in efficiency (Ewing, 1910). Historical empirical results are given by Ewing (1910) to support this, presenting a small single cylinder engine producing 0.75kW of useful mechanical power and exhibiting a total steal demand of 13.2kg/hr with a steam jacket and 17.7kg/hr without.

2.4.5 Summary: Current State of the Condensing Engine

Section 2.4 has reviewed the Mk.II condensing engine built and tested at the University of Southampton as the most recent example of a modernised practical model. The review highlighted that whilst the Mk.II engine with steam expansion displayed comparable second law efficiencies to ORC systems seen in literature, around 40%, there were significant sources of inefficiency contributing to a large difference between practical and theoretical performance. These were related to system pressure, friction, and heat recovery effectiveness. This further justifies that continued development of a modern-day atmospheric condensing engine is needed. The following improvements were identified for testing on the next iteration of engine:

- Use of a uniflow cylinder. The evacuation ports will allow for improved steam evacuation and therefore reduced cylinder pressure for improved engine performance. Thermal losses from the cylinder are also reduced. This is a novel configuration not yet tested on an atmospheric condensing engine.
- Use of a single acting cylinder. This removes the need for a bottom cylinder section which can become choked with condensate. It also reduces friction by replacing the beam and parallelogram. Furthermore, it also allows for multiple cylinders to be attached to one crank shaft more easily, giving greater flexibility during future scale up. This can be used in combination with the proposed uniflow configuration.
- Use of a steam jacket to prevent thermal losses from the cylinder.
- Improved valve selection for reduced minor head loss.
- Use of a two-stage condensation system with an intermediate flat plate heat exchanger for heat recovery. This will allow sufficient residence time of steam in the intermediate section for heat recovery to occur without preferential condensation. Use of a flat plate heat exchanger will maximise evacuation of condensate preventing re-evaporation under vacuum.

2.5 Literature Review Summary

Section 2.5 summarises the main points highlighted in the literature review and signposts the remainder of the thesis. Sections 2.1 and 2.2 reviewed low grade heat availability and the current technologies that can be used for its recovery:

- Substantial low-grade heat exists, both as waste heat from industry and from renewable sources such as solar thermal collectors. For example, 100TWh/yr of waste heat exists below the temperature of 200^{o}C in Europe.
- Conversion of low-grade heat into mechanical or electrical power is more flexible, and therefore more desirable, than direct heat use technologies.
- ORC systems are the most commonly used heat to power LGWH recovery technology.
- When operated in the chosen temperature range, or at small scales, ORC's achieve typical electrical efficiencies 5% - 15% and second law efficiencies between 20% - 40%.
- ORC systems utilise organic refrigerants which require safety and environmental consideration. However, they have a lower boiling point than water allowing higher pressures to be used and greater energy density achieved.
- It was concluded that the atmospheric condensing engine has benefits over the ORC in low power applications of low temperature thermal energy recovery. A potential power scale of 1kW - 200kW was proposed.

Section 2.3 subsequently introduced the atmospheric condensing engine, identifying its potential benefits:

- It uses simple technologies implying cost effectiveness.
- It operates at atmospheric pressure or below and uses water as a safe and sustainable working fluid.
- It has a theoretical efficiency of up to 17.7% at a heat source temperature of 100^{o}C, when using steam expansion.

Section 2.4 reviewed the MK.II condensing engine built at the University of Southampton as the most recent practical example of the technology. This review found that:

- Maximum thermal and second law efficiencies of 5.5% and 55% were achieved when utilising steam expansion. This was calculated using piston power and therefore not directly comparable to current ORC systems, but gives an indication of the technology's potential.
- Significant mechanical friction was observed, as much as 60% of power output.

- Sub-optimal system pressures were observed, limited by restrictions to steam evacuation from the cylinder to the condenser.
- Heat recovery could not be achieved without negatively affecting engine performance.
- The target heat source temperature range for the condensing engine technology should be around 50°C - 150°C, with the upper range to be tested in future literature to better understand the benefits.

As part of its critical review, Section 2.4 also proposed the following solutions to improve the condensing engine design:

- Use of a uniflow condensing engine configuration to improve steam evacuation.
- Use of a single acting engine to reduce friction and allow use of multiple cylinders.
- Source improved valving with increased orifice diameter and reduced minor head loss coefficient.
- Use a steam jacket to further minimise thermal losses.

In addition to the above, the heat recovery attempted during operation of the MK.II engine should be explored further in this project. The critical review of the heat recovery work found that improvement on the previous attempts could be achieved through:

- A two-stage condensation process, with the first stage recovering heat and the second stage fully condensing the residual steam.
- Use of a flat plate heat exchanger for intermediate heat recovery to maximise evacuation of condensate and prevent re-evaporation.
- Theoretical investigation to understand thermal energy available for recovery and quantification of re-use potential.

As a result of this literature review, this research project undertook the development and testing of a novel modernised single acting uniflow condensing engine. It also investigated heat recovery on the condensing engine, identifying novel concepts for further improvement of the technology. This is in response to the aims and objectives identified in the introduction. Chapter 3 investigates the single acting uniflow engine theory and estimates the theoretical efficiency of the engine, justifying its further development. Chapter 4 details the work performed on the development of the first prototype of this type of engine, the Mk.III. This involved both experimental work on the practical model as well as theoretical modelling of steam evacuation to guide future design. Chapter 5 used the lessons learned from the Mk.III work to propose an updated design for the Mk.IV single acting uniflow engine. This work was performed as a part of a collaboration to integrate the engine with solar thermal collectors, allowing discussion on the integration of the technology into wider systems and the challenges faced. This concludes the work performed on

the single acting uniflow engine as part of this research. Chapter 6 details the work performed on the heat recovery on the condensing engine. This includes both theoretical modelling to justify the potential of heat recovery and re-use as well as practical experiments to show proof of concept without negatively affecting engine performance. Finally, Chapter 7 concludes the findings of this research project and make some further recommendations for future work.

Chapter 3 Single Acting Uniflow Condensing Engine Theory

Chapter 3 presents an assessment of the theoretical efficiency of the proposed single acting uniflow condensing engine using a mathematical model. First, the concept of the engine configuration is explained, including steam admission and evacuation phases. Next, the method used in the model is presented, namely the equations which describe the power production throughout the cycle. Finally, the theoretical efficiency results and analysis are presented before conclusions are drawn on the suitability of this type of engine arrangement. This type of theoretical assessment is the first known analysis of its kind for a modernised version of this arrangement of condensing engine, furthering the knowledge of the technology.

3.1 Single Acting Uniflow Engine Concept

Whilst the uniflow concept has historical links (Hills, 1989), to the best of the author's knowledge this is the first known use on a modernised condensing engine and is therefore treated as a prototype. The system consists of a cylinder, a piston which also serves as a slide valve for a steam exit port in the cylinder wall, and two solenoid valves which allow further control of the steam inlet and outlet. The Mk.III single acting uniflow arrangement is shown schematically in Figure 3-1. The downstroke is described by phases 1 and 2 in Figure 3-1. These are similar to those of the previous iterations of the condensing engine reviewed already in Chapter 2, with steam admission beginning the downstroke in phase 1 and the steam inlet valve being closed in phase 2 to allow for steam expansion.

The upstroke is described by phases 3 and 4 of the cycle shown in Figure 3-1, where the first differences in arrangement operation are observed. During phase 3 the piston reaches 'Bottom Dead Centre' (BDC) and the uniflow evacuation port is revealed by the piston to allow rapid evacuation of steam to the condenser. This translates the partial vacuum into the cylinder and during phase 4 the piston begins its upstroke and closes the port. An outlet solenoid valve is also opened in phase 3 to maintain connection between the cylinder and condenser, allowing evacuation of any residual steam. The atmospheric pressure external to the piston drives the piston against the vacuum inside the cylinder and produces work during phase 4. This is because of the single acting nature of this configuration, with only a single working chamber in the cylinder and the piston being attached to a traditional crank shaft located underneath the cylinder.

The additional cross-sectional area provided by the uniflow exit port reduces the pressure drop and energy losses experienced during steam evacuation from the cylinder. It can be seen by comparing Figure 3-1 with the Mk.II engine schematic, seen in Figure 2-13, that the uniflow arrangement allows two routes for steam evacuation allowing for a greater pressure difference driving force for power production.

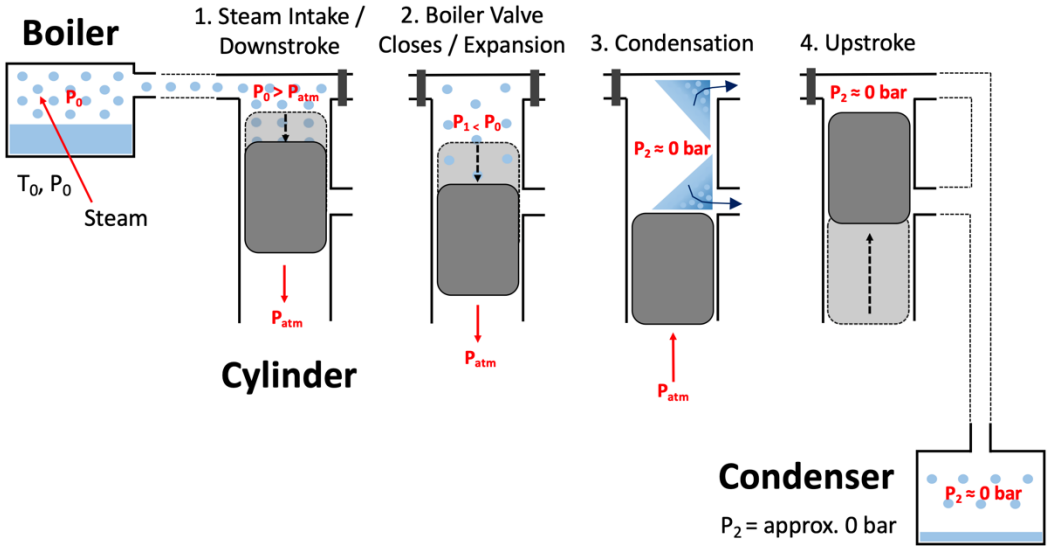

Figure 3-1 Mk.III condensing engine single acting uniflow arrangement phases of operation.

3.2 Theoretical Efficiency Model Method

The model was developed in Matlab using XSteam data tables (Holmgren, 2007). The model was built for a cylinder bore diameter of 50mm and stroke length of 100mm, relevant to the Mk.III engine design given in Chapter 4.

The model first simulates the downstroke and then the upstroke of the single acting uniflow engine, using equations which describe power production based on pressure driving force and volume swept. These equations are those already reviewed in Chapter 2, but applied in the appropriate context here for the different engine configuration. As these are isentropic equations, they assume the engine to be both adiabatic and reversible. This assumes no heat losses and no friction losses from the system and therefore gives an ideal case not achievable in practice. This is a commonly used method in heat engine theory to estimate potential system performance and is required to simplify the analysis (Cengel & Boles, 2011).

During phase 1, steam admission is controlled by the inlet solenoid valve opening, beginning the downstroke of the piston. During phase 2, the inlet valve can be closed part way through the stroke to achieve steam expansion for increased efficiency. This downstroke cycle is unchanged from the double acting engine employed on the Mk.II engine. The model uses the boundary work equation, see Equation (3.1), to calculate the work output during phase 1 for the cylinder volume passed under constant cylinder pressure.

$$W_{d,1} = P_{cyl} V_{bdy} \tag{3.1}$$

Where:

- $W_{d,1}$ is the boundary work produced during the downstroke (J).
- V_{bdy} is the boundary volume passed by the piston (m^3).
- P_{cyl} is cylinder pressure (Pa).

Next, the model uses the ideal gas laws for isentropic expansion, see Equations (3.2) and (3.3), to calculate the work produced in phase 2 of the CE downstroke.

$$W_{d,2} = \frac{1}{\gamma - 1}(P_0 \cdot V_0 - P_1 \cdot V_1) \tag{3.2}$$

$$P_1 = P_0 \times \left(\frac{V_0}{V_1}\right)^{\gamma} \tag{3.3}$$

Where:

- $W_{d,2}$ is the work produced during expansion in the downstroke (J).
- V_0, P_0 are cylinder volume (m^3) and pressure (Pa) at the start of expansion.
- V_1, P_1 are cylinder volume (m^3) and pressure (Pa) at the end of expansion.
- γ is the adiabatic coefficient of expansion, with a value of 1.08 for this research (Muller, et al., 2018).

Finally for the downstroke, the model uses Equation (3.4) to calculate the work removed due to pressure resisting the direction of motion of the piston. The back pressure is atmospheric in this case due to the single acting arrangement. The total energy produced during the downstroke is then calculated using Equation (3.5).

$$W_{d,3} = P_{atm} V_{cyl} \tag{3.4}$$

$$W_d = W_{d,1} + W_{d,2} - W_{d,3} \tag{3.5}$$

Where:

- $W_{d,3}$ is the work removed from the system by back pressure forces (J).
- V_{cyl} is the volume passed by the entire downstroke (m^3).
- P_{atm} is atmospheric pressure (Pa).
- W_d is the total work produced over the downstroke of the uniflow engine (J).

During the upstroke (phases 3 and 4) the atmospheric pressure external to the piston drives the piston against the vacuum inside the cylinder and produces work. The model calculates this using Equation (3.6), assuming a constant pressure on both sides of the piston during the entire upstroke.

$$W_u = (P_{atm} - P_{cyl}) V_{cyl} \tag{3.6}$$

Where:

- W_u is the work produced in the upstroke (J).
- V_{cyl} is the volume passed by the entire upstroke (m^3).
- P_{atm} is atmospheric pressure (Pa).
- P_{cyl} is cylinder pressure (Pa), assumed to be equal to condenser pressure following evacuation.

The model assumes pump losses to be negligible and therefore omits them from the analysis, as commonly done in heat engine theory (Cengel & Boles, 2011). The equation for pumping losses is given by Cengel & Boles (2011) as Equation (3.7)

$$W_{pump} = v_l \times (P_2 - P_1) \tag{3.7}$$

Where:

- W_{pump} is the work required in the pump (J).
- v_l is the specific volume of the fluid (m^3/kg).
- P_2 and P_1 are fluid pressures after and before pumping respectively (Pa).

Assuming a boiler pressure of 1bar and condenser pressure of 0.02bar, associated with temperatures of 100°C and 20°C inside the boiler and condenser respectively, the pump is required to increase fluid pressure by 0.98bar (or 98kPa). Assuming water has a density of 1000 kg/m^3 it has

a resulting specific volume of 0.001 m^3/kg. Therefore, using Equation (3.7) the pump work can be estimated as 98 J/kg. This is just 0.06% of the power output calculated by the model for the case with no expansion, justifying the assumption that pump losses are negligible.

Next, the model calculates the total work across a single stroke of the single acting uniflow condensing engine using Equation (3.8).

$$W_{out} = W_d + W_u \tag{3.8}$$

Where:

- W_{out} is the total work produced over one entire revolution of the uniflow engine (J).
- W_u is the work produced in the upstroke (J).
- W_d is the work produced in the downstroke (J).

Finally, the model calculates the thermal energy input required for the steam, see Equation (3.9), and calculates the associated thermal efficiency in Equation (3.10).

$$Q_{in} = (h_g - h_l) \times m_s \tag{3.9}$$

$$\eta_{th} = \frac{W_{out}}{Q_{in}} \tag{3.10}$$

Where:

- η_{th} is the thermal efficiency as a decimal fraction.
- Q_{in} is the thermal energy requirement for the input steam (J).
- h_g is the enthalpy of the vapour at boiler temperature (J/kg).
- h_l is the enthalpy of the feed water at associated temperature (J/kg).
- m_s is the mass of steam (kg).

3.3 Theoretical Efficiency Results and Analysis

The described model was used to simulate single acting uniflow condensing engine theoretical efficiencies for a series of increasing expansion ratios. A boiler temperature of 100°C and condenser temperature of 20°C were used, chosen to analyse boiler and condenser pressures of 1bar and 0.02bar respectively as realistic optimum cases for the atmospheric condensing engine. Fully saturated steam was also assumed in this initial theoretical study, deemed by the author to be suitable as the model simulates an ideal case. The results are shown in Figure 3-2. Maximum theoretical efficiencies approach 19% at expansion ratios around *n* = 10, beginning to plateau prior

to reaching the *Carnot* efficiency value of 21%. This justifies the development of this engine arrangement as part of this research, discussed in Chapter 4 and Chapter 5.

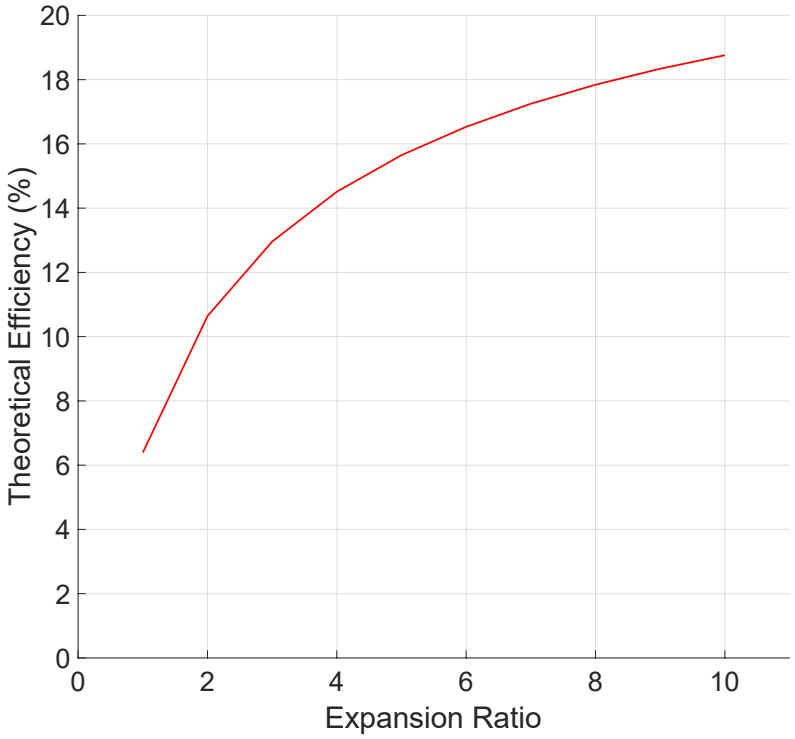

Figure 3-2 Theoretical efficiency of the single acting uniflow condensing engine with outlet valve, calculated using isentropic expansion equations for increasing expansion ratios.

3.4 Theoretical Analysis Discussion

The theoretical efficiency results presented in Figure 3-2 have justified continued investigation of the proposed single acting uniflow engine arrangement. The calculated maximum efficiency of 19%, presented as an ideal case using isentropic equations, mirrors those also reported by (Muller, et al., 2018) and (Bortolin, et al., 2021) for different engine arrangements, both reporting maximum ideal efficiencies around 18%. This suggests that the high theoretical efficiencies associated with the condensing engine with steam expansion are linked to the principles of the technology itself and that engine arrangement selection should be based on the ability to maximise practical efficiency. It has been explained already how the single acting uniflow engine arrangement should allow for better practical performance of the engine. In the context of the theoretical model, this reduces pressure inside the cylinder during the upstroke and therefore increases the pressure driving force in Equation (3.6) to generate more work. Whilst practical efficiencies are not expected to approach the maximum shown here due to thermal and mechanical losses, the above analysis demonstrates the potential of this technology.

However, it is also important to understand the potential negative implications of the theoretical equations described in Section 3.2. Specifically, it can be understood from Equation (3.5) that for the atmospheric single acting uniflow engine the work produced in the downstroke is zero when operating with expansion ratio $n = 1$ and negative when $n > 1$. This is due to the final pressure inside the cylinder being less than atmospheric which resists the downstroke motion. Therefore, the atmospheric single acting uniflow condensing engine only produces positive power when the work produced in the upstroke outweighs that lost in the downstroke and is used to overcome the losses. This is a characteristic of the chosen design and gives rise to a greater need for power balancing when compared with a double acting engine.

However, the benefits of the single acting variant are considered worthwhile, and therefore a flywheel and/or multiple cylinders should be used to balance the single acting uniflow engine power output. Additionally, future work could also explore the effect of increasing the boiler pressure to increase energy density and reduce losses in the downstroke, as discussed in Section 2.4.4.5. For example, communication with the University of Stellenbosch Solar Thermal Energy Research Group (STERG) identified that the boiler in the combined system detailed in Chapter 5 could be operated at a pressure of 1.5bar without being classified as a pressurised vessel.

3.5 Conclusions

A theoretical model of the single acting uniflow condensing engine was developed and used to simulate theoretical efficiencies for the technology for a series of expansion ratios. The theoretical equations describing the engine arrangement were also critically discussed to understand potential implications on design. The conclusions drawn from this work were:

- The single acting uniflow condensing engine allows for improved steam evacuation through increased area for steam flow during evacuation.
- Maximum theoretical efficiencies approach 19% when steam expansion approaches $n = 10$ for boiler and condenser temperatures of 100°C and 20°C respectively. This justifies the single acting uniflow condensing engine as suitable for further investigation.
- The single acting uniflow arrangement theoretical efficiency is similar to those of the double acting engine investigated in previous literature, highlighting that the arrangement has limited effect on theoretical performance and should be selected on practical performance instead.
- The single acting uniflow condensing engine loses power in the downstroke. The upstroke power must therefore be greater in magnitude to overcome this, with power balancing measures such as a flywheel or multiple cylinders to ensure a smooth power output.

Chapter 4 The Mk.III Engine: Design & Testing

The Mk.III engine is the first known iteration of a modernised single acting uniflow condensing engine. The Mk.III engine was built and tested at the University of Southampton as part of this research, with the associated work reported in Chapter 4. Firstly, an overview of the engine system is given. Secondly, power and efficiency tests performed on the engine are reported and the results discussed in the context of other available technologies. Thirdly, friction test results are reported and linked to the conclusions of the power tests. Next, a theoretical model developed for simulating steam evacuation from the cylinder is outlined and the results discussed. Validated against the Mk.III engine real pressure data, this model allows for improved design of future iterations. Next, a critical review of the Mk.III engine design is given with discussion on its effectiveness and recommendations made for future work. Finally, conclusions are made about the implications of the Mk.III engine work.

4.1 Mk.III Engine System Overview

The engine was designed, assembled, and tested by the author of this research with guidance from the project supervisory team and support from laboratory technicians. Production of technical drawings was completed by Hanley Design and the components manufactured by Quayside Engineering Ltd. Technical drawings are available in the data repository, the contents of which are outlined in Chapter 9. Photographs of the engine are also available in the data repository as well as the design review discussion in Section 4.5. The system diagram for the engine is shown in Figure 4-1. The assembled engine is shown photographed in the laboratory in Figure 4-2.

The engine used two separate boilers, operating at atmospheric pressure. The first supplied the main engine cylinder. The second supplied the steam jacket. The use of separate boilers prevented pressure fluctuations in the main engine line effecting supply to the jacket. The manual valve (V1) was used to control flow to the steam jacket. An electronically activated solenoid valve (SV1) controlled the steam admission to the cylinder during the downstroke. The piston sealed the outlet port until it reached BDC. Then, the inlet valve closed, and steam was evacuated through the uniflow outlet port. At piston BDC the outlet valve (SV2) opened to aid evacuation, maintain connection between cylinder and condenser, and limit steam compression.

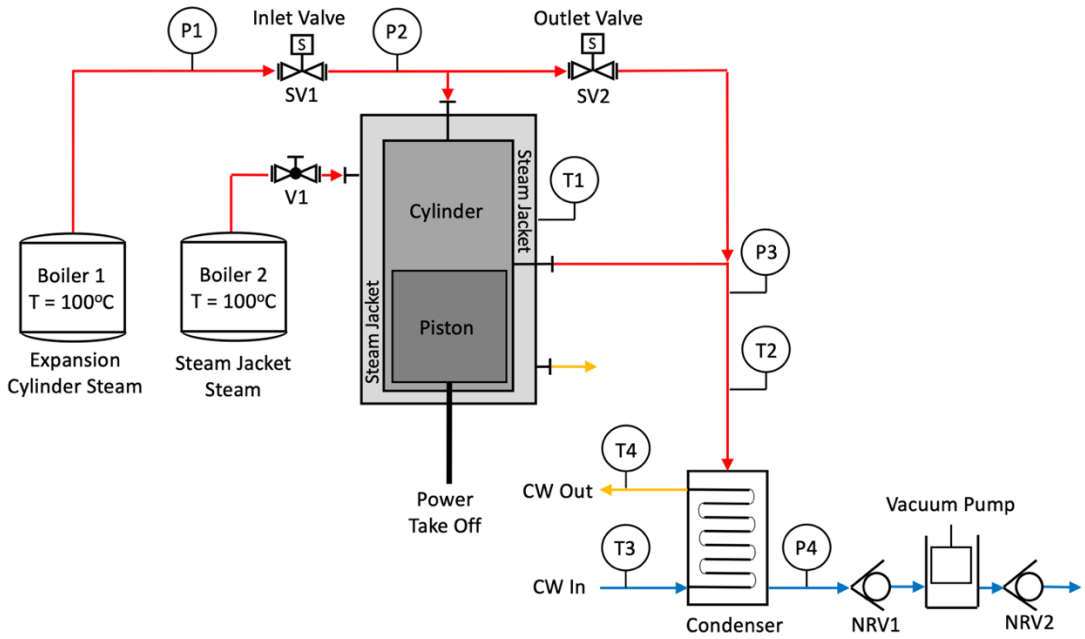

Figure 4-1 Process schematic for the Mk.III Condensing Engine. V = Valve. SV = Solenoid Valve. P = Pressure measurement. NRV = Non-Return Valve. T = Temperature measurement. CW = Cooling Water.

A single cylinder was used to reduce prototype cost, requiring a flywheel to store energy. A single evacuation port was also used on this first prototype to assess effectiveness. It is noted that the chosen evacuation port geometry on the Mk.III cylinder resembled that of a slot, longer in the horizontal plane than the vertical, see Figure 4-13. This enabled its surface area to be revealed more quickly by the vertical piston motion and thus maximise evacuation rate to allow a rapid drop in pressure in the cylinder. A chamfer was cut on the inside of the port to minimise friction against the piston. A brass cylinder and piston were used to maintain consistency and allow comparison with the Mk.II engine. PTFE packing was used to seal the piston, chosen to reduce friction. A piston vertical length equal to the engine stroke length was chosen to ensure the evacuation slot was sealed for the entirety of the downstroke. The piston design is discussed in more detail in Section 4.5.

A steam jacket, a steam filled space around the cylinder, was used to maintain the cylinder temperature and avoid steam condensation inside of the working cylinder. Historic steam engine literature has demonstrated this to have a positive effect on engine efficiency by reducing total steam demand (Ewing, 1910). It was also found that on the Mk.III condensing engine the steam jacket was critical in preventing uneven thermal expansion causing jamming of the piston, reviewed further in Section 4.5. The steam flow was controlled by a manual valve which for these tests was fully open to ensure sufficient heating.

The two cylinder outlet flows combined in a tee junction before entering the condenser re-used from Mk.II engine tests, see Figure 2-22. Cooling water was used in the condenser to achieve steam condensation, in this case from laboratory mains supply as used on the Mk.II engine, with a temperature of around 15°C. Mains water in the UK ranges in temperature between 5°C - 20°C, depending on time of year, and therefore allows for a suitable heat sink (Davies, et al., 2016). The achieved condensation created a partial vacuum inside the cylinder and allowed external atmospheric pressure to drive the piston through its upstroke towards Top Dead Centre (TDC).

The power take-off translated this rotational movement into useful power. Mechanical power output was measured using a standard friction brake commonly found in thermodynamic texts, eg. (Rajput, 2006), through use of a rope, weight, and loadcell; see Figure 4-18. This measurement method was chosen as a simple and cost-effective solution for a prototype technology. The vacuum pump evacuated the condensate from the condenser and maintained low system pressure. Non return valves were used either side of the pump to ensure the correct direction of flow. When the piston returned to TDC the process was repeated. Key Mk.III engine component dimensions were chosen to remain consistent with the Mk.II engine. Nominal values are given in Table 4-1 with tolerances where available. The piston was redesigned as part of the Mk.III engine testing, see Section 4.5.2, and therefore tolerances are not specified for this. Tolerances are also not specified for the condenser re-used from the Mk.II engine. This is because both the piston and condenser were manufactured according to nominal values. Whilst some dimensions are specified to three decimal places it is not believed by the author to be necessary for successful operation of the engine and would increase manufacturing costs. This could be investigated in future work associated with the scaling and economics of the technology.

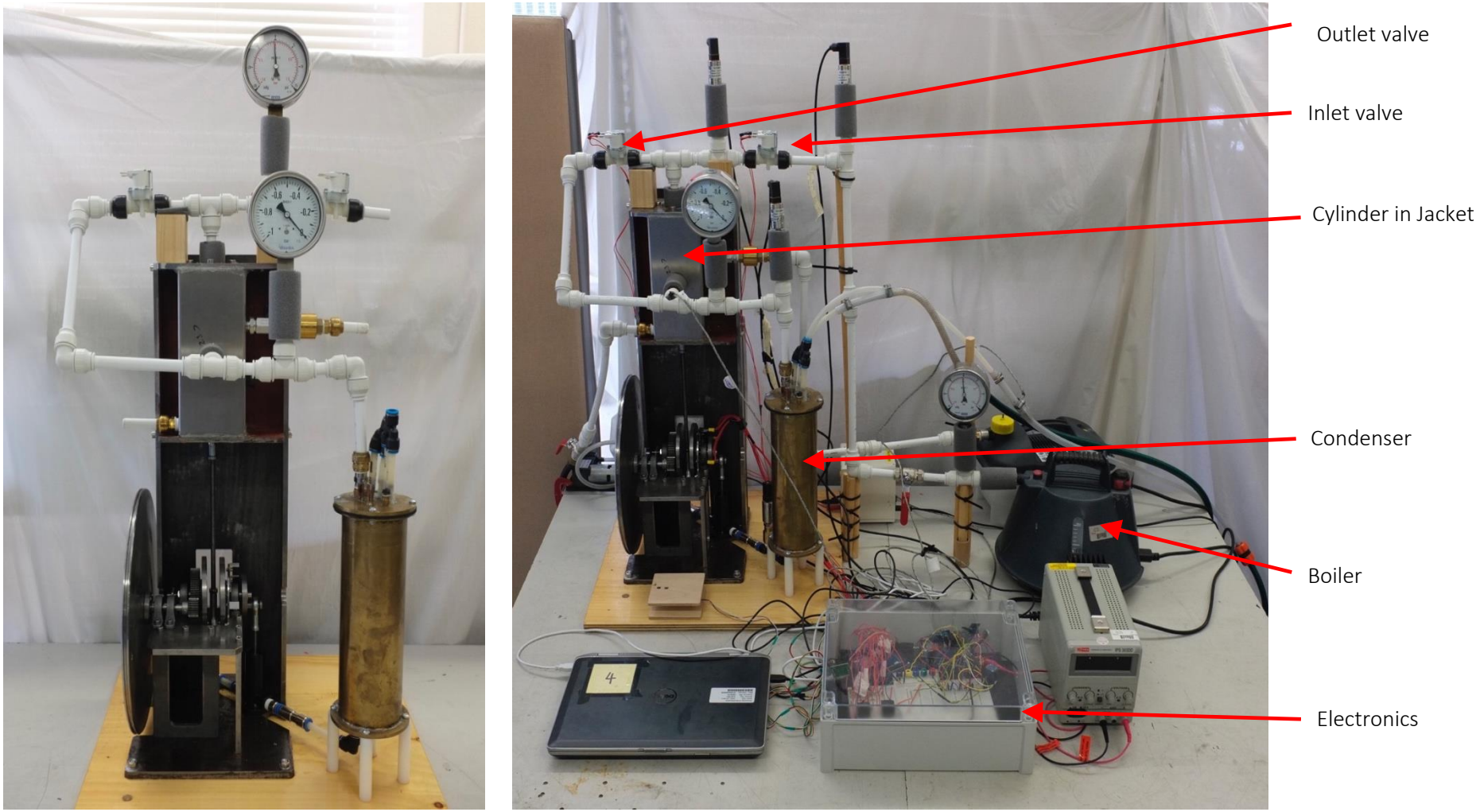

Figure 4-2 Photographed Mk.III condensing engine in the hydraulics laboratory. LEFT: Ancillaries removed. RIGHT: Engine set up for testing.

Table 4-1 Mk.III condensing engine component technical information. Tolerances are given as specified on the technical drawings where available, either as a ± value or as a range. Dimensions not specified on the drawing, eg. stroke lengths, do not have any quoted tolerances in this table. The updated piston and re-used condenser also do not have tolerances as these were manufactured to a nominal value.

Component	Parameter	Value / Unit
Cylinder	Bore diameter	50.000 – 50.025 mm
	Stroke length	100 mm
	Exit port height	5.0 ± 0.5 mm
	Exit port width	6.0 ± 0.5 mm
Updated Piston (See Section 4.5.2)	Diameter	49.98 mm
	Length	112.5 mm
	Sealing collar height	7.0 mm
Steam Jacket	Cavity depth	10 mm
Condenser	Bore diameter	88.9 mm
	Bore length	300 mm
	Copper pipe internal diameter	6 mm
	Height of copper coil	200 mm
	No. of copper coil turns	20
Vacuum Pump	Bore diameter	25.200 – 25.221 mm
	Stroke length	50 mm
	Piston diameter	25.180 – 25.193 mm
Power Take Off	Crank disk diameter	110.0 ± 0.5 mm
	Gear transmission	1:3
Flywheel	Diameter	328.0 ± 0.5 mm
	Thickness	10.0 ± 0.5 mm
	Material	Mild Steel
	Estimated mass	6.6 kg

A simplified electronic control system was also designed for the Mk.III engine to allow manual control, shown schematically in Figure 4-3 and photographed in Figure 4-20. This used three optical sensors and a reflective strip on the crank disk to identify the piston's position at key points of the engine stroke, see Figure 4-3. Sensors (A) and (B) were fixed and indicated BDC and TDC respectively. Sensor (C) could be manually adjusted through 90° to control when expansion was employed, shown in the position for n = 2 in Figure 4-3. The signal was translated to the solenoid valves using a microcontroller which also used the signals to determine engine speed.

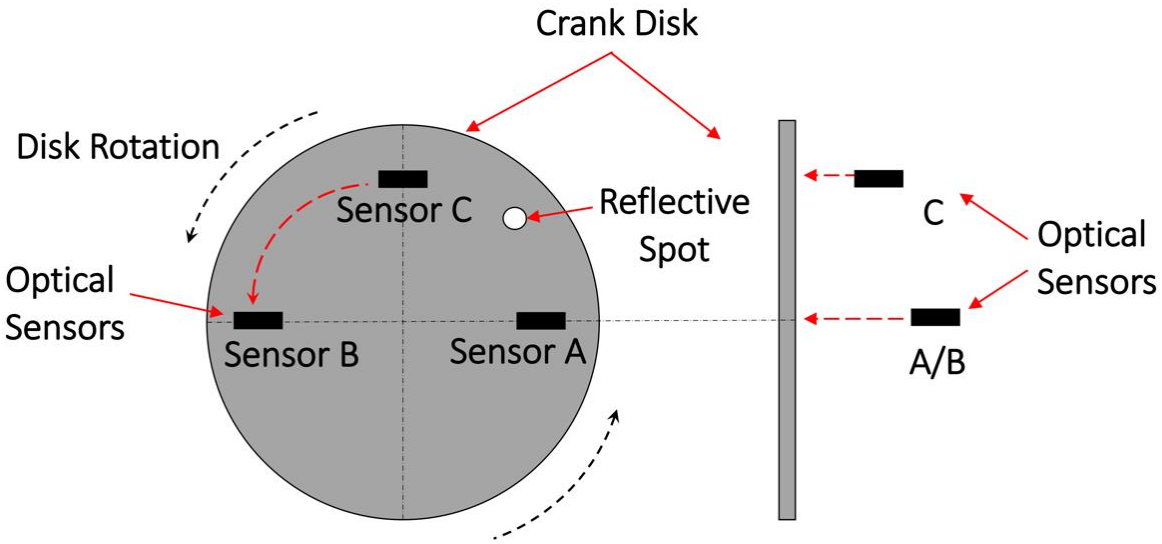

Figure 4-3 Mk.III condensing engine optical sensor control schematic.

The microcontroller was also used to record pressure and temperature data for analysis. Pressure transducers and k-type thermocouples were re-used as legacy items from the previous Mk.II engine testing to reduce cost. The types listed in Table 4-2 were chosen as they were capable of operating within the required pressure and temperature ranges, were resistant to corrosion from steam, and had suitable accuracy for a proof-of-concept study. Details of further electronic component used on the Mk.III engine are also given in Table 4-2 below.

Table 4-2 Mk.III condensing engine electrical component technical information.

Component	Parameter	Value / Unit
Engine control system	Optical sensor type Microcontroller type	ONSEMI QRD1114 Arduino Mega 2560
Solenoid valves	Type Orifice diameter Maximum response time	RPE srl 1175 BC 11 mm 25 milliseconds

Component	Parameter	Value / Unit
Pressure transducers	Type Operating pressure Operating temperature Reported accuracy	RS Pro 797-4970 -1 to +9 bar(g) -200 to +135°C +/- 0.25%
K type thermocouples	Thermocouple type Conditioner type Thermocouple accuracy Conditioner accuracy Combined accuracy	RS Pro 334-2622 Adafruit AD8495 +/-1.5°C +/-2.0°C +/-2.5°C
Load cell	Type Accuracy	5kg + HX711 amplifier +/-2g

4.2 Mk.III Power and Efficiency Tests

The MK.III condensing engine discussed so far in this chapter was tested in the UoS hydraulics laboratory to assess performance. This consisted of understanding system pressures as well as output power and thermal and second law efficiencies. These results were compared against the Mk.II condensing engine as well as current ORC systems in literature. For the single acting uniflow concept to be deemed a success the following criteria were required to be met:

- Improved steam evacuation compared to the Mk.II, represented by faster reduction in cylinder pressure at piston BDC.
- Improved power output and thermal efficiency compared to the Mk.II when operating under the same conditions.
- Comparative second law efficiencies to current ORC systems in literature.

4.2.1 Power and Efficiency Test Method

In total, 10 test runs were performed on the Mk.III engine before mechanical losses prevented further data gathering. These tests were conducted without expansion (n = 1) with engine speeds ranging from 27rpm - 52rpm. Atmospheric pressure steam was used as the heat source. Cooling water flow rates and temperatures of around 0.15 kg/s and 15°C were used in the condenser. This

research uses power and efficiency for comparison of technologies, defined below. Project delays prevented testing with steam expansion, which should be conducted in future work.

4.2.1.1 Piston Power

Piston power is an important characteristic as it allows understanding of engine performance independent of internal friction. Work produced by the piston was calculated theoretically by applying Equation (3.1) to (3.8) to six pressure profiles for each test run, taken over a period of stable operation, and finding the average. This was converted into a piston power using average engine speed, see Equation (4.1).

$$\dot{W}_{pis} = W_{rev} \times \frac{N}{60} \tag{4.1}$$

Where:

- $\dot{W}_{pis}$ is piston power output (W).
- W_{rev} is the work produced during an engine revolution (J), found using Equation (3.1) to (3.8).
- N is engine speed (rpm).

4.2.1.2 Mechanical Friction Brake Power

Mechanical power output was measured during five tests using a friction brake, also known as a rope brake dynamometer (Rajput, 2006). This involves fitting a rope inside a groove in the flywheel and hanging two weights. One weight hangs freely providing friction and the second sits on a load cell. The change in load cell reading during operation defines the frictional force and can be related to the flywheel power output using Equation (4.2) (Rajput, 2006).

$$\dot{W}_{fb} = \frac{(H - F)\pi\left(d_{fly} + d_{rope}\right)N_{fly}}{60} \tag{4.2}$$

Where:

- $\dot{W}_{fb}$ is friction brake power (W).
- H is the hung weight (N).
- F is the change in load cell reading experienced during engine operation (N).
- d_{fly} is the is flywheel diameter (m).
- d_{rope} is the rope diameter (m).
- N_{fly} is flywheel speed (rpm).

4.2.1.3 Thermal Energy Input

The Mk.III condensing engine thermal energy input is the sum of the thermal energy required for the working cylinder steam and for the steam jacket, see Equation (4.3). Working steam energy requirement is the product of the mass of steam required and the difference between vapour and liquid enthalpy at boiler conditions. A theoretical approach was developed to estimate the minimum steam jacket thermal energy input requirement, assumed to equal the heat losses from the cylinder and piston that it must balance, using *Newton's* law of cooling for each source of loss, with energy losses being summed to give a total.

$$\dot{Q}_{in} = \left[Q_{ws} \times \frac{N}{60}\right] + \dot{Q_{sJ}} = \left\{\left[(h_g - h_l) \times m_s\right] \times \frac{N}{60}\right\} + \left[\sum_{i=1}^{n}\left(h_i \cdot A_{ht,i} \cdot \Delta T_i\right)\right] \quad (4.3)$$

Where:

- $\dot{Q}_{in}$ is the thermal power input required in the engine working steam (W).
- Q_{ws} is the energy required per revolution for the cylinder working steam (J).
- $\dot{Q_{sJ}}$ is the thermal power required per revolution for the steam jacket steam (W).
- m_s is the mass of steam required per revolution (kg).
- h_g is the enthalpy of vapour at steam conditions (J/kg).
- h_l is the enthalpy of liquid water at boiler feed water conditions (J/kg).
- h_i is the local heat transfer coefficient for element *i* (W/m^2.K). A value of 13.75 W/m^2.K was used for average heat transfer with air via free convection (Kosky, et al., 2012).
- $A_{ht,i}$ is the heat transfer surface area for element *i* (m^2).
- ΔT_i is the change in temperature during heat transfer for element *i* (^{o}C).
- *N* is engine speed (rpm).

It has been proven in historical testing that the mass of steam required to operate the steam jacket is less than the mass of steam that would be lost through cooling losses and condensation if the jacket was not employed, see Section 2.4.4.6. It has also been estimated in literature that these cooling losses amount to approximately 30% of working steam requirements (Muller, et al., 2018). Therefore, the steam jacket steam requirement is expected to be less than 30% of the working steam requirement. It is noted that the methodology given above results in an estimated steam jacket requirement of 10% - 20% of the working steam. This gives confidence in the methodology.

4.2.1.4 Thermal and Second Law Efficiency

Thermal and second law efficiencies were used for analysis of Mk.III engine effectiveness and comparison to other technologies. The concept of these efficiencies has already been introduced

when reviewing current ORC technologies in the literature review. Thermal and second law efficiency relationships for the Mk.III engine are given in Equations (4.4) and (4.5) respectively.

$$\eta_{th} = \frac{\dot{W}_{out}}{\dot{Q}_{in}} \tag{4.4}$$

$$\eta_{II} = \frac{\eta_{th}}{\eta_C} = \frac{\eta_{th}}{\left(1 - \frac{T_{sat,co}}{T_{sat,cyl}}\right)} \times 100 \tag{4.5}$$

Where:

- η_{th} is the thermal efficiency (%).
- $\dot{W}_{out}$ is power produced by the engine (W), either piston or friction brake.
- $\dot{Q}_{in}$ is the thermal power input required in the engine working steam (W).
- η_{II} is the second law efficiency (%).
- η_C is the *Carnot* efficiency (%).
- $T_{sat,cyl}$ is the heat source temperature, associated with cylinder conditions (K).
- $T_{sat,co}$ is the heat sink temperature, associated with condenser conditions (K).

In this research the MK.III engine heat source was the saturation temperature associated with maximum cylinder pressure during steam inlet. The heat sink temperature was the saturation temperature associated with average condenser pressure. These assumptions represent the heat source and sink temperatures actually translated to the cylinder and condenser rather than those defined by boiler and cooling water temperature. The defined heat sink has been used previously in published literature (Muller & Howell, 2021). Whilst typical heat engine literature would define the heat source as the evaporator temperature, the Mk.II and Mk.III engines experienced a sub-optimal pressure drop from boiler to cylinder and therefore this alternative method has been employed to allow prediction of engine effectiveness between the heat source and sink it experienced. This can also be extrapolated to understand expected performance of an engine operating in a wider temperature range. This method has been deemed as suitable by the author of this work for this prototype technology to best understand the technology's potential, and the effects of this analysis on comparison with other technologies has been included in the relevant discussions later in the thesis.

4.2.1.5 Isentropic Efficiency

The isentropic efficiency has been used in this thesis for predicting future engine performance. The isentropic efficiency is defined as the percentage of the maximum ideal isentropic work achieved in practice, see Equation (4.6). The isentropic work is that estimated using isentropic equations, as presented in Chapter 3.

$$\eta_{isen} = \frac{\dot{W}_{out}}{\dot{W}_{isen}} \tag{4.6}$$

Where:

- η_{isen} is the isentropic efficiency (%).
- $\dot{W}_{out}$ is useful output power produced by the engine (W).
- $\dot{W}_{isen}$ is the maximum ideal isentropic power estimated for given engine conditions (W).

4.2.2 Power and Efficiency Test Results and Analysis

4.2.2.1 Cylinder Pressure Profiles

Figure 4-4 shows representative pressure profiles recorded during tests at 29rpm and 52rpm respectively. These represent the lower and upper speeds within the tested range respectively and have been given to provide comparison. The engine downstroke is represented by the increase in cylinder pressure as it is charged with steam from the boiler. The engine upstroke, the power stroke, is represented by the reduction in cylinder pressure to its minimum point.

The key takeaway from Figure 4-4 is that evacuation of steam through the exit port was successful, thus confirming that the uniflow arrangement has fulfilled its purpose. This is shown by the sharp gradient in cylinder pressure reduction. For example, it required approximately 200 milliseconds to drop from a peak cylinder pressure of around 0.95bar to a minimum of around 0.40bar. For context, this meant the Mk.III engine achieved a minimum cylinder pressure during the upstroke before reaching piston TDC, not something that was achieved on the Mk.II engine. This allowed a rapid generation in pressure driving force for power production during the engine upstroke, seen by the difference between cylinder and atmospheric pressure in the upstroke. This is especially true at slower speeds.

Generally, slower speeds allowed more time for pressure profiles to be properly developed. It is seen at 52rpm that during the upstroke the residual steam was compressed by the piston, observed as a spike in cylinder pressure. This is not observed at 29rpm as the residual steam has more time to be evacuated through the outlet valve before being compressed. This allowed for greater efficiency at slower speeds, analysed later. This highlights that condensing engine speed is naturally limited by the ability to evacuate steam from the cylinder and achieve the necessary sub-atmospheric pressures through condensation. There will be a maximum speed beyond which insufficient evacuation of steam takes place and the engine speed cannot increase further. This peak can be maximised by improving steam evacuation and condensation. This reinforces the need for the uniflow configuration, improved valving, and improved condenser performance. Future

tests at boiler pressures above atmospheric could also allow an increase in maximum engine speed by increasing the pressure driving force available in the cylinder in the downstroke. Likewise, there will be a minimum speed, below which there is insufficient energy to overcome losses in the system. This can be improved by having multiple cylinders operating out of phase.

It is also noted that the condenser pressure was higher at slower engine speeds indicating a high condenser heat load. Condenser load should be reduced at slower engine speeds due to a reduced steam flow rate. High condenser pressures at slow engine speeds could be caused by the reduced pump rate and therefore reduced evacuated volume.

On average, maximum cylinder pressure reached 0.95bar during the downstroke, representing a heat source temperature of around 98^{o}C. However, average cylinder pressure in the downstroke was around 0.1bar lower than maximum, limiting power production. This can be improved through revised steam inlet valve selection with a reduced minor head loss coefficient. Average condenser pressures during testing were around 0.3bar – 0.4bar, representing an average heat sink temperature of 72^{o}C, insufficiently low to maximise engine potential. This can be improved by increasing the relative size of the condenser and pump system to better handle thermal loads.

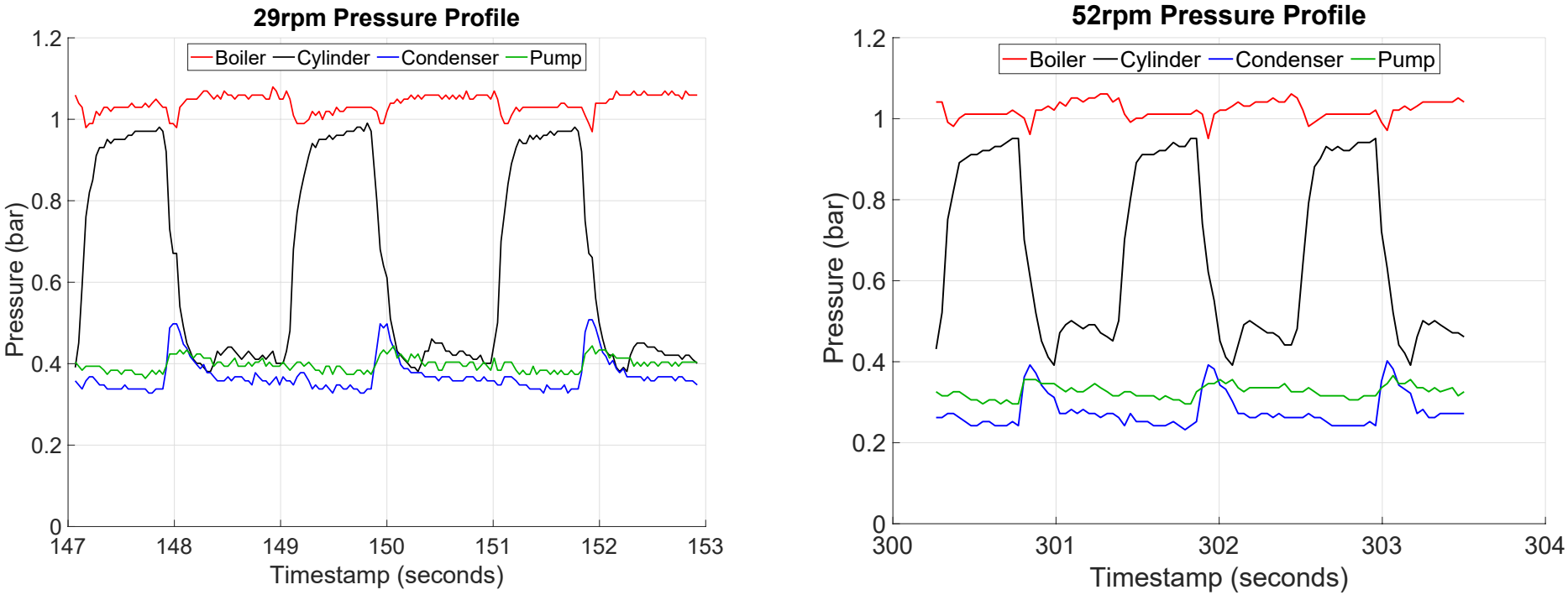

Figure 4-4 Mk.III condensing engine pressure profiles for three revolutions at speeds of 29rpm and 52rpm.

4.2.2.2 Engine Power

Figure 4-5 shows piston power as a function of engine speed. This has been plotted using a second order polynomial relationship with fixed y-axis intercept through the origin. This is because internal friction increases with engine speed causing the rate of increase in power output to decline. Additionally, the power output is expected to plateau at a maximum value, beyond which the engine speed is too high to allow effective evacuation of steam and engine performance is negatively affected as a result. This phenomenon has already been observed in the pressure plots at higher engine speeds in the previous section.

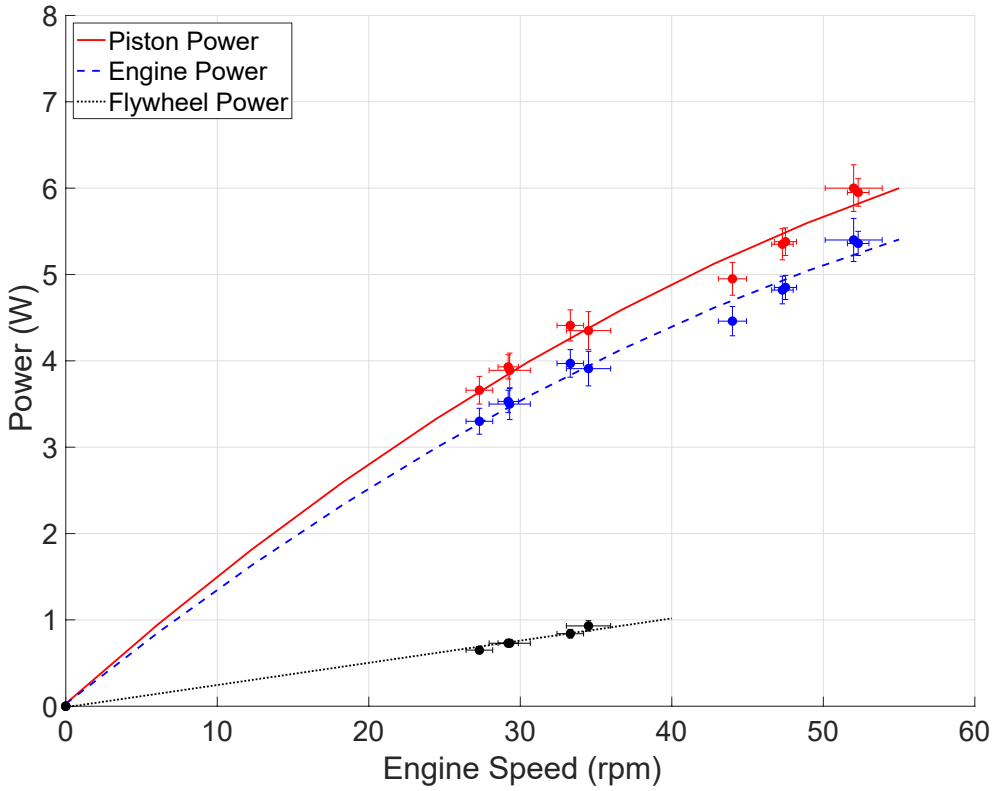

Figure 4-5 Mk.III condensing engine testing power versus engine speed.

Testing showed that piston power increased with engine speed, as expected, reaching a maximum value of 6.0W. Five friction brake power measurements were taken during testing at lower engine speeds, achieved by applying load to the flywheel, identifying mechanical losses up to approximately 80% of associated piston power. The friction was caused by mechanical losses in the crank shaft as well as friction between the piston and cylinder wall. The former was found to be caused by sub-optimal bearings which should be improved on the next iteration. The latter was caused by thermal expansion and the PTFE sealing mechanism being unable to adjust to the changing gap between piston and cylinder wall. Piston rings could be used to overcome this on

future models. It is also acknowledged that at extreme conditions, such as idling and light loads, mechanical friction can be significantly increased (Wong & Tung, 2016). Therefore, the test regime of the Mk.III engine, limited by the factors outlined above, likely worsened frictional losses.

Furthermore, it is expected following discussion with the EDMC that smaller prototype models suffer more significantly from friction and as the engine size increases the percentage loss to friction reduces. This is because cylinder volume increases as a function of the square of the diameter whereas the circumference increases linearly with the diameter. The former dictates power production and the latter dictates surface area contact between piston and cylinder wall and therefore friction. Scaling the uniflow condensing engine therefore becomes an important area of investigation for future work.

For this analysis, an 'adjusted engine power' value is presented in Figure 4-5, hereby known simply as 'engine power' in the remainder of this thesis. This has been used to calculate subsequent thermal and second law efficiencies. This assumes internal losses of 10%, a suitable assumption for an engine operating under typical conditions (Wong & Tung, 2016). The use of 10% mechanical losses represents the Mk.III condensing engine outputs with an optimised mechanical power take off and operation. This allows more realistic comparison to ORC systems in literature than just using piston power alone, which would be an overestimation. However, it must be noted that 10% mechanical losses need to be achieved practically on a future engine to demonstrate proof of this theory. Maximum engine power was measured as 5.4W using this method.

4.2.2.3 Thermal and Second Law Efficiencies

The resulting engine thermal and second law efficiencies are shown in Figure 4-6 and Figure 4-7, also plotted using second order polynomial relationships. This relationship was expected, caused by the non-linear relationship of the power output, of which the efficiency is a function. The cause of the non-linear relationship in the power output has been discussed above. The use of a second order polynomial was also supported by achieving the maximum R^2 value, around 0.8 for both thermal and second law efficiencies. It is noted that an artificial point was added when plotting the data in Matlab at an engine speed of 60rpm and an efficiency equal to the minimum recorded point in the data series. This was introduced to inhibit the polynomial trendline from unrealistically rising at the end of the data series. Additional data gathering over a wider engine speed range will negate the need for this in future work.

Thermal efficiency, shown in Figure 4-6, ranged between 2.1% - 2.5%. Whilst these values seem low, this is restricted by the small temperature difference between heat source and sink, just 30^{o}C on average. This is a characteristic of LGWH heat recovery but exacerbated in this case by the high

condenser pressures. The maximum thermal efficiency achieved represented 39% of the ideal isentropic efficiency shown in Figure 3-2 for the engine with an expansion ratio of *n* = 1. Use of steam expansion would also allow for increased thermal efficiencies. The error bars in Figure 4-6 seem significant but in fact represent an uncertainty of 3% - 7% and appear distorted by the narrow range of values used on the y-axis to properly demonstrate the non-linear relationship of the data points. The uncertainty analysis method and impact on results is discussed in greater detail in Section 4.2.3.4.

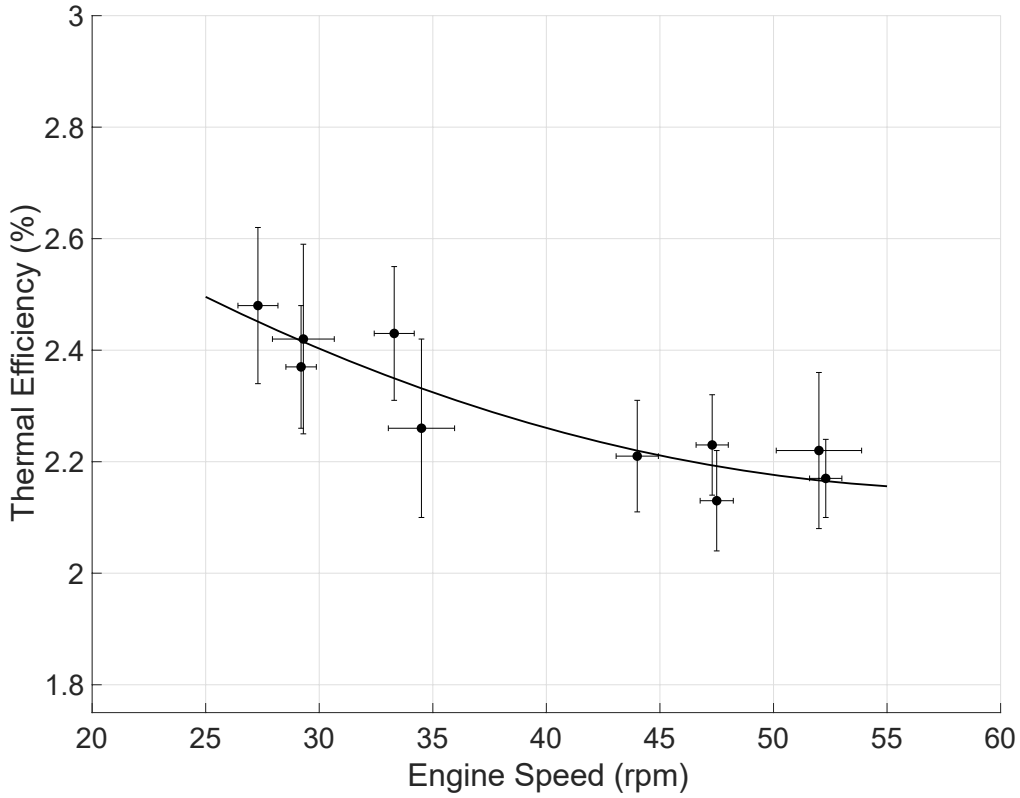

Figure 4-6 MK.III condensing engine thermal efficiency versus engine speed.

Second law efficiency, shown in Figure 4-7, is independent of heat source and sink temperatures and gives an understanding of effectiveness, which can be extrapolated to understand future performance. Second law efficiencies ranged from 26.6% - 43.1% for the Mk.III engine, demonstrating suitable performance.

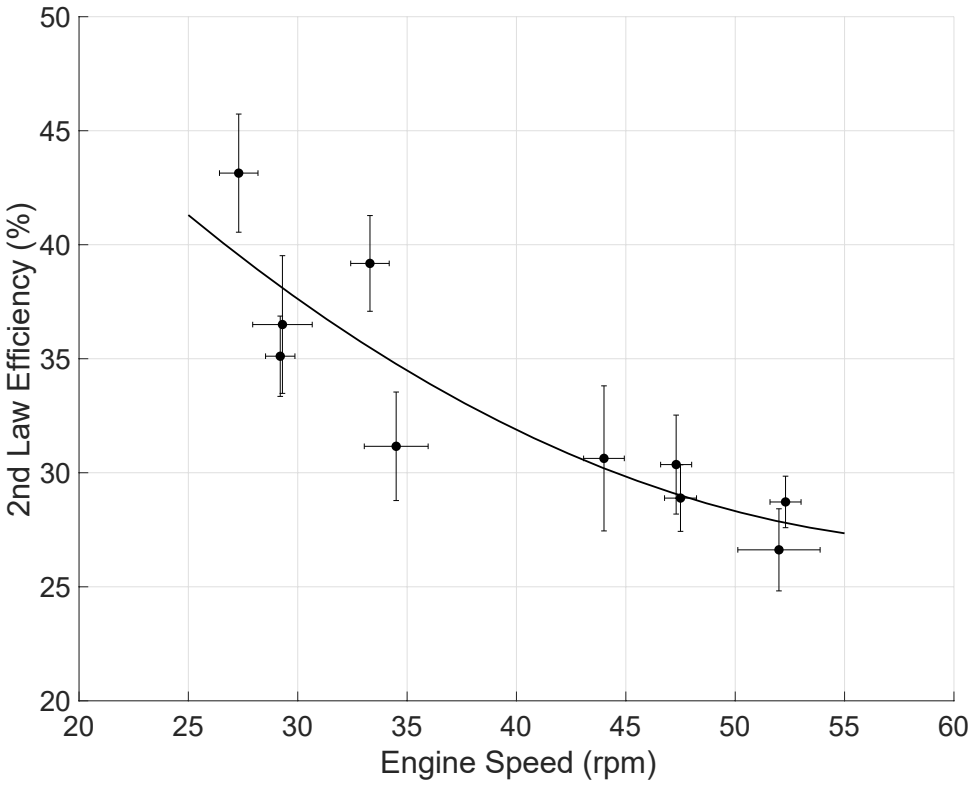

Figure 4-7 MK.III condensing engine second law efficiency versus engine speed.

It can also be seen in Figure 4-6 and Figure 4-7 that both thermal and second law efficiency decreased with increasing engine speed. This is a result of reduced time for cylinder pressure to reach that of the condenser and residual steam to be evacuated. This phenomenon has already been discussed in relation to the pressure profiles at 29rpm and 52rpm. This identifies an interesting operational consideration. Increased engine speed is desirable as it increases power output. However, if a scenario favoured recovery efficiency over power output, then engine speed should be minimised, based on these results. Whilst the speeds seen during this testing seem low, historic evidence suggests these types of engines operate with a maximum speed of just 120rpm - 150rpm (Bortolin, et al., 2021). This is limited by the ability to effectively evacuate steam from the condenser and create the necessary pressure driving force around the piston at higher speeds, as discussed already in the pressure results section.

4.2.3 Power and Efficiency Test Discussion

4.2.3.1 Comparison with Previous Condensing Engine Models

Table 4-3 shows efficiencies from condensing engines reported in literature as well as the average Mk.III data, all operating without expansion (n = 1). The Mk.III engine data shows a distinct improvement in efficiency compared to the Mk.II model, achieving increases of around 25% in both

maximum thermal and second law efficiency. This is despite the Mk.III engine analysis incorporating an estimate for the steam jacket thermal energy requirement in efficiency calculations. This accounted for thermal losses from the engine, not incorporated into the Mk.II analysis which used cylinder steam use only without any losses factor. The cylinder pressures recorded during testing indicated that entry and exit losses were significantly reduced, explaining the improvement in performance. Operational considerations, such as engine speed, have also been identified as factors. A reduced engine speed means that the maximum Mk.III engine power output was an 80% reduction compared to the maximum Mk.II power output, achieved at a speed of around 120rpm. Comparing similar engine speeds, around 30rpm - 50rpm, results in comparable power outputs between the two models, despite the Mk.II value being given as piston power and the Mk.III value being given as piston power minus 10% for assumed mechanical losses. These results confirm that the Mk.III engine made greater use of available energy compared to the Mk.II engine for similar heat source and sink temperatures.

Table 4-3 Comparison of current and historic condensing engine performance operating without expansion (n = 1).

	Davey's Engine (1885) (Josse, 1870) (Muller & Howell, 2021)	**Mk.II Engine** (Muller, et al., 2018)	**Mk.III Engine**
Mechanical Power (W)	740 - 800	5 - 27	3.3 – 5.4
Thermal Efficiency (%)	2.7 - 3.7	1.0 - 2.0	2.1 - 2.5
Second Law Efficiency (%)	18 - 25	17 - 34	27 - 43

The full-scale tests of Davey's engine reported in Revue Industrielle (Josse, 1870) achieved a higher maximum thermal efficiency of 3.7%. However, it should be noted that the engine tested in 1885 was much larger, with a cylinder diameter of 174mm, implying reduced friction losses relative to the overall power output. This suggests that larger iterations of the Mk.III engine will benefit from this and demonstrates another area for improvement. Future work could quantify this by incorporating friction into the already developed uniflow engine model and performing a sensitivity analysis. Davey's engine also operated within a wider temperature range allowing for increased thermal efficiency as per the *Carnot* theorem. It is also observed that the Mk.III condensing engine had an improved second law efficiency compared to Davey's engine despite achieving a lower thermal efficiency, again caused by the reduced temperature range the Mk.III engine operated

within due to high condenser pressures. This highlights the potential of the single acting uniflow engine if tested in a wider temperature range.

4.2.3.2 Comparison with Current ORC Systems

The literature review found the main competitor to the modernised condensing engine for LGWH recovery to be the ORC. The thermal efficiencies demonstrated by the Mk.III engine are comparable to those observed in Chapter 2 for ORC systems with similar power scales, further demonstrating the potential of the uniflow condensing engine. However, when comparing the Mk.III condensing engine to current low temperature, small scale ORC systems, it was found that the heat source and sink temperatures used were not consistent. The second law efficiency normalises the effect of different operating temperature ranges and should therefore be used to compare the test results for different technologies. This comparison is shown in Table 4-4.

Second law efficiency highlights that the percentage of the available energy being converted in the Mk.III condensing engine was comparative to that achieved by ORC systems operating in the same temperature range, despite not employing steam expansion. However, it is noted that the Mk.III engine second law efficiency value assumes no losses between boiler and cylinder, through the definition of heat source temperature, as well as only 10% mechanical losses in power take-off, applied to the piston power. These must be achieved in practice for the Mk.III second law efficiency values shown in Table 4-4 to be achieved when directly comparing against ORC literature. Nonetheless, this analysis demonstrates the potential of the uniflow condensing engine technology and justifies further research. It also identifies valving and friction as important areas for optimisation.

Table 4-4 Comparison of second law efficiency values for the Mk.III CE and comparative ORC systems for LGWH recovery at small power ratings.

	ORC (Landelle, et al., 2017) (Muller & Howell, 2021)	Mk.III Engine
Second Law Efficiency (%)	20 – 40	27 – 43

Further comparison of the current state of the condensing engine and small-scale ORC systems in literature is given in Figure 4-8. This is the second law efficiency plot of various ORC systems first produced by Landelle, et al. (2017), discussed in Section 2.2.4 of this thesis. The original figure has been modified by the author of this research by adding shading to the power range relevant to the condensing engine, both the expected commercial range and the range tested in the lab, as well as adding data points for the Davey's engine, Mk.II engine, and Mk.III engine second law efficiencies

for an expansion ratio of *n* = 1. The power and efficiency values are given in Table 4-3 for these cases.

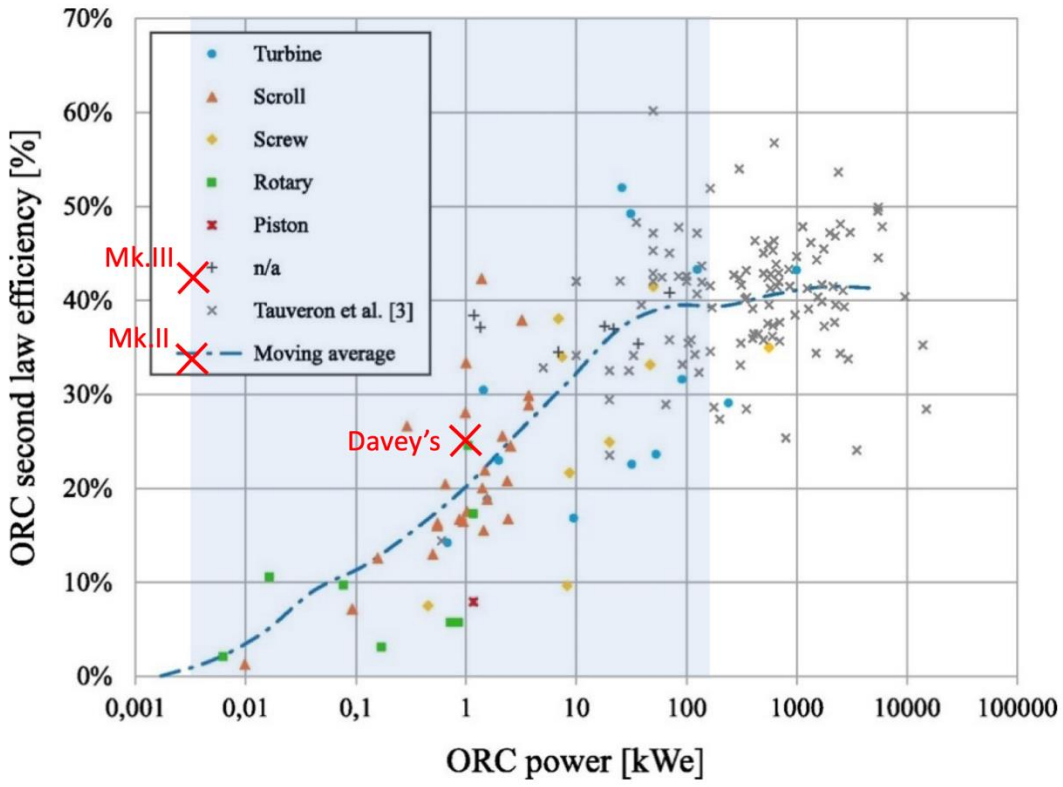

Figure 4-8 Original ORC second law efficiency plot by Landelle, et al. (2017) modified to show results from recent condensing engine literature (red crosses) as well as current and future condensing engine target power range (blue shading) in comparison to current ORC systems. Reproduced from (Landelle, et al., 2017) with permission from Elsevier.

Figure 4-8 shows that Davey's engine was already an effective heat engine, despite being a historic example of the technology, when compared against current ORC systems. This discovery was also highlighted in recent literature (Muller & Howell, 2021). The Mk.II and Mk.III condensing engines have each demonstrated improvement in second law efficiency when operating with an expansion ratio of *n* = 1. According to Figure 4-8, they achieve second law efficiencies comparative to that of ORC systems of increased power scale.

However, it is again reiterated that the values shown for the Mk.II and Mk.III engines in Figure 4-8 are indicative results showing the potential of the technology given the definition of heat source temperature in the second law efficiency calculation, the use of piston power by the Mk.II engine reporting, and use of an artificial mechanical power for the Mk.III engine by assuming 10% mechanical losses from the piston power. As Figure 4-8 gives the electrical efficiency for the

investigated ORC systems, direct comparison of the condensing engine will result in the plotted condensing engine data points to move down the y-axis.

Nonetheless, Figure 4-8 shows that there is scope for a decrease in condensing engine efficiency when future work optimises the system to allow realistic values to still be comparable with the ORC system. This justifies continued development of the technology. Realistic efficiency values would only exhibit a reduction in those shown in Figure 4-8 if mechanical losses on the optimised system were greater than 10% of piston power and/or if losses between boiler and cylinder could not be eliminated.

4.2.3.3 Predicting Uniflow Condensing Engine Development Potential

Development of the Mk.III engine has identified that improved inlet and outlet valves as well as a larger evacuation port area are required to improve cylinder pressures. Additionally, an improved condenser and larger relative pump size is required to improve condenser pressure. Friction must also be reduced by improving the power take off. Additional areas for investigation also include use of thermally insulating materials to remove the need for the steam jacket as well as using multiple cylinders to improve power stability. Steam expansion is also required to realise the condensing engine's full potential.

A theoretical analysis can be performed to understand the effect of these changes. Assuming an improved condensing engine could operate with actual heat source and sink temperatures of 100^{o}C and 20^{o}C respectively, it would have a *Carnot* efficiency of 21.4%. Assuming also that this improved condensing engine could achieve the same second law efficiency as the MK.III condensing engine, the thermal efficiency achieved would be in the region of 5.8% - 9.2%. To achieve this steam expansion would need to be employed, as the isentropic efficiency for the condensing engine without expansion (n = 1) is limited to around 6% as shown in Figure 3-2.

Another theoretical analysis can be performed using the isentropic efficiency, defined in Equation (4.6). The maximum theoretical thermal efficiency for a condensing engine operating between a heat source of 100^{o}C and heat sink of 20^{o}C and with an expansion ratio of n = 1 is 6.4%, determined in Chapter 3. Therefore, the Mk.III engine achieved an isentropic efficiency of 33% - 39%. The maximum condensing engine thermal efficiency when utilising steam expansion was predicted in Chapter 3 as around 19%. Therefore, if the Mk.III operated as effectively under those conditions, allowing the achieved isentropic efficiency to be applied to the maximum theoretical efficiency, a maximum practical thermal efficiency can be estimated as around 6.3% - 7.4% for the Mk.III engine. Higher expansion ratios are difficult to achieve in practice, and at a more realistic

expansion ratio of n = 4 the ideal thermal efficiency was around 14% giving predicted Mk.III thermal efficiencies of 4.6% - 5.5%.

These two pieces of theoretical analysis use different methods but support predicted Mk.III thermal efficiency ranges of 5.5% - 9.2% when operating between a wider temperature range and at higher expansion ratios. These values are in line with current ORC technologies operating within this temperature range, discussed in Chapter 2. This justifies additional research.

4.2.3.4 Uncertainty Analysis and Recommendations for Future Experiment Improvement

The experimental uncertainty analysis used in this thesis followed a method given by the National Physical Laboratory (Bell, 2001). It accounted for the pertinent uncertainties in the reported values through an uncertainty budget and combined them using the summation of quadrature method. A coverage factor of k = 2 was also applied to give a 95% confidence interval, plotted as error bars in Figure 4-5, Figure 4-6, and Figure 4-7. The full method of calculation is detailed in Chapter 9 and the raw data can be found in the associated file stored in this project's data repository.

The power and efficiency values presented in Figure 4-5, Figure 4-6, and Figure 4-7 were not directly measured and required multiple calculation steps to be determined. Each measured value included in the function of the final plotted value was accounted for and compounded appropriately. It is noted that pressure data was used most frequently, relevant to the work done on the piston and used to determine associated saturation temperatures and steam characteristics such as density and enthalpy. The uncertainty associated with the pressure transducers was limited by the stated accuracy of +/- 0.25%, the calibration performed by the manufacturer prior to supply (RS Pro, 2023), and the accuracy check performed as part of this work as detailed in Chapter 9. However, future testing should endeavour to limit the number of calculation steps required in obtaining the final reported values. This can be achieved by optimising the power take off and using a direct useful output power measurement device. Furthermore, measuring the mass of consumed steam directly will reduce the required calculation steps associated with thermal energy input and increase the accuracy of efficiency analysis. It is noted that the steam jacket steam use was a theoretical estimation in this work and not included in the uncertainty analysis in this case, as discussed in Chapter 9.

The error bars shown in Figure 4-5 represented an uncertainty of 3% - 5% in the engine power. The error shown bars in Figure 4-6 represented an uncertainty of 3% - 7% in the thermal efficiency. The error bars shown in Figure 4-7 represented an uncertainty of 4% - 10% in the second law efficiency. The uncertainty increases with each plot as they compound with each calculation step. The uncertainty data quoted above is reported as a range to reflect the individual uncertainty values

calculated for each data point, as discussed in Chapter 9. The uncertainty estimated for this testing is considered by the author of this research to be sufficiently small, given the prototype nature of this work, to give confidence in the discussion of the results already made in Section 4.2.3.

4.2.4 Power and Efficiency Test Conclusions

During this piece of work the Mk.III condensing engine was tested for power and efficiency at a range of engine speeds, from 27rpm - 52rpm. It operated with average heat source and sink temperatures of 98°C and 72°C respectively. It also operated without steam expansion (n = 1) due to limitations in testing. In summary, the single acting uniflow configuration was a success. Analysis and discussion of results allowed for the following conclusions to be drawn:

- The single acting uniflow configuration was successful in achieving rapid initial evacuation of steam from the cylinder, resulting in increased pressure driving force for power production. This testing justified further research into the technology.
- The Mk.III condensing engine achieved a maximum power output of 5.4W, assuming 10% friction losses from the calculated piston power, comparable with the Mk.II engine at similar engine speeds.
- The Mk.III engine achieved a maximum thermal efficiency of 2.5%, representing an increase of 25% over the previous Mk.II model when also operating without steam expansion.
- The Mk.III engine achieved a maximum second law efficiency of 43%, assuming no losses between boiler and cylinder, comparable with current ORC technologies in literature and an increase of around 25% over the Mk.II model.
- Analysis allows future thermal efficiencies as high as 9% to be predicted for an engine with increased operating temperature range (100°C heat source and 20°C heat sink) and steam expansion.
- Higher efficiencies were observed at slower engine speeds, identifying an interesting characteristic for future operation of the engine.
- Improvements in valve selection, maximisation of evacuation port area, improved condenser and pump system, and reduced mechanical friction were identified as areas for future improvement.
- Direct measurement of engine power and steam use should be used on future tests to limit calculation steps required and therefore limit uncertainty associated with the results.

4.3 Mk.III Friction Tests

The MK.III engine was a demonstration model not yet optimised. Additionally, friction is relatively large in comparison to power output at small scales such as this. Friction was therefore to be expected and testing was performed to better understand the source and scale of mechanical losses, already shown to be significant during engine power testing. This sub-section gives the methodology and results for friction testing performed on the Mk.III engine. This was measured prior to engine power tests being conducted.

4.3.1 Friction Test Method

Two types of friction were measured. Firstly, the mechanical friction of the power take off was tested. Secondly, the friction associated with the piston sealing mechanism against the cylinder wall was measured. These were summed and compared against the friction measured during engine operation. The methods of analysis are given below.

4.3.1.1 Power Take Off Friction Test Method

Energy was put into the engine by hand and the engine was then allowed to come to a stop, with all energy loss assumed to be a result of friction. The test was performed without the piston PTFE packing in order to remove piston-based friction and give a reliable result. The speed of the engine was measured by the engine control system and outputted once per revolution along with a timestamp. According to the gear ratio used on the MK.III engine the flywheel speed was three times that of the engine. The flywheel speed was used to calculate the stored kinetic energy at each time step using Equation (4.7); (Gidzewicz, 2016).

$$KE_{fly} = \frac{1}{2} \times I_{fly} \times {\omega_{fly}}^2 \tag{4.7}$$

Where:

- KE_{fly} is the kinetic energy stored in the flywheel (J).
- I_{fly} is the moment of inertia of the flywheel, defined by Equation (4.8), (kg/m^2).
- ω_{fly} is the angular speed of the flywheel, defined by Equation (4.9), (rad/s).

$$I_{fly} = \frac{1}{2} \times m_{fly} \times {r_{fly}}^2 \tag{4.8}$$

$$\omega_{fly} = N_{fly} \times \frac{2\pi}{60} \tag{4.9}$$

Where:

- m_{fly} is the mass of the flywheel (kg).
- r_{fly} is the radius of the flywheel (m).
- N_{fly} is the flywheel speed (rpm).

Kinetic energy was plotted versus timestamp. The rate of power loss was found to be dependent on engine speed. Therefore, the energy loss gradient was taken at the relevant engine speed to give rate of power loss. The gradient of the line is the energy lost (J) per unit time (s) and therefore gives the average power loss (W) due to friction during this time. The author of this research deemed this experiment to be of a repeatable nature, due to it not depending on any human input other than putting initial energy into the engine, and therefore five repeat tests were deemed sufficient. This is supported by the small spread in the data represented in the uncertainty value given in Table 4-5.

Whilst the author believes this method to be an appropriate measure of friction at this early stage of the engine's development, it is acknowledged that this method has limitations. Specifically, the test was performed without sealing rings fitted on the piston meaning that the piston rested against the cylinder wall during operation introducing additional friction. However, it would be difficult to achieve zero contact between piston and cylinder wall during this experiment. Additionally, this test included losses associated with the piston displacing the air around it, not present during condensing engine tests. This was mitigated by maintaining the cylinder open to atmosphere and therefore achieving a zero-pressure difference across the piston. During engine testing, a positive pressure difference around the piston will be experienced. Future engine friction analysis could be performed during engine operation if improved mechanical power take-off is achieved, which should be the preferred method to remove the uncertainty associated with the above method.

4.3.1.2 Piston Sealing Friction Test Method

This was performed using the updated Mk.III piston design, as discussed in Section 4.5. The PTFE packing was applied to the piston. One end of some string was tied to the gudgeon pin where the piston would connect to the piston rod in normal operation. The other end was tied to a hanging force gauge. The piston was inserted into the cylinder and the force gauge, held above the cylinder top opening, used to hang the piston. This is shown in Figure 4-9.

The force exerted by the hanging piston was measured by the gauge and manually recorded. This was corroborated by also weighing the piston. The piston was then pulled slowly through the cylinder by lifting the gauge. The force required to induce movement of the piston was measured

from the gauge and manually recorded. It was assumed that the difference between the force exerted by the hanging weight and the force required to pull the piston indicated the friction present between piston and cylinder wall. The measured average friction force was multiplied by the distance travelled during one revolution of the engine to give the work lost due to piston friction, in Joules. This was then divided by the average time of a revolution to calculate the lost power due to this friction. An engine speed of 30rpm was assumed for this analysis in correspondence with the engine speeds experienced when using the friction brake during Mk.III testing, 27rpm - 35rpm, against which the results of this analysis were compared.

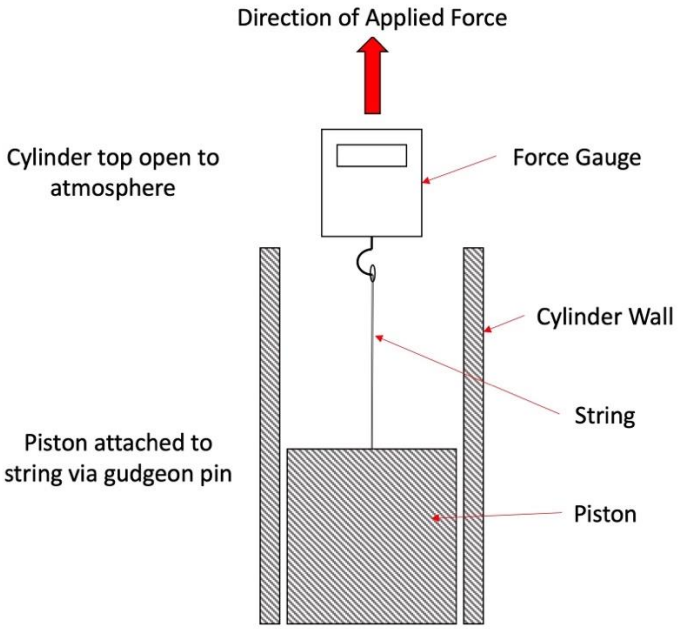

Figure 4-9 Simplified diagram of the experimental method employed to test frictional losses between the piston and cylinder wall. Piston sealing mechanism not directly shown but present during testing and in contact with the cylinder wall.

The author of this research deemed this test methodology to be less repeatable than the kinetic energy method described previously. This was because it involved a human element in the form of the force applied during the lifting of the force gauge. As a result, the author performed ten repeats of this test to ensure confidence in the reported result. Additional tests reduce the uncertainty associated with the overall average value by increasing the denominator of the equation for standard error, which is the square root of the number of tests performed. A detailed insight into the thesis' uncertainty analysis methodology can be found in Chapter 9. This decision is supported by the small spread in the data, demonstrated through the small uncertainty value given in Table 4-5.

4.3.2 Friction Test Results and Analysis

An example flywheel kinetic energy versus timestamp plot generated during the power take off friction tests is shown in Figure 4-10. At low flywheel speeds a linear trend has been used to give the gradient of the energy curve. This is at a flywheel speed of approximately 100rpm. Engine speed is one third of this, due to gearing ratios, giving an engine speed representative of Mk.III tests. The gradient in the example shown suggests that 1.23W of power is lost from the engine at this engine speed due to friction in the power take-off.

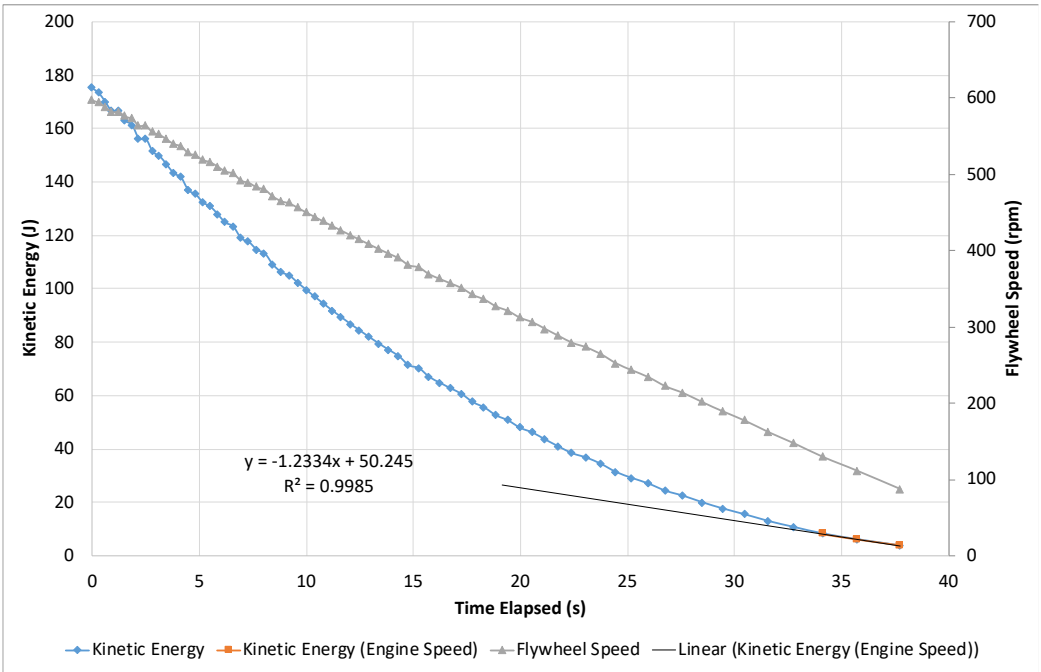

Figure 4-10 Example power take off friction analysis plot. Kinetic energy stored in the flywheel is plotted against time elapsed. The loss of energy per unit time allows calculation of power loss.

The average predicted total power loss due to friction found using the two analysis methods described above is given in Table 4-5. It can be understood from these results that over 70% of the predicted engine friction found during these tests is attributed to friction in the power take-off. This supports observations made during engine testing that the bearings and crank disk assembly were not stable enough for optimum operation of the engine, ultimately limiting the ability to thoroughly test the engine.

The uncertainty values given in Table 4-5 represent the standard error calculated as the standard deviation in the data points divided by the square root of the number of data points (Bell, 2001). This gives the uncertainty associated with the spread of the data, and a coverage factor of $k = 2$ was applied to give a confidence interval of 95% or two standard deviations. The greater number of tests performed for the piston friction test allowed a reduced uncertainty value associated with

spread despite the human dependency of the test. It is noted that this is a simplification of a full uncertainty analysis, deemed suitable by the author of this research given the inherent uncertainty associated with the test methodology which should be improved upon in future work. The accuracy of the instruments used can be found in Chapter 9, related to the Mk.III engine tests full uncertainty analysis, with the exception of the force gauge which had an accuracy of +/- 100g or 0.98N (KERN, nd).

Table 4-5 Friction analysis prediction for an average engine speed of 30rpm using test data. Standard error calculated with a 95% confidence interval.

	Average Power Loss (W)
Power take-off (flywheel) friction	1.39 ± 0.088
Piston friction	0.58 ± 0.031
Combined friction	**1.97** ± 0.093

4.3.3 Friction Test Discussion

The friction predicted for an engine speed of 30rpm is shown in Table 4-5. This speed was chosen for analysis as it closely matches the speed of the Mk.III engine during friction brake tests, 27rpm - 35rpm, against which the friction results were compared. The predicted friction accounts for, on average, 60% of the friction measured during Mk.III engine testing. The measured friction was calculated as the difference between theoretical piston power and measured friction brake power. This was found to account for approximately 80% power loss during Mk.III engine power tests. Whilst 60% seems a low percentage, the crudeness of the methods employed during data acquisition on this prototype engine mean a percentage difference is to be expected. Also, the friction tests were performed with the engine at ambient temperature. During actual engine tests thermal expansion likely increases friction experienced by the piston and this could account for some of the missing 40%. Whilst not included in the scope of this work, this could be investigated using the thermal expansion equation given in Equation (4.12) by calculating the increase in diameter of the piston at different temperatures and estimating the additional force exerted against the cylinder wall. This further highlights the need for piston rings on the next iteration of engine. Furthermore, the friction brake tests applied load to the flywheel likely unbalancing the power take-off even further and introducing further friction. This highlights the need for alternative power measurement on the next iteration of engine, such as a connected motor for electricity production. This would be an interesting next phase in the engine development, perhaps to power a small electrical device as a showcase.

The key takeaway from this analysis is that the estimated and measured MK.III engine friction values are in the same order of magnitude and reasonable phenomenon exist to explain the difference in values. Identification of significant sources of friction from two separate sets of testing confirm that future work is needed to minimise mechanical losses. Importantly, the corroboration of the measured friction with the estimated value also supports the piston and friction brake power values from which the former was calculated. This therefore provides support for the theoretical piston power values used to justify that the Mk.III engine had made improvements over the previous model.

4.3.4 Friction Test Conclusions

Prior to Mk.III engine power tests the system friction was measured to understand expected mechanical losses. This consisted of friction from the power take off as well as the piston inside the cylinder. The following conclusions were drawn from this testing:

- Combined mechanical losses were measured as 1.97W.
- Over 70% of measured mechanical losses were attributed to the power take-off, supporting previous statements that the bearings in the Mk.III engine limited performance.
- The measured mechanical losses account for around 60% of the friction measured during Mk.III testing, with the missing percentage being attributed to the effect of thermal expansion as well as increased load during actual testing.
- Significant mechanical losses measured both during this work and the Mk.III tests support the need for improved mechanical design as well as corroborating the theoretical piston power analysis used to assess Mk.III engine performance.

4.4 Mk.III Engine Steam Evacuation Theoretical Model

The next phase of work for the single acting uniflow engine advancement as part of this research was development of a model to predict cylinder pressure during steam evacuation. A more detailed analysis of steam evacuation in the uniflow engine was considered important to (a) assess whether choking occurs which would delay evacuation, and (b) to develop a methodology for predicting steam evacuation to aid future dimensioning of uniflow exit ports on the condensing engine.

4.4.1 Evacuation Model Method

The evacuation model was built in Matlab utilising the XSteam data tables available from MathWorks (Holmgren, 2007). The model first calculates slot open time using the engine's radial speed and the radial distance travelled by a point on the crank disk whilst the slot is open, see Equation (4.10). This is dependent on engine speed and slot dimensions.

$$t_{slot} = \theta \div \left[\frac{N \times 2\pi}{60}\right] \tag{4.10}$$

Where:

- t_{slot} is the slot open time (s).
- θ is the angular distance travelled during slot open time (rad).
- N is the engine speed (rpm)

Bernoulli's equation, see Equation (4.11), is used to iteratively calculate steam evacuation velocity during the slot open time. The overall minor head loss coefficient K is the summation of each individual resistance to flow in the pipe, values for which can be found in literature, eg. (Cengel & Cimbala, 2010).

$$v_i = \sqrt{\frac{2(P_{cyl} - P_{con})}{(1 + K)\rho_i}} \tag{4.11}$$

Where:

- v_i is steam evacuation velocity for the given iteration (m/s).
- P_{cyl} is cylinder pressure during the iteration (Pa).
- P_{con} is condenser pressure during the iteration (Pa).
- K is the total minor head loss coefficient.
- ρ_i is average steam density during the iteration (kg/m^3).

Once confirmed as not being choked, the velocity is used to calculate the steam mass evacuated during the iteration using port area, steam density, and time step. This allows a residual steam mass inside the cylinder to be found which is converted to a cylinder steam density by dividing by cylinder volume. In combination with steam enthalpy, evacuation being assumed as an isenthalpic process, this allows the new cylinder pressure to be called from the XSteam data tables (Holmgren, 2007). This process is repeated, and pressure values plotted to create a predicted cylinder pressure profile during steam evacuation.

During modelling, a pressure profile was predicted for a series of arbitrary minor head loss coefficient values and calibrated against real test data. The real cylinder pressure data was extracted from the pressure profile data analysed during the equilibrium period of operation for each test, see Section 4.2.1. For each test an average timestamp and cylinder pressure was calculated to give an average pressure profile during evacuation. The pressure data was only analysed for the period during evacuation from the uniflow port, defined as the point from initial reduction in cylinder pressure to the point of minimum cylinder pressure. Analysis of the real test data for tests 1 - 5 found average cylinder pressure before and after evacuation of 0.95bar and 0.37bar respectively, and an average engine speed of 49rpm. These values were used as inputs in the evacuation model for this analysis.

4.4.2 Evacuation Model Results and Analysis

Figure 4-11 presents the predicted output of the evacuation model alongside measured pressure data from Mk.III engine tests. Tests 1-5 are shown due to having faster engine speeds closer to that expected to be used on future engines. The model was tested with increasing minor head loss coefficients (K). It is observed that a match is obtained between the model prediction and the real engine pressure profiles when a minor head loss coefficient (K) of 250 is used. This is more clearly shown in Figure 4-12, which plots the pressure profile predicted by the model for a minor head loss coefficient (K) of 250 against the overall average pressure profile observed during testing. The model prediction overpredicts cylinder pressure in the initial phase of evacuation, matches closely in the middle phase of the profile, and underpredicts pressure in the final phase of evacuation. Analysis shows an accuracy of the model within 6% of the average test data at any given timestamp. This is suitable for future modelling of steam evacuation from the single acting uniflow engine and can be used to guide cylinder design.

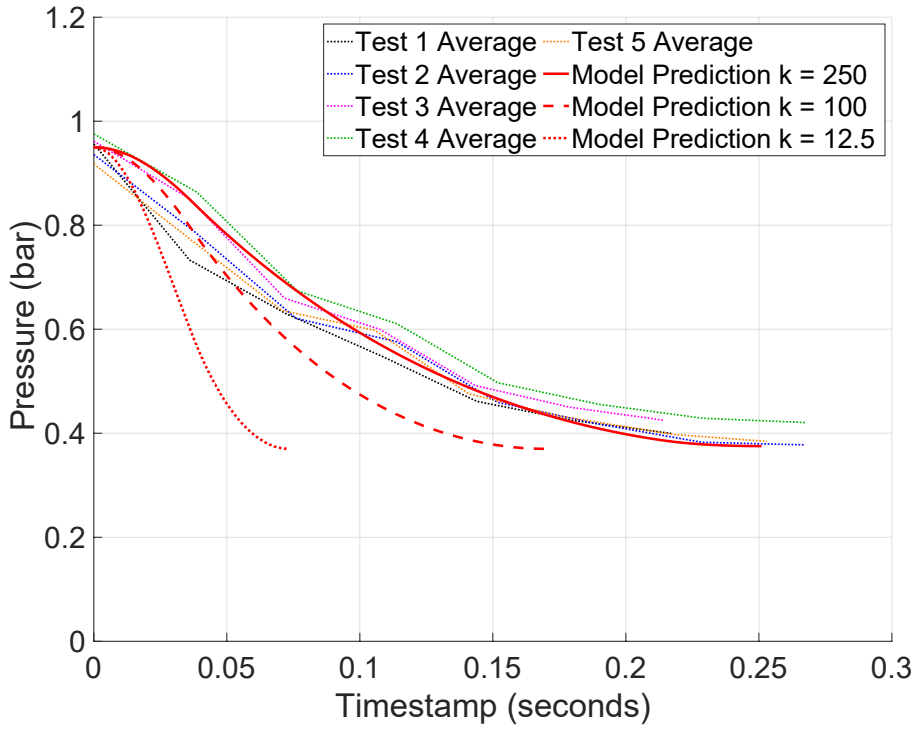

Figure 4-11 Uniflow evacuation model predicted pressure profile versus real engine data for tests 1 to 5.

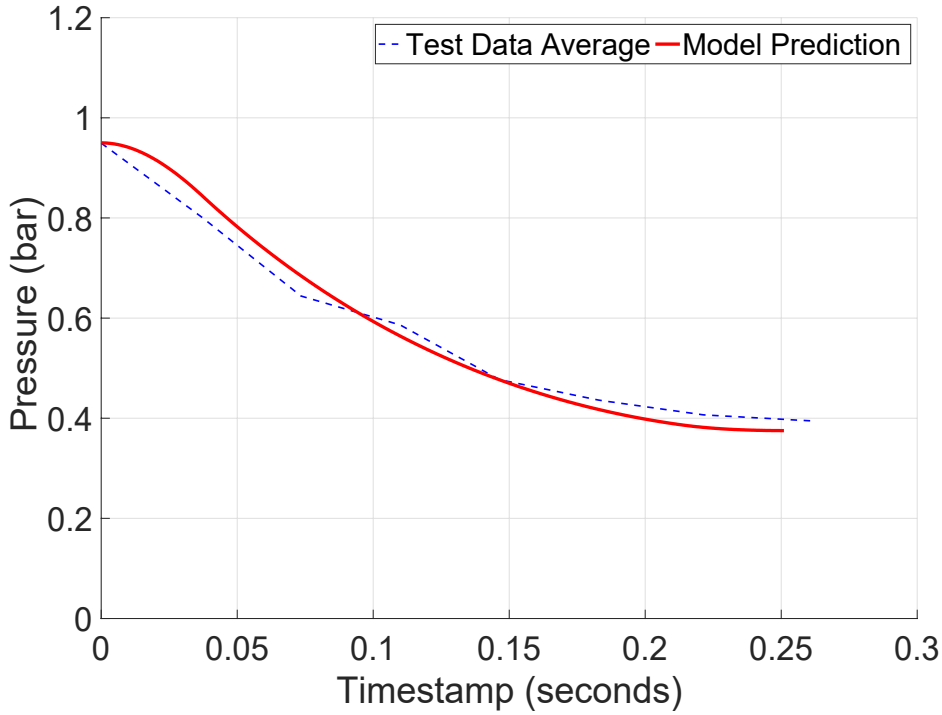

Figure 4-12 Uniflow evacuation model predicted pressure profile versus overall average real pressure profile for tests 1 to 5.

4.4.3 Evacuation Model Discussion

There is no literature which has also predicted the minor head loss coefficient of the uniflow port for the condensing engine. However, the minor head loss coefficient required to give a good match between prediction and real data can be compared against other values in literature to give context to its magnitude. Typical values already presented in this thesis include that for entry and exit of a cylinder, around 0.5 and 1.0 respectively (Cengel & Cimbala, 2010). The evacuation port could be considered as a combination of these elements. Therefore, the obtained value of 250 is significantly greater. As a result, it is suggested that the minor head loss coefficient is acting to correct some inaccuracy in the theory of the model, and therefore should be treated more as a 'correction factor' than a true minor head loss coefficient value in this case. Nonetheless, the model with use of this factor has shown suitable accuracy against real data for future use in design of the uniflow condensing engine.

4.4.4 Evacuation Model Conclusions

A theoretical model was developed to allow prediction of the steam evacuation pressure profile from the uniflow condensing engine. This was compared against real data from Mk.III engine tests to validate the results. Key conclusions drawn from this work were:

- The developed model shows accurate prediction of the steam evacuation profile, validated against real data.
- A minor head loss coefficient value of 250 was used to obtain the accurate match between model and real data.
- Comparison to typical minor head loss coefficients finds this value to be relatively large, suggesting it is acting as a 'correction factor' for the model.
- The model can be used to aid future design of the uniflow condensing engine.

4.5 Review of Mk.III Engine Design Effectiveness

The final phase of Mk.III engine development was to review the effectiveness of the Mk.III engine design given the context of the results presented above. It is useful to present this sub-section last in the Mk.III engine chapter as it allows all previously discussed data and analysis to be included in the review of the detailed design. This is used to make further recommendations for future design improvements and ensure lessons are learned from the prototype Mk.III engine.

4.5.1 Cylinder

4.5.1.1 Evacuation Slot

A traditional uniflow engine would feature a series of ports, or slots, around the entire circumference of the cylinder, feeding into a single manifold. However, after consultation with Hanley Design, it was chosen to use a single slot on the MK.III engine to reduce manufacturing costs, simplify the design of the exhaust manifold, and assess concept suitability in stages. With the engine in the prototype stage, an arbitrary slot dimension was chosen during design meetings with Hanley Design. The horizontal slot had a height of 5.0mm and a rectangular width of 6.0mm with radial ends; see Figure 4-13.

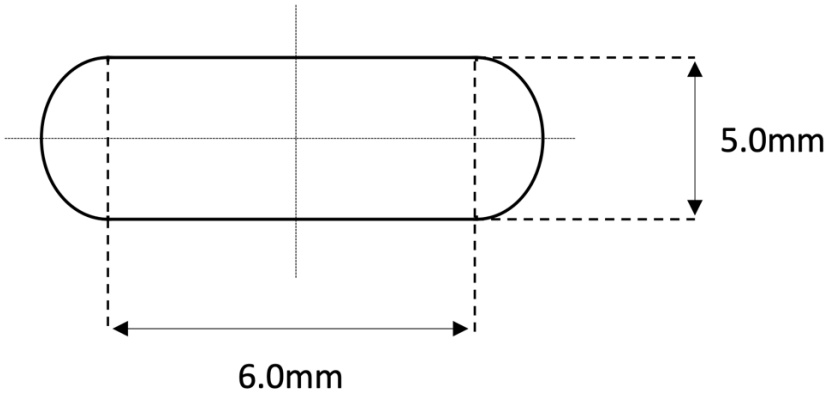

Figure 4-13 Diagram of Mk.III condensing engine cylinder uniflow evacuation slot geometry.

The mathematical model developed for understanding steam evacuation was used to confirm the suitability of these dimensions during initial design. However, as this model was yet to be calibrated a theoretical minor head loss coefficient value was used for the slot only, taken as K_i = 0.5 from (Cengel & Cimbala, 2010). This predicted that the slot would be suitable to allow for full evacuation of the cylinder up to a speed of 60rpm with a condenser temperature of 20°C. However, testing has now shown a significantly higher total minor head loss coefficient value of K = 250 between the steam inlet and condenser inlet pressure transducers. This supports the need for an increased number of evacuation ports on future designs.

This is supported by the cylinder pressure profiles observed during testing, with the outlet valves restricting flow and causing compression of the residual steam. The initial concept was for the uniflow port to support the outlet valve in steam evacuation. However, it is apparent that the port worked more successfully than the outlet valve, and therefore the valve should support the port in evacuation and serve the purpose of maintaining connection between cylinder and condenser. It was also hypothesised during testing that only having one slot creates an uneven suction force on the piston potentially causing friction against the cylinder wall and contributing to jamming effects.

This is an important observation for design of this type of engine and future work should use multiple slots equally spaced around the cylinder circumference to balance this force on the piston and maximise steam evacuation.

It is noted that during assembly and testing a chamfer was added to the inside of the port to prevent friction between the slot edges and the sealing mechanism/piston as it passed over the slot. This should be included in future engine designs. To allow a piped connection to the cylinder outlet a 3D printed manifold was manufactured and bonded with adhesive to the cylinder wall, sealed with silicone to prevent air ingress. This worked successfully and could be used on future engines of this type. Figure 4-14 shows photographs of the cylinder taken during assembly of the engine, showing both the slot and the 3D printed exhaust manifold.

Figure 4-14 LEFT: Mk.III engine cylinder with slot shown. RIGHT: Mk.III engine cylinder with 3D printed exhaust manifold.

4.5.1.2 Thermal Expansion

Thermal expansion was considered during engine design, using the relationship for the change in length due to thermal expansion, see Equation (4.12), which can equally be applied to a radius.

$$\Delta L = \alpha_{te} \times L_0 \times \Delta T \tag{4.12}$$

Where:

- α_{te} is the linear thermal expansion coefficient (m/m.K)
- ΔL is the change in length of material (m)
- L_0 is the original length of the material (m)
- ΔT is the change in temperature from ambient (K)

The cylinder and piston were both manufactured from brass and therefore expand at an equal rate according to their linear thermal expansion coefficient value of 18×10^{-6} m/m.K (MatWeb, 2020). Calculation in Chapter 9 showed that if the cylinder and piston were maintained at equal temperatures, thermal expansion would not cause jamming. Further evaluation was performed during design, also included in Chapter 9, that showed cylinder temperature would need to be approximately 30°C cooler than the piston for jamming to occur due to differences in thermal expansion. This risk was not believed to be significant during initial design.

However, during testing the difference in temperature between piston and cylinder resulted in un-equal thermal expansion and jamming of the piston in the cylinder bore. This was caused by excessive cooling of the cylinder by the surrounding air and was mitigated by use of a steam jacket around the cylinder to maintain cylinder temperature. It was also exacerbated by the small tolerances between piston and cylinder wall, which was mitigated by an updated piston design, see Section 4.5.2. It is acknowledged that historical hobbyist work had previously identified the potential for thermal expansion problems when using the uniflow engine cylinder design (Kimmel, 2012). However, this work operated at 30bar - 40bar and therefore the temperature differences were significantly increased compared to the atmospheric Mk.III engine. Therefore, because of the above theoretical work the atmospheric engine was believed by the author of this research to have reduced risk of encountering thermal expansion issues.

Future work should, as a minimum, include a steam jacket to prevent jamming to due to thermal expansion. It could also investigate more conventional piston ring designs to prevent the piston coming into contact with the cylinder wall. Future work could also investigate use of thermally insulating cylinder and piston materials, to minimise cooling losses and remove the need for the steam jacket. PTFE is a potential material choice, and whilst acknowledged that this has a higher thermal expansion coefficient in comparison to brass, 151×10^{-6}m/m.K (Hechtel, 2014), material

temperatures should be lower due to its thermally insulating properties. Nevertheless, thermal expansion should still be considered in this case.

4.5.2 Piston

The piston was originally designed to be a solid piece of brass to add mass, resulting in an initial piston weight of 1.6kg. Whilst understood to be atypical for an engine design, this was chosen due to the nature of the power cycles experienced by the uniflow engine. The single acting uniflow engine loses power in the downstroke and gains it in the upstroke. The proposal to increase piston weight aimed to introduce potential energy at the top of the piston stroke, generating more work in the downstroke. The additional weight would then remove work from the upstroke as the additional weight needed to be lifted again. Therefore, the expectation was a transfer of work from the upstroke to the downstroke resulting in a more balanced power output.

It was found during testing that this design negatively affected engine performance, resulting in maximum engine speeds that were too slow to sustain engine rotation. Therefore, through consultation with University of Southampton Engineering and Design Manufacturing Centre (EDMC) a new piston was developed. This piston was hollow, allowing a reduction in weight to 0.9kg, and was made up of a main body piece and a threaded cap to seal the piston internal cavity. The reduction in weight allowed for increased engine speeds to be achieved and improved the design.

During piston re-design, the sealing mechanism was also re-evaluated. The original design aimed to maximise piston diameter to create a thin condensate film between cylinder wall and piston. This was expected to seal air from entering the cylinder. This is the same principle that was successfully used on the Mk.II engine. However, the small tolerance between piston and cylinder wall contributed to thermal expansion jamming on the single acting uniflow condensing engine.

To allow for a new sealing mechanism the updated piston had a bottom piece which when fitted created a groove in the piston to allow testing of a variety of sealing types. A brass sealing collar was manufactured with the updated piston as the primary option. This had a diameter marginally wider than the piston body to allow a better seal to be made using the original condensate film principle. Off the shelf piston rings were also tested. Both options created too much friction. Engine grease was tested, and whilst successful for short engine runs was lost too quickly out of the slot due to the suction of the vacuum. Finally, experimentation identified PTFE tape packed into the groove created the optimal seal for the Mk.III engine and allowed testing to proceed. PTFE is a low friction material, the thickness of the packing could be adjusted as required, and the seal was found to be reliable.

The updated piston allowed more stable operation of the engine and enabled test data to be gathered. Therefore, future engines should minimise piston weight on the uniflow engine and opt for a more modern piston sealing mechanism. This should be piston rings, if possible, but Mk.III testing has shown PTFE tape packing to be a simple and suitable backup if required. Photographs of the updated piston are shown in Figure 4-15. Dimensions of the updated piston were recorded in a basic drawing included with the main technical drawing pack listed in Chapter 9.

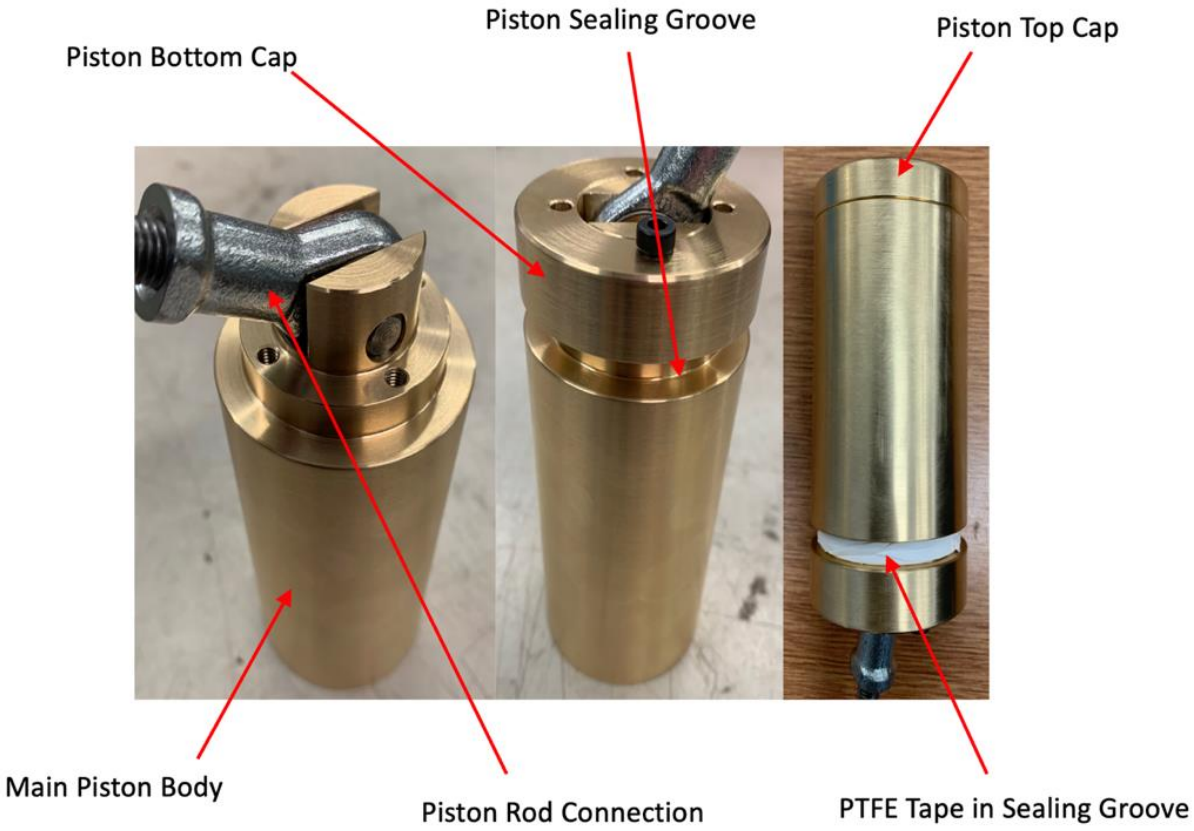

Figure 4-15 Photographed updated Mk.III engine piston.

4.5.3 Power Take Off

4.5.3.1 Crank Shaft Design

The crank shaft transmits the power produced by the piston to both the flywheel and the vacuum pump. The MK.III engine uses two crank disks to achieve this, equal in diameter to the engine stroke length, to which the piston rod end is attached. Spacers were included in the original design to position the rod end centrally between the disks and prevent it from moving, see Figure 4-16. However, this was found to be unstable under load during testing and therefore a custom spacer tube was machined, by hollowing out a piece of solid rod, to set the desired space between the crank disks. A bolt was used to lock the disks in place, passed through the inside of the spacer.

Ultimately, this connection became too unstable to allow extended engine testing. On future engines a solid crank shaft should be employed, if possible, to increase stability.

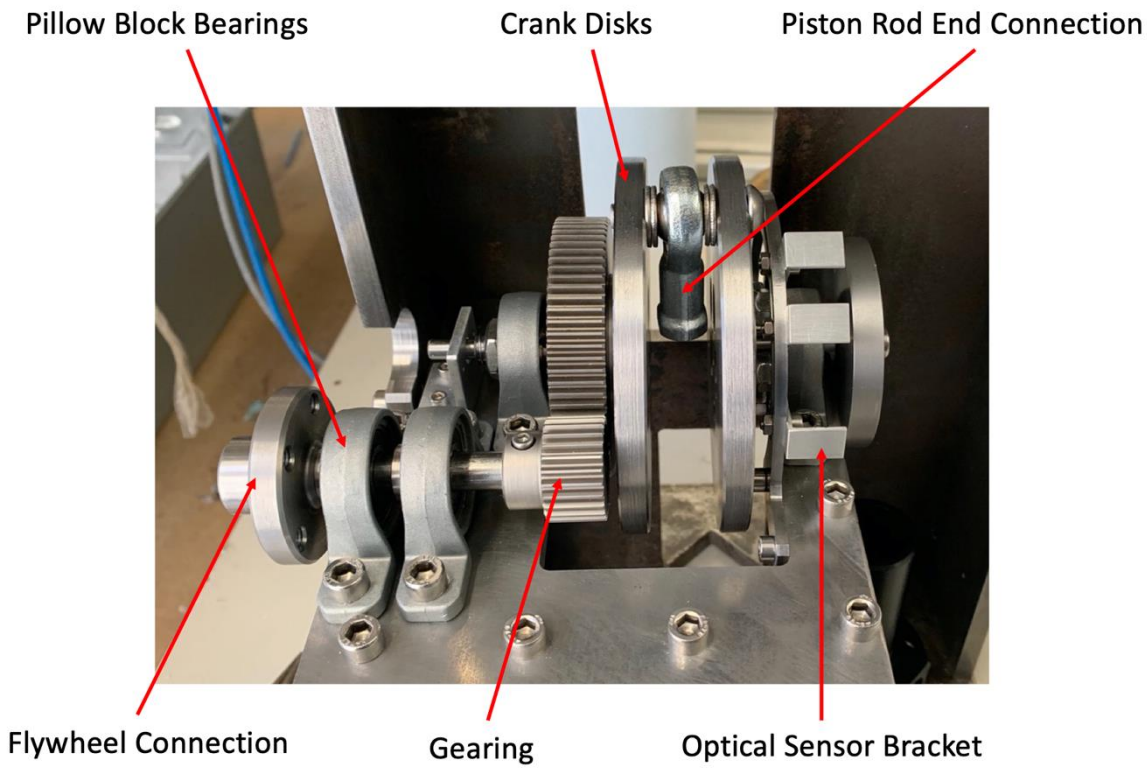

Figure 4-16 MK.III engine crank shaft during assembly. Note that the flywheel, vacuum pump connecting rod, and piston rod are not shown in this image.

It can also be seen in Figure 4-16 that the pillow block bearings adjacent to the crank disks were not used in pairs. The initial design expected that the bearings employed either side of the crank disks would operate as a pair if the crank disk assembly was sufficiently rigid, in turn preventing unstable motion. Due to the issues in the stability of the crank disk and piston rod assembly this was not achieved and is expected to have contributed significantly to the mechanical losses in the engine. This design was initially chosen to reduce space requirement. On future engines, these bearings should be used in pairs either side of the crank assembly, as was done adjacent to the small gear which worked well under testing.

4.5.3.2 Flywheel Energy Storage

A flywheel was needed to store and distribute power to overcome the uneven power output of the single acting MK.III engine, shown photographed in Figure 4-17. To store energy effectively the flywheel should be heavy and have a large diameter, to increase the moment of inertia, and a high rotation speed to maximise energy storage (Gidzewicz, 2016). The chosen gear ratio ensured the flywheel rotated at three times the speed of the engine. Consultation with Hanley design and previous MK.II drawings resulted in a flywheel diameter of 300mm and a thickness of 10.0mm. The

flywheel material was specified as mild steel, giving a weight of 6.6kg. This was comparable to the flywheel used on the Mk.II engine and was therefore deemed appropriate for use. A confirmatory calculation was performed to support this assessment using Equation (4.7). Calculation in Chapter 9 finds that the moment of inertia of the designed Mk.III flywheel was 0.09 kg/m^2. At an engine speed of 60rpm this was theoretically capable of storing 15.9J.

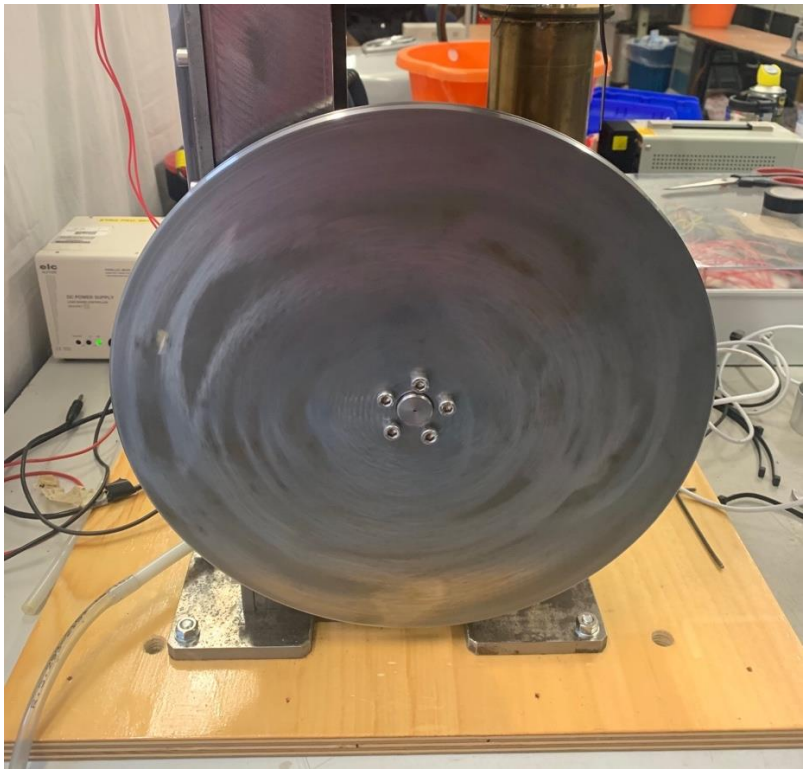

Figure 4-17 Photograph of Mk.III engine flywheel assembled onto engine to demonstrate scale.

To understand if this would be sufficient energy storage the mathematical model developed to estimate the theoretical efficiency of the uniflow Mk.III engine was used to predict energy losses and gains during one revolution. This estimated that at an expansion ratio of n = 1 and heat source and sink of 100°C and 20°C, the downstroke loses 0.26J per revolution and the upstroke gains 19.4J per revolution. Therefore, at an engine speed of 60rpm the downstroke theoretically loses 0.26W and the upstroke gains 19.4W. This confirmed the flywheel design as suitable during initial design as it could be suitably charged during the upstroke to overcome the losses of the downstroke.

However, the engine operated at a minimum speed of around 30rpm during tests. At this speed the designed flywheel can theoretically store 4.0J. At this speed the engine downstroke loses 0.13W and the upstroke gains 9.7W. This crude calculation demonstrates that at slower speeds the flywheel is less capable of balancing power, with the small storage capacity in this case unlikely to overcome both the power loss of the downstroke as well as mechanical friction measured to be significant. This is relevant as this thesis has highlighted the interesting concept of operating the engine at slower speeds to allow an increase in efficiency in situations where the trade off in power

output is acceptable. It is therefore recommended that in future engines multiple cylinders be used to provide more effective power balancing, especially in cases with low engine speeds. Additionally, an increase in boiler pressure above atmospheric pressure should be investigated, reducing losses associated with downstroke of the single acting uniflow engine allowing a more stable power output.

4.5.3.3 Friction Brake Setup

The friction brake, or rope brake dynamometer, was chosen for use on the Mk.III engine as a cost effective and simple solution for measuring mechanical engine power from the flywheel (Rajput, 2006). A schematic is shown in Figure 4-18. The change in loadcell reading indicates the power produced by the engine to overcome the friction caused by the hung weight which resists the flywheel rotation. The equation governing the calculation of output power using this setup has already been described in Section 4.2. Whist this setup was successful in allowing Mk.III mechanical power to be estimated, supported by separate piston power and friction analysis, an improved methodology is recommended for future tests to reduce the load applied on the engine. The loading of weight onto the flywheel was considered to have destabilised the power take off, compounding the friction challenge. Additionally, the loading of weight reduces the speed the engine can be tested at. Future tests could use a torque transducer, for example.

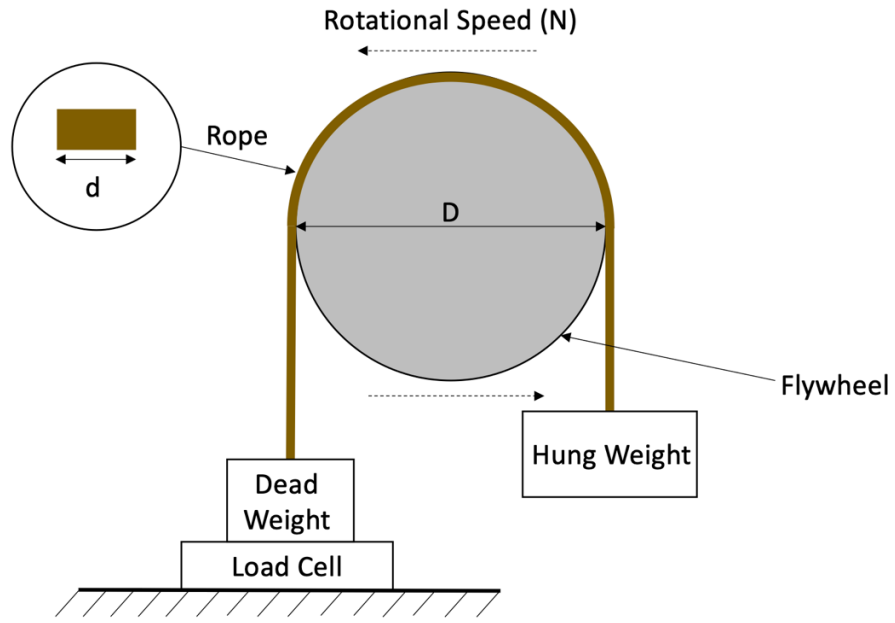

Figure 4-18 Schematic of friction brake setup used on Mk.III engine to estimate mechanical power output.

4.5.4 Vacuum Pump

The vacuum pump evacuates condensate and any air ingress from the system, maintaining the negative pressure necessary for power production. The MK.III vacuum pump had a bore of 25mm and a stroke length of 50mm, chosen as half the cylinder dimensions to maintain comparability with the MK.II engine. A photograph of the vacuum pump cylinder and piston during assembly is shown in Figure 4-19.

Figure 4-19 Vacuum pump cylinder and piston during assembly.

Calculation was performed in Chapter 9 to confirm that this would be suitably sized, finding an evacuated volume per stroke of 2.45×10^{-5} m^3. In comparison, just 1.16×10^{-7} m^3 of condensate is theoretically produced by each engine stroke with an expansion ratio of $n = 1$, as a worst-case scenario. The analysis presented in response to Mk.III engine testing showed that condenser pressures were insufficiently low. This was linked to the condenser heat transfer effectiveness as well as pump size. Whilst it is more likely to be a function of the former, the latter could be increased to give the system more evacuation power on the next design iteration.

The vacuum pump cylinder was made from an aluminium alloy and the vacuum pump piston from Ultra High Molecular Weight Polyethylene (UHMWPE). The aluminium offers a more cost-effective alternative to brass. UHMWPE has a low friction coefficient, is considered a thermal insulator, and is recyclable (Redwood, 2018; DM, 2020). To ensure that a seal could be achieved on the MK.III engine, the piston was designed with grooves to allow use of rubber o-rings if necessary although not found to be required during Mk.III engine testing. It is concluded from Mk.III engine testing that

this material combination was a success and demonstrates a potential modernised material combination for future engine designs.

The next engine iteration could utilise aluminium alloy as an expansion cylinder material with the option of a UHMWPE piston. However, the temperatures experienced in the vacuum pump are considerably lower than in the cylinder. In theory, the vacuum pump experiences temperatures associated with the cooling water temperature, whereas the cylinder experiences temperatures associated with the boiler. As thermal expansion is linked to temperature, see Equation (4.12), the increased temperatures in the cylinder increase the risk of thermal expansion differences and therefore jamming compared to the vacuum pump. Therefore, use of the above material combination on a main engine cylinder requires careful consideration of thermal expansion, supporting the need for the steam jacket on future iterations which use alternative material combinations.

It is commonly accepted in thermodynamic assessment of heat engines that the power required to operate the pump is negligible compared to the useful power output and therefore is not included in the calculations in typical work (Cengel & Boles, 2011). The work presented in Chapter 3 confirmed this in the case of the condensing engine. In the analysis of the Mk.III engine tests, the pump losses are included in the assumed 10% mechanical losses applied to the calculated piston power. This represents an ideal case and was used to allow fair analysis of the Mk.III without the excessive friction experienced. On future condensing engines with improved power take off and reduced friction, the final mechanical or electrical power output should be used to report engine performance and will therefore account for pump losses.

4.5.5 Condenser

To confirm that the re-used condenser from the Mk.II tests, see Figure 2-22, would be suitable for use on the Mk.III engine, average heat loads from both engines during expected operation were compared. The average heat load is the thermal energy that must be absorbed by the condenser per second, found using Equation (4.13).

$$\dot{Q}_{avg} = (h_{g,cyl} - h_{l,cond}) \times \dot{m}_s \tag{4.13}$$

Where:

- $\dot{Q}_{avg}$ is the average thermal power loaded on the condenser (kW).
- $h_{g,cyl}$ is the enthalpy of water vapour at conditions leaving the cylinder (kJ/kg).
- $h_{l,cond}$ is the enthalpy of condensate at condenser operating temperature (kJ/kg).
- $\dot{m}_s$ is the mass flow rate of steam passing through the system (kg/s).

Mk.III engine average heat loads have been calculated in Chapter 9, using an expansion ratio of n = 1 as a worst-case scenario with maximum steam volume flow rate. These were found to be 0.3kW and 0.6kW for engine speeds of 60rpm and 120rpm respectively. Figure 2-20 gives the Mk.II engine condenser average heat load as 0.69kW, demonstrating that up to a speed of 120rpm the Mk.III engine has reduced heat loads compared to the previous model. Therefore, the condenser was deemed suitable by the author of this research for re-use on the Mk.III engine. Re-using the condenser allowed a more accurate comparison of condensing engine technologies. The improvement in cylinder pressure reduction on the Mk.III engine can therefore be attributed to the use of the uniflow evacuation port without need to quantify the effect of any change in condenser power. This is omitting the effect of cooling water temperature and flow rate, which was kept as comparable as possible during testing.

During testing, Mk.III engine condenser pressures were similar to those experienced during Mk.II testing. This supports that the condenser was suitable for the prototype engine for initial proof of concept and data gathering. However, future engine iterations should investigate whether increased condenser heat transfer area would allow for reduced pressures and therefore improved performance. Reduced cooling water temperature would improve condenser performance and could be included as a test in future projects to further assess potential uniflow engine effectiveness. This was not included in the scope of this research project.

4.5.6 Engine Control

4.5.6.1 Electronics

A new simplified electronic control system was developed for the Mk.III engine. The aim of the new system was to allow for future elimination of the microcontroller, for simplicity and cost reduction, as well as to allow manual control of expansion ratio during operation. This was to eliminate issues experienced with encoders on previous iterations and make the engine control easier to maintain in small scale domestic settings. The chosen system utilising optical sensors on a bracket opposite a reflective strip on the crank disk to trigger valve operation has already been explained. A photograph of the assembly is shown in Figure 4-20. The engine control system was deemed a success during testing. It performed reliably and triggered valving at the correct times. Future engine iterations could employ this improved engine control system.

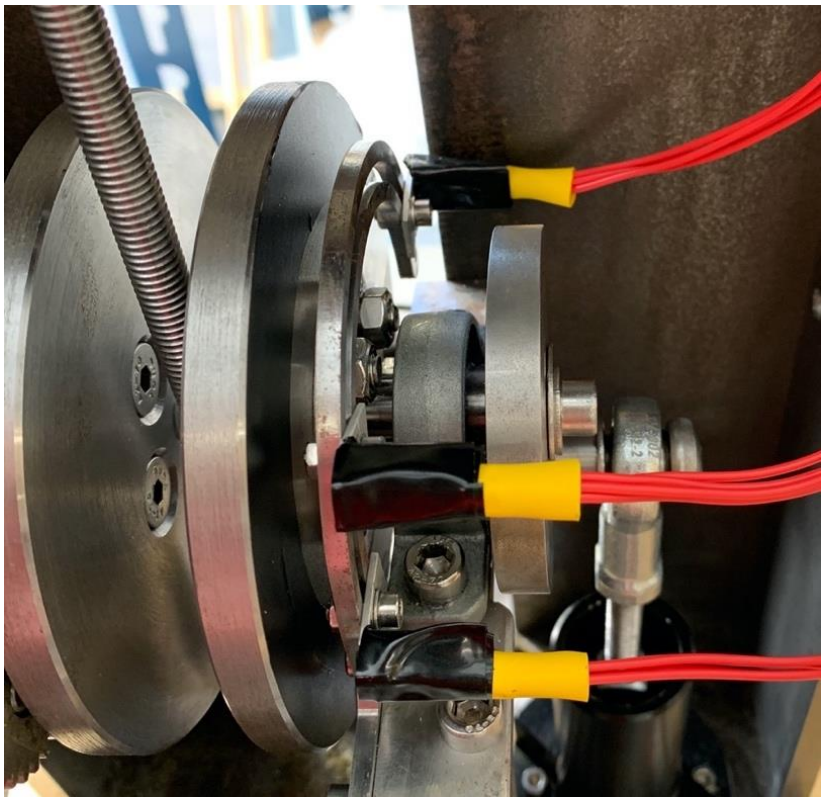

Figure 4-20 MK.III engine sensors mounted on bracket facing crank disk.

The Mk.III engine made use of an Arduino microcontroller to read signals from the optical sensors and transmitted corresponding signals to the valves. An Arduino microcontroller was used because of its large set of digital input pins and widely available coding libraries for integration of sensors and transducers. It was also recommended by colleagues in the Electrical Engineering department. A microcontroller was required on this prototype to test proof of concept of the optical sensors. However, future engine designs should focus on developing this further to use the signals from the optical sensors to directly trigger the valves. A challenge will be outputting engine speed without a microcontroller, calculated on the Mk.III engine by the Arduino using the time between optical sensors pulses.

4.5.6.2 Valves

The second key element of the engine control were the valves, chosen because of their cost effectiveness and orifice diameter of 11mm, equal to that of the piping used on the engine; see Figure 4-21. However, analysis of Mk.III engine test data identified that steam evacuation was choked resulting in compression of residual steam even at low speeds. Therefore, it can be understood that the orifice diameter alone is not limiting the evacuation. It is proposed that the resistance to flow created by the steam path through the valve is also a significant contributing factor. Therefore, future engine work should look to identify a more suitable alternative on the market or to design a proprietary valve with minimised head loss coefficient to achieve significant gains in engine performance.

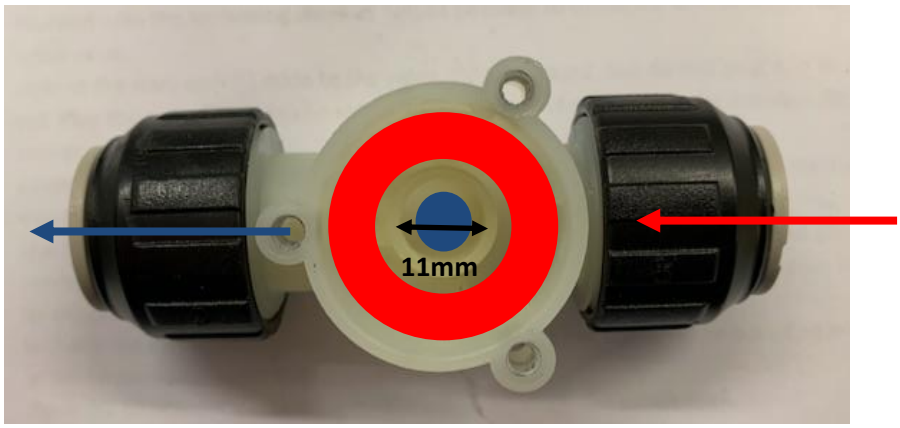

Figure 4-21 Annotated photograph of RPE srl 1175BC solenoid valve internals. The fluid flows from right to left, first filling the outside channel (red ring). When the solenoid valve is actuated the seal is lifted and the flow is allowed to exit the valve via the inside orifice (blue circle).

The electrical energy required to operate engine control and data acquisition have not been included in the efficiency analysis in the Mk.III engine manuscript to allow more direct comparison with the Mk.II engine. The Mk.III engine control valves have a power consumption of 5.4W each when held open (SolenoidValveWorld, 2020). At any point in time one valve will be held open during operation, giving a total valve power consumption of 5.4W. This is as great as the maximum mechanical power obtained from the Mk.III engine due to the engine's relatively small size. This prompts the need to scale the engine if the valves are to be powered by electricity produced by the engine without significantly reducing engine efficiency.

As a result of the above analysis, it is expected by the author of this research that the limited energy density associated with the atmospheric condensing engine compared to high pressure engines will result in electronic valves being unsuitable for use on the developed model. As a result, alternative valve options are required. The literature review identified that slide valves could be an ideal option, both to reduce pressure losses through the valve and to allow for mechanical operation. A prototype slide valve was developed as part of this project but experienced excessive friction and was not used on the Mk.III engine tests. The proposed slide valve design and lessons learned from its testing are included in Section 4.5.7.

4.5.6.3 Engine Start-Up

The start-up procedure of the Mk.III engine involved the manual turning of the engine using a handle inserted in the flywheel. Turning the engine triggered the engine control system using the optical sensors, allowing steam to be admitted to the cylinder and evacuated to the condenser. Following condensation and generation of sub-atmospheric pressures the engine began to sustain operation and the handle could be removed from the flywheel. Manual start-up of the Mk.III

engine was suitable for its prototype nature and is considered an advantage where simplicity is required, for example in remote and rural communities as discussed in Chapter 5. However, if modern engines require automation, a starter motor could be employed to turn the engine for a set time period and then switched off, allowing the pressures in the system to sustain operation. Engine speed could be subsequently maintained/controlled using a mechanical governor, see Section 2.4.4.4.

It is acknowledged that prior to the manual start-up of the Mk.III engine, the system also required 'priming'. This involved allowing the boiler to generate steam which was subsequently drawn through the system to raise the cylinder and piston temperature to prevent initial condensation of steam during start up when admitted to the cylinder. This also acts to remove any air from the system. This was achieved by holding the inlet valve in the open position and the piston at BDC to allow flow through the uniflow port. It is acknowledged that in Mk.III testing, an electronic vacuum pump was used to evacuate air prior to passing steam through the engine to raise temperature. This was to aid steam flow and ensure no air was present, but in future engines this is not considered to be a necessary step. Future automated engines could implement a control system to perform the priming process.

4.5.7 Prototype Slide Valve

It was identified during Mk.III engine testing that improved valving is critical for the development of future condensing engines. Requirements include reduced minor head loss coefficient, to reduce pressure drop across the valve and restriction to flow, as well as the need for a mechanical mechanism to eliminate the need for electrically powered valving. The literature review identified the slide valve as a good example from historical engines. The slide valve allows a more direct steam flow path, reducing losses, and is mechanically linked to the engine's motion. This research project therefore designed and built a slide valve to be used with the Mk.III engine. However, excessive friction rendered the valve unusable and solenoid valves were used during engine testing instead, as discussed already in this chapter. The valve can be seen photographed in Figure 4-22 and Figure 4-23. The original CAD files are also available in the data repository; see Chapter 9.

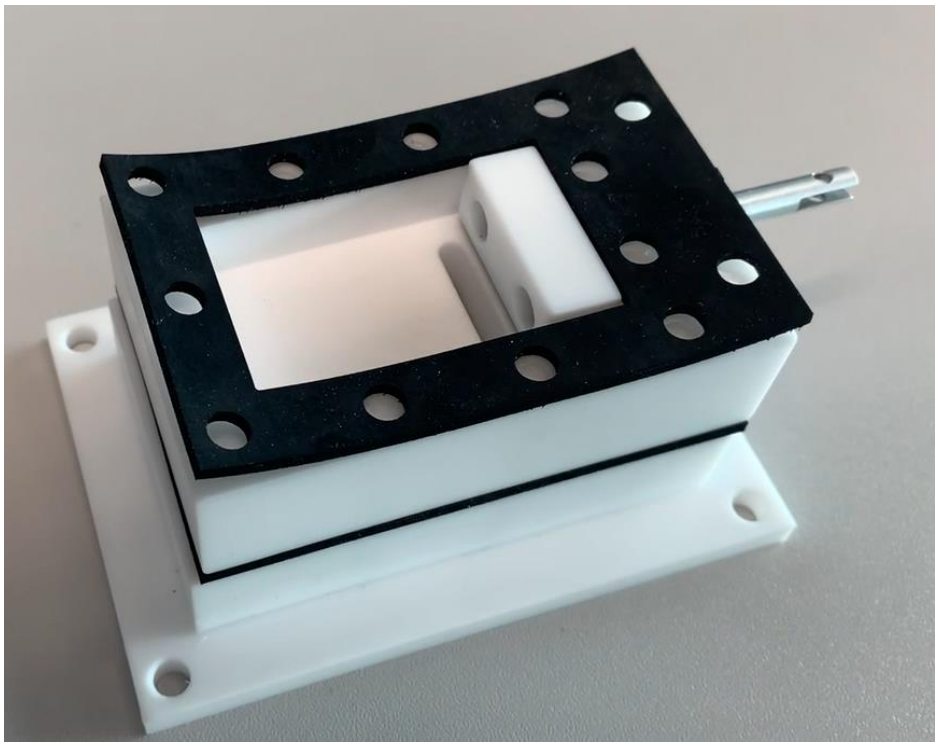

Figure 4-22 Prototype condensing engine slide valve shown with top piece removed and slide piece in 'valve open' position.

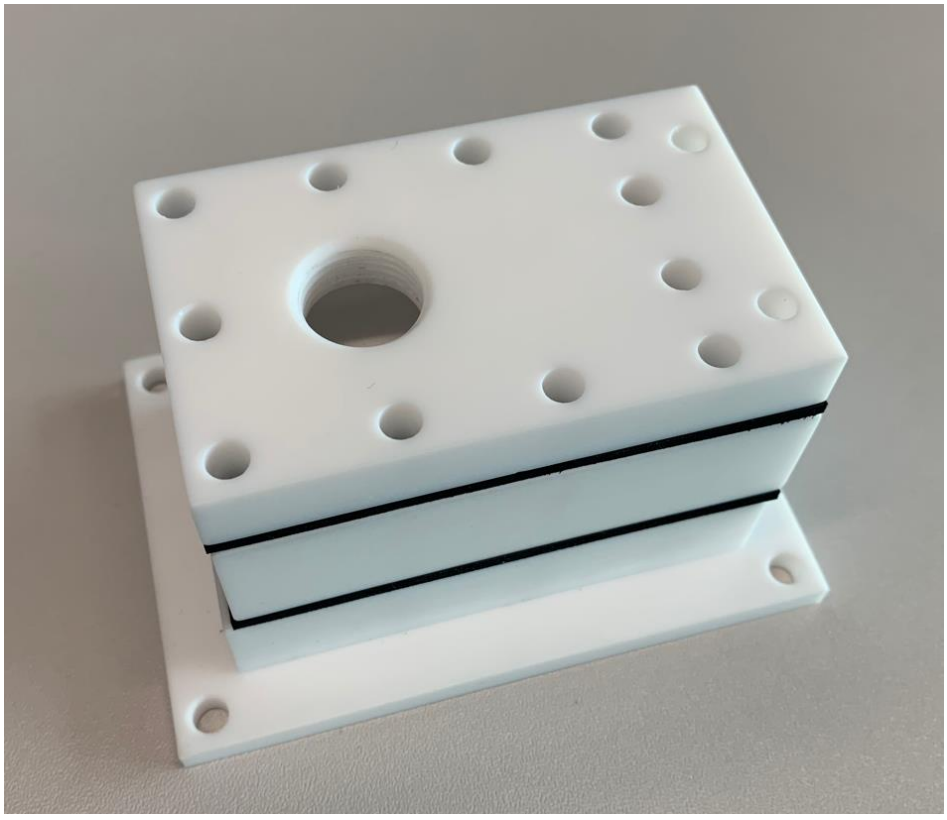

Figure 4-23 Prototype condensing engine slide valve shown as an assembled unit (without bolts and pipe connections).

The prototype slide valve was chosen to be operated by an electronic solenoid in the case of the Mk.III engine, to be mechanically linked at a later stage of design. The actuation of the solenoid caused a plunger to move back and forth. A 'slide piece' was attached to the plunger, and therefore the actuation could move this piece to 'open' and 'close' the valve orifice. The plunger was inserted through the valve casing wall, with nitrile rubber o-rings used to seal against air ingress from the external atmosphere. The slide piece also had holes cut into it to allow steam through and eliminate build-up of pressure around the slide piece. The valve orifice was cut as a slot, mirroring the uniflow evacuation port geometry on the Mk.III engine cylinder. The slide piece had a nitrile rubber seal adhered to the bottom, to seal over the orifice when the valve was closed. The valve casing was formed of three sections. The bottom section formed the downstream chamber of the valve and provided a flange for attaching the valve body to the engine frame. The middle section formed the separation between the upstream and downstream chambers and had the orifice cut into it. The top section encased the upstream chamber of the valve. The valve body was assembled using bolts and nitrile rubber gaskets. The pipe connections to the valve body used threaded pipe fittings with PTFE tape. The valve body and slide piece were manufactured from PTFE to reduce friction.

It is acknowledged that this was not a direct replication of the slide valve concept discussed in the literature review, where the slide valve body was itself actuated, sliding along the cylinder wall to reveal the orifice. The author chose to attempt a design which could be easily mass produced and that simplified connection to engines of different types and sizes. Unfortunately, testing experienced excessive friction between the nitrile rubber seals and the moving slide piece and plunger. This resulted in the valve being unsuitable for use, with the solenoid unable to overcome the losses. Friction must be reduced on future designs by carefully considering material sections. The concept of the slide valve being an integral part of the cylinder body design should also be revisited, replicating historical designs.

4.6 Conclusions

The Mk.III condensing engine was developed and tested using a novel single acting uniflow arrangement with the aim of creating a simple and potentially cost-effective heat engine for low temperatures. Engine control was also successfully updated to allow simplification and manual control as part of this work. Small scale model tests were conducted to assess its functionality, and to determine the performance parameters. The results were compared with previously reported condensing engine tests as well as recent ORC systems working at comparable temperatures and power scales. The following conclusions have been drawn:

- The single acting uniflow configuration successfully improved cylinder evacuation creating improved pressure driving force for power production. It should be used on future engine iterations.
- The Mk.III engine achieved a maximum power output of 5.4W, assuming 10% friction losses from the calculated piston power, comparable to the Mk.II engine for similar operation.
- The Mk.III engine achieved a maximum thermal efficiency of 2.5% respectively, representing an increase of 25% compared to the previous Mk.II model operating without steam expansion. Analysis showed that thermal efficiencies as high as 9% could be achieved with further development of the technology.
- The Mk.III engine achieved a maximum second law efficiency of 43%, assuming no losses between boiler and cylinder, comparable with existing ORC systems operating in the same temperature range and an increase of around 25% over the Mk.II model.
- Tests at higher engine speeds increased power output but reduced efficiency, identifying different operating regimes for future investigation.
- The theoretical model developed to simulate steam evacuation from the cylinder closely matched real engine data and can be used to aid future design.

In summary, the uniflow engine configuration was a success and warrants further investigation and development. This is the first research of its kind to identify this, and as such has several experimental learnings and recommendations which should be used to guide future work:

- Future work must understand whether the assumption of 10% mechanical losses from calculated piston power and negligible losses between boiler and cylinder can be achieved in practice. The effect on the comparison of the technology against ORC systems in literature should be discussed.
- The Mk.III uniflow engine was prone to jamming due to thermal expansion of the piston. This was mitigated through use of steam jacket. Future iterations should use a steam jacket or alternatively investigate use of thermally insulating materials for cylinder and piston.
- The original solid piston used on the Mk.III engine had too great a mass. This was improved by hollowing the piston. Future iterations could investigate lightweight piston materials. Future work should also optimise piston sealing, for example through use of piston rings.
- The Mk.III engine power take off suffered from excessive friction. This should be improved with appropriate bearing selection and updated crank design.
- The Mk.III engine solenoid valves choked steam evacuation once the uniflow port was closed in the upstroke. Therefore, future iterations should maximise the evacuation port area and investigate improved valve selection. This could include a custom valve design,

such as a slide valve to reduce the associated minor head loss coefficient. Slide valve optimisation should focus on minimising friction and achieving mechanical timing.

- Future testing should maximise condenser heat transfer area and test reduced cooling water temperatures.
- The power loss in the Mk.III uniflow downstroke could not be overcome by the flywheel at the low engine speeds tested. Future iterations should incorporate multiple cylinders to mitigate this. Increased boiler pressure could also overcome losses associated with the downstroke of the single acting uniflow condensing engine.
- The Mk.III engine was tested without steam expansion. Future iterations should employ this to increase efficiency.
- Scaling the uniflow condensing engine has been identified as required to reduce the impact of friction. This could be quantitatively assessed by incorporating friction into the already developed uniflow engine model and performing a sensitivity analysis.

Chapter 5 The Mk.IV Engine: Integration into a Combined System

Following Mk.III engine testing and critical review of the design, a further iteration of the single acting uniflow engine (the Mk.IV) was designed using the lessons learned. The Mk.IV engine was developed as part of a collaboration with the University of Stellenbosch Solar Thermal Energy Research Group (STERG) integrating the engine with solar thermal collectors. As discussed in the introduction, such a system can provide both electricity and water purification to remote communities through the thermal distillation process occurring in the system. South Africa presents an ideal location for the use of solar collector technology due to its high solar irradiation levels, around 2,000 kWh/m^2 per year in Cape Town (The World Bank (a), 2020) compared to around 1,000 kWh/m^2 in London (The World Bank (b), 2020). Chapter 5 discusses the integration of the condensing engine with solar thermal panels as well as the design of the engine itself to further improve performance compared to the previous Mk.III model. This combined system has been manufactured and built in Stellenbosch ready for testing. Engine tests are part of the ongoing project and therefore the results have not been included as part of this thesis.

5.1 The Combined System: Water Purification and Energy Production

5.1.1 System Overview

The combined water purification and energy production system consists of three main stages: (1) steam generation, (2) steam expansion to produce power, and (3) steam condensation and water collection. This is shown schematically in Figure 5-1.

The steam is produced from solar collectors on the roof of the laboratory at the University of Stellenbosch, in South Africa, where the system has been built. A heat transfer fluid is passed through the solar collectors, in a double pass configuration, to achieve sensible heating. In initial experiments the heat transfer fluid is to be water, kept in the liquid phase, but this could be swapped for special thermal fluids in future tests. The heated fluid transfers thermal energy to the feed water in the boiler to produce steam before returning to the solar collector array as part of a closed circuit. This design was chosen by the team in Stellenbosch to prevent fouling inside the

collector tubes. A boiler blow down will be used to prevent excessive total dissolved solids (TDS) build up in the boiler vessel. The liquid evacuated during the boiler blow down process will have a higher concentration of contaminants, as a result of evaporation, and suitable disposal routes are therefore required according to the quality of the water.

An External Compound Parabolic Concentrator (XCPC) collector type, built by Arctic Solar in the USA, has been chosen for this setup by the University of Stellenbosch STERG to provide the solar thermal energy to the boiler. Six collectors have been used with a total surface area of 16.2m^2, sized to produce 4.4L/s of steam at atmospheric pressure. This is sufficient for maximum expected working steam requirement plus approximately 15% for steam jacket use, determined using Mk.III engine analysis. This can also be supplemented with an on-site boiler if necessary for testing purposes. The solar collector and boiler system will operate up to a pressure of 1.5bar during tests to prevent classification as a pressure vessel.

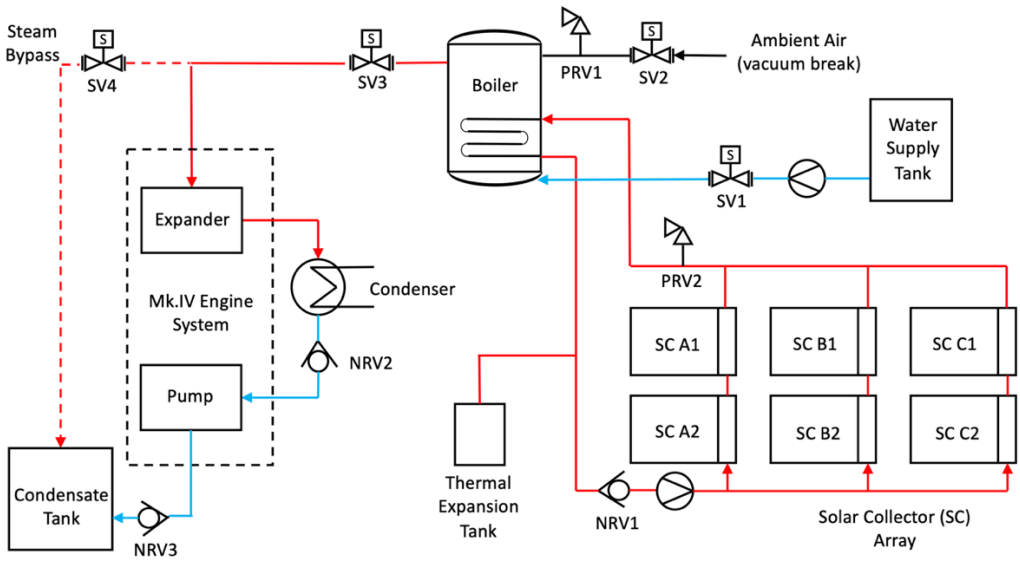

Figure 5-1 Schematic of combined Mk.IV engine and solar thermal collector system for water purification and energy production. SV = Solenoid Valve. PRV = Pressure Relief Valve. NRV = Non-Return Valve. SC = Solar Collector. A1,A2,B1,… = SC Array Identifier.

The generated steam is used to supply the condensing engine, acting as the expander to produce mechanical work. If steam demand from the engine is less than that supplied by the solar collector system either a steam bypass or pressure relief valve can be used to vent excess steam from the system. This is a prototype, and in an optimised system the bypassed steam would be recovered in the feed acting as pre-heat or directly condensed and collected. Condensing engine outlet steam passes to the condenser as normal, where the partial vacuum is generated to drive the engine, and condensate is pumped to a collection tank using the mechanical power of the engine. The condenser was re-used from previous University of Stellenbosch tests and was deemed

appropriate to handle the heat load by the team based there. The collected condensate can be tested for purity to assess the effectiveness of the thermal distillation by comparing to the contaminated feed water. Photographs of the system built in Stellenbosch can be found in Figure 5-2 and Figure 5-3.

Figure 5-2 Photograph of combined system solar collectors and boiler cylinder built on laboratory roof at the University of Stellenbosch. Reproduced with permission from Dr Michael Owen from University of Stellenbosch Solar Thermal Energy Research Group.

Figure 5-3 Photograph of boiler and Mk.IV condensing engine built behind the boiler cylinder on laboratory roof at the University of Stellenbosch. Reproduced with permission from Dr Michael Owen from University of Stellenbosch Solar Thermal Energy Research Group.

The Mk.IV engine was designed by the author of this research, based on lessons learned from the Mk.III engine, with guidance from the UoS EDMC and the project supervisory team. The EDMC were responsible for the production of the engine technical drawings. The engine components were manufactured by the University of Stellenbosch Engineering Workshop, as this is the site for testing. The solar thermal collectors, boiler, and condenser systems were designed and assembled by the University of Stellenbosch STERG. The team in Stellenbosch also assembled the Mk.IV condensing engine. Original plans for the author of this research to visit Stellenbosch and assemble and test the engine were disrupted by the COVID-19 pandemic.

5.1.2 Condensing Engine Integration: A Discussion

It became apparent during Mk.IV engine design that the main area of focus when integrating the condensing engine into a wider system is ensuring synergy between steam supply and demand. During operation, the condensing engine can demand different steam flow rates depending on engine speed and steam expansion ratio. This resulted in two scenarios which required thought: (1) steam supply exceeds demand (2) steam demand exceeds supply. This can be managed by equipment design as well as specified control regimes.

When steam supply exceeds demand, this creates the need for a bypass to prevent overpressure, discussed in the system overview section. This requires further optimisation on future projects to recover the thermal energy lost in the bypass. When steam demand exceeds supply, the engine will naturally slow to reduce the required steam volume flow rate. However, it is preferable to maintain a constant engine speed to produce stable power output, especially when connected to electrical components such as generators. Therefore, during Mk.IV engine control design, it was proposed that in this scenario the steam expansion ratio should be increased. This reduces the steam demand for the same speed creating better synergy with steam supply. The use of steam expansion for control within a combined system is a novel idea and another benefit of steam expansion not previously identified.

It is acknowledged that the solar collectors built as part of this project were specially designed for the Mk.IV engine. The condensing engine technology will also be combined with existing systems, for example waste heat recovery in industrial settings. The condensing engine could also be integrated with existing bio-steam projects, introduced in Section 2.1, which could also take advantage of thermal distillation for water purification. In these scenarios the engine size must be designed according to the available steam supply. This will set optimum engine size, operating speed, and operating expansion ratio. In such scenarios it may be possible to avoid the need for a

bypass, drawing the waste heat needed by the system and no more. This would need investigation on a case-by-case basis.

5.2 Mk.IV Engine Design

Section 5.2 details the design of the Mk.IV engine itself. Firstly, an overview of the engine system is given, including some key component dimensions as per the technical drawings. Secondly, a more detailed overview of some of the key design improvements is given, documenting the advancement of the technology beyond the Mk.III prototype during this research project. The engine updates have been designed in consultation with the University of Southampton EDMC and should be included on future iterations of the engine, pending successful testing.

5.2.1 Mk.IV Engine Overview

Many principles of the Mk.IV engine design were retained from the previous Mk.III model. Firstly, a single acting uniflow arrangement was again used, shown to be effective during Mk.III engine testing. Secondly, steam jackets were again included in the design to reduce thermal losses and prevent jamming due to differences in thermal expansion. Thirdly, the control scheme developed for the Mk.III engine was replicated on the Mk.IV. Finally, the principles of the modified Mk.III piston design were also re-used on the Mk.IV engine. However, some key advancements were also made, shown in the Mk.IV engine cylinder schematic, see Figure 5-4, and the photographed assembled engine, see Figure 5-5.

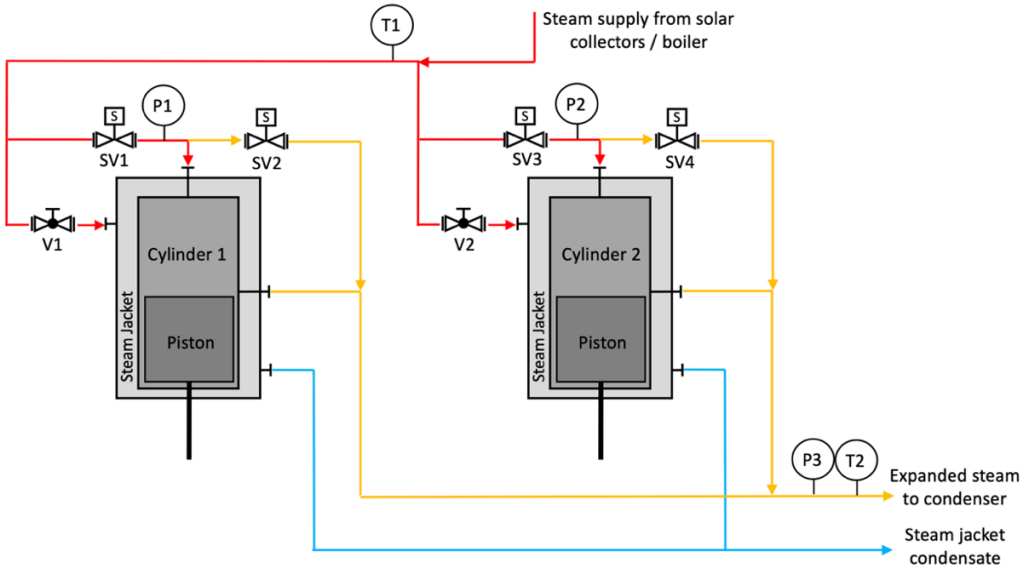

Figure 5-4 Process flow schematic for the Mk.IV condensing engine cylinders. T = Temperature. P = Pressure. SV = Solenoid Valve. V = Valve.

The Mk.IV engine was designed to be a twin-cylinder engine to give a smoother power output and allow for increased engine speeds. Furthermore, the Mk.IV engine was designed to be modular, with frame and crankshaft pieces that can be added for each new cylinder. This gives greater flexibility for future scale up and commercialisation and is a further novel advancement in the design of the modern condensing engine. Importantly, the Mk.IV engine cylinder, piston, and power take-off were also updated based on lessons learned from the Mk.III prototype, discussed in more detail in Section 0.

Figure 5-5 Mk.IV condensing engine assembled in University of Stellenbosch laboratory. Reproduced with permission from Dr Michael Owen from University of Stellenbosch Solar Thermal Energy Research Group.

The Mk.IV engine was also scaled up to produce an estimated maximum of 90W of mechanical power from each cylinder at an engine speed of 90rpm and an expansion ratio of n = 1. Required stroke dimensions were determined using isentropic equations with a boiler temperature of 100°C, a condenser temperature of 20°C, and an estimated isentropic efficiency of 50%. Using an estimated isentropic efficiency allowed for the actual desired output power to be designed for rather than an ideal value, important for future iteration design. A value of 50% was higher than that the 33% - 39% range achieved by the Mk.III engine, with improvements expected to be achieved on the Mk.IV model. An isentropic efficiency equal to the Mk.III engine would give an estimated Mk.IV power output of 55W. Therefore, the two cylinder Mk.IV engine is expected to produce between 110W - 180W of power, depending on the achieved improvement in isentropic

efficiency. Cylinder bore diameter to stroke length ratio was decreased on the Mk.IV from 1:2 to 1:1.6 in order to reduce friction. Calculations surrounding Mk.IV engine sizing are given in Chapter 9. Some key Mk.IV engine dimensions are given in Table 5-1.

Table 5-1 Nominal Mk.IV engine dimensions. Tolerances are given as specified on the drawings. Tolerances are given either as $\pm$ or as a range, depending on the specification on the technical drawings. Dimensions not specified on the drawing, eg. stroke lengths, do not have any quoted tolerances in this table.

Component	Parameter	Value / Unit
Maximum Steam Demand (90rpm, n = 1)	Steam volume Steam mass (at 1 bar)	3.75 L/s 2.21 x 10^{-3} kg/s
Cylinder	Bore diameter Stroke length Exit port diameter Number of exit ports	100.000 – 100.087 mm 160 mm 10.0 $\pm$ 0.2 mm 10
Piston	External Diameter Top Cap Length Body Length Bottom Cap Length Sealing Housing Length Assembled Piston Length	99.5 – 99.6 mm 5.0 $\pm$ 0.2 mm 175 $\pm$ 0.5 mm 5.0 $\pm$ 0.2 mm 20 $\pm$ 0.5 mm 185 $\pm$ 0.6mm
Steam Jacket	Gap Between Cylinder Wall	20 mm
Vacuum Pump	Bore diameter Stroke length Piston diameter Piston length	75.000 -75.074 mm 75 mm 64.5 – 74.5 mm 28.0 $\pm$ 0.2 mm
Power Take Off	Gear transmission	1:4
Flywheel	Diameter Thickness Material Mass	240 $\pm$ 0.5 mm 50.0 $\pm$ 0.2 mm Carbon Steel 11.037 kg

It is acknowledged that manufacturing to tolerances of micrometres, as specified for some Mk.IV engine components, would significantly increase cost. Whilst these tolerances have been specified by the EDMC on these drawings, it is not expected that such tight tolerances are required in order for the engine to successfully run. This should be further investigated during future work.

5.2.2 Mk.IV Engine Design Notes

5.2.2.1 Cylinder, Exhaust Manifold, and Steam Jacket

Two cylinders have been used on the Mk.IV engine. The control ensures these run out of phase to improve power smoothness, engine stability, and allow higher engine speeds. This was found to be important in Mk.III prototype testing and should be included on all future single acting uniflow engines. The Mk.IV engine cylinders have also been designed to maximise the number of uniflow ports to optimise steam evacuation and reduce cylinder pressures in the upstroke, as suggested in the Mk.III engine analysis. Port placement had 3 criteria:

1. Required one whole port diameter between each port to maintain cylinder structural integrity, as recommended by the EDMC.
2. No ports on the front or back of the cylinder. This was due to the motion of the engine creating greater force on these parts of the cylinder wall and the presence of ports creating possible friction.
3. Required an even port placement, symmetrical on each side, to avoid preferential suction of the piston into the side of the cylinder wall by the generated partial vacuum. This was identified during Mk.III testing.

This resulted in 10 ports on each cylinder, each 10mm in diameter. The resulting area for steam evacuation was confirmed as suitable by the previously developed uniflow evacuation model. This was defined as an ability to bring cylinder pressure down to condenser pressure, for boiler and condenser pressures of 1bar and 0.02bar respectively, for engine expansion ratios of n = 1 - 4 and a maximum engine speed of 90rpm. The evacuation ports themselves were specified as drilled holes to reduce parallel cuts in the cylinder which could create more friction, as experienced on the Mk.III engine, and simplify manufacture. The Mk.IV engine cylinder is shown in Figure 5-6, highlighting the multiple evacuation ports.

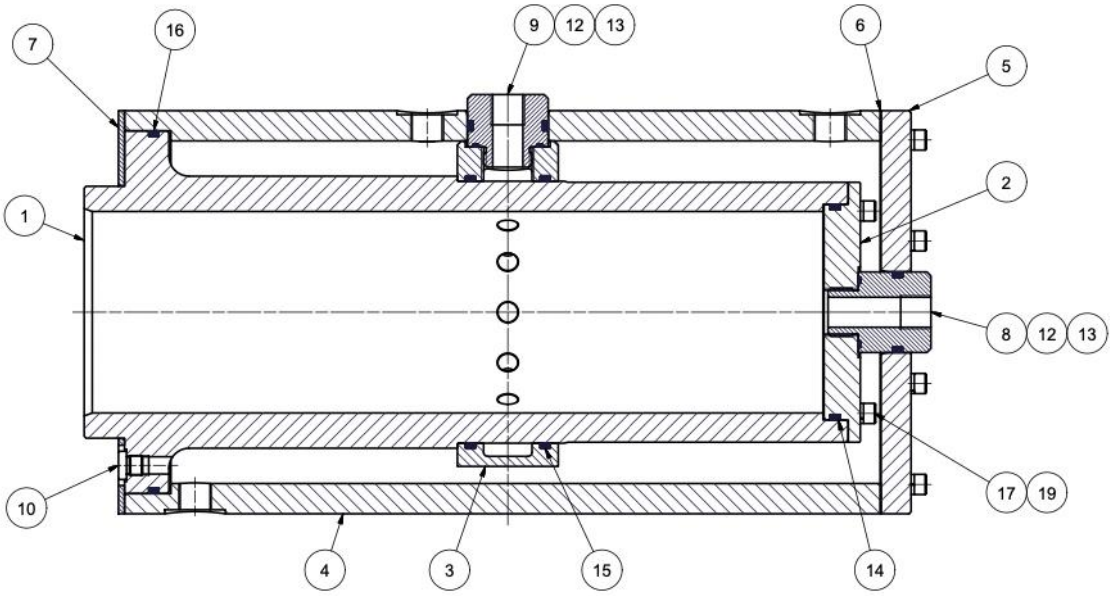

Figure 5-6 Section of 'Sub Assembly of Expansion Cylinder' technical drawing produced by the University of Southampton EDMC for this project. Section highlights the multiple ports and manifold and steam jacket assembly. (1) = Cylinder body. (2) = Cylinder end cap. (3) = Exhaust manifold. (4) = Steam jacket body. (5) = Steam jacket end plate. (6) = Cylinder gasket. (7) = Cylinder insulation ring. (8) = Cylinder inlet port. (9) = Cylinder exhaust port. (10) = Hydraulic blanking plug. (12 – 16) = O-rings. (17) = Screw. (19) = Washer.

Figure 5-6 also highlights the new cylinder and steam jacket assembly developed as part of the Mk.IV design. This was necessary to accommodate the multiple steam evacuation ports and the resulting requirement for a manifold to collect evacuated steam and allow connection of pipework. The external cylinder surface was designed with a step, acting as a seat for the manifold to sit on. The manifold can therefore be slid over the cylinder as one piece, sealing against the cylinder wall using an o-ring. The steam jacket is placed over the top of this, and pipework connected to the manifold and cylinder through holes in the steam jacket. This is a simplification of the assembly process used on the Mk.III engine despite more complicated requirements. This was easily constructed and assembled by the team in Stellenbosch and deemed a success. The manifold and steam jacket were specified to be manufactured out of acetal copolymer (acrylic) to provide better thermal insulation than the jacket used on the Mk.III engine

The Mk.IV engine cylinders were designed to be manufactured from aluminium and then coated on the inside surface. Aluminium is lightweight and cost effective, simplifying manufacture and assembly, especially on larger engines. The coating was specified in the design to be Nickasil, a trademarked silicon carbide coating commonly used on engine components to provide a surface that has low friction and increased wear and corrosion resistance. In the event this is not available,

hard anodising can be used instead to provide the necessary corrosion and wear resistance and increase cylinder life. Hard anodised coatings can be impregnated with PTFE to also provide the low friction characteristic that will improve engine performance.

5.2.2.2 Piston

The core principles of the Mk.IV piston design are unchanged from the modified Mk.III piston. The piston was designed to be hollow and allows for multiple sealing mechanisms to be tested inside a machined groove revealed by a cap. The Mk.IV piston was developed beyond that of the Mk.III by allowing for a sealing mechanism at both the top and bottom of the piston, more crucial for this engine due to the longer piston. This will help guide the piston inside the cylinder bore and reduce friction, thus increasing performance. Three sealing options were planned as part of the Mk.IV piston design, two of which are improvements over the sealing used on the Mk.III engine. This gives flexibility and allows optimisation of the engine during testing. The options are shown in Figure 5-7 and listed below.

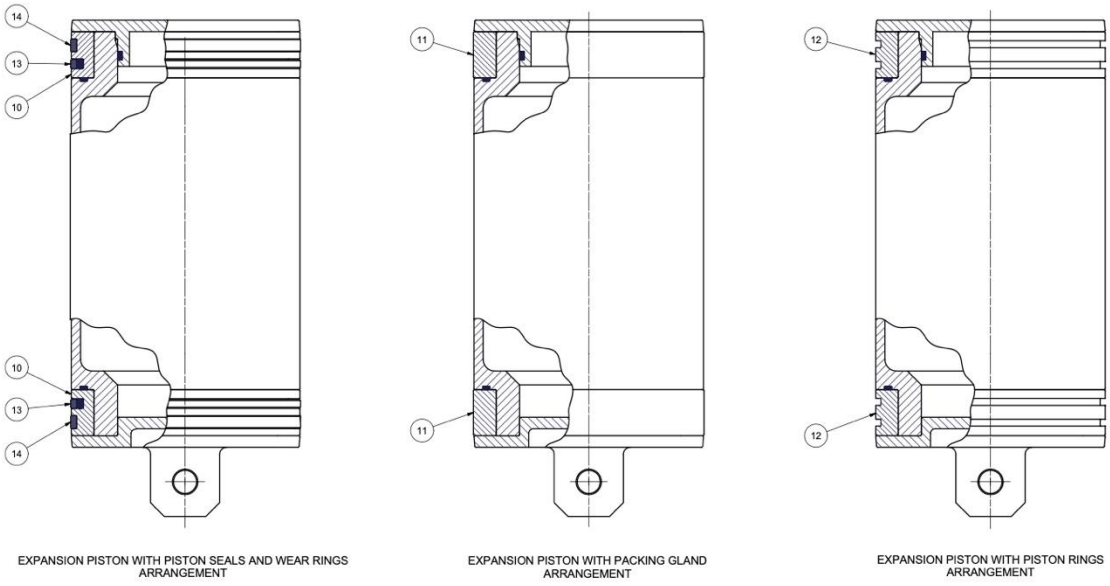

Figure 5-7 Section of 'Sub Assembly of Expansion Piston' technical drawing produced by the University of Southampton EDMC for this project. Section highlights the piston design and available sealing options. (10) = Piston sealing mechanism housing. (11) = Piston PTFE packing. (12) = Piston ring housing. (13) = Energised PTFE ring. (14) = Wear ring.

The sealing options are:

1. Conventional piston rings. These can be sourced for the 100mm cylinder bore and grooves machined as necessary.
2. PTFE piston ring and energised o-ring. The o-ring sits behind the piston ring and can be compressed with shims to give desired force pressing the PTFE piston ring against the cylinder wall. PTFE is used for low friction. Trelleborg Turcon Glyd Rings were specified in the standard component item list (Trelleborg, na).
3. Use of PTFE packing tape. This is the least preferred option but can be used as a last resort, shown to be effective on the Mk.III engine.

The piston was also specified to be manufactured out of aluminium, to be lightweight and cost effective, and to be given a hard anodised coating for wear and corrosion resistance. The coating of the cylinder bore and piston eliminates concern of potential friction between similar metals, discouraged by the UoS EDMC during design phase communication. Importantly, the piston diameter was also reduced to give greater clearance to the cylinder wall to prevent jamming. In the absence of an industry standard, a clearance of 0.5mm was chosen in consultation with the EDMC design engineers.

5.2.2.3 Frame, Bearings, and Crank Shaft

The frame was designed using upright plates on the Mk.IV engine, as seen in Figure 5-5. Housings in the plates enabled use of multiple bearings to improve stability, an issue on the Mk.III engine. Dowels in the plates allowed accurate alignment to prevent loss of power through unnecessary friction. The frame design also allows for the modular nature of the Mk.IV engine. Additional upright plates can be added to the existing frame structure to house the necessary extra bearings and crank shaft sections, allowing additional cylinders to be added.

The crank shaft was designed to allow additional sections to be added, completing the modular design. The other key improvement to the power take-off was use of a more traditional crank shaft and piston rod connection. For example, counterweights are used opposite the piston rod connection point to ensure the centre of gravity remains in the middle of the shaft for better stability than that experienced on the Mk.III engine.

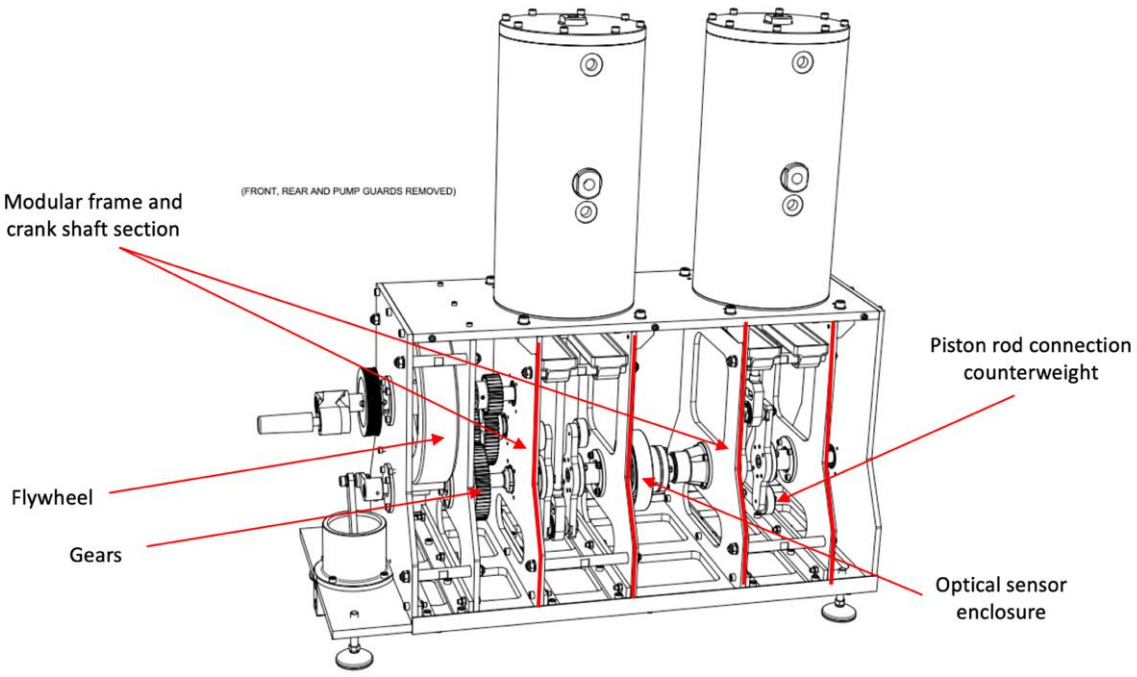

Figure 5-8 Section of 'Assembly of MK.IV Condensing Engine' technical drawing produced by the University of Southampton EDMC for this project. Section annotated to show modular nature of design as well as highlight key crankshaft components.

Figure 5-8 above shows the part of the technical assembly drawing for the Mk.IV condensing engine. It has been annotated to highlight the modular sections which can be repeated to increase the number of cylinders used in the engine. It also indicates key crank shaft details, such as the counterweight mentioned above as well as the flywheel and gearing system. Finally, the figure also highlights the optical sensor enclosure for the control system taken from the previous iteration.

5.2.2.4 Vacuum Pump

The Mk.IV vacuum pump cylinder was specified to be manufactured from aluminium with hard anodised coating, the same as the expansion cylinder. The vacuum pump piston was specified to be manufactured from Acetal plastic. Energised piston rings, like those specified from Trelleborg for the expansion piston, were chosen to seal the pump. The main change to the pump design compared to the Mk.III engine was the outlet port being located on the bottom. This should allow for improved evacuation, aided by gravity, and therefore improved partial vacuum generation within the system. This is shown in Figure 5-9.

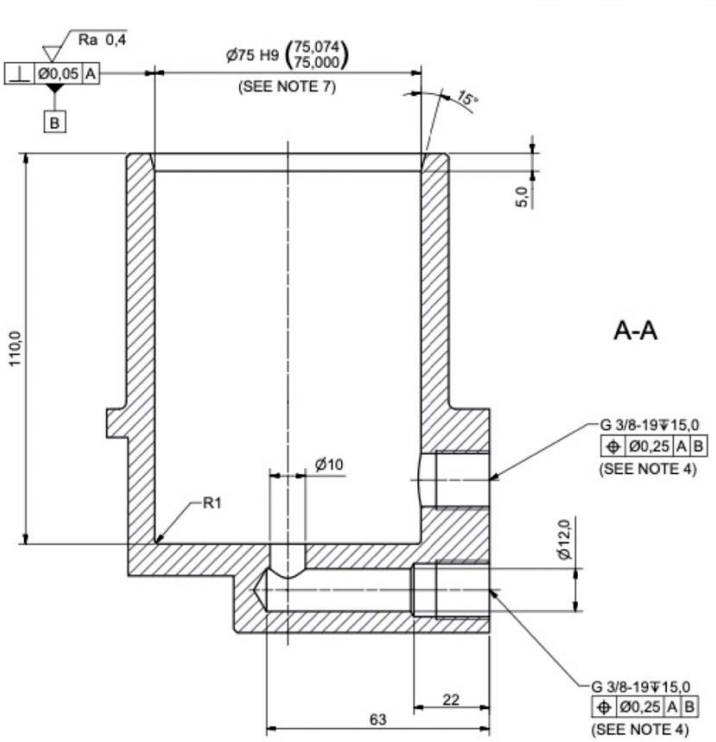

Figure 5-9 Section of 'Sub Assembly of Expansion Cylinder' technical drawing produced by the University of Southampton EDMC for this project. Section highlights the pump outlet being aided by gravity via connection to the bottom surface of the cylinder bore. See full drawing for note details, signposted in Chapter 9.

5.3 Conclusions

The next iteration of the single acting uniflow condensing engine, the Mk.IV, has been designed and built as part of a collaboration to create a combined system for water purification and energy production. Conclusions can be made about both the design itself and the integration of the engine:

- Primary focus is synergy of steam supply and demand, managed by equipment design and control regime.
- A steam bypass is required where steam supply could exceed demand. This requires further optimisation on future projects to recover the thermal energy lost to the bypass.
- The condensing engine steam expansion ratio can be increased to reduce steam demand when supply drops, allowing the engine to maintain a constant speed. This is a novel discovery for the control of the engine and an additional benefit of steam expansion not seen in literature.

Some key Mk.IV engine design points are also summarised below:

- The Mk.IV engine was designed in a single acting uniflow configuration following the success of the Mk.III engine.
- The Mk.IV engine was designed to produce a realistic 110W – 180W mechanical power output using expected isentropic efficiencies. This was only possible following the Mk.III prototype testing.
- The Mk.IV engine design is modular. This is novel and gives greater flexibility to future scale up and commercialisation.
- The Mk.IV engine uses two-cylinders out of phase to provide a more stable steam demand and allow increased power output and engine speeds.
- The Mk.IV engine is designed with multiple ports to improve steam evacuation and resulting engine performance, as suggested following Mk.III testing.
- The Mk.IV engine design introduced use of aluminium cylinders and piston for reduced cost and weight, with coated cylinder bores for wear resistance and reduced friction.

Testing of the Mk.IV engine was out of the scope of this thesis as it is part of an ongoing project. Engine data will allow further commentary on the suitability of the design and for further improvements to be proposed for the next iteration. In the absence of this data, the Mk.IV design is considered to be the optimum single acting uniflow condensing engine design currently available in literature.

Chapter 6 Condensing Engine Heat Recovery and Re-Use

The literature review introduced the concept of heat recovery on the condensing engine as well as the results of tests performed during Mk.II engine development. These previous tests were unsuccessful, and discussion of results in the literature review identified the following questions to be answered as part of this research:

1. Is there significant enough energy available for recovery during steam condensation, specifically at higher engine expansion ratios?
2. Can heat recovery be successfully achieved during steam condensation at a high enough temperature for re-use without negatively affecting engine performance?
3. What are the theoretical increases in performance achievable through re-use of the recovered thermal energy?

Firstly, a theoretical analysis was performed to predict energy availability during steam condensation at different expansion ratios. To do so, a concept for heat recovery using a two-stage condensation process was proposed. Secondly, an experiment was performed to show successful proof of concept of heat recovery using a two-stage condensation process. Finally, the theoretical analysis was extended to include heat re-use. To do so, a further concept for heat re-use was proposed, driving a second sub-atmospheric cylinder stage. This work is detailed in this chapter.

6.1 Heat Recovery Potential: Theoretical Analysis

6.1.1 Heat Recovery Concept: Two-Stage Condensation

The previous work attempted to both recover thermal energy and fully condense the steam in a single heat exchanger split into two sections using different sets of copper coils. The recovery of latent heat was expected to occur in the top section and condensation of residual steam in the bottom section. During testing, preferential condensation of steam occurred in the lower section inhibiting heat recovery. If heat recovery was maximised in the bottom section, by reducing cooling water flow rates, it resulted in insufficiently low pressures to effectively drive the CE. This has been discussed in the literature review.

To solve this problem, this research focusses on a two-step condensation process, as shown in Figure 6-1, using two separate pieces of heat exchanger equipment. Firstly, an intermediate heat exchanger achieves partial condensation of steam allowing recovery of the latent heat to take place. Being a separate piece of equipment allows a larger heat transfer area to be used and a longer residence time of steam in the heat recovery section. This is shown in Figure 6-1 as a flat plate heat exchanger (FPHE), identified in the literature review as an ideal option to encourage removal of condensate from the unit and prevent re-evaporation under vacuum. Residual wet steam subsequently passes into the final condensation stage (CON1) where total condensation is achieved to maintain the sub-atmospheric pressures needed to drive the condensing engine. The FPHE cooling water inlet can have a higher starting temperature and lower flow rate than that used in the condenser to ensure the FPHE outlet water temperature is of a high enough quality for re-use following latent heat recovery. This allows the condenser to maximise heat transfer by using faster water flow rates at lower temperatures.

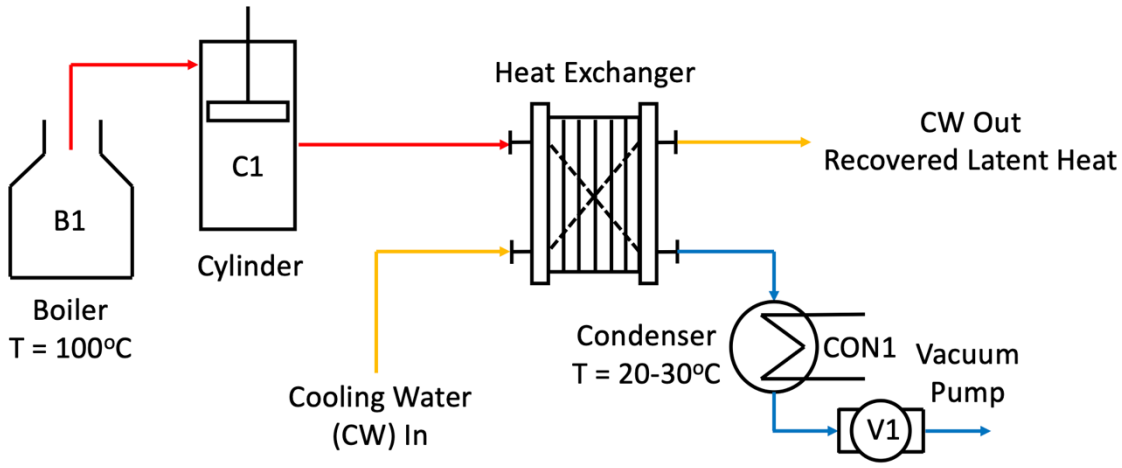

Figure 6-1 Schematic for proposed condensing engine two-stage heat recovery. B = Boiler. C = Cylinder. CON = Condenser. V = Vacuum Pump. CW = Cooling Water.

Two factors limit the energy available for recovery in this setup. Firstly, it is expected that an efficient condensing engine will be operated with steam expansion, already discussed at length in this thesis. In doing so, the expanded steam supplied to the intermediate FPHE is of a lower temperature and pressure, limiting potential for latent heat recovery. This is a characteristic of heat recovery on the condensing engine, the effect of which has not before been understood.

Secondly, as steam condenses, the pressure inside the FPHE will reduce. This is the phenomena which drives the condensing engine and is caused by the pulsed nature of steam flow. The new pressure subsequently sets a new saturation temperature for the remaining steam. Thus, the saturation temperature of the steam inside the FPHE is continually falling during condensation.

When the steam inside the FPHE reaches a saturation temperature equal to the temperature of the FPHE cooling water inlet, no further condensation can occur. Therefore, using a higher cooling water inlet temperature to maximise outlet temperature limits the range of thermal energy that can be recovered.

The theoretical analysis which follows has investigated the effect of both increasing expansion ratios and higher FPHE cooling water inlet temperatures on energy available for recovery. The aim of this work was to satisfy that despite these factors, sufficient energy remains available for recovery and re-use on the atmospheric condensing engine.

6.1.2 Heat Recovery Mathematical Model Method

The theoretical model was built in MATLAB using XSteam data tables (Holmgren, 2007). The model operates on a 1kg basis of steam entering the first cylinder (C1). It was assumed that boiler (B1) temperature was 100°C and condenser (CON1) temperature was 20°C. An intermediate FPHE cooling water inlet temperature of 50°C - 70°C was studied using the model, chosen to allow a sufficiently high outlet temperature. Expansion ratios from n = 1 to n = 5 were tested during analysis. Expansion ratios higher than this are not expected to be used with heat recovery due to the associated reduction in steam quality exiting the cylinder.

Energy available for recovery in the FPHE is calculated using Equation (6.1). Enthalpy can be calculated using Equation (6.2). The FPHE inlet enthalpy term is defined by the cylinder expansion ratio and the resulting outlet steam conditions. The FPHE outlet enthalpy term is defined by the cooling water inlet temperature. Expected outlet dryness fractions were understood by plotting the process cycle on T-s charts, see Chapter 9, and the values defined as inputs in the model for the relevant cases tested. Therefore, these terms allow Equation (6.1) to account for the effect of expansion ratio and cooling water inlet temperature on the energy available for recovery.

$$E_a = m_s \times (h_{FPHE,in} - h_{FPHE,out}) \tag{6.1}$$

$$h = (h_g \cdot x) + h_l(1 - x) \tag{6.2}$$

Where:

- E_a is energy available for recovery (kJ).
- m_s is mass of steam (kg).
- $h_{FPHE,in}$ and $h_{FPHE,out}$ are FPHE steam inlet and outlet enthalpy respectively (kJ/kg).
- h_g and h_l are water vapour and liquid enthalpies at relevant conditions respectively (kJ/kg).
- x is steam dryness fraction.

To understand the available energy as a percentage of the input energy, the thermal energy required to raise the steam in the boiler is also calculated using Equation (6.3). The percentage available for recovery is found by calculating the ratio of answers obtained from Equation (6.1) and Equation (6.3). This analysis normalises the results of this work and allows them to be applied to any scale of engine.

$$Q_{in} = (h_{g,b} - h_{l,b}) \times m_s \tag{6.3}$$

Where:

- Q_{in} is the thermal energy input (J).
- $h_{g,b}$ is enthalpy of steam at boiler conditions (kJ/kg).
- $h_{l,b}$ is enthalpy of liquid at boiler feed conditions (kJ/kg).

An initial analysis assuming a boiler steam dryness fraction of x = 1, i.e. totally dry saturated steam, is presented in Section 6.1.3. This represents an ideal theoretical case. A sensitivity analysis investigating the effect of boiler steam dryness fraction is analysed in Section 6.1.4.

6.1.3 Heat Recovery Model Results, Analysis & Discussion

Figure 6-2 shows the theoretical thermal energy available for recovery during condensation of 1kg of steam for different FPHE cooling water temperatures and cylinder expansion ratios. Figure 6-3 shows the energy available as a percentage of the boiler input energy. Boiler and condenser temperatures of 100°C and 20°C were assumed respectively. These results have been modelled using an assumption of totally dry saturated steam exiting the boiler, x = 1, and therefore represent an ideal theoretical case. This is important to understand the maximum energy available for recovery. A sensitivity analysis investigating the effect of boiler steam dryness fraction is analysed in Section 6.1.4.

Energy available for recovery reduces with increasing expansion ratio and increasing cooling water temperature, as expected. This is due to the narrowing of the enthalpy band in Equation (6.1). Energy available for recovery has been shown to be significant, with as much as 75% of input energy being theoretically recoverable in the case without expansion and cooling water inlet of 50°C.

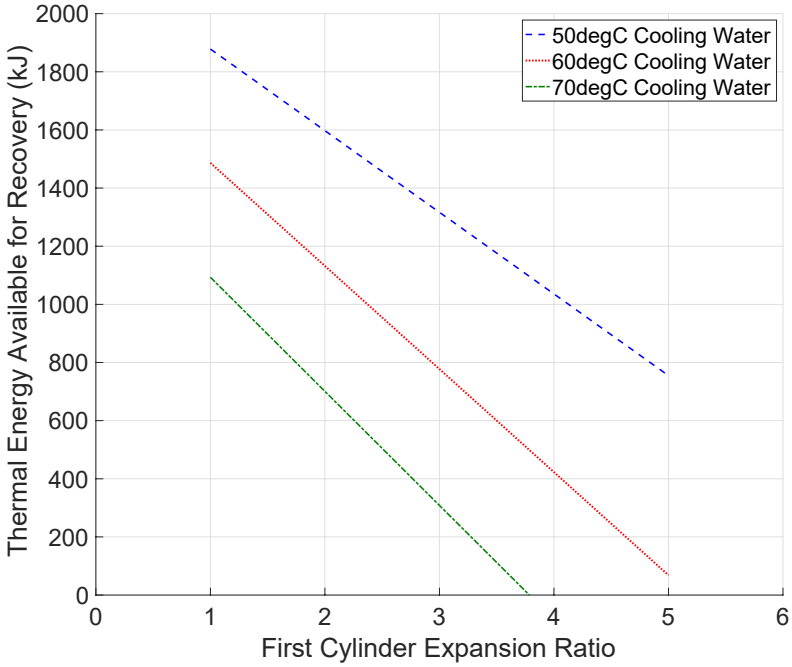

Figure 6-2 Thermal energy available for recovery during condensation of 1kg of steam. Results shown for different FPHE cooling water temperatures and engine expansion ratios. Boiler temperature of 100°C and condenser temperature of 20°C assumed.

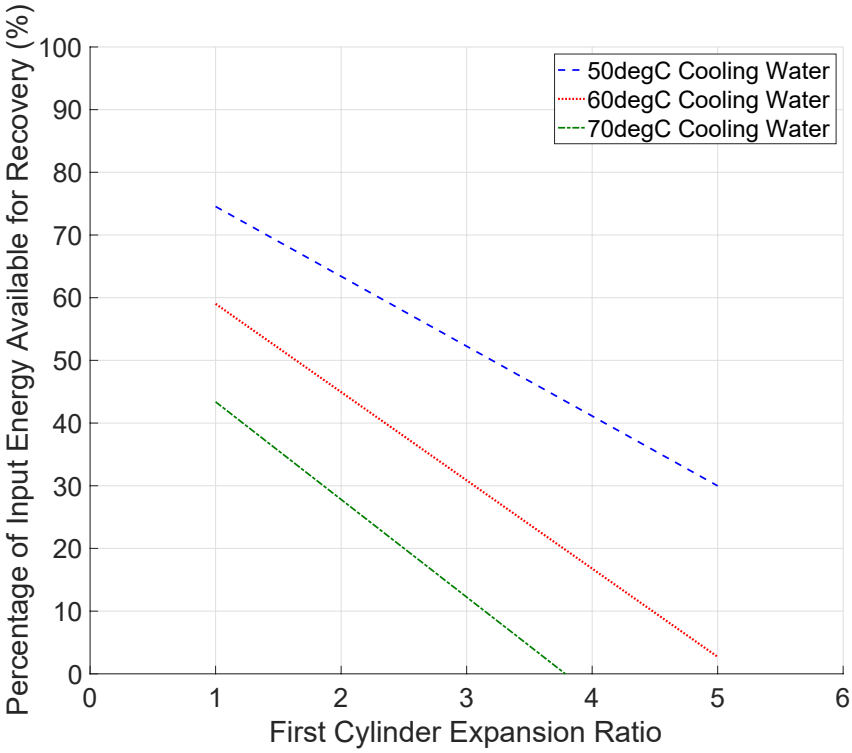

Figure 6-3 Thermal energy available during heat recovery as a percentage of input energy for different intermediate cooling water temperatures and expansion ratios. Boiler temperature of 100°C and condenser temperature of 20°C assumed.

It is expected that expansion on a practical engine will not increase much beyond a ratio of n = 4 due to the response time required by the valves and cooling losses in the cylinder where thermally insulating materials or a steam jacket are not present. In this scenario, as much as 1000kJ of energy is theoretically available for recovery from each kilogram of working steam, accounting for 40% of input energy according to the line of best fit. This analysis justifies that heat recovery is worthwhile on the condensing engine, even when operating with expansion.

The analysis also suggests that a FPHE cooling water inlet temperature of 50°C would be the optimum of those tested. A cooling water inlet temperature of 60°C reduces the available energy for recovery. A cooling water inlet temperature of 70°C limits the cylinder expansion ratio to a value of n < 4 due to steam saturation temperature being too low. This analysis highlights cooling water inlet temperature as an important characteristic when optimising the proposed system.

6.1.4 Heat Recovery Steam Dryness Fraction Sensitivity Analysis

The results reported in Section 6.1.3 assumed a boiler steam dryness fraction of x = 1 in the mathematical model, i.e. totally dry saturated steam. Whilst the author has considered this a suitable assumption in the thesis to this point, for example in the uniflow engine modelling, this has been because use of isentropic equations has meant an idealised case was already being evaluated. Isentropic equations represent a maximum value that cannot be achieved in practice, allowing for a totally dry saturated steam to be assumed. However, the analysis in Section 6.1 aims to evaluate a realistic energy available for recovery in the intermediate heat exchanger. Therefore, the assumption of totally dry steam may not be valid in all cases. The steam dryness fraction is defined as the ratio of the weight of dry steam to the weight of the total steam mass including any entrained water, see Equation (6.4). In reality, water droplets will be entrained in the steam when leaving the boiler. Additionally, any thermal losses from the steam during its transportation in pipework and through valves can result in small amounts of condensation. These effects will cause a reduction in steam dryness fraction (Bosch, 2023) and as a result a reduction in steam enthalpy. The effect of boiler steam dryness fraction on condensing engine efficiency has already been shown by Bortolin, et al. (2021) in Figure 2-16.

$$x = \frac{m_g}{m_{tot}} \tag{6.4}$$

Where:

- x is the steam dryness fraction.
- m_g is the mass of the gaseous/vapour fraction of the steam (kg).
- m_{tot} is the total mass of the steam (kg).

Literature pertaining to steam use in industry gives an indication of steam dryness fractions achievable in practice. For example, steam sterilisation literature suggests that a steam dryness fraction below $x = 0.90$ is considered as 'wet' steam, which will hold less energy than dry steam and therefore is typically not used (Mechler, 2022). An accepted value for steam dryness fractions for use in sterilisation is given as $x = 0.95$ or above (Mechler, 2022). Bosch, a boiler manufacturer, suggest that saturated steam has a technical standard of $x = 0.97$ or greater (Bosch, 2023). SpiraxSarco, a steam solutions expert, state that most shell and tube type boilers can produce steam with dryness fractions of $x = 0.95$ to $x = 0.98$ (SpiraxSarco, 2023). These high steam dryness values hold true for solar steam generation projects reported in literature, directly relevant to the condensing engine as discussed in Chapter 5, all achieving steam dryness fractions of $x > 0.95$; for example (Mustafa & Hadi, 2021; Kamboj, et al., 2019; Jamil & Hassan, 2019).

It is expected that optimised condensing engine projects should achieve similar steam dryness fractions entering the cylinder to those quoted above. This can be achieved by using a separator to remove entrained water at the boiler outlet as well as properly lagged pipework and valving between the boiler and cylinder. Therefore, a sensitivity analysis was performed testing boiler steam dryness fractions from $x = 1.0$ to $x = 0.9$ by changing the associated input in the mathematical model. The model calculations estimate the associated steam dryness fraction exiting the cylinder after expansion and therefore the enthalpy of steam entering the FPHE. The FPHE outlet enthalpy was calculated using steam dryness fractions already inputted from the T-s chart analysis, see Chapter 9, limited by the cooling water inlet temperature. These range from $x = 0.85$ to $x = 0.25$ depending on the extent of achievable condensation and can be found in the model script available in this project's data repository. This method allowed the new energy available for recovery in the FPHE at reduced boiler steam dryness fractions to be assessed. This was tested for expansion ratios of $n = 1$ to $n = 5$, a FPHE cooling water inlet temperature of 50°C, boiler temperature of 100°C, and condenser temperature of 20°C. Figure 6-4 shows the energy available for recovery from 1kg of steam. Figure 6-5 shows the energy available for recovery as a percentage of the boiler thermal energy input.

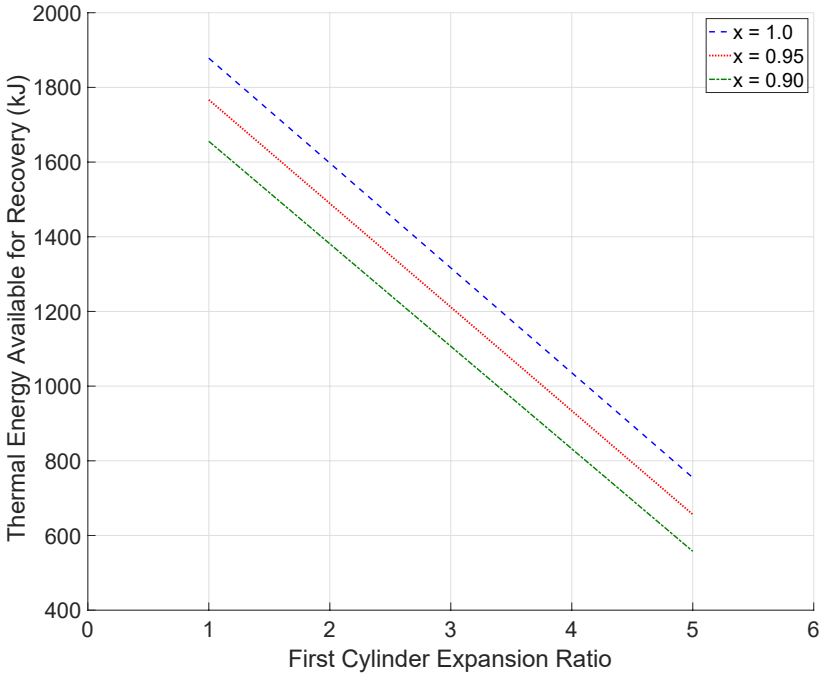

Figure 6-4 Energy available for recovery from 1kg of steam for different boiler steam dryness fractions and expansion ratios. Assumed boiler and condenser temperatures of 100 °C and 20°C. FPHE cooling water temperature of 50°C.

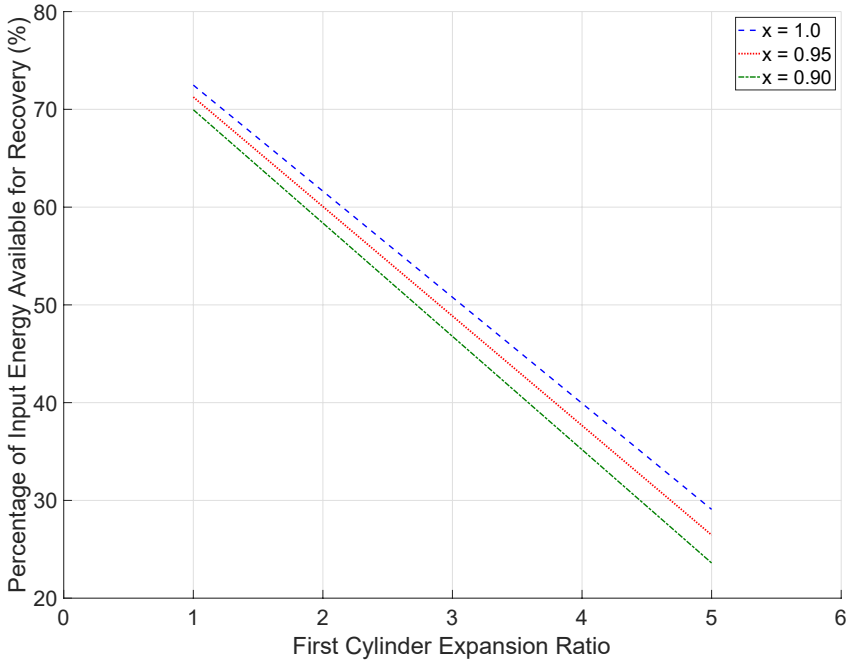

Figure 6-5 Energy available for recovery as a percentage of boiler thermal energy input for different boiler steam dryness fractions and expansion ratios. Assumed boiler and condenser temperatures of 100 °C and 20°C. FPHE cooling water temperature of 50°C.

According to Figure 6-4, as boiler steam dryness fraction reduces the energy available for recovery during heat exchange also reduces, as expected. At an expansion ratio of n = 4, reducing the boiler steam dryness fraction from x = 1.0 to x = 0.9 reduces the energy available for recovery by 17%. However, by reducing the boiler steam dryness fraction the energy required in the boiler is also reduced as less water is converted to steam. This is because it was assumed that the reduction in steam dryness was a result of steam carrying water droplets out of the boiler and not due to condensation of steam in the pipework, which could be mitigated with lagging and would require more complex modelling to fully understand. As a result, Figure 6-5 shows that the reduction in boiler steam dryness fraction has reduced effect on the fraction of the thermal energy input available for recovery in the heat exchanger. At an expansion ratio of n = 4, reducing the boiler steam dryness fraction from x = 1.0 to x = 0.9 reduces the boiler thermal input energy available for recovery in the heat exchanger by 9.5%. Whilst not an insignificant value, this analysis finds that even at steam boiler dryness fractions of $x < 1$, there is still sufficient energy available for recovery at higher cooling water temperatures and expansion ratios to justify further investigation into the concept.

However, it is acknowledged by the author of this research that the model described throughout Chapter 6 for the assessment of heat recovery and re-use on the condensing engine presents a simplified case. This was to allow for the analysis to be accommodated within the wider scope of this project and provide insight into the potential of the concept. Specifically, the author notes that the FPHE outlet steam dryness fraction is treated as a fixed point in the model to simplify the analysis and was unchanged when simulating boiler steam dryness fractions of $x < 1$. This could be improved upon in future work by modelling the problem more accurately, considered outside the scope of this work, for example by using real gas data as performed by Bortolin, et al. (2021); see Section 2.3.3. Figure 2-16 shows that at an expansion ratio of n = 4, the condensing engine efficiency reduces by approximately 15% when boiler steam dryness fraction reduces from x = 1.0 to x = 0.9, as modelled by Bortolin, et al. (2021) using real gas data. This is similar to the reduction in energy available in the steam for recovery estimated by this research, of which the engine efficiency is a function. This could support the work presented in this section. However, until more accurate modelling is performed and a more thorough comparison conducted, the values calculated by this sensitivity analysis should not be taken directly but instead used to demonstrate the significant potential of heat recovery on the condensing engine.

6.1.5 Heat Recovery Potential Conclusions

A two-stage condensation process using a FPHE has been proposed for improved heat recovery on the condensing engine. It was identified that the amount of energy available for recovery is

affected by cylinder expansion ratio and FPHE inlet cooling water temperature. These parameters were investigated in a theoretical model, testing cooling water inlet temperatures of 50°C - 70°C and expansion ratios of n = 1-8. Key conclusions drawn were:

- A FPHE cooling water inlet temperature of 50°C was the optimum of those tested, with a temperature of 60°C reducing available energy for recovery and a temperature of 70°C limiting expansion ratios that could be used in the cylinder.
- Without steam expansion as much as 75% of boiler input energy is theoretically available for recovery in the FPHE, when operating with cooling water inlet temperature of 50°C and fully saturated boiler steam.
- At a realistic cylinder expansion ratio, chosen as n = 4, as much as 40% of boiler input energy is still theoretically available for recovery in the FPHE with a cooling water inlet temperature of 50°C and fully saturated boiler steam.
- Sensitivity analysis tested steam dryness fractions down to x = 0.9, concluding that at an expansion ratio of n = 4 the energy available for recovery reduced by 17% and the boiler thermal energy input available for recovery reduced by 9.5%. However, more accurate modelling using real gas data has been identified as necessary, and the results of the sensitivity analysis in this thesis should be taken with caution until corroborated.
- This work justified the significant potential of heat recovery on the condensing engine using the proposed two-stage condensation process.

6.2 Heat Recovery Tests: Proof of Concept

The experimental proof of concept was developed using the two-stage condensation concept illustrated in Figure 6-1, building on the theoretical analysis outlined above. The aim of this experimental work was to demonstrate that the proposed heat recovery concept can successfully recover latent heat during steam condensation without negatively impacting condensing engine performance. Following the review of previous work, three important criteria were required to be met to deem proof of concept a success:

1. Suitably high heat recovery efficiency in the intermediate FPHE.
2. Sufficiently high FPHE outlet water temperature to allow re-use at a high energy quality.
3. Partial vacuum to be maintained in the system throughout, suitably low for effective operation of the condensing engine.

All three must be met for heat recovery to be viable in practice on the condensing engine. This had not before been achieved and constitutes a novel development of the knowledge.

6.2.1 Heat Recovery Test Method

6.2.1.1 Experimental Rig Description

The proof-of-concept setup was developed as a standalone experiment, as shown in Figure 6-6. The boiler was reused from the Mk.III engine tests to supply steam to the experiment. The steam was pulsed into the heat exchanger at atmospheric pressure, using an electronically controlled solenoid valve (SV1), to replicate the conditions in the engine. It is acknowledged that the pulse profiles created in this experiment differ from those on the condensing engine, with the former having a constant flow of steam whilst the valve is open due to the constant supply from the boiler and the latter having a reducing flow rate of steam to the heat exchanger due to the reducing pressure in the cylinder. However, this experiment matches engine conditions as closely as possible without testing on an actual engine. Testing on a condensing engine was deemed unfavourable at this stage due to the added complexity and risk of engine performance effecting the experiment. The solenoid valves selected for the Mk.III engine tests were used during this experiment. Pressure was measured at boiler outlet (P1) and FPHE inlet (P2) to allow steam flow rate to be calculated using *Bernoulli's* equation and to understand system pressures.

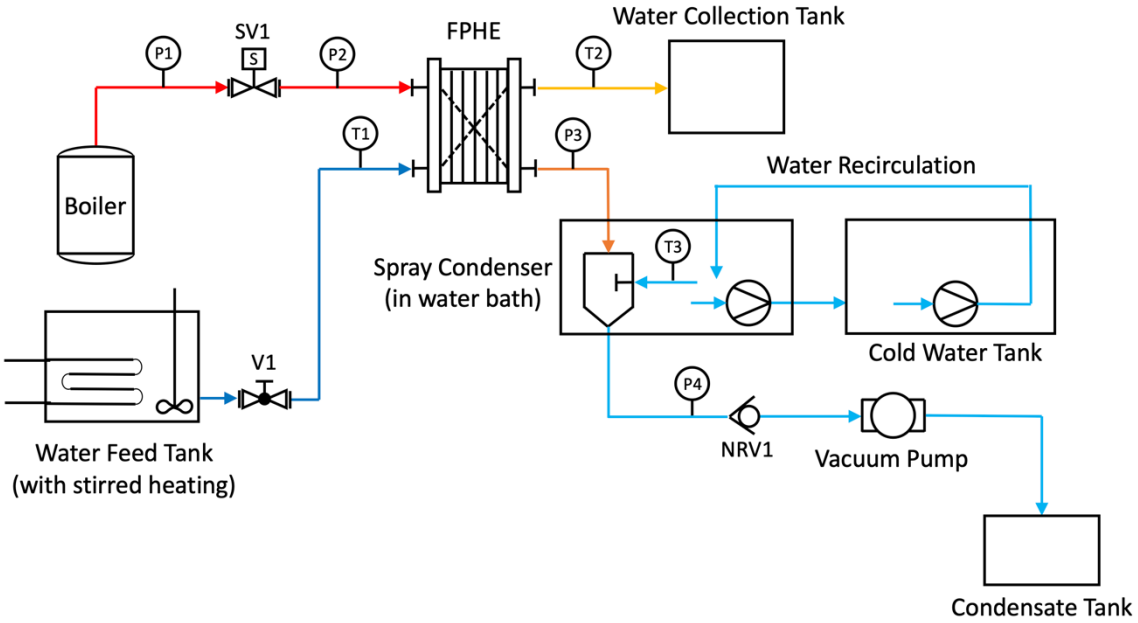

Figure 6-6 Process diagram of the heat recovery experimental setup. SV = Solenoid valve. V = Valve. NRV = Non-Return Valve. FPHE = Flat Plate Heat Exchanger. T = Temperature. P = Pressure. Line colour indicates temperature (red = hot, blue = cold).

A custom FPHE was designed to act as the intermediate heat exchanger for this experiment. This type of heat exchanger uses a series of plates to create channels for fluid media to pass through. Hot and cold heat transfer media pass via alternate channels, transferring heat through the plate.

As a result, the FPHE can achieve truer counter-current flow and are easier to maintain and inspect compared to alternative options. The FPHE design is discussed in greater detail in Section 6.2.1.2. Fouling of the heat exchanger was not considered to be an issue by the author of this research. Instead, it was assumed that fouling would be a concern in the boiler where evaporation takes place and TDS concentrations increase. This was mitigated by using boiler blow down procedures, performed by replacing water in the boiler when it reached low levels. However, material and surface coating selections were made for the Mk.III and MK.IV condensing engines to provide corrosion resistance, for example hard anodising the cylinder bore. Therefore, future heat recovery heat exchangers on the condensing engine could employ the same corrosion resistance, if found to be required, with a pre-requisite that heat exchange effectiveness is not negatively impacted.

The cooling water was heated to 50^{o}C in the supply tank, chosen following the analysis performed in Section 6.1. The cooling water flow rate, achieved by storing the water tank at a raised height of around 1m above FPHE water inlet, was controlled using a manually operated gate valve (V1) adjusted according to flow rate measurement and desired operation. The water flow rate was measured manually at the FPHE outlet by recording the time taken to fill a known volume. A thermocouple was used to measure FPHE outlet water temperature (T2).

The pressure of the wet steam exiting the FPHE (P3) was measured to understand condensation pressure. The wet steam entered the second and final condensation phase, a spray condenser re-used from preliminary Mk.II engine tests (Muller, et al., 2018). Water was supplied to the spray condenser from a primary water bath. Two water baths with pumping were used to achieve mixing and minimise water bath temperature. A thermocouple (T3) was used to monitor primary water bath temperature for interest.

Finally, the condensate was evacuated from the system using an electronic vacuum pump. Whilst use of an electronic pressure reduction device seems counterintuitive in an experiment measuring pressure as a key performance indicator, in this instance the vacuum pump is acting as an ideal condensation and pumping stage, the effects of which could be realised in practice on an optimised condensing engine.

Two microcontrollers were also used. The first controlled the solenoid valve timing using a basic code. The timing could be adjusted by the operator to reduce the effective steam flow rate. The second recorded pressure and temperature data to an SD card for analysis. Key equipment data is given in Table 6-1. Pressure transducers and thermocouples were re-used from previous testing, as discussed in relation to the Mk.III engine tests.

Table 6-1 Heat recovery experiment equipment list.

Equipment	Parameter	Value
Boiler	Rated Power	1.8kW
Solenoid Valve	Internal Orifice Diameter	11mm
Water Heater	Rated Power Maximum Temperature Resolution	1.2kW 95°C +/- 0.1°C
Pressure Transducer	Type Pressure Range Operating Temperature Accuracy	RS Pro 797-4970 -1 to +9 bar(g) -200 to +135°C +/- 0.25%
Thermocouple	Thermocouple Type Conditioner Type Thermocouple Accuracy Conditioner Accuracy Combined Accuracy	RS Pro 334-2622 K-type Adafruit AD8495 +/- 1.5°C +/- 2.0°C +/- 2.5°C
Spray Condenser	External Surface Heat Transfer Area	0.03 m^2
FPHE	End Plates # / Material Heat Transfer Plate # / Material Number of Channels Total Heat Transfer Area	2 / Perspex 9 / Aluminium 10 0.13m^2
Microcontroller	Controller Type SD Card Shield Type	Arduino Mega 2560 Seeed Studio SD Card Shield V4.0
Vacuum Pump	Type Rated Vacuum	Zerone VN-C4 -85 kPa

6.2.1.2 Flat Plate Heat Exchanger Design

The design of the FPHE for intermediate heat recovery on the condensing engine was not trivial. This is because the heat exchanger performs the condensation of a pulse of steam. As the pulse of steam is condensed a partial vacuum is created and the pressure inside the system drops. As the

steam's saturation temperature is dependent on pressure this results in a changing saturation temperature.

As a result, an arbitrary FPHE design of 9 heat transfer plates, 2 end plates, and 10 channels was chosen. This gave a heat transfer area of approximately 0.13m^2. An arbitrary value was deemed appropriate given the unknown accuracy of traditional theory. However, theory was still used to corroborate the arbitrary design to give confidence in the experiment. This was performed using the effectiveness-NTU (e-NTU) method (Lee, 2019). This method can be used when there is insufficient information to calculate the log mean temperature difference across the heat exchanger (Lee, 2019), true in this case as intermediate temperatures were not defined. The e-NTU method defines the area required by a heat exchanger using Equation (6.5) (Lee, 2019).

$$A_{ht} = \frac{NTU \times C_{min}}{U} \tag{6.5}$$

Where:

- A_{ht} is heat transfer area required (m^2).
- *NTU* is the dimensionless 'Number of Transfer Units' required.
- C_{min} is the minimum heat capacity rate (J/K).
- *U* is the overall heat transfer coefficient (W/m^{2}K).

Several correlations for the value of NTU exist. This research chose the relationship representing a counter flow heat exchanger, as shown in Equation (6.6) (Lee, 2019).

$$NTU = \frac{1}{1 - C_r} \ln\left(\frac{1 - \varepsilon C_r}{1 - \varepsilon}\right) \tag{6.6}$$

Where:

- C_r is the heat capacity rate ratio, see Equation (6.7). This is the ratio of C_{min} over C_{max}, the minimum and maximum values of the hot and cold side heat capacity rates, see Equation (6.8).
- ϵ is the heat exchanger effectiveness, defined as the ratio of recovered energy to available energy and chosen to be 70% in this research as an initial target.

$$C_r = \frac{C_{min}}{C_{max}} \tag{6.7}$$

$$C_{cold/hot} = m_{cold/hot} \cdot Cp_{cold/hot} \tag{6.8}$$

Where:

- m is the mass of either cold or hot side fluid (kg).
- C_p is the specific heat capacity of either cold or hot side fluid (J/kg K).

The overall heat transfer coefficient, ignoring the effects of fouling, is given as Equation (6.9).

$$U = \frac{1}{\frac{1}{h_{t,c}} + \frac{1}{h_{t,h}} + R_w} \tag{6.9}$$

Where:

- $h_{t,c}$ and $h_{t,h}$ are the cold and hot side heat transfer coefficients respectively (W/m^{2}K).
- R_w is the thermal resistance of the heat transfer plate (m^{2}K/W).

Heat transfer coefficients were found from the relevant *Nusselt* number correlations, see Equation (6.10).

$$h_t = \frac{Nu \times k}{L} \tag{6.10}$$

Where:

- Nu is the dimensionless *Nusselt* number.
- k is the thermal conductivity of the fluid (W/m.K).
- L is the length/height of the heat transfer area of the designed plate (m).

Assessment of the *Reynold*s number of the expected water side flow suggested laminar flow. Therefore, the relevant *Nusselt* number correlation was used to estimate the water side heat transfer coefficient, see Equation (6.11) (Lee, 2019). This required knowledge of the *Reynolds* and *Prandtl* numbers, defined in Equations (6.12) and (6.13).

$$Nu_{lam} = 0.664 Re^{\frac{1}{2}} Pr^{\frac{1}{3}} \tag{6.11}$$

$$Re_L = \frac{\rho u L}{\mu} \tag{6.12}$$

$$Pr = \frac{\mu C_p}{k} \tag{6.13}$$

Where:

- C_p is the specific heat capacity of the fluid (kJ/kg.K).
- u is the velocity of the fluid (m/s).

However, condensation occurs on the hot (steam) side of the heat exchanger. Therefore, a relevant *Nusselt* number correlation is required. In this case, the *Nusselt* correlation given for film wise condensation on a flat plate was used (Rose, 1988), see Equation (6.14).

$$Nu_{cond} = 0.943 \left[\frac{\rho_l(\rho_l - \rho_v) g h_{lg} L^3}{k_l \mu_l (\Delta T)} \right]^{\frac{1}{4}} \quad (6.14)$$

Where:

- ρ_l and ρ_v are the density of condensate and vapour respectively at relevant bulk fluid temperature (kg/m^3).
- g is acceleration due to gravity (m/s^2).
- h_{lg} is the enthalpy of vaporisation at relevant bulk fluid temperature (kJ/kg).
- k_l is the conductivity of the condensate at relevant bulk fluid temperature (W/m.K).
- μ_l is the viscosity of the condensate at relevant bulk fluid temperature (Pa.s).
- ΔT is the difference between the steam bulk average temperature and the wall temperature (°C).

Calculation in Chapter 9 used the e-NTU method to confirm suitability of the chosen FPHE dimensions by estimating steam flow rate based on operation at an expansion ratio of n = 1 and speed of 60rpm, relating the experimental work back to the condensing engine. It was assumed that an effectiveness of 0.7 was to be achieved, recovering 0.17kW of heat. This assessment assumed that steam would have a minimum outlet temperature of 50°C, as any lower and the inlet cooling water in the experiment could not achieve heat exchange, and therefore a bulk temperature of 75°C would be present. Water temperature was assumed to enter at 50°C and be heated to 70°C, as an estimation. Heat transfer wall temperature was estimated as the average of the four inlet and outlet temperatures. This analysis found that a heat transfer area of 0.04m^2 would be suitable for this experiment, well below the 0.13m^2 of the chosen design. Whilst this theoretical method was considered to have significant margin of error, the much greater actual heat transfer surface area compared to theoretical gave confidence in the design.

The plates were designed to have a smooth surface to encourage condensate removal from the channels, preventing re-evaporation under sub-atmospheric pressure between steam pulses. The steam side heat transfer area was also shaped to have a funnel at the bottom to encourage flow of condensate to the exit channel. The funnel extended below the bottom of the water side heat transfer area meaning that condensate collected at the bottom of the steam side channel could not remove heat from the cooling water side and re-evaporate. As a result, the FPHE heat transfer area calculation accounts only for the area where both steam and water are on opposite sides of

the plate. This is shown in Figure 6-7. Aluminium plates were chosen as being readily available and having a good heat transfer coefficient. Perspex end plates were used to allow viewing of fluid behaviour and provide insulation. Foam insulation was also wrapped around the aluminium plates during experimentation. Technical drawings for the custom FPHE can be found in the project's data repository, properly signposted in Chapter 9.

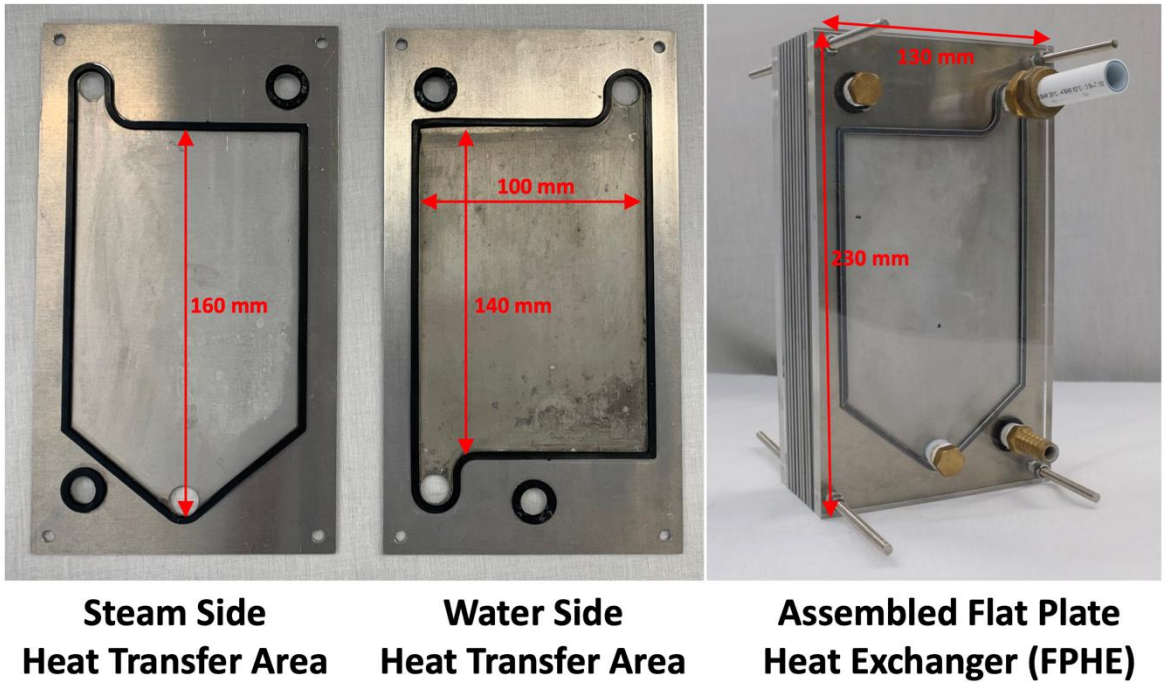

Figure 6-7 Photographs of flat plate heat exchanger custom designed for the heat recovery experiment. Photos show the chosen steam and water side heat transfer area geometries as well as clear Perspex end plates and rubber seals.

6.2.1.3 Data Analysis Methods

Temperature and pressure were measured directly by the microcontroller and required no intermediate analysis. Heat recovery efficiency was calculated using Equation (6.15).

$$\eta_{FPHE} = \frac{\dot{Q}_r}{\dot{Q}_a} \times 100 \tag{6.15}$$

Where:

- η_{FPHE} is the heat recovery efficiency (%).
- $\dot{Q}_a$ is the thermal power available for recovery per second (kW).
- $\dot{Q}_r$ is the thermal power recovered in the FPHE per second (kW).

Recovered energy was calculated using Equation (6.16).

$$\dot{Q}_r = \dot{m}_{cw} \times C_p \times \Delta T \tag{6.16}$$

Where:

- $\dot{m}_{cw}$ is cooling water mass flow rate (kg/s).
- ΔT is the change in cooling water temperature (°C).
- C_p is the cooling water specific heat capacity (kJ/kg.K).

Energy available for recovery in the heat exchanger was calculated using Equation (6.17).

$$\dot{Q}_a = \dot{m}_s \times (h_{in} - h_{out}) \tag{6.17}$$

Where:

- $\dot{m}_s$ is the mass flow rate of steam (kg/s).
- h_{in} and h_{out} are FPHE steam inlet and outlet enthalpies respectively (kJ/kg).

FPHE inlet enthalpy was read from steam tables at the corresponding inlet pressure. Using steam tables assumes that the steam is saturated, i.e. totally dry. The discussion in Section 6.1.4 highlights that this is unlikely to be true, as water will be entrained in the steam leaving the boiler and any heat losses in the pipework and valve contribute to a reduction in steam dryness. However, it was outside the scope of this work to measure steam dryness during the experimental procedure. Assuming a dryness value of $x = 1$ in the analysis presents a worst-case scenario where the maximum FPHE inlet enthalpy is assumed. This results in an underestimation of the FPHE heat recovery efficiency and therefore was deemed by the author of this research a suitable assumption for this proof-of-concept testing. However, a recommendation is made that future work should investigate steam dryness fractions surrounding the boiler and FPHE through practical experiment and assess the accuracy of this assumption. The FPHE outlet steam enthalpy was calculated using Equation (6.18) using conditions relating to the inlet cooling water temperature by which condensation would be limited. Vapour and liquid fraction enthalpies were read from steam tables. The dryness fraction at the FPHE outlet was estimated by plotting the engine cycle on T-s charts for different expansion ratios and reading the dryness fraction at the associated FPHE cooling water inlet temperature part way through the condensation process. This method is described in more detail in Chapter 9. Whilst this method allowed a simplification of the analysis for this high level work, it is noted that the manual nature meant the transition from expanded steam to condensate was drawn using a linear relationship, shown in fact by (Bortolin, et al., 2021) in Figure 2-14 to be

non-linear. Such detailed analysis using real gas data modelling was not included as part of the scope of this work, but it has already been included as a recommendation for future investigation.

$$h = (h_g \cdot x) + h_f(1 - x) \tag{6.18}$$

Where:

- h_g and h_f are water vapour and liquid enthalpies at relevant conditions respectively (kJ/kg).
- x is steam dryness fraction.

Finally, effective mass flow of steam was calculated using steam velocity, pipe cross section, steam average density and known pulse duration. Steam velocity was calculated using *Bernoulli's* equation with minor head losses (Cengel & Cimbala, 2010) between points upstream and downstream of the inlet solenoid valve.

6.2.1.4 Test Regimes

Experimental testing used three different solenoid valve regimes to test three different effective steam flow rates. The valve open time was maintained at 500ms whilst the closed time was tested at 500ms for test 1, 1000ms for test 2, and 1500ms for test 3. The first test was chosen to simulate conditions during engine operation at 60rpm and an expansion ratio of n = 1. Tests 2 and 3 were chosen to simulate reduced steam flow rate to reduce heat load on the condenser and understand heat recovery potential. A minimum of five repeats were performed for each regime, testing a range of cooling water flow rates between 4 – 20 mL/s.

6.2.2 Heat Recovery Test Results & Analysis

Heat recovery experiment efficiency, temperature, and pressure results are given in Figure 6-8, Figure 6-9, and Figure 6-10 respectively. For reference, average effective steam flow rates for tests 1 to 3 were 2.4×10^{-3} kg/s, 1.9×10^{-3} kg/s, and 1.5×10^{-3} kg/s respectively.

Figure 6-8 shows that heat recovery efficiency increased with reduced steam flow rate and increased cooling water flow rate. Therefore, heat recovery could be more effective at slower engine speeds on the practical engine. A second order polynomial relationship was formed where efficiency gains plateaued, limited by heat exchanger design. Importantly, at higher cooling water flow rates energy recovery efficiencies over 50% were achieved during test 1, increasing to almost 60% for test 3. This supports the hypothesis that 70% heat recovery could be achieved with optimised heat exchanger design, as assumed in the FPHE design and theoretical re-use analysis given in Section 6.3.

Figure 6-9 shows that cooling water outlet temperature increased with increased steam flow rate and reduced cooling water flow rate, presenting a linear relationship. Importantly, cooling water outlet temperatures ranging from 65°C - 90°C support that heat recovery has been successful. These temperatures would be suitable for use in a second sub-atmospheric boiler in the heat re-use concept shown in Figure 6-11.

Figure 6-10 shows that the minimum heat exchanger pressure observed, a critical parameter as this will be translated to the condensing engine cylinder and directly effects power production, decreased linearly during test 1 with increasing cooling water flow rate. Tests 2 and 3 both exhibited a minimum pressure which was limited by the constraints within the experiment. During all three tests, minimum FPHE pressures of around 0.2bar were achieved. Importantly, this is suitable for condensing engine operation without negatively effecting power output based on recent Mk.II and Mk.III engine tests.

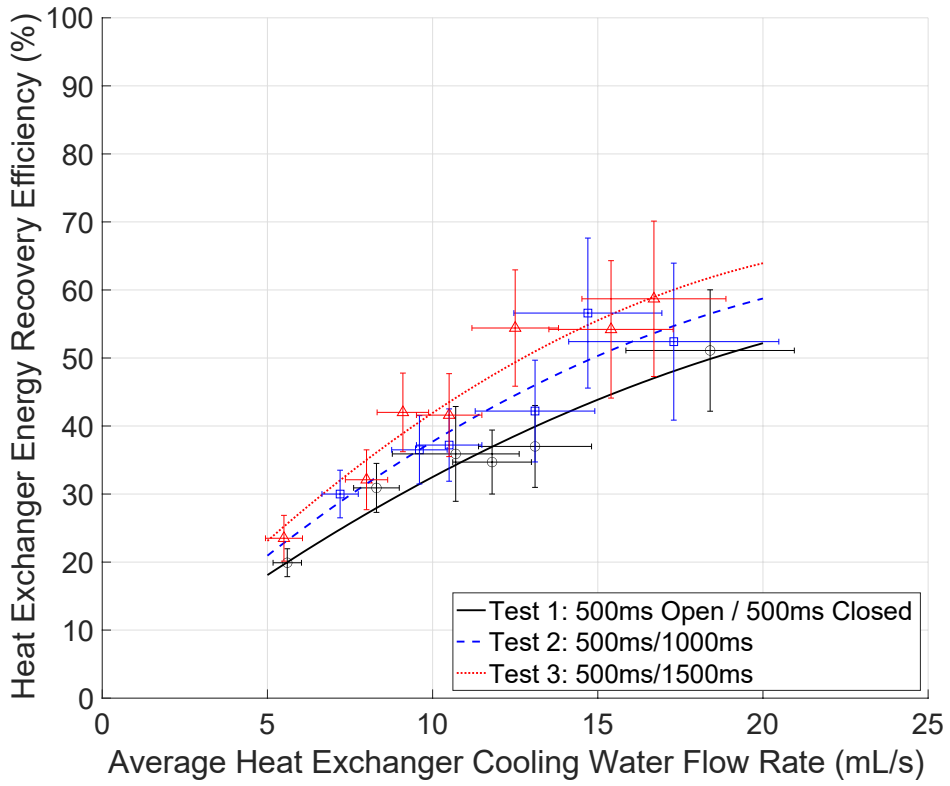

Figure 6-8 Heat recovery efficiency versus cooling water flow rate for different steam control valve open and closed times.

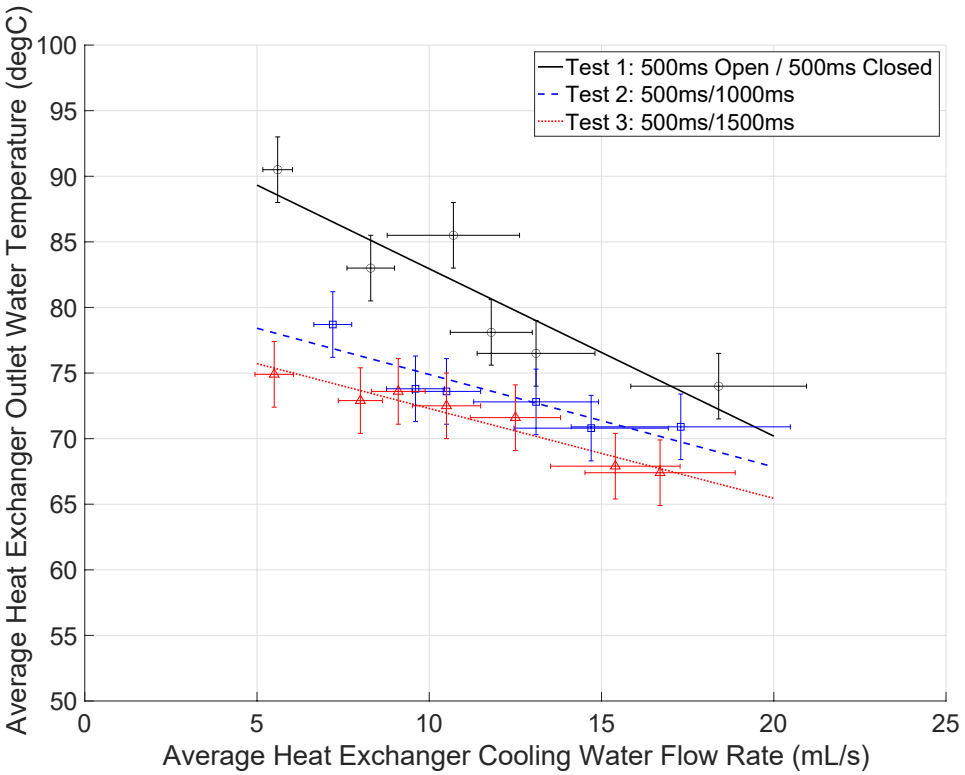

Figure 6-9 Average heat exchanger outlet temperature versus cooling water flow rate for different steam control valve open and closed times.

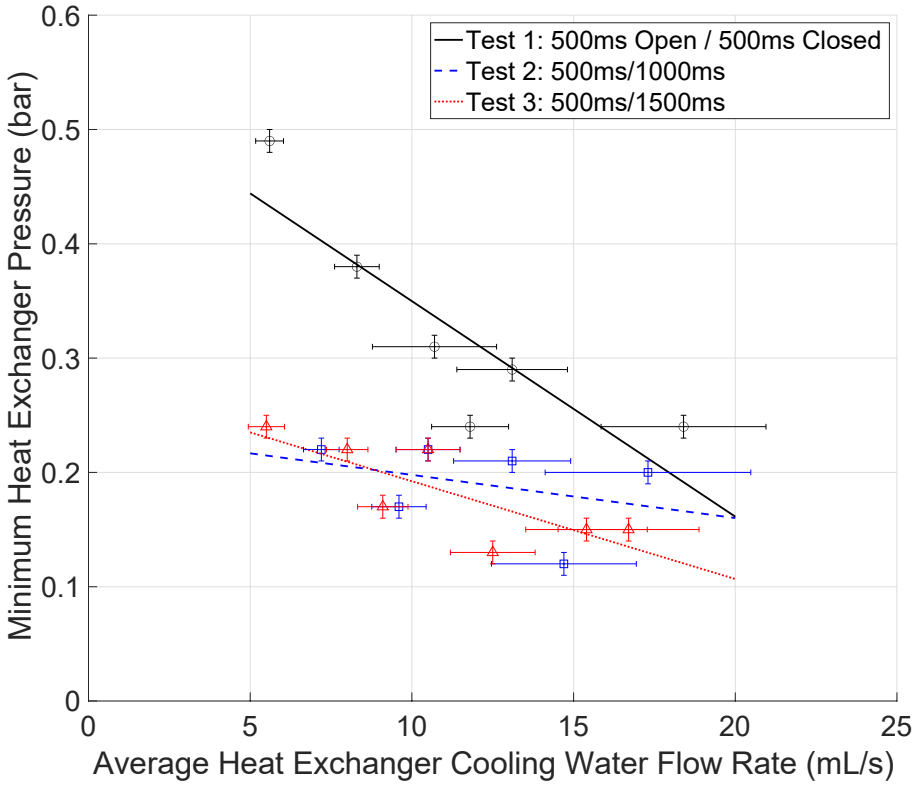

Figure 6-10 Minimum heat exchanger pressure versus cooling water flow rate for different steam control valve open and closed times.

6.2.3 Heat Recovery Test Discussion

6.2.3.1 Heat Recovery Success

The heat recovery shown in Figure 6-8 was more successful than previous attempts at the UoS. This supports use of the two-stage condensation system employed in this experiment to increase residence time of steam in the heat recovery section. Importantly, it was also observed during testing that the steam side end plate demonstrated condensate being successfully drawn to the bottom of the heat exchanger. This supports the custom design of the FPHE for this experiment, minimising re-evaporation of condensate during pulses of low pressure to maximise heat recovery efficiency. Future work could investigate the impact of relative size of intermediate heat exchanger and final condenser.

6.2.3.2 Optimisation Discussion

Considering Figure 6-8, Figure 6-9, and Figure 6-10 together, it is observed that a trade-off exists when selecting cooling water flow rate. To maximise heat recovery efficiency, cooling water flow rate should be maximised, also benefitting system pressure. However, this negatively impacts outlet water temperature. It is suggested that when designing a heat recovery setup for the CE the system pressure should take priority as it directly impacts the operation of the CE itself. Once a suitable range of cooling water flow rates is selected, giving suitable expected system pressures, a point within this range should be chosen to give suitable heat recovery efficiency and outlet temperature. Counterintuitively, it is suggested that heat recovery efficiency is the least important factor out of the three analysed, as anything greater than zero is an improvement over the current system and the water outlet temperature and system pressure directly impact the ability of the system to operate as desired. Following the above discussion, an example operation to be chosen from this work's testing could be a cooling water flow rate around 15mL/s, allowing for an average heat recovery efficiency around 50%, average water outlet temperature around 70^{o}C, and an average system minimum pressure around 0.2bar. However, it must be acknowledged that not favouring heat recovery efficiency during optimisation has associated economic implications. For example, reduced efficiency impacts required heat exchanger surface area, with larger equipment increasing capital cost. This must also be accounted for when optimising a heat recovery system on the condensing engine. Further advancement of the concept, for example improved heat exchange, will allow for all factors to be considered during optimisation.

It is also acknowledged that this experiment simulated engine operation where steam is pulsed from the cylinder to the condenser. This replicates operation of the most recent Mk.II and Mk.III condensing engines built at the UoS. This is because they were single cylinder engines. However, it

has been suggested that future condensing engines should make use of multiple cylinders to provide a more stable power output. In doing so, the flow of steam to the condenser becomes more continuous with each cylinder added, as they will run out of phase. Therefore, future work could investigate the effect of this on the ability to recover heat in the intermediate FPHE. It is expected that so long as a sufficiently large FPHE heat transfer area is provided, heat recovery should still be achievable. Furthermore, the removal of the pulsed nature of the steam flow simplifies heat exchanger design.

6.2.3.3 Uncertainty Analysis and Recommendations for Future Experiment Improvement

The experimental uncertainty analysis followed a method given by the National Physical Laboratory (Bell, 2001) and accounted for the pertinent uncertainties in the reported values, using an uncertainty budget, and combined them using the summation of quadrature method. A coverage factor of $k = 2$ was also applied to give a 95% confidence interval, plotted as error bars on Figure 6-8, Figure 6-9, and Figure 6-10. The full method of calculation is detailed in Chapter 9. This analysis allows discussion surrounding the credibility of the results and the suitability of the experimental method.

Firstly, it is acknowledged that the error bars suggest significant uncertainty. This is a result of the experimental technique used to measure the cooling water flow rate, the uncertainty in which is compounded into the efficiency value through use in the necessary calculation. Using a fixed volume to be filled with water and measuring the time taken means that as water flow rate increases the time measurement reduces and therefore errors in the value become a larger percentage of the measured value. Additionally, this method requires the precision of the beaker and human reaction time to be incorporated into the uncertainty analysis. If future experiments instead filled a beaker for a measured period of time and weighed the collected water, the human reaction time uncertainty could be mitigated by using the given value on the stopwatch and the greater accuracy of the scale would reduce the resolution uncertainty associated with instrumentation. Taking larger/longer samples for flow rate measurement would also reduce the relative uncertainty as a percentage of the measured value which would reduce the size of the error bars. Additionally, this testing used k-type thermocouples which resulted in uncertainty of +/- 2.5^{o}C in the recorded temperature measurements. Future testing should endeavour to reduce this uncertainty by using an alternative type of temperature probe, such as a PT100 which has reported accuracies as low as +/- 0.1^{o}C.

However, despite the above discussion, the author of this work believes all reported data to still show successful proof of concept of heat recovery in practice. Taking the reported data as a range that includes the extremities of the error bars, the conclusions surrounding the success of this work

hold true. For example, the heat recovery efficiency ranged from around 18% - 70%. The low end of the range has already been explained by reduced cooling water flow rate. Cooling water outlet temperature and minimum FPHE pressure data also still show promise, with ranges of 65°C - 93°C and 0.12bar - 0.50bar respectively when including the uncertainty ranges. The entire temperature range given above is useful, with the higher part of the range achieved by reducing cooling water flow rate. The minimum part of the pressure data is useful whilst the upper part of the range is not, although this is not a result of the error bars but instead of the reduced condensing power at lower cooling water flow rates.

6.2.4 Heat Recovery Test Conclusions

An experimental setup was built and tested at the UoS to show successful proof of concept of heat recovery on the condensing engine. This used the two-stage condensation concept with intermediate FPHE, originally proposed in Section 6.1. Results were promising, demonstrating that heat recovery can be achieved during steam condensation at a high enough temperature for re-use without negatively affecting condensing engine performance. This justifies further research surrounding heat recovery on the condensing engine. Key conclusions from testing were:

- Heat recovery efficiencies as high as 60% were achieved, confirming the ability to recover latent heat during steam condensation.
- FPHE water outlet temperatures as high as 90°C were observed, suitably high for re-use.
- System pressures as low as 0.2bar were observed, satisfactory for the effective operation of the condensing engine with heat recovery.
- Discussion identified that cooling water flow rate must be carefully selected to give the optimum heat recovery efficiency, outlet temperature, and system pressure. System pressure is the priority for optimisation, with water outlet temperature second most important and heat recovery efficiency least important.
- An example operation was selected to demonstrate suitable optimisation of all conditions. During testing a cooling water flow rate of 15mL/s and inlet temperature of 50°C allowed an average heat recovery efficiency of 50%, average water outlet temperature of 70°C, and average system pressure of 0.2bar.
- Recommendations were made for improving the uncertainty associated with measured data, including updated cooling water flow rate measurement and use of PT100 temperature probes. This will allow for optimisation of the heat recovery performance to take place.

6.3 Heat Re-Use: Theoretical Analysis

Heat recovery on the condensing engine has been shown to be viable, both in its theoretical potential and through experimental proof of concept. It is important to also understand the potential benefits of re-using the recovered heat. Heat re-use could occur both internally in the condensing engine system to improve power output or in an external system where a low temperature heat sink exists. The latter case gives the condensing engine with heat recovery the ability to operate in systems where a temperature step down is required, providing power production as a result. In scenarios where a heat sink does not exist, the recovered heat is better re-used within the condensing engine system itself. The remainder of this section focusses on this concept as the most flexible option for heat re-use, providing theoretical analysis of the benefits through development of a mathematical model.

6.3.1 Heat Re-Use Concept: Second Sub-Atmospheric Cylinder

To re-use the recovered thermal energy, it is proposed that a second boiler (B2), cylinder (C2), and condenser (CON2) stage should be employed in the condensing engine, operating sub-atmospherically, as shown in Figure 6-11.

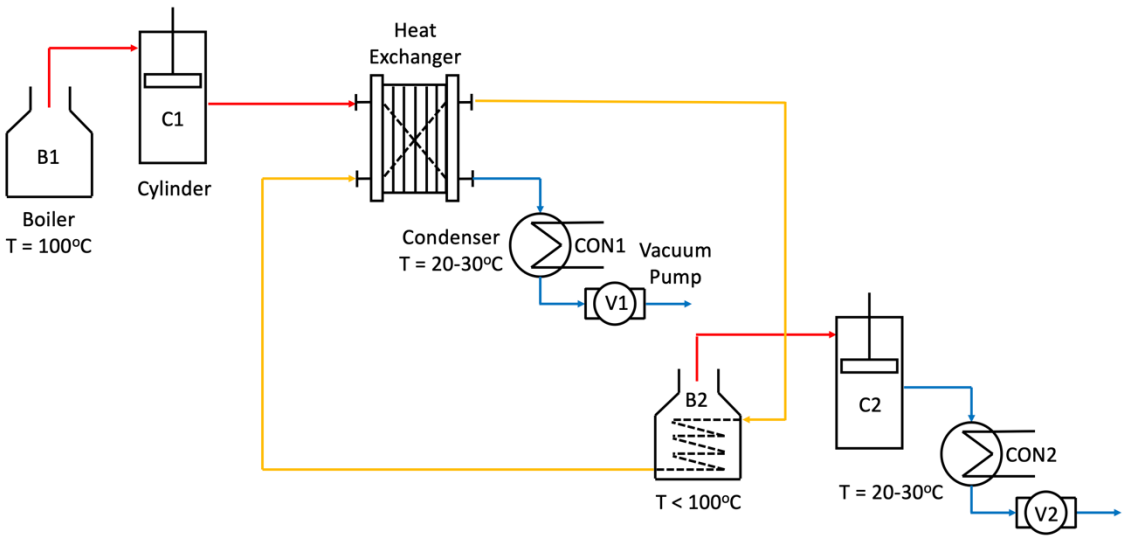

Figure 6-11 Schematic for proposed condensing engine two-stage heat recovery with re-use in sub-atmospheric second stage. B = Boiler. C = Cylinder. CON = Condenser. FPHE = Flat Plate Heat Exchanger. V = Vacuum Pump. CW = Cooling Water.

The ability to operate below atmospheric pressure was demonstrated experimentally on the Mk.II engine (Muller, et al., 2018) and reviewed in Section 2.4. By operating the boiler at sub-atmospheric pressure, a boiler temperature <100°C can be used to generate steam. Providing that boiler temperature and pressure are still above that of the condenser, a driving force still exists, and the engine can produce mechanical power. Therefore, providing a sufficiently high cooling water circuit temperature can be achieved during heat recovery a second boiler could feasibly be operated. The proposed condensing engine heat recovery and re-use concept has been modelled theoretically in this research with the aim of understanding the potential performance gains.

6.3.2 Heat Re-Use Mathematical Model Method

The theoretical model was developed by extending the energy availability model described in Section 6.1, built in MATLAB using XSteam data tables (Holmgren, 2007). The model assumes a double acting engine arrangement is being used to simplify the equations used, described in this document's literature review, but the results are relevant for all engine arrangements including the uniflow. The model operates on a 1kg basis of steam entering the first cylinder (C1). It was assumed that boiler temperature was 100°C and condenser temperature (CON1, CON2) was 20°C. It was assumed that 70% of the energy available for recovery in the heat exchanger during partial steam condensation was successfully recovered in the cooling water for re-use, validated in the experimental phase of this research. An intermediate heat exchanger cooling water inlet temperature of 50°C - 70°C was studied using the model, chosen to allow a sufficiently high outlet temperature. First cylinder (C1) expansion ratios from n = 1-8 were also tested during analysis.

First, the model calculates the work produced during steam inlet to the primary cylinder (C1). This uses Equation (6.19) which describes work produced during the passing of a given volume by the piston with constant cylinder pressure. This equation is first applied to the boundary cylinder volume passed without steam expansion and therefore constant pressure, associated with that of the boiler.

$$W_{bdy} = P_b V_{bdy} \tag{6.19}$$

Where:

- W_{bdy} is the boundary work produced (J).
- P_b is boiler pressure (Pa).
- V_{bdy} is boundary volume passed by the piston prior to expansion (m^3).

Work produced during steam expansion is calculated next. Where previous analysis in this thesis used isentropic gas laws to estimate final steam pressure and work production following steam expansion, the analysis presented below has taken the opportunity to demonstrate an alternative method which could be utilised in future condensing engine modelling. In this case, the boundary work equation has been used to understand expansion work production. Because this equation assumes a constant pressure the process must be iterated throughout the cylinder volume with step sizes sufficiently small to ensure close to constant pressure within each step to limit error.

Firstly, each iteration calculates the new steam enthalpy, found by taking steam enthalpy at the start of steam expansion and removing steam expansion work produced per kilogram, see Equation (6.20). Secondly, expansion is assumed as isentropic, see Equation (6.21). Steam enthalpy and entropy are subsequently used to find the steam pressure for the iteration using the XSteam data tables (Holmgren, 2007), see Equation (6.22). This pressure is used to calculate the work produced during the iteration step using the boundary work formula, see Equation (6.23). The cumulative expansion work is summed at the end of each iteration, see Equation (6.24). This research used 100 volume steps and demonstrated a maximum percentage difference of 2.5% between thermal efficiency values estimated using the above method and the isentropic equations used in Chapter 3 when simulating between an expansion ratio of n = 1 and n = 10. The associated data is available in the data repository. The author of this research deemed this as suitable for use in this analysis as a negligible difference, confirming that this method can be used in future condensing engine modelling if required.

$$h_{i,exp} = h_s - \frac{W_{exp}}{m} \tag{6.20}$$

$$s_{i+1,exp} = s_{i,exp} \tag{6.21}$$

$$P_{i,exp} = P_s \text{ @ } h_{i,exp} \text{ \& } s_{i,exp} \tag{6.22}$$

$$W_{i,exp} = P_{i,exp} \Delta V_{i,exp} \tag{6.23}$$

$$W_{exp} = \sum_{i=1}^{i=n} W_{i,exp} \tag{6.24}$$

Where:

- i is iteration number from 1 to n.
- $h_{i,exp}$ is the steam specific enthalpy during the relevant iteration (J/kg).
- h_s is the steam specific enthalpy at the start of expansion (J/kg).
- W_{exp} is the cumulative work produced during expansion per kilogram of steam (J).

- m is the mass of steam being expanded (kg).
- s is steam specific entropy (J/kg.K).
- $P_{i,exp}$ is the pressure following expansion during the relevant iteration (Pa).
- P_s is steam pressure associated with defined specific enthalpy and entropy values (Pa).
- $W_{i,exp}$ is work produced during the expansion iteration i (J).
- $\Delta V_{i,exp}$ is the volume step passed during iteration i (m^3).

The back pressure losses are then calculated using Equation (6.25) and the total work produced over the stroke found using Equation (6.26).

$$W_{loss} = P_{con} V_{cyl} \tag{6.25}$$

$$W_{out} = W_{bdy} + W_{exp} - W_{loss} \tag{6.26}$$

Where:

- W_{out} is the total work produced over the stroke (J).
- W_{loss} is the work lost due to back pressure resistance (J).
- P_{con} is condenser pressure (Pa).
- V_{cyl} is total cylinder volume passed (m^3).

Next, the model calculates energy available for recovery in the heat exchanger using Equations (6.27) and (6.28). This part of the method has been discussed in Section 6.1 already. Here, the steam enthalpy at the heat exchanger inlet is taken from the iterated process described above, therefore accounting for the dryness fraction of the steam following expansion. Where steam expansion is not present the dryness fraction of steam exiting the cylinder is assumed to be equal to that of the boiler, defined as an input to the model. FPHE outlet dryness fraction is estimated using T-s charts as before.

$$E_a = m \times (h_{in} - h_{out}) \tag{6.27}$$

$$h = (h_g \cdot x) + h_f(1 - x) \tag{6.28}$$

The thermal energy per unit mass of steam recovered in the heat exchanger is then calculated using the pre-defined heat recovery efficiency, see Equation (6.29).

$$E_r = \varepsilon \times E_a \tag{6.29}$$

Where:

- E_r is recovered thermal energy (J).
- ε is heat recovery efficiency, assumed to be 70% in this research.

Next, the model simulates the transfer of the recovered energy to the second boiler (B2). It is assumed that 100% transfer is achieved. The operating pressure of the second boiler (B2) is defined as the saturation pressure associated with the temperature of the water circuit exiting the boiler and returning to the heat exchanger. The enthalpy increase required, at the defined operating temperature, from boiler feed water to steam is used along with the energy recovered in the heat exchanger to calculate the mass of steam raised in B2; see Equation (6.30).

$$m_{s,b2} = \frac{E_r}{h_g - h_l} \tag{6.30}$$

Where:

- $m_{s,b2}$ is mass of steam raised by the recovered thermal energy in the second stage boiler (kg).
- h_g is enthalpy of steam produced in B2 (J/kg).
- h_l is liquid enthalpy associated with B2 feed water (J/kg).

Next, the model tests increasing expansion ratios to determine the maximum that can be used in the second cylinder (C2) whilst still maintaining a final pressure, after expansion, greater than that in the second condenser (CON2). This is achieved using the ideal gas law for isentropic expansion, given in Equation (6.31). From this, the work produced in the second cylinder can be calculated using the same method described in Equations (6.19) to (6.26) inclusive.

$$P_1 = P_0 \times \left(\frac{V_0}{V_1}\right)^{\gamma} \tag{6.31}$$

Finally, the model outputs are determined. The thermal efficiency for the single stage condensing engine without heat recovery is given in Equation (6.32). The thermal efficiency of the two-stage condensing engine with heat recovery is given in Equation (6.33). Thermal energy input is given by Equation (6.34).

$$\eta_{therm,1} = \frac{W_1}{Q} \tag{6.32}$$

$$\eta_{therm,2} = \frac{W_1 + W_2}{Q_{in}} \tag{6.33}$$

$$Q_{in} = (h_g - h_l) \times m_{s,1} \tag{6.34}$$

Where:

- $\eta_{therm,1}$ is CE efficiency with one cylinder stage (no heat recovery) given as a decimal fraction.
- $\eta_{therm,2}$ is CE efficiency with heat recovery and two-cylinder stages, given as a decimal fraction.
- W_1 is the work produced in the first cylinder stage (J).
- W_2 is the work produced in the second stage when heat recovery is employed (J).
- Q_{in} is the thermal energy input (J).
- $m_{s,1}$ is the steam produced in boiler 1 (kg), chosen as 1kg in this analysis.

6.3.3 Heat Re-Use Model Results , Analysis & Discussion

The results from the theoretical analysis are shown in Figure 6-12. Second order polynomial fits have been plotted through the two-stage engine theoretical efficiencies, as efficiency reaches a plateau at higher expansion ratios. As expected, minimising heat exchanger cooling water inlet temperatures improves the overall efficiency of the two-stage engine, a product of improved heat recovery in the heat exchanger.

The results show that using heat recovery does not allow the maximum efficiency for the engine to be increased. This is due to the laws of thermodynamics, and the single stage engine maximum efficiency already approaching the *Carnot* efficiency. However, a key observation is that the proposed heat re-use allows equal overall efficiencies to be achieved at lower expansion ratios in the first cylinder (C1). For example, it has been suggested that a practical engine is not expected to operate with expansion ratios much higher than n = 4 due to valve timing and cooling losses. A condensing engine with heat recovery and a first cylinder expansion ratio of n = 4 achieves a thermal efficiency around 17.8%. A single stage engine without heat recovery would need to operate at an expansion ratio of n = 7 to achieve this same efficiency. Operating with reduced expansion ratio is beneficial to engine performance. It allows the engine to have a smoother power output, an increased steam throughput and therefore increased power output, a simpler control system, and reduced thermal losses in the system. These benefits of operating at lower expansion ratios without compromising on efficiency justify the need for heat recovery and re-use on the condensing engine.

It is also important to note that the efficiencies of the system with heat recovery reach a maximum point before reducing slightly to be equal with the single stage condensing engine. This is because at increased expansion ratio the steam temperature exiting the cylinder is too low for heat

recovery to occur given the higher inlet cooling water temperatures, as discussed previously. Therefore, during design this maximum inflection point for the two-stage system needs to be understood.

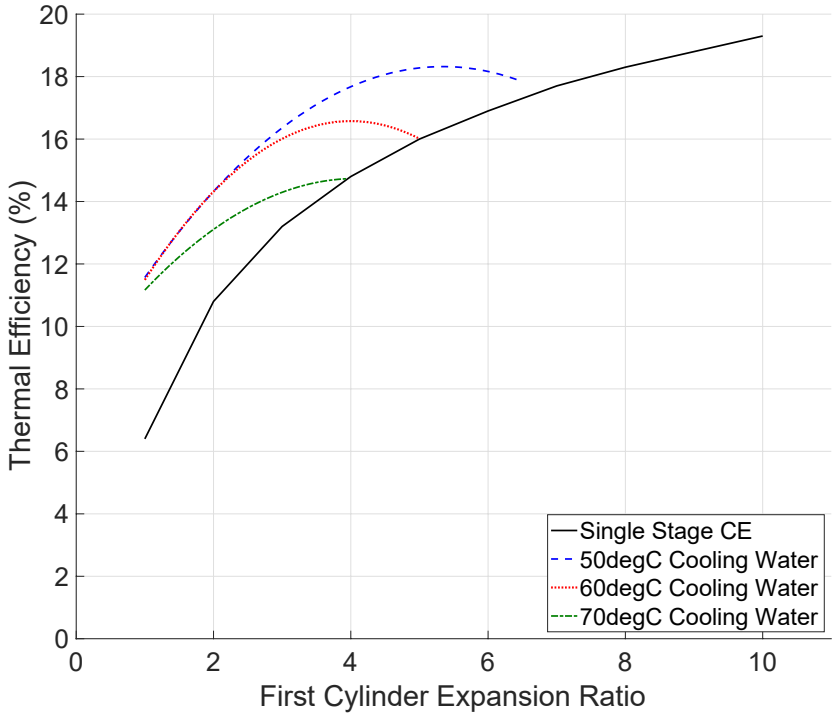

Figure 6-12 Comparison of condensing engine with and without heat recovery for different expansion ratios and cooling water inlet temperatures.

6.3.4 Heat Re-Use Steam Dryness Fraction Sensitivity Analysis

It is noted that the results plotted in Figure 6-12 were modelled assuming totally dry saturated steam produced in the boiler, i.e. $x = 1$. Discussion in Section 6.1.4 highlighted that this represents an ideal case. A sensitivity analysis with boiler steam dryness fractions ranging from $x = 1.0$ to $x = 0.9$ was performed on the two-stage engine efficiency with heat recovery for a FPHE cooling water temperature of 50°C and expansion ratios of $n = 1$ to $n = 4$. The results are shown in Figure 6-13.

Figure 6-13 shows that at an expansion ratio of $n = 4$, highlighted in this section's analysis as a potential optimum selection, the two-stage engine theoretical thermal efficiency is reduced from 17.8% to 17.3% when boiler steam dryness fraction is reduced from $x = 1.0$ to $x = 0.90$. This represents a 2.8% reduction, much smaller than the decrease of around 15% shown by Bortolin, et al. (2021) in Figure 2-16 for the single stage engine using real gas data.

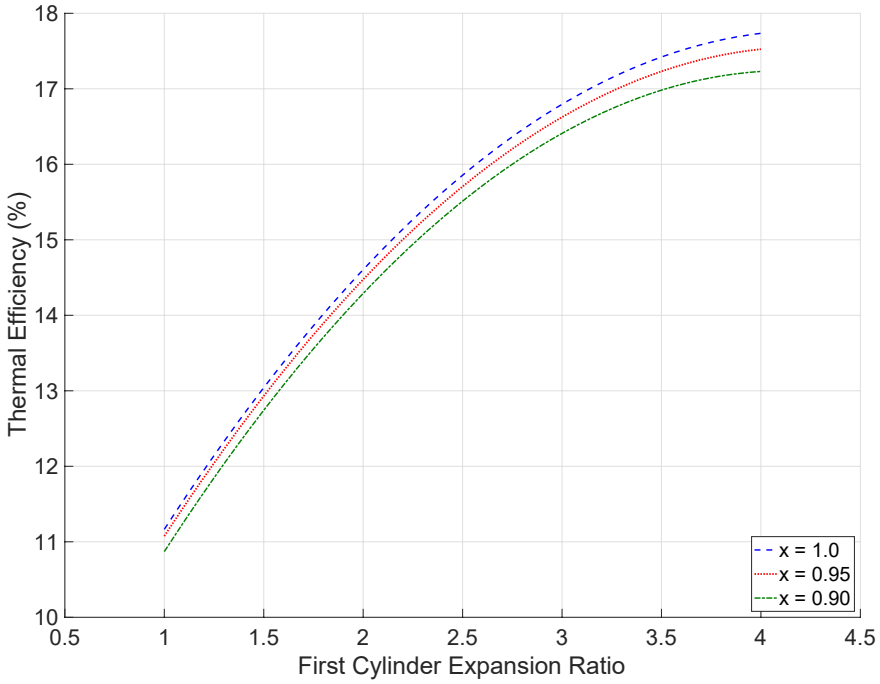

Figure 6-13 Two stage engine with heat recovery theoretical thermal efficiency for different boiler steam dryness fractions. Heat source: 100°C. Heat sink 20°C. Heat exchanger water temperature: 50°C.

This indicates that the model developed in this research may not simulate the effect of dryness fraction as well as more accurate methods. The simplifications of this research's model, which could have contributed to this difference, have been analysed already in Section 6.1.4. It is also noted that a further difference could be attributed to the assumption used surrounding the cause of the reduction in steam dryness. This research assumed that the reduction in dryness fraction was caused by steam carrying water droplets out of the boiler and not due to condensation of steam between the boiler and cylinder. This results in a reduction in calculated boiler energy required, because the mass of dry steam produced in the boiler is lower, which acts to offset any reduction in power output and therefore equalise the resulting efficiency. Condensation in pipework could be mitigated with proper lagging and was therefore ignored. The most appropriate assumptions to be made surrounding steam dryness and the effect on thermal energy input are dependent on system setup, and future work could experimentally demonstrate which is more suitable. Despite the need for more investigation into the effect of steam dryness fraction, the heat recovery results in Figure 6-13 demonstrate significant potential in heat recovery and re-use on the condensing engine.

6.3.5 Heat Re-Use Conclusions

A mathematical model was built to simulate heat recovery and re-use on the condensing engine, with a two-stage condensation process driving a second sub-atmospheric boiler. This was used to test heat recovery heat exchanger inlet water temperatures of 50°C - 70°C and first cylinder expansion ratios of n = 1-8. Key conclusions drawn from this work were:

- Re-using recovered heat to drive a second sub-atmospheric boiler and cylinder stage allows for expansion ratio to be reduced without affecting efficiency.
- For example, the condensing engine with heat recovery can achieve a theoretical thermal efficiency of 17.8% at an expansion ratio of n = 4 compared to n = 7 without heat recovery, when assuming fully saturated boiler steam is used.
- Operating at lower expansion ratios simplifies control, increases engine power, and allows for more stable operation. This has identified a novel way of operating the condensing engine for improved performance.
- Sensitivity analysis testing boiler steam dryness values demonstrated negligible impact on the efficiency of the condensing engine with heat recovery. For example, at an expansion ratio of n = 4 and cooling water temperature of 50°C, the two-stage system efficiency reduces by just 2.8% when the boiler steam dryness fraction reduces from x = 1.0 to x = 0.9. However, more accurate modelling using real gas data has been identified as necessary, and the results of the sensitivity analysis in this thesis should be taken with caution until corroborated.

6.4 Conclusions

A two-stage condensation process was proposed to allow for heat recovery during steam condensation on the condensing engine. A sub-atmospheric cylinder was also proposed to make use of the recovered heat in a novel way. A theoretical analysis was performed to highlight the energy available for recovery as well as demonstrate the potential of the proposed system. Experiments were conducted using a custom flat plate heat exchanger to demonstrate proof of concept. Key conclusions drawn from this work were:

- This work justifies the need for heat recovery on the condensing engine even with steam expansion, something not previously quantified.
- Theoretical analysis identified that as much as 75% of input energy is available for recovery during steam condensation, with a value around 40% being more realistic when operating

with an expansion ratio of n = 4, cooling water inlet temperature of 50°C, and totally dry saturated boiler steam.

- Sensitivity analysis tested steam dryness fractions down to x = 0.9, concluding that at an expansion ratio of n = 4 the energy available for recovery reduced by 17% and the boiler thermal energy input available for recovery reduced by 9.5%. However, more accurate modelling using real gas data has been identified as necessary, and the results of the sensitivity analysis in this thesis should be taken with caution until corroborated.
- Empirical results demonstrated proof of concept using two-stage condensation and an intermediate FPHE cooling water inlet temperature of 50°C. Maximum heat recovery efficiencies of around 60% were achieved with cooling water outlet temperatures of 65°C - 90°C and minimum system pressures of 0.2bar. This demonstrates that heat recovery can be performed without negatively effecting engine performance and is a critical step in the development of the technology. Recommendations were made for the improvement of future experiments to allow optimisation of the heat recovery process. This consisted of a reduction in uncertainties through improved water flow rate measurement and PT100 temperature probes.
- A novel concept for recovered thermal energy re-use in the condensing engine was proposed, driving a second sub-atmospheric cylinder to further contribute to engine performance. Theoretical analysis identified that this could maintain efficiency whilst operating at lower expansion ratios. For example, the condensing engine with heat recovery can achieve a theoretical thermal efficiency of 17.8% at an expansion ratio of n = 4 compared to n = 7 without heat recovery. Reduced expansion allows increased power output and more stable operation. This constitutes a further advancement in the knowledge surrounding the operation of the technology.
- Sensitivity analysis testing boiler steam dryness values of x = 1.0 to x = 0.9 demonstrated negligible impact on the efficiency of the condensing engine with heat recovery. However, the effects of steam dryness fraction are not expected to have been fully captured by the simplified analysis presented in this thesis, and whilst this research should serve as justification for more thorough modelling the results should be taken with caution until corroborated.

Chapter 7 Conclusions and Recommendations

7.1 Conclusions

The condensing engine is a heat engine for low temperature heat recovery, between 50°C - 150°C. It was identified in this project that the technology is most suited for low power scale applications in the range of 1kW - 200kW. The technology can provide benefits to domesticated applications and those in remote/rural settings where use of water as a working fluid and low operating pressures are desirable. In this project, a modernised condensing engine with a novel configuration (single acting uniflow) was investigated theoretically and experimentally. Reported results are considered indicative and use assumptions to mitigate losses of efficiency that can be optimised on future engines. This work demonstrated the significant potential of the engine when compared against existing technologies as well as improvement over previous technology iterations. An improved concept for heat recovery within the engine system was also experimentally tested, showing proof of concept, and the future potential benefits investigated theoretically. This work has successfully met the aims and objectives set out in the introduction of this thesis and advanced the condensing engine technology. The key conclusions of this research were:

- The Mk.III single acting uniflow condensing engine achieved a maximum power output of 5.4W, assuming 10% friction losses from the calculated piston power, comparable with the Mk.II engine for similar operation. It also achieved a maximum thermal efficiency of 2.5%, representing an increase of 25% compared to the maximum value achieved by the previous Mk.II engine under similar operation. Analysis predicts thermal efficiencies as high as 9% could be achieved with development of the technology. Second law efficiencies of 27% - 43% were achieved, assuming no losses between boiler and cylinder, around 25% better than the Mk.II model and comparable with the 20% - 40% observed from existing ORC systems operating in the same temperature range and power scale.
- Using lessons learned from the Mk.III engine, an advanced Mk.IV single acting uniflow condensing engine design was developed and built as part of a collaboration with the University of Stellenbosch for a novel water purification and energy production system. Advancements in engine control were required to achieve this, specifically the use of

steam expansion to reduce steam demand at a constant engine speed and create better synergy with steam supply.

- Theoretical analysis identified that as much as 75% of input energy is available for recovery during steam condensation, with a value around 40% being more realistic when operating with an expansion ratio of n = 4, cooling water inlet temperature of 50°C, and fully saturated boiler steam. Sensitivity analysis tested steam dryness fractions down to x = 0.9, concluding that at an expansion ratio of n = 4 the energy available for recovery reduced by 17% and the boiler thermal energy input available for recovery reduced by 9.5%. However, more accurate modelling using real gas data has been identified as necessary, and the results of the sensitivity analysis in this thesis should be taken with caution until corroborated.
- Experimental testing demonstrated successful heat recovery proof of concept using an intermediate flat plate heat exchanger as part of a two-stage condensation process. Maximum heat recovery efficiencies of almost 60% were achieved, along with water outlet temperatures of 65°C - 90°C and minimum system pressures of 0.2 bar.
- Theoretical analysis of a novel concept for re-use of the recovered energy, driving a second sub-atmospheric cylinder stage, identified an advancement in future condensing engine operation, achieving equal efficiency at reduced steam expansion ratios. For example, the condensing engine with heat recovery and second sub-atmospheric stage can achieve a theoretical thermal efficiency of 17.8% at an expansion ratio of n = 4, compared to n = 7 without heat recovery, when assuming fully saturated boiler steam. Reduced steam expansion allows more stable operation, increased power output, and simplified valve control. Sensitivity analysis demonstrated negligible impact on reported system efficiencies. However, more accurate modelling using real gas data has been identified as necessary, and the results of the sensitivity analysis in this thesis should be taken with caution until corroborated.

In summary, the single acting uniflow arrangement was proven to be an improvement to the condensing engine technology. Additionally, heat recovery during steam condensation is not only possible but was shown to have significant potential to further advance the performance and operation of the condensing engine. As a result of this work, it can be concluded that the modernised condensing engine is justified of continued development, and that a single acting uniflow arrangement with two-stage condensation for latent heat recovery warrants further research and optimisation. This research was the first of its kind and therefore several recommendations have been made for future work to benefit from. These are summarised below.

7.2 Recommendations

Lessons learned during both the theoretical and empirical phases of this project have allowed for several further recommendations to be made to guide future investigation of the single acting uniflow condensing engine technology. These include:

- Future work must understand whether the assumption of 10% mechanical losses from calculated piston power and negligible losses between boiler and cylinder can be achieved in practice. The effect on the comparison of the technology against ORC systems in literature should be discussed.
- Investigate improved valving, minimising minor head loss coefficient and maximising steam evacuation. This could be in the form of a slide valve, building on the work performed in this project. Slide valve optimisation should focus on minimising friction and achieving mechanical timing which allows for higher expansion ratios to be used.
- Reduce mechanical losses to improve performance. Employ more accurate friction analysis methods to quantify any improvement.
- Directly measure engine power output and steam mass use in future condensing engine tests to limit the number of calculation steps required in determining the final reported value. This will simplify analysis and reduce the associated uncertainty.
- Investigate thermally insulating cylinder and piston materials, such as a synthetic polymer like PTFE, which could remove the need for the steam jacket. This would reduce engine complexity as well as steam use and therefore improve engine efficiency even further. Thermal expansion must be considered for any new material selection.
- Investigate improved condenser design to reduce condenser pressure.
- Optimise heat recovery through further testing. Experimental technique should be updated as per recommendations in this thesis, namely improved water flow rate measurement and use of PT100 temperature probes, to reduce the uncertainty in the reported values.
- Measure steam dryness fraction throughout the condensing engine with heat recovery. Compare results against the assumptions made in this thesis during sensitivity analysis and feed into an updated analysis as necessary.
- Perform more accurate theoretical modelling of the condensing engine with heat recovery and re-use using real gas data to understand the effect of boiler steam dryness fraction.
- Once heat recovery has been optimised experimentally, and the effect of steam dryness fraction understood, heat recovery should be implemented on a practical condensing engine to demonstrate the next step in the proof of technology.

- Test uniflow engine performance for different boiler and condenser temperatures, analysing cases with pressures above atmospheric to increase energy density and reduce downstroke losses. This may be required to ensure favourable scale and economics.
- Investigate the scalability of the condensing engine technology and understand the optimum power scale range it could be commercially implemented in, given the identified reduced energy density in comparison to competing technologies. This step requires knowledge of an optimised efficiency value, and therefore should be conducted after the previous recommendations have been addressed.
- Investigate commercial engine economics and compare against other technologies on the market, such as the Organic Rankine Cycle.
- Finally, readers of this work should also consider any recommendations made following Mk.IV engine testing, to be performed at the University of Stellenbosch.

Chapter 8 Works Cited

Ammar, Y. et al., 2012. Low grade thermal energy sources and uses from the process industry in the UK. *Applied Energy,* 89(1), pp. 3-20.

Arduino, 2021. *Arduino Mega 2560 Rev3.* [Online]
Available at: https://store.arduino.cc/products/arduino-mega-2560-rev3
[Accessed 4th February 2023].

Armitage, C., 2017. *How waste steam is helping firms go green..* [Online]
Available at: https://www.recyclingwasteworld.co.uk/in-depth-article/how-waste-steam-is-helping-firms-to-go-green/160999/
[Accessed 10 July 2022].

ASCO, 2012. *Solenoid Valves: Direct Operated for High Pressure Fluids 1/8 - 1/4.* [Online]
Available at: https://www.valves-direct.com/product/e262k090s1n00h1-series-262-brass-body-24v-dc-g14-22-nc-solenoid-valves-direct-operated-for-high-pressure-fluids-47687?v=79cba1185463
[Accessed 18 June 2019].

BEIS, 2022. *Quarterly Energy Prices: UK July to September 2022 and estimates for 2022,* s.l.: Department for Business, Energy, & Industrial Strategy.

Bell, S., 2001. *Measurement Good Practice Guide No. 11 (Issue 2): A Beginner's Guide to Uncertainty of Measurement,* Teddington: National Physical Laboratory.

Bianchi, M. et al., 2019. Experimental analysis of a micro-ORC driven by piston expander for low-grade heat recovery. *Applied Thermal Engineering,* 148(1), pp. 1278-1291.

Black, N. & Davis, H., 1913. *Practical physics for secondary schools. Fundamental principles and applications to daily life.* London: Macmillan & Comp.

Blatter, M., 2014. *File:T-s-diagram-steam.png.* [Online]
Available at: https://commons.wikimedia.org/wiki/File:T-s-diagram-steam.png
[Accessed 4 August 2020].

Bortolin, V. et al., 2021. Thermodynamical model of an atmospheric steam engine. *Journal of the Brazlian Society of Mechanical Sciences and Engineering,* Volume 43, p. 493.

Bosch, 2023. *Bosch planning tool for steam boiler systems.* [Online]
Available at: https://www.boiler-planning.com/technology/steam/
[Accessed 4th January 2023].

Bruckner, S. et al., 2015. Industrial waste heat recovery technologies: An economic analysis of heat transformation technologies. *Applied Energy,* 151(1), pp. 157-167.

Brueckner, S., Arbter, R., Pehnt, M. & Laevmann, E., 2017. Industrial Waste Heat Potential in Germany - A Bottom - Up Analysis. *Energy Efficiency,* 10(1), pp. 513-525.

Cengel, Y. & Boles, M., 2011. *Thermodynamics: An Engineering Approach.* 7th Edition ed. NY: McGraw Hill.

Cengel, Y. & Cimbala, J., 2010. *Fluid Mechanics: Fundamentals and Applications.* 2nd ed. s.l.:McGraw-Hill.

CES Energy, 2019. *ORC Technology Overview.* [Online]
Available at: https://www.cesenergy.com/what-we-do/waste-heat-to-power/
[Accessed May 2019].

Chin, J. et al., 2018. *State-of-the-Art Technologies on Low-Grade Heat Recovery and Utilization in Industry.* [Online]
Available at: https://www.intechopen.com/books/energy-conversion-current-technologies-and-future-trends/state-of-the-art-technologies-on-low-grade-heat-recovery-and-utilization-in-industry
[Accessed May 2019].

Chu, J., 2018. *Sun-soaking device turns water into superheated steam.* [Online]
Available at: http://news.mit.edu/2018/sun-device-heats-water-superheated-steam-1211
[Accessed May 2019].

Cooper, T. & Wallace, J., 2008. *Design of a 200kWe Solar Thermal Power Plant for Ontario.* Jacksonville, ASME, pp. 1-16.

Dahash, A., Ochs, F., Janetti, M. & Streicher, W., 2019. Advances in seasonal thermal energy storage for solar district heating applications: A critical review on large-scale hot-water tank and pit thermal energy storage systems. *Applied Energy,* 239(1), pp. 296-315.

Davies, G. et al., 2016. *Large scale cooling systems using mains water.* Edinburgh, Gustav Lorentzen Conference.

Dellicompagni, P., Saravia, L., Altamirano, M. & Franco, J., 2018. Simulation and testing of a solar reciprocating steam engine. *Energy,* May, Issue 1, pp. 662-674.

DM, 2020. *UHMW (Ultra-High-Molecular-Weight Polyethylene).* [Online]
Available at: https://dielectricmfg.com/knowledge-base/uhmw/
[Accessed 09 April 2020].

efunda, 2020. *Aluminium.* [Online]
Available at: https://www.efunda.com/materials/elements/TC_Table.cfm?Element_ID=Al
[Accessed 06 May 2020].

Element Energy, 2014. *The potential for recovering and using surplus heat from industry (Report for UK Government Department of Energy & Climate Change).* [Online]
Available at:
https://assets.publishing.service.gov.uk/government/uploads/system/uploads/attachment_data/file/294900/element_energy_et_al_potential_for_recovering_and_using_surplus_heat_from_industry.pdf
[Accessed 11 October 2018].

Energy Solutions, 2018. *Off Grid Guide 2018.* [Online]
Available at: https://www.energy-solutions.co.uk/guides/off-grid-guide.pdf
[Accessed May 2019].

Engineering Toolbox (a), nd. *Water - Density, Specific Weight and Thermal Expansion Coefficient.* [Online]
Available at: https://www.engineeringtoolbox.com/water-density-specific-weight-d_595.html
[Accessed 04 May 2020].

Engineering Toolbox (b), nd. *Water - Dynamic and Kinemtaic Viscosity.* [Online]
Available at: https://www.engineeringtoolbox.com/water-dynamic-kinematic-viscosity-d_596.html
[Accessed 04 May 2020].

Engineering Toolbox (c), nd. *Water - Specific Heat.* [Online]
Available at: https://www.engineeringtoolbox.com/specific-heat-capacity-water-d_660.html
[Accessed 04 May 2020].

Engineering Toolbox (d), nd. *Water - Thermal Conductivity.* [Online]
Available at: https://www.engineeringtoolbox.com/water-liquid-gas-thermal-conductivity-temperature-pressure-d_2012.html
[Accessed 04 May 2020].

Engineering Toolbox (e), nd. *Water Vapor - Specific Heat.* [Online]
Available at: https://www.engineeringtoolbox.com/water-vapor-d_979.html
[Accessed 04 May 2020].

Ewing, J., 1910. *The Steam Engine and Other Heat Engines.* 3rd Edition ed. Cambridge: Cambridge University Press.

Farey, J., 1827. *A Treatise on the Steam Engine: Historical, Practical, and Descriptive.* London: A & R Spottiswoode.

Faux, D. & Godolphin, J., 2019. Manual timing in physics experiments: Error and uncertainty. *American Journal of Physics,* Volume 87.

Frate, G., Ferrari, L. & Desideri, U., 2019. Analysis of suitability ranges of high temperature heat pump working fluids. *Applied Thermal Engineering,* 150(1), pp. 628-640.

Gao, C., Lee, S. & Yang, Y., 2017. Thermally Regenerative Electrochemical Cycle for Low-Grade Heat Harvesting. *ACS Energy Letters,* 2(10), pp. 2326-2334.

Ghoreishi-Madiseh, S. et al., 2019. Application of Borehole Thermal Energy Storage in Waste Heat Recovery from Diesel Generators in Remote Cold Climate Locations. *Energies,* 12(4).

Gidzewicz, C., 2016. *Physics: Engineering Physics AQA A-Level Year 2.* London: HarperCollins.

Haddad, C. et al., 2014. Some efficient solutions to recover low and medium waste heat: competitiveness of ther thermoacoustic technology. *Energy Procedia,* Volume 50, pp. 1056-1069.

Hartley, G., 2018. *What is district heating?.* [Online]
Available at: https://energysavingtrust.org.uk/blog/what-district-heating
[Accessed 20 May 2020].

Hechtel, K., 2014. *Turning Up the Heat: Considerations for High Temperature Applications,* s.l.: The IAPD Magazine.

Hills, R., 1989. *Power from Steam: A History of the Steam Engine.* Cambridge: Cambridge University Press.

Ho Chan, C. et al., 2017. *Mechanical Engineering Masters Group Design Project Main Report: Design, Build and Test of an Atmospheric Steam Engine (unpublished report - available on request),* Southampton: University of Southampton, Faculty of Engineering & the Environment.

Holmgren, M., 2007. *XSteam: Thermodynamic Properties of Water and Steam.* [Online]
Available at: https://uk.mathworks.com/matlabcentral/fileexchange/9817-x-steam-thermodynamic-properties-of-water-and-steam
[Accessed 21 July 2021].

Hyeongwook, I. et al., 2016. High-efficiency electrochemical thermal energy harvester using carbon nanotube aerogel sheet electrodes. *Nature,* Volume 7.

IEA-SHC, 2020. *Solar Update Vol 71: July 2020.* [Online]
Available at: https://www.iea-shc.org/Data/Sites/1/publications/2020-07-Solar-Update-Newsletter.pdf
[Accessed 14 July 2020].

IRENA, 2019. *FUTURE OF SOLAR PHOTOVOLTAIC: Deployment, investment, technology, grid integration and socio-economic aspects (A Global Energy Transformation: paper),* Abu Dhabi: International Renewable Energy Agency.

IRENA, 2022. *Solar Energy.* [Online]
Available at: https://www.irena.org/Energy-Transition/Technology/Solar-energy
[Accessed 23rd February 2023].

Jamil, U. & Hassan, M. F., 2019. *Land area requirement analysis for dish thermal solar field.* s.l., AIP Conference Proceedings 2126, 150004.

Josse, H., 1870. *Revue Industrielle.* [Online]
Available at: https://gallica.bnf.fr/ark:/12148/bpt6k97674548
[Accessed 20 March 2020].

Jouhara, H. et al., 2018. Waste Heat Recovery Technologies and Applications. *Thermal Science and Engineering Progress,* 6(1), pp. 268-289.

Kalogirou, S. A., 2004. Solar thermal collectors and applications. *Progress in Energy and Combustion Science,* 30(3), pp. 231-295.

Kamboj, V., Agrawal, H., Malan, A. & Yadav, A., 2019. Thermal performance of the steam boiler based on Scheffler solar concentrator for domestic application: Experimental investigation. *Australian Journal of Mechanical Engineering,* 19(5), pp. 521-531.

Kennedy, K. M. et al., 2022. The role of concentrated solar power with thermal energy storage in least-cost highly reliable electricity systems fully powered by variable renewable energy. *Advances in Applied Energy,* Volume 6.

KERN, nd. *KERN CH50K100.* [Online]
Available at: https://docs.rs-online.com/7e7e/0900766b8168379e.pdf
[Accessed 12th February 2023].

Kim, H. & Jung, T., 2018. Independent solar photovoltaic with Energy Storage Systems (ESS) for rural electrification in Myanmar. *Renewable and Sustainable Energy Reviews,* Volume 82, pp. 1187-1194.

Kimmel, T., 2012. *Advanced Uniflow Engine - Dan Gelbart.* [Online]
Available at: http://www.kimmelsteam.com/gelbart-uniflow.html
[Accessed 18 August 2022].

Konig, J. et al., 2018. *Thermoelectric waste heat recovery (Conference: Low Temperature and Waste Heat Use in Communal and Industrial Energy Supply Systems).* Bremen, Hochschule Bremen City University.

Kosky, P., Balmer, R., Keat, W. & Wise, G., 2012. *Exploring Engineering: An Introduction to Engineering and Design.* 3rd ed. s.l.:Academic Press.

Kumar, A. & Dibakar, R., 2021. A critical review on waste heat recovery utilisation with special focus on Organic Rankine Cycle applications. *Cleaner Engineering and Technology,* Volume 5.

L.R. Ingersoll Physics Museum, 2023. *Centrifugal Governor.* [Online]
Available at:
https://www.physics.wisc.edu/ingersollmuseum/exhibits/mechanics/centrifugalgovernor/
[Accessed 24th February 2023].

Landelle, A. et al., 2017. Organic Rankine cycle design and performance comparison based on experimental database. *Applied Energy,* 204(1), pp. 1172-1187.

Langhan, M. & O'Toole, K., 2017. A new technology for cost effective low grade waste heat recovery. *Energy Procedia,* Volume 123, pp. 188-195.

Lee, H., 2019. *ME539 Chapter Five Compact Heat Exchangers.* [Online]
Available at: http://homepages.wmich.edu/~leehs/ME539/Chapter%205%20HSL.pdf
[Accessed 23 April 2020].

Li, G., 2019. Organic Rankine cycle environmental impact investigation under various working fluids and heat domains concerning refrigerant leakage rates. *International Journal of Environmental Science and Technology,* Volume 16, pp. 431-450.

Li, L., Tao, L., Li, Q. & Hu, Y., 2021. Experimentally economic analysis of ORC power plant with low-temperature waste heat recovery. *International Journal of Low-Carbon Technologies,* Volume 16, pp. 35-44.

Liu, C. et al., 2013. The environmental impact of organic Rankine cycle for waste heat recovery through life-cycle assessment. *Energy,* 56(1), pp. 144-154.

Ma, F.-K.et al., 2017. Parameter Optimization on the Uniflow Scavenging System of an OP2S-GDI Engine Based on Indicated Mean Effective Pressure (IMEP). *Energies,* 10(3), p. 368.

Mahmoudi, A., Fazli, M. & Morad, M., 2018. A recent review of waste heat recovery by Organic Rankine Cycle. *Applied Thermal Engineering,* Volume 143, pp. 660-675.

MatWeb, 2020. *Gilding Copper, UNS21000, OSO50 Temper.* [Online]
Available at:
http://www.matweb.com/search/DataSheet.aspx?MatGUID=35deceed46274e66af6cee9f392ee617&ckck=1
[Accessed 08 April 2020].

Mauthner, F., 2014. *SOLTRAIN Training Course: Solar Heat for Industrial Applications, Design Study Part II.* [Online]
Available at:
http://www.crses.sun.ac.za/files/services/events/workshops/07_Solar%20Heat%20for%20Industrial%20Applications_Mauthner.pdf

Mechler, S., 2022. *How to Validate an Autoclave: Steam Quality Testing.* [Online]
Available at: https://consteril.com/steam-quality-testing/
[Accessed 4th January 2023].

Meyer, F., 2018. *Energy Supply and Heat Utilization on Today's Merchant Vessels Today's Solutions and Improved Heat Energy Recovering Principles (Conference: Low Temperature and Waste Heat Use in Communal and Industrial Energy Supply Systems).* Bremen, Hochschule Bremen City University.

Mikielewicz, D. & Wajs, J., 2018. *High-temperature heat pumps new devices for heat recovery and production of technological steam (Conference: Low Temperature and Waste Heat Use in Communal and Industrial Energy Supply Systems).* Bremen, Hochschule Bremen City University.

Muhammad, U., Imran, M., Lee, D. & Park, B., 2015. Design and experimental investigation of a 1kW Organic Rankine Cycle system using R245fa as a working fluid for low-grade waste heat recovery from steam. *Energy Conversion and Management,* Volume 103, pp. 1089-1100.

Muller, G., 2013. The atmospheric steam engine as energy converter flor low and medium temperature thermal energy. *Renewable Energy,* Volume 53, pp. 94-100.

Muller, G. et al., 2018. The Condensing Engine: A Heat Engine for Operating Temperatures of 100C and Below. *Proceedings of the Institution of Mechanical Engineers, Part A: Journal of Power and Energy,* 232(4), pp. 437-448.

Muller, G. & Howell, C., 2021. Comparitive analysis of recent and historic low power heat engines for low grade waste heat recovery. *Applied Engineering,* Volume 5, pp. 7-13.

Muller, G. & Parker, G., 2015. Experimental investigation of the atmospheric steam engine with force expansion. *Renewable Energy,* Volume 75, pp. 348-355.

Mustafa, A. & Hadi, M., 2021. A Comparative Study of Multi-form Steam Generators Using Concentrated Solar Power. *Journal of Advanced Research in Fluid Mechanics and Thermal Sciences,* 88(2), pp. 157-168.

NuclearPower, 2020. *Thermal Conductivity of Water and Steam.* [Online]
Available at: https://www.nuclear-power.net/nuclear-engineering/heat-transfer/thermal-conduction/thermal-conductivity/thermal-conductivity-of-water-and-steam/
[Accessed 04 May 2020].

OVO Energy, nd. *How much electricity does a home use?.* [Online]
Available at: https://www.ovoenergy.com/guides/energy-guides/how-much-electricity-does-a-home-use.html
[Accessed 29 November 2019].

Papapetrou, M. et al., 2018. Industrial waste heat: Estimation of the technically available resource in the EU per industrial sector, temperature level and country. *Applied Thermal Engineering,* Volume 138, pp. 207-216.

Pretorius, I., Piketh, S. & Burger, R., 2015. The impact of the south african energy crisis on emissions. *WIT Transactions on Ecology and the Environment,* Volume 198.

Quoilin, S. et al., 2013. Techno-economic survey of Organic Rankine Cycle (ORC) systems. *Renewable and Sustainable Energy Reviews,* Volume 22, pp. 168-186.

Rahbar, K. et al., 2017. Review of organic Rankine cycle for small-scale pplications. *Energy Conversion and Management,* Volume 134, pp. 135-155.

Rajput, R., 2006. *Thermal Engineering.* 6th Edition ed. New Delhi: Laxmi Publications.

Redwood, 2018. *UHMW (Polyethylene).* [Online]
Available at: https://redwoodplastics.com/products/uhmw-polyethylene/
[Accessed 09 April 2020].

Renewable Energy Hub UK, 2019. *Photovoltaic vs Solar Thermal.* [Online]
Available at: https://www.renewableenergyhub.co.uk/main/solar-panels/photovoltaic-vs-solar-thermal/
[Accessed May 2019].

Rogers, G. & Mayhew, Y., 1995. *Thermodynamic and Transport Properties of Fluids.* 5th Edition ed. s.l.:Blackwell Publishing.

Rose, J., 1988. SOME ASPECTSOF CONDENSATION HEAT TRANSFER THEORY. *INT. COMM. HEAT MASS TRANSFER,* Volume 15, pp. 449-473.

RS Pro, 2023. *Datasheet: RS Pro Pressure Sensor for Air.* [Online]
Available at: https://docs.rs-online.com/01b0/A700000008971853.pdf
[Accessed 6th May 2023].

RS Pro, nd. *RS PRO Type K Thermocouple 20mm Length, 5mm Diameter → +750°C.* [Online]
Available at: https://docs.rs-online.com/d352/A700000007350686.pdf
[Accessed 6th May 2023].

RS-Pro, nd. *RS Pro Portable Scale 2028725: Data Sheet.* [Online]
Available at: https://docs.rs-online.com/a53d/A700000006961186.pdf
[Accessed 4th February 2023].

Schmidt, D. et al., 2017. Low Temperature District Heating for Future Energy Systems. *Energy Procedia,* 116(1), pp. 26-38.

Science Museum Group, nd. *Diagram of Short D Slide Valve (balanced).* [Online]
Available at: https://collection.sciencemuseumgroup.org.uk/objects/co8033038/diagram-of-short-d-slide-valve-balanced-paper-model
[Accessed 24th February 2023].

Semmens, P. & Goldfinch, A., 2000. *How Steam Locomotives Really Work.* Oxford: Oxford University Press.

SolenoidValveWorld, 2020. *15mm Solenoid Valve Nylon Normally Closed Water Appliance 1175BC.* [Online]
Available at: https://www.solenoid-valve.world/product/72/rpe-srl/15mm-solenoid-valve-nylon-normally-closed-water-appliance-1175bc
[Accessed 14 April 2020].

Sommer, K., 2018. *Future-Proof Thermal Energy Systems (Conference: Low Temperature and Waste Heat Use in Communal and Industrial Energy Supply Systems).* Bremen, Hochschule Bremen City University.

Sparkfun, nd. *Load Cell Amplifier HX711 Breakout Hookup Guide.* [Online]
Available at: https://learn.sparkfun.com/tutorials/load-cell-amplifier-hx711-breakout-hookup-guide?_ga=2.69316240.1285038029.1672740423-1369705097.1672740423
[Accessed 3rd January 2023].

SpiraxSarco, 2023. *Learn about Steam: Pipeline Ancillaries, Separators.* [Online]
Available at: https://www.spiraxsarco.com/learn-about-steam/pipeline-ancillaries/separators
[Accessed 4th January 2023].

Su, Z. et al., 2021. Opportunities and strategies for multigrade waste heat utilization in various industries: A recent review. *Energy Conversion and Management,* Volume 229.

Tauveron, N., Colasson, S. & Gruss, J.-A., 2015. *Conversion of waste heat to electricity: cartography of possible cycles due to hot source characteristics.* Pau, s.n.

TCE, 2019. News in Numbers. *The Chemical Engineer*, March, pp. 5-6.

Tchanche, B., Lambrinos, G., Frangoudakis, A. & Papadakis, G., 2011. Low-grade heat conversion into power using organic Rankine cycles - A review of various applications. *Renewable and Sustainable Energy Reviews,* 15(8), pp. 3963-3979.

The World Bank (a), 2020. *Global Solar Atlas, Solar GIS.* [Online]
Available at: https://solargis.com/maps-and-gis-data/download/south-africa
[Accessed 17 December 2022].

The World Bank (b), 2020. *Global Solar Atlas, Solar GIS.* [Online]
Available at: https://solargis.com/maps-and-gis-data/download/united-kingdom
[Accessed 17 December 2022].

Thurston, R., 1878. *History of the growth of the Steam engine.* New York: D. Appleton & Co.

TLV, 2019. *Recovering Steam Clouds and Waste Heat.* [Online]
Available at: https://www.tlv.com/global/UK/steam-theory/steam-clouds-waste-heat-recovery.html
[Accessed May 2019].

Tocci, L., Pal, T., Pesmazoglou, I. & Franchetti, B., 2017. Small Scale Organic Rankine Cycle (ORC):. *Energies,* 10(413), pp. 1-26.

Trelleborg, na. *Turcon Gyd Ring.* [Online]
Available at: https://www.trelleborg.com/en/seals/products-and-solutions/hydraulic-piston-seals/turcon-glyd-ring
[Accessed 17 August 2022].

US DOE, 2008. *Waste Heat Recovery - Technology and Oppurtunities in US Industry,* s.l.: BCS.

US DOE, 2017. *Advanced Manufacturing: Waste Heat Recovery Resource Page.* [Online]
Available at: https://www.energy.gov/eere/amo/articles/waste-heat-recovery-resource-page
[Accessed 11 October 2018].

US EPA, 2017. *Geothermal Energy.* [Online]
Available at: https://archive.epa.gov/climatechange/kids/solutions/technologies/geothermal.html
[Accessed 30 March 2020].

Velez, F., 2014. Selecting Working Fluids in an Organic Rankine Cycle for Power Generation from Low Temperature Heat Sources. *DYNA,* 81(188), pp. 173-180.

Wajs, J. & Mikielewicz, D., 2018. *High-efficiency mini and micro heat exchangers for domestic ORC (Conference: Low Temperature and Waste Heat Use in Communal and Industrial Energy Supply Systems).* Bremen, Hochschule Bremen City University.

Wang, S. et al., 2019. Ecological cumulative exergy consumption analysis of organic Rankine cycle for waste heat power generation. *Journal of Cleaner Production,* Volume 218, pp. 543 - 554.

Wang, X. & Zhao, H., 2019. A High-Efficiency Two-Stroke Engine Concept: The Boosted Uniflow Scavenged Direct-Injection Gasoline (BUSDIG) Engine with Air Hybrid Operation. *Engineering,* 5(3), pp. 535-547.

Wong, V. & Tung, S., 2016. Overview of automotive engine friction and reduction trends– Effects of surface, material, and lubricant-additive technologies. *Friction,* 4(1), pp. 1-28.

Xu, Z., Wang, R. & Chun Yang, 2019. Perspectives for low-temperature waste heat recovery. *Energy,* Volume 176, pp. 1037-1043.

Yan, B., He, S., Sun, K. & Wang, S., 2020. Complexity and Multistability in the CentrifugalFlywheel Governor System WithStochastic Noise. *IEEE Access,* Volume 8, pp. 30092-30103.

Zhang, X. et al., 2019. Economic Analysis of Organic Rankine Cycle Using R123 and R245fa as Working Fluids and a Demonstration Project Report. *Applied Sciences,* 9(2), pp. 1-26.

Chapter 9 Appendices

Appendix A Data Repository Contents

Data files associated with this thesis have been stored on the University of Southampton Pure database for future access. Below is a list of the data with associated DOI numbers. Table 9-1 and Table 9-2 give more detailed descriptions of the coded files and technical drawings respectively.

Mk.III Engine Files (DOI: 10.5258/SOTON/D2330):

- Mk.III technical drawings (.pdf).
- Mk.III engine and slide valve CAD files (.stp .dxf).
- Mk.III engine control code, both with and without steam expansion (.txt).
- Mk.III engine and slide valve photos and videos (.jpeg .mov).
- Mk.III theoretical efficiency model code (.txt).
- Mk.III steam evacuation profile theoretical model code (.txt).
- Mk.III engine raw data and data analysis file (.xlsx).
- Condensing engine project sensor calibration files (.xlsx).

Mk.IV Engine Files (DOI: 10.5258/SOTON/D2334):

- Mk.IV technical drawings (.pdf).
- Mk.IV engine item list (.xlsx).

Heat Recovery and Re-Use Files (DOI: 10.5258/SOTON/D2333):

- Heat recovery potential theoretical model code (.txt).
- Heat recovery experiment technical drawings (.pdf).
- Heat recovery experiment control code (.txt).
- Heat recovery experiment raw data and data analysis files (.xlsx).
- Heat recovery experiment photos and videos (.tiff .mov).

Appendix B Mathematical Models and Control Code Descriptions

This section of the Appendices gives all mathematical and microcontroller code built for the completion of this project. The code names with descriptions are given in Table 9-1. Code script is stored in the University of Southampton repository. Code files listed below have been validated using hand calculation wherever possible.

Table 9-1 List of mathematical code built during the completion of this project along with description of their use.

Code Title	Program	Description
Uniflow_Engine_Isentropic_V2.txt	Matlab (.m)	Simulation of Mk.III uniflow condensing engine theoretical efficiency using isentropic equations.
MkIII_Uniflow_Evacuation_Real_Test_Check_V1.txt	Matlab (.m)	Simulation of steam evacuation from the Mk.III engine. Used in comparison against real engine test data.
Uniflow_Evacuation_Slot_Simulation_V1.txt	Matlab (.m)	Simulation of steam evacuation from the Mk.III engine. Used to predict evacuation pressure profile of the uniflow engine.
MkIII_Engine_Control_No_Expansion_V1.txt	Arduino IDE (.ino)	Control script for the Mk.III engine operating without expansion. Used to control valves and output engine speed and friction brake power.
MkIII_Engine_Control_Expansion_V1.txt	Arduino IDE (.ino)	Control script for the Mk.III engine operating with expansion. Used to control valves and output engine speed and friction brake power.
Two_Stage_Engine_Simulation_V1.txt	Matlab (.m)	Simulation of condensing engine system with heat recovery and re-use via second sub-atmospheric cylinder stage.
Sensor_Datalogger_V1.txt	Arduino IDE (.m)	Code for pressure and temperature datalogging, used during heat recovery experiments.
HR_Experiment_Valve_Control_V1.txt	Arduino IDE (.m)	Control code for valve operation during heat recovery experiments.

Appendix C Technical Drawings List

Technical drawing numbers relating to this thesis are listed in Table 9-2 along with a description. Drawings are stored in the University of Southampton data repository.

Table 9-2 Technical drawing list with document references and descriptions

Item Description	Drawing Reference	Drawing Description
MK.III Engine	UOS10000-00-000_A	Assembly Drawing
MK.III Engine	UOS10000-00-000_B	Assembly Drawing
MK.III Engine	UOS10000-00-000_C	Assembly Drawing
MK.III Engine	UOS10000-01-001_A	Base Plate
MK.III Engine	UOS10000-01-002_B	Frame Rear Upright
MK.III Engine	UOS10000-01-003_A	Lower Cylinder Shelf
MK.III Engine	UOS10000-01-004_B	Crank Mounting Plate
MK.III Engine	UOS10000-01-005_A	Mounting Plate Support
MK.III Engine	UOS10000-01-009_B	Frame Side Support
MK.III Engine	UOS10000-01-010_A	Upper Cylinder Shelf
MK.III Engine	UOS10000-01-012_A	Slide Valve Actuator Mounting Bracket
MK.III Engine	UOS10000-01-013_A	Threaded Bar, M5, Slide Valve
MK.III Engine	UOS10000-01-014_A	Bracket, Slide Valve Solenoid Mount
MK.III Engine	UOS10000-01-015_A	25T Gear, Modified
MK.III Engine	UOS10000-01-016_A	75T Gear, Modified
MK.III Engine	UOS10000-02-001_B	Condensing Cylinder
MK.III Engine	UOS10000-02-002_A	Condensing Piston
MK.III Engine	UOS10000-02-003_A	Thermal Insulation Sheet 2mm
MK.III Engine	UOS10000-02-004_A	Condenser to Crank Connecting Stud
MK.III Engine	UOS10000-02-005_A	Cylinder Saddle Clamp
MK.III Engine	UOS10000-03-001_A	Crank Disk

Item Description	Drawing Reference	Drawing Description
MK.III Engine	UOS10000-03-002_A	Flywheel
MK.III Engine	UOS10000-03-005_A	Shaft, Vacuum Pump
MK.III Engine	UOS10000-03-006_A	Shaft, Flywheel
MK.III Engine	UOS10000-03-008_A	Crank Disk – Vacuum Pump
MK.III Engine	UOS10000-03-010_A	Spacer Cylinder, Flywheel
MK.III Engine	UOS10000-03-011_B	Sensor Mounting Bracket
MK.III Engine	UOS10000-03-012_A	Shaft, Encoder
MK.III Engine	UOS10000-03-013_A	Photoelectric Sensor Bracket
MK.III Engine	UOS10000-03-015_A	Encoder Bracket
MK.III Engine	UOS10000-04-001_A	Vacuum Pump Cylinder
MK.III Engine	UOS10000-04-002_A	Vacuum Pump Piston
MK.III Engine	UOS10000-04-004_A	Connecting Stud, Vacuum Pump
MK.III Engine	UOS10000-04-005_A	Vacuum Pump Lower Bracket
MK.III Engine	UOS10000-04-007_A	Vacuum Pump Upper Bracket
MK.III Engine	MkIII-Updated-Piston	Updated Piston Design Dimensions
MK.III Engine	MkIII-Electronics-Schematic	Electronics and Wiring Schematic
MK.III Engine	MkIII-Breadboard-Schematic	Breadboard Wiring Diagram
FPHE	CRH-CDS1-A1	FPHE Assembly
FPHE	CRH-CDS1-0001	FPHE End Plate One
FPHE	CRH-CDS1-0003	FPHE Steam Plate Seal
FPHE	CRH-CDS1-0004	FPHE Port Seal
FPHE	CRH-CDS1-0005	FPHE Steam Plate
FPHE	CRH-CDS1-0006	FPHE Water Plate Seal
FPHE	CRH-CDS1-0007	FPHE Water Plate
FPHE	CRH-CDS1-0008	FPHE End Plate Two

Item Description	Drawing Reference	Drawing Description
MK.IV Engine	0125-000	General Assembly of Steam Condensing Engine
MK.IV Engine	0125-001-B	Base Plate
MK.IV Engine	0125-002-A	Top Plate
MK.IV Engine	0125-003-B	Vertical Plate 1
MK.IV Engine	0125-004-A	Vertical Plate 2
MK.IV Engine	0125-005-A	Vertical Plate 3
MK.IV Engine	0125-006-A	Vertical Plate 4
MK.IV Engine	0125-007-A	Vertical Plate 5
MK.IV Engine	0125-008-A	Vertical Plate 6
MK.IV Engine	0125-009-B	Vertical Plate 7
MK.IV Engine	0125-010-A	Bottom Bracket
MK.IV Engine	0125-011-A	Top Bracket
MK.IV Engine	0125-012-A	Long Post
MK.IV Engine	0125-013-A	Short Post
MK.IV Engine	0125-014-A	Side Guard Rail
MK.IV Engine	0125-015-A	Bearing Housing
MK.IV Engine	0125-016-A	Long Crankshaft
MK.IV Engine	0125-017-A	Short Crankshaft
MK.IV Engine	0125-018-A	Crankshaft Web
MK.IV Engine	0125-019-A	Crank Pin
MK.IV Engine	0125-020-A	Crankshaft Counterweight
MK.IV Engine	0125-021-A	Crank Pin Shim
MK.IV Engine	0125-022-A	Crank Pin Spacer
MK.IV Engine	0125-023-A	15mm ID Bearing Retaining Plate

Item Description	Drawing Reference	Drawing Description
MK.IV Engine	0125-024-A	20mm ID Bearing Retaining Plate
MK.IV Engine	0125-025-A	25 ID Bearing Retaining Plate
MK.IV Engine	0125-026-A	Lay Shaft
MK.IV Engine	0125-027-A	Output Shaft
MK.IV Engine	0125-028-A	Output Shaft Spacer
MK.IV Engine	0125-029-A	Layshaft Spacer
MK.IV Engine	0125-030-A	27 Teeth Modified Spur Gear
MK.IV Engine	0125-031-A	54 Teeth Modified Spur Gear
MK.IV Engine	0125-032-A	Flywheel
MK.IV Engine	0125-033-A	Crankshaft Coupling, Cylinder 1 Side
MK.IV Engine	0125-034-A	Crankshaft Coupling, Cylinder 2 Side
MK.IV Engine	0125-035-A	Crankshaft Coupling Spacer
MK.IV Engine	0125-036-A	RPM Sensor Fixed Bracket
MK.IV Engine	0125-037-A	RPM Sensor Lock Nut
MK.IV Engine	0125-038-A	RPM Sensor Adjustable Bracket
MK.IV Engine	0125-039-A	RPM Sensor Target Disk
MK.IV Engine	0125-040-A	Pump Cylinder
MK.IV Engine	0125-041-A	Pump Crank Arm
MK.IV Engine	0125-042-A	Pump Piston
MK.IV Engine	0125-043-A	Pump Piston Pivot Plate
MK.IV Engine	0125-044-A	Pump Piston Pin
MK.IV Engine	0125-045-A	Pump Link
MK.IV Engine	0125-046-A	Pump Spacer
MK.IV Engine	0125-047-A	Pump Piston Gasket
MK.IV Engine	0125-048-A	Pump Piston Without Sealing

Item Description	Drawing Reference	Drawing Description
MK.IV Engine	0125-049-A	Sub Assembly of Expansion Cylinder
MK.IV Engine	0125-050-A	Expansion Cylinder
MK.IV Engine	0125-051-A	Expansion Cylinder End Cap
MK.IV Engine	0125-052-A	Expansion Cylinder Exhaust Manifold
MK.IV Engine	0125-053-A	Expansion Cylinder Jacket Body
MK.IV Engine	0125-054-A	Expansion Cylinder Jacket End Plate
MK.IV Engine	0125-055-A	Expansion Cylinder Jacket Gasket
MK.IV Engine	0125-056-A	Expansion Cylinder Insulation Ring
MK.IV Engine	0125-057-A	Expansion Cylinder Inlet Port
MK.IV Engine	0125-058-A	Expansion Cylinder Exhaust Port
MK.IV Engine	0125-059-A	Sub Assembly of Expansion Piston
MK.IV Engine	0125-060-A	Expansion Piston Body
MK.IV Engine	0125-061-A	Expansion Piston Top Cap
MK.IV Engine	0125-062-A	Expansion Piston Bottom Cap
MK.IV Engine	0125-063-A	Expansion Piston “O” Ring Housing
MK.IV Engine	0125-064-A	Expansion Piston “O” Ring Shim, 7.00mm Thick
MK.IV Engine	0125-065-A	Expansion Piston “O” Ring Shim, 7.15mm Thick
MK.IV Engine	0125-066-A	Expansion Piston “O” Ring Shim, 7.30mm Thick
MK.IV Engine	0125-067-A	Expansion Piston “O” Ring Shim, 7.45mm Thick
MK.IV Engine	0125-068-A	Expansion Piston “O” Ring Shim, 7.60mm Thick
MK.IV Engine	0125-069-A	Expansion Piston Seal & Wear Ring Housing

Item Description	Drawing Reference	Drawing Description
MK.IV Engine	0125-070-A	Expansion Piston Packing Gland
MK.IV Engine	0125-071-A	Expansion Piston Piston-Ring Housing
MK.IV Engine	0125-072-A	Sub Assembly of Conrod
MK.IV Engine	0125-073-A	Conrod Shaft
MK.IV Engine	0125-074-A	Conrod Crankshaft Connection
MK.IV Engine	0125-075-A	Conrod Piston Connection
MK.IV Engine	0125-076-A	Expansion Piston Pin Spacer
MK.IV Engine	0125-077-A	40T Modified Timing Belt Pulley
MK.IV Engine	0125-078-A	Condensate Trip Tray
MK.IV Engine	0125-079-B	Front Guard
MK.IV Engine	0125-080-B	Rear Guard
MK.IV Engine	0125-081-A	Pump Guard

Appendix D Calculations

D.1 Mk.III Engine Thermal Expansion

The piston with nominal radius of 24.992mm is made of brass with a thermal expansion coefficient of 18×10^{-6} m/m.K. The linear thermal expansion equation can be applied to the radius of a thin ring, defined as:

$$\Delta R = R_1 \times \alpha_{te} \times \Delta T$$

In this case, the ambient condition is 20°C and the piston is assumed to come to equilibrium at 100°C. This represents the worst-case scenario. Therefore, the theoretical increase in piston radius due to thermal expansion is:

$$\Delta R = 24.992 \times 18 \times 10^{-6} \times 80 = 0.036mm$$

The cylinder with nominal internal bore radius of 25.006mm also made from brass and heated from 20°C to 100°C undergoes the following thermal expansion:

$$\Delta R = 25.006 \times 18 \times 10^{-6} \times 80 = 0.036mm$$

This shows that at equal temperatures the piston and cylinder should expand by equal amounts preventing jamming due to thermal expansion.

Thermal expansion theory can be used to show that the cylinder must be 31°C cooler than the piston before this gap is closed and jamming occurs.

$$\Delta R = 25.006 - 24.992 = 0.014mm$$

$$\Delta T = \frac{\Delta R}{R_1 \times \alpha_{te}} = \frac{0.014}{24.992 \times 18 \times 10^{-6}} = 31℃$$

D.2 MK.III Engine Condenser Heat Loads

On the MK.III engine one revolution equals one cylinder volume of steam sent to the condenser. When the engine is running at 60rpm and an expansion ratio of *n* = 1 (worst case) this equates to a steam volume of:

$$V_{s,rev} = \frac{\pi \times d^2}{4} \times L = \frac{\pi \times (50 \times 10^{-3})^2}{4} \times (100 \times 10^{-3}) = 1.96 \times 10^{-4} m^3$$

At 1 bar this is known to give a steam mass of:

$$m_{s,rev} = V_{s,rev} \times \rho_s = 1.96 \times 10^{-4} \times 0.59 = 1.16 \times 10^{-4} kg$$

At 1 bar the enthalpy of steam is 2675kJ/kg (Rogers & Mayhew, 1995). Assuming the condenser is operating with a heat sink temperature of 20°C the enthalpy of the condensate is 83.9kJ/kg. This allows the heat load per revolution to be calculated:

$$Q_{rev} = (2675 - 83.9) \times 1.16 \times 10^{-4} = 0.3\ kJ$$

At an engine speed of 60rpm one engine revolution occurs each second, giving a condenser heat load of 0.3kW. At an engine speed of 120rpm two engine revolutions occur each second, giving a condenser heat load of 0.6kW.

D.3 MK.III Engine Vacuum Pump Evacuation Calculations:

MK.III pump has a bore of 25mm and a stroke length of approximately 50mm. Using these specified dimensions, the volume evacuated from the pump per stroke, equal to one cylinder's volume, is:

$$V_{pump,rev} = \frac{\pi \times d^2}{4} \times L = \frac{\pi \times (25 \times 10^{-3})^2}{4} \times (50 \times 10^{-3}) = 2.45 \times 10^{-5} m^3$$

In a worst-case scenario, with no expansion, the mass of steam passed through the engine per stroke is 1.16E-4kg (see Mk.III condenser calculation). This mass of steam will be condensed in the condenser. The density of water is taken as an approximate value of 1000kg/m^3 giving a condensate volume of:

$$V_{con,rev} = 1.16 \times 10^{-4} \div 1000 = 1.16 \times 10^{-7} m^3$$

Therefore, the vacuum pump evacuates a considerably larger volume per stroke than that of the condensate produced.

D.4 MK.III Engine Flywheel Stored Energy Calculation:

The moment of inertia of the flywheel can be found as:

$$I_{fly} = \frac{1}{2} \times m \times r^2 = \frac{1}{2} \times 6.58 \times (165 \times 10^{-3})^2 = 0.09 \ \frac{kg}{m^2}$$

The kinetic energy stored in the flywheel can be found as:

$$KE_{fly} = \frac{1}{2} \times I \times \omega^2$$

Where:

$$\omega = rpm \ \times \frac{2\pi}{60}$$

Therefore, for the case where the engine has a speed of 60rpm and the flywheel therefore has a speed of 180rpm:

$$\omega = 180 \times \frac{2\pi}{60} = 18.8 \frac{rad}{s}$$

$$KE_{fly} = \frac{1}{2} \times 0.09 \times 18.8^2 = 15.9 \, J$$

For the case where the engine has a speed of 30rpm and the flywheel therefore has a speed of 90rpm:

$$\omega = 90 \times \frac{2\pi}{60} = 9.42 \frac{rad}{s}$$

$$KE_{fly} = \frac{1}{2} \times 0.09 \times 9.42^2 = 4.0 \, J$$

D.5 FPHE Initial Design Calculations

The MK.III engine, with expansion ratio of *n* = 1 and speed of 60rpm, has a mass flow rate 1.16 x10^{-4} kg/s (see condenser heat load calculation). The steam entering the FPHE is assumed to be at boiler conditions and therefore has a density of 0.59 kg/m^3 (Rogers & Mayhew, 1995). If the steam is limited by a minimum temperature of 50^{o}C, its density when saturated is 0.08 kg/m^3 (Rogers & Mayhew, 1995).

Therefore, the dryness fraction of the steam leaving the FPHE is limited to (see prediction of FPHE outlet dryness fraction calculation methodology in next section for more details on this method):

$$x = \frac{0.08}{0.59} = 0.14$$

The enthalpy of saturated steam at boiler conditions, i.e. FPHE inlet, is taken from steam tables as 2675 kJ/kg (Rogers & Mayhew, 1995). The enthalpy of steam at FPHE outlet conditions is calculated as:

$$h = (2591.4 \times 0.14) + [209.3 \times (1 - 0.14)] = 542.8\ kJ/kg$$

Therefore, the enthalpy available for recovery in the FPHE is estimated to be:

$$h_a = 2675 - 542.8 = 2132\ kJ/kg$$

This can be multiplied by the estimated steam flow rate to give the thermal power available for recovery:

$$E_a = 1.16 \times 10^{-4} \times 2132 = 0.25\ kW$$

It is also defined that we require 70% of this to be recovered, therefore giving the thermal power to be recovered as:

$$E_r = 0.25 \times 0.7 = 0.17\ kW$$

This must be recovered in the cooling water. To determine the required flow rate of cooling water, an allowed temperature rise must be defined. It will enter at 50^{o}C. It is expected that an outlet temperature of up to 90^{o}C be expected. This gives a minimum required flow rate of:

$$\dot{m}_{cw} = \frac{0.17}{4.2 \times\ 40} = 0.001\ kg/s$$

Using a density of water as 1000kg/m^3 this gives a cooling water volume flow rate estimation of:

$$\dot{V}_{cw} = \frac{0.001}{1000} = 1 \times 10^{-6}\,\frac{m^3}{s} = 1\ \frac{mL}{s}$$

Now the heat transfer coefficients on the water and steam sides can be calculated to find the overall heat transfer coefficient.

First, the water side. To know which Nusselt correlation to use, the Reynold's and Prandtl numbers need to be found. For these the water velocity must be known, assumed to be the velocity over the plate. This is found using the arbitrarily defined FPHE dimensions as:

$$u_{cw} = \frac{\dot{m}}{\rho} \times \frac{1}{CA} \times \frac{1}{No.\,of\ channels} = \frac{0.001}{978} \times \frac{1}{(100 \times 10^{-3} \times 2 \times 10^{-3})} \times \frac{1}{5} = 0.001\ m/s$$

$$Re_L = \frac{\rho u L}{\mu} = \frac{978 \times 0.001 \times (150 \times 10^{-3})}{0.0004} = 367$$

$$Pr = \frac{\mu C_p}{k} = \frac{0.0004 \times 4.2 \times 10^3}{0.66} = 2.55$$

Where:

- m is the mass flow rate of the cooling water (kg/s);
- ρ is the density of the water, taken as 978 kg/m^3 at an average temperature of 70°C from (Engineering Toolbox (a), nd);
- μ is the viscosity of the water, taken as 0.0004 Pa.s at an average temperature of 70°C from (Engineering Toolbox (b), nd);
- C_p is the specific heat capacity of the water, taken as 4.2 kJ/kg.K at an average temperature of 70°C from (Engineering Toolbox (c), nd);
- k is the thermal conductivity of water, taken as 0.66 W/m.K at an average temperature of 70°C from (Engineering Toolbox (d), nd);
- CA is the cross-sectional area of the channel the water flows through, defined by the chosen FPHE design dimensions (m^2);
- No. of channels is the 5 defined channels that the overall water flow is separated between in the heat exchanger.
- L is the length/height of the heat transfer area of the designed plate (m)

The Reynold's number suggests that the water flow is in the laminar phase, meaning that the water side Nusselt correlation is given by:

$$Nu_{lam} = 0.664 Re^{\frac{1}{2}} Pr^{\frac{1}{3}} = 0.664 \times 367^{\frac{1}{2}} \times 2.55^{\frac{1}{3}} = 17.4$$

Therefore, the water side heat transfer coefficient can be found as:

$$h_{t,cw} = \frac{Nu \times k}{L} = \frac{17.4 \times 0.66}{150 \times 10^{-3}} = 76.5\ \frac{W}{m^2 \cdot K}$$

Next, the steam side. This uses the Nusselt correlation for condensation on a flat plate. Here, liquid state refers to the steam condensate. Assuming that the steam be brought down to the minimum of 50°C, the bulk steam temperature will be approximately 75°C. Therefore, for this initial design calculation property data is read at this temperature. The wall temperature is also required. At this early stage this is estimated to be around the average of the four inlet/outlet temperatures, estimated as 70°C for this early calculation.

$$Nu_{cond} = 0.943\left[\frac{\rho_l(\rho_l - \rho_v)gh_{lv}L^3}{k_l\mu_l(\Delta T)}\right]^{\frac{1}{4}}$$

$$= 0.943\left[\frac{975(975 - 0.24)\cdot 9.81\cdot 2321\times 10^3\cdot(150\times 10^{-3})^3}{0.66\cdot 0.0004\cdot(75-70)}\right]^{\frac{1}{4}} = 2572$$

Where:

- ρ_l is the density of condensate at 75°C, taken as 975 kg/m^3 from (Engineering Toolbox (a), nd);
- ρ_v is the density of the steam at 75°C, taken as 0.24 kg/m^3 from (Rogers & Mayhew, 1995);
- g is acceleration due to gravity, known to be 9.81 m/s^2;
- h_{lv} is the enthalpy of vaporisation at 75°C, found as 2321 kJ/kg from (Rogers & Mayhew, 1995);
- k_l is the conductivity of the condensate at 75°C, found as 0.66 W/m.K from (Engineering Toolbox (d), nd);
- μ_l is the viscosity of the condensate at 75°C, found as 0.0004 Pa.s from (Engineering Toolbox (b), nd);
- ΔT is the difference between the steam bulk average temperature and the wall temperature (°C).

Therefore, the steam side heat transfer coefficient is:

$$h_{t,s} = \frac{Nu\times k}{L} = \frac{2572\times 0.023}{150\times 10^{-3}} = 394\ \frac{W}{m^2\cdot K}$$

Where:

- k is the thermal conductivity of steam, taken as 0.023 W/m.K at an average temperature around 75°C from (NuclearPower, 2020).

Before the overall heat transfer coefficient can be found, the thermal resistance for the plate itself must also be found:

$$Rw = \frac{dx}{k} = \frac{3 \times 10^{-3}}{237} = 1.27 \times 10^{-5} \frac{m^2 \cdot K}{W}$$

Where:

- k is the thermal conductivity of the aluminium plate, taken as 237 W/m.K for typical aluminium plate from (efunda, 2020).

Finally, the overall heat transfer coefficient, ignoring effects of fouling, can be found as:

$$U = \frac{1}{\frac{1}{h_1} + \frac{1}{h_2} + R_w} = \frac{1}{\frac{1}{76.5} + \frac{1}{394} + 1.27 \times 10^{-5}} = 64 \ \frac{W}{m^2 \cdot K}$$

With the overall heat transfer calculated, the remaining terms required as part of the effectiveness-NTU method can be calculated.

First, the mass heat capacity for the water and steam must be found:

$$C_{cold} = m_{cold} Cp_{cold} = 0.001 \times 4.2 \times 10^3 = 4.2 \ \frac{J}{K}$$

$$C_{hot} = m_{hot} Cp_{hot} = 1.16 \times 10^{-4} \times 1.9 \times 10^3 = 0.22 \ \frac{J}{K}$$

Where:

- $C_{p,hot}$ is the specific heat capacity of steam, taken as 1.9 kJ/kg.K at 70°C from (Engineering Toolbox (e), nd).

Therefore, the mass specific heat capacity ratio is given as:

$$C_r = \frac{C_{min}}{C_{max}} = \frac{0.22}{4.2} = 0.05$$

The effectiveness of the heat exchanger has already been defined as 70%. Therefore, the number of transfer units can be calculated as:

$$NTU = \frac{1}{1 - C_r} \ln\left(\frac{1 - \varepsilon C_r}{1 - \varepsilon}\right) = \frac{1}{1 - 0.05} \ln\left(\frac{1 - (0.7 \cdot 0.05)}{1 - 0.7}\right) = 1.23$$

Finally, the required heat transfer area for the heat exchanger is given as:

$$A_{ht} = \frac{NTU \times C_{min}}{U} = \frac{1.23 \times 0.22}{64} = 0.04 \ m^2$$

The plate area can then be used to determine how plates are needed:

$$No.\,of\ plates = \frac{Required\ HTA}{Plate\ HTA} = \frac{0.04}{100 \times 10^{-3} \times 140 \times 10^{-3}} = 2.9 \rightarrow 3$$

This therefore rounds up to 3 whole plates being required. The proposed arbitrary design used 9 heat transfer plates giving room for error in this calculation.

D.6 Predicting FPHE Steam Outlet Dryness Fraction

The estimation of the enthalpy of steam exiting the FPHE during heat recovery requires knowledge of the steam dryness fraction. Assuming maximum condensation occurs, this can be estimated through two methods:

1. Density ratios using conditions entering and exiting the FPHE.
2. Assessment of T-s charts by plotting the expansion and condensation process.

The first method finds the density of steam entering and leaving the FPHE from known temperature and/or pressure conditions and calculates the ratio. This represents the change in volume for the given mass, assumed to be through condensation.

The second method plots the steam cycle on a T-s chart and reads steam dryness fraction at the intermediate condensation point. The first point in the engine cycle can be found at that of saturated steam at 100°C, along the saturation line. Expansion occurs inside the cylinder, in the example of Figure 9-1 an expansion ratio of n = 2 is assumed, shown by the vertical line due to assumed isentropic expansion. The end point of the steam expansion line is known by the steam outlet pressure, which can be found using ideal gas laws for the given expansion ratio. The third step is condensation. This is a sloped line, taking the process back to the saturated liquid part of the saturation curve. The end point of this line is known by the final condenser temperature, and therefore the two known points can be connected to draw this line. The line is sloped because in this case condensation is not isothermal. This is due to the generation of partial vacuum during condensation which results in a changing condenser pressure and associated steam saturation temperature. This has been discussed in the main thesis. This has been shown as a linear process in this case to simplify the analysis. More accurate modelling using ideal gas laws not included as part of the scope of this work, see Figure 2-14, suggests a non-linear transition introducing uncertainty into this analysis. This was identified in the main thesis as being an area of improvement in future work.

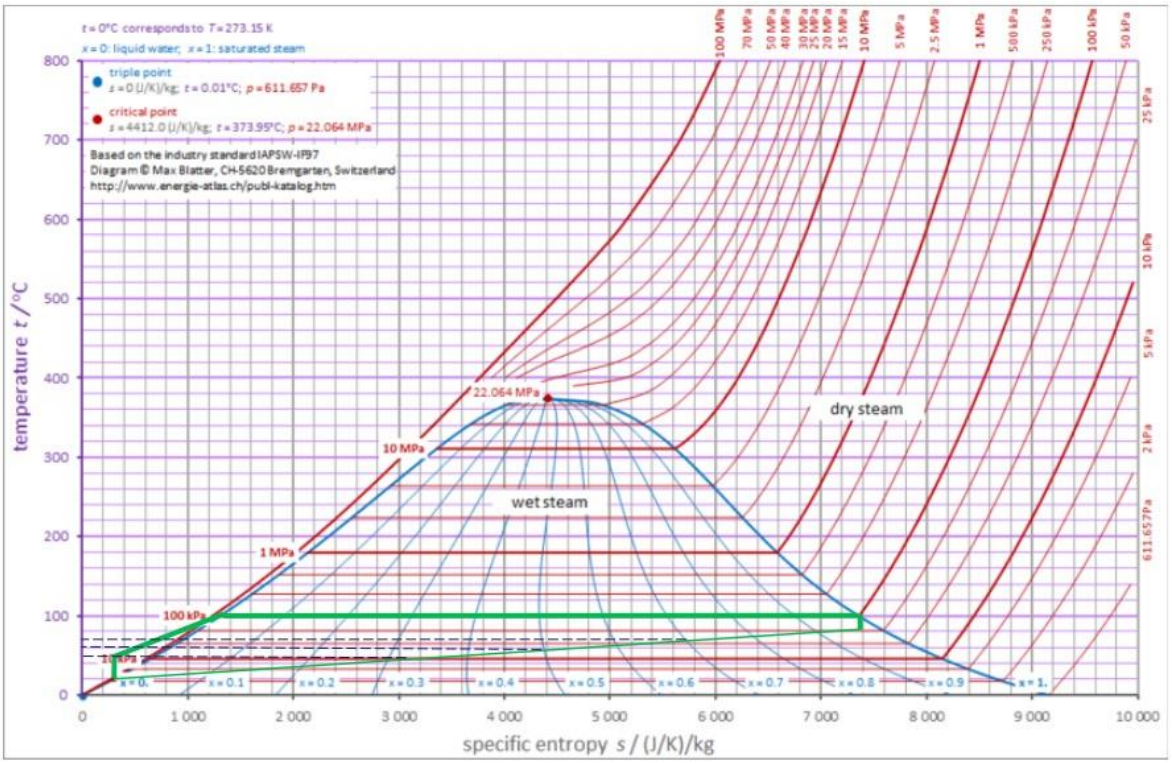

Figure 9-1 Reproduced from (Blatter, 2014) under CC BY-SA 4.0. Original work adapted by the author of this research by adding green condensing engine thermodynamic process lines and blue dotted temperature intercept lines. Case shown for steam cycle with expansion ratio of n = 2.

To understand the dryness fraction at the intermediate stage of the condensation, specifically the outlet of the FPHE, horizontal lines can be drawn along the constant temperature lines on the T-s chart for the corresponding FPHE inlet cooling water temperature. One line for each chosen FPHE operating temperature is shown on Figure 9-1. The intersection between the constant temperature line and the condensation process line gives the intermediate point in the condensation process. Here, the dryness fraction can be read from the T-s chart.

Comparison of these two methods was performed, with the difference in predicted dryness fraction given in Table 9-3 and the difference in resulting two-stage system efficiencies following heat recovery and re-use given in Table 9-4. The results were obtained from the two_stage_simulation mathematical model developed during the heat recovery project. Whilst percentage differences seem high, this is caused by the low magnitude of the values being compared. The similarity in efficiencies calculated with the two methods corroborates the values obtained and supports use of either method. This is especially true for the case using a cooling water inlet temperature of 50°C, which is the main case discussed in this thesis to provide justification for the potential of heat recovery and re-use. Only the T-s chart method has been reported in the main body of this thesis.

Table 9-3 Comparison of FPHE outlet steam dryness fraction using T-s chart and density ratio methods. Results obtained from two_stage_simulation mathematical model. Boiler pressure and condenser temperature of 1 bar and 20°C assumed.

Cooling Water Temperature (°C)	First Cylinder Expansion Ratio	Dryness Value (x)		
		T-s Chart Method	Density Ratio Method	Difference (%)
50	1	0.26	0.14	46.2
	2	0.32	0.28	13.8
	3	0.4	0.42	-3.9
	4	0.45	0.56	-24.1
	5	0.65	0.70	-8.2
	6	0.76	0.85	-11.9
60	1	0.4	0.22	44.8
	2	0.5	0.43	13.4
	3	0.64	0.65	-1.9
	4	0.7	0.88	-25.1
70	1	0.52	0.34	35.4
	2	0.7	0.66	5.9
	3	0.85	0.94	-10.9

Table 9-4 Comparison of heat recovery and re-use predicted efficiencies of the two-stage system using the T-s chart and density ratio methods for predicting FPHE steam outlet dryness fraction. Results obtained from two_stage_simulation mathematical model. Boiler pressure and condenser temperature of 1 bar and 20°C assumed.

Cooling Water Temperature (°C)	First Cylinder Expansion Ratio	Model Two Stage Efficiency Values (%)		
		T-s Chart Method	Density Ratio Method	Difference (%)
50	1	11.1	11.9	-6.6
	2	14.9	15.1	-1.4
	3	16.6	16.5	0.6
	4	17.8	17.1	3.7
	5	17.7	17.4	1.9
	6	17.9	17.3	3.1
60	1	11.4	12.8	-12.5
	2	14.6	15.1	-3.7
	3	15.6	15.5	0.6
	4	16.6	15.2	8.4
70	1	11.1	12.9	-15.7
	2	13.3	13.7	-2.9
	3	14.1	13.2	6.2

D.7 Mk.IV Engine Dimension Check

The total cylinder volume is found as:

$$V_{Mk.IV,cyl} = \frac{\pi \times (100 \times 10^{-3})^2}{4} \times (160 \times 10^{-3}) = 1.25 \times 10^{-3} m^3$$

The Mk.IV engine is assumed to operate at 1 bar. Therefore, the downstroke energy produced at *n* = 1, according to the boundary work equation commonly used in this thesis, is:

$$W_d = P_b dV = 1 \times 10^5 \times 1.25 \times 10^{-3} = 125\, J$$

The downstroke back pressure losses are:

$$W_{d,loss} = P_{atm} dV = 101325 \times 1.25 \times 10^{-3} = 127\, J$$

Therefore, the downstroke work term is:

$$W_d = 127 - 125 = -2\, J$$

The upstroke work is produced at constant pressure and therefore uses the boundary work equation for the entire cylinder volume. The pressure driving force is calculated as atmospheric versus cylinder pressure, which is assumed to have been brought to condenser pressure:

$$W_u = P \times dV = (101325 - 0.02337 \times 10^5) \times 1.25 \times 10^{-3} = 124\, J$$

Therefore, the work produced across a revolution is:

$$W_{rev} = 124 - 2 = 122\, J$$

The isentropic power produced at the defined speed of 90rpm is:

$$\dot{W_{isen}} = W_{rev} \times \frac{N}{60} = 122 \times \frac{90}{60} = 183\, W$$

The Mk.III engine had an isentropic efficiency of 33% - 39%. In order to predict potential realistic Mk.IV engine power outputs, an isentropic efficiency range of 30% - 50% is applied in this analysis. This allows for some improvement in the effectiveness of the technology. It is acknowledged that the Mk.III engine efficiencies were achieved at lower speeds, but this analysis gives an idea of the potential of the Mk.IV engine. The resulting Mk.IV potential realistic power range is approximately 55W - 90W.

$$\dot{W} = W_{isen} \times \eta_{II} = 183 \times 0.5 = 91.5\, W$$

$$\dot{W} = W_{isen} \times \eta_{II} = 183 \times 0.3 = 54.9\, W$$

The working steam volume requirement per cylinder can be calculated as:

$$\dot{V}_{s,cyl} = V_{s,rev} \times \frac{N}{60} = 1.25 \times 10^{-3} \times \frac{90}{60} = 1.88 \times 10^{-3} \ \frac{m^3}{s}$$

This is per cylinder, giving a total Mk.IV engine steam volume flow rate of:

$$\dot{V}_{s,Mk.IV} = 1.88 \times 10^{-3} \times 2 = 3.75 \times 10^{-3} \ \frac{m^3}{s}$$

This gives a mass flow rate of:

$$\dot{V}_{s,Mk.IV} = 3.75 \times 10^{-3} \times 0.59 = 2.21 \times 10^{-3} \frac{kg}{s}$$

D.8 Mk.IV Engine Vacuum Pump Size Calculation

The MK.III engine had a main cylinder stroke displacement volume of:

$$V_{cyl,MKIII} = \frac{\pi \times (50 \times 10^{-3})^2}{4} \times 100 \times 10^{-3} = 1.96 \times 10^{-4} \ m^3$$

The MK.III pump had a stroke volume of:

$$V_{pump,MKIII} = \frac{\pi \times (25 \times 10^{-3})^2}{4} \times 50 \times 10^{-3} = 2.45 \times 10^{-5} \ m^3$$

The two-cylinder MK.IV engine has a cylinder stroke volume of:

$$V_{cyl,MKIV} = 2 \times \frac{\pi \times (100 \times 10^{-3})^2}{4} \times 160 \times 10^{-3} = 2.50 \times 10^{-3} \ m^3$$

Therefore, the volume of displacement during one engine revolution has increased by a factor of:

$$\frac{V_{cyl,MKIV}}{V_{cyl,MKIII}} = \frac{2.50 \times 10^{-3}}{1.96 \times 10^{-4}} = 12.8$$

Therefore, the MK.IV vacuum pump should undergo at least an equal increase in volume:

$$V_{pump,required} = 2.45 \times 10^{-5} \ \times 12.8 = 3.14 \times 10^{-4} \ m^3$$

$$V_{pump,MKIV} = \frac{\pi \times (75 \times 10^{-3})^2}{4} \times 75 \times 10^{-3} = 3.31 \times 10^{-4} \ m^3$$

$$V_{pump,MKIV} > V_{pump,required}$$

Therefore, the designed vacuum pump is sufficiently sized.

D.9 Mk.IV Flywheel Confirmatory Calculation

The moment of inertia of the flywheel can be found as:

$$I_{fly} = \frac{1}{2} \times m \times r^2 = \frac{1}{2} \times 11.0.37 \times (120 \times 10^{-3})^2 = 0.08 \frac{kg}{m^2}$$

The kinetic energy stored in the flywheel can be found as:

$$KE_{fly} = \frac{1}{2} \times I \times \omega^2$$

Where:

$$\omega = rpm \times \frac{2\pi}{60}$$

Therefore, for the case where the engine has a speed of 90rpm and the flywheel therefore has a speed of 360rpm:

$$\omega = 360 \times \frac{2\pi}{60} = 37.7 \frac{rad}{s}$$

$$KE_{fly} = \frac{1}{2} \times 0.08 \times 37.7^2 = 56.9\, J$$

The Mk.IV engine flywheel is intended to be used when the Mk.IV engine is running with only one cylinder in operation. When two cylinders are in operation, they are expected to power balance themselves. At an expansion ratio of *n* = 1, the MK.IV single cylinder engine has been designed to produce around 90W when operating at 90rpm. This equates to 90J/s and 1.5 revolutions per second. Therefore, the average energy production per revolution is:

$$KE_{MKIV} = \frac{90}{1.5} = 60 \frac{J}{rev}$$

Therefore, the flywheel proposed by the University of Southampton EDMC has sufficient energy storage capacity for almost the entire energy production during a revolution.

Appendix E Additional Background

E.1 Sensor Calibration and Accuracy Checks

Pressure transducers, thermocouples, and a load cell were all used as sensors for data acquisition during this project. The pressure transducers and thermocouples are pre-calibrated by the

manufacturer, but a confirmatory check was performed to ensure accuracy against known conditions. The load cell required calibration through specification of a calibration factor in the code to give an accurate reading. The detail of this work is given below to support the analysis presented in this thesis.

E.1.1 Pressure Transducer Accuracy Check

Pressure transducers used in this project were a legacy item re-used from previous testing in the laboratory on the Mk.II engine. These were assumed to have been pre-calibrated by the manufacturer (RS Pro, 2023); however, an accuracy check was performed to ensure that these already used sensors still read accurately. This was performed in the context of the heat recovery tests as this work was performed before the Mk.III engine tests in the chronology of the project timelines due to the required design and manufacture times of the engine. As a result, three transducers were tested to be used for boiler inlet, heat exchanger inlet, and condenser inlet. The electronic vacuum pump used in the heat recovery tests was used to generate differing sub-atmospheric pressures in a pipeline, with a manual ball valve open to atmosphere adjusted to manipulate the pressure in the line. An analogue gauge was used to control the pressure in the line and readings taken using the pressure transducers. Twenty values were outputted using the transducers and compared against the reading from the analogue gauge. This was repeated three times for pressures of -0.2barg (gauge pressure), -0.5barg, and -0.8barg and the average pressure transducer readings taken for analysis. These values were chosen to cover the pressures expected during testing as well as allowing for the trendline y-axis intercept to be analysed against known atmospheric pressure, i.e. 0.0 barg.

Average pressure transducer values were plotted against analogue gauge values and trendlines plotted, shown in Figure 9-2. The y-axis error bars are plotted using the precision of the analogue gauge (+/- 0.01bar) and the x-axis error bars are plotted using the accuracy value given by the manufacturer for the pressure transducers (+/- 0.0025 bar, estimated as a maximum value at 1bar as the transducers have an accuracy of +/- 0.25%). Full agreement between the transducers and analogue gauge would result in linear trendline gradients of unity. At atmospheric pressure the y-axis intercept should be 0.0 barg for each transducer, a known pressure. The average difference between transducer and analogue gauge for transducer 1 to 3 respectively was -0.01barg, -0.01barg, and 0.00barg. Maximum variance of +/- 0.01bar was deemed by the author as being suitable for use in testing.

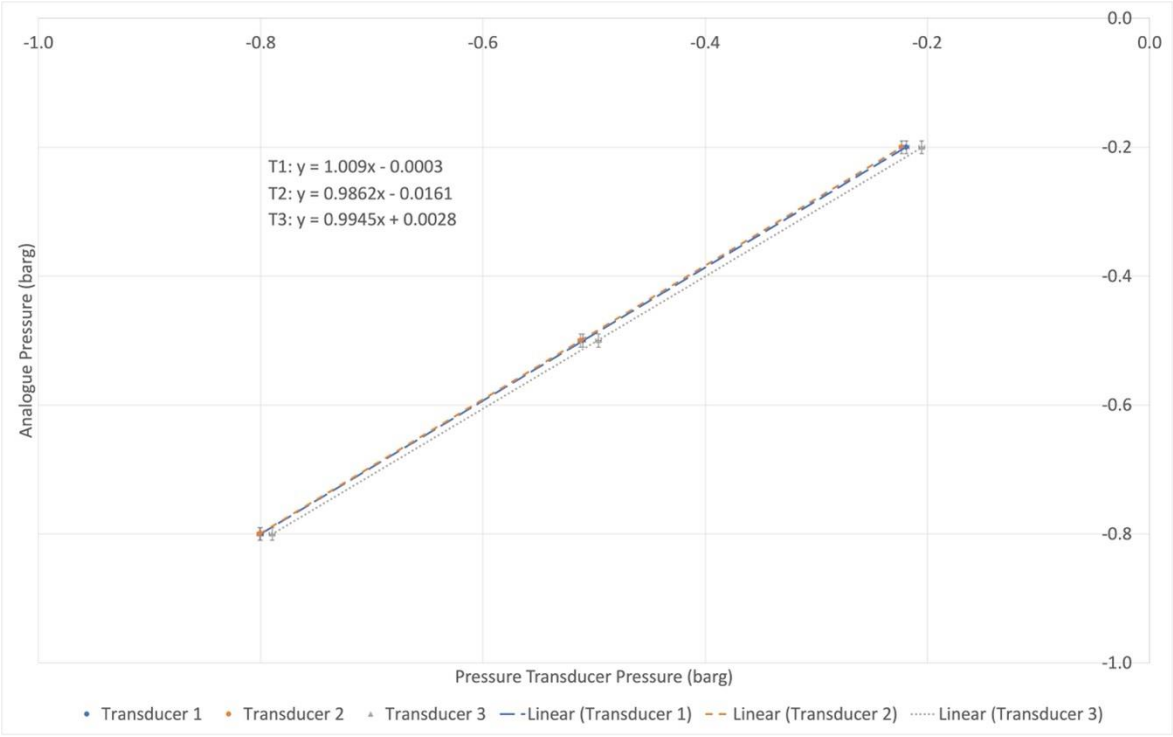

Figure 9-2 Pressure transducer accuracy check data analysis. Pressure transducer average readings versus analogue gauge readings.

E.1.2 Thermocouple Accuracy Check

A sous vide heater was used for heating the supply water in a water bath during heat recovery testing. This is not a scientific instrument, typically used in the household for cooking applications, but was used to allow for the desired design/operation of the experiment. Therefore, the accuracy of the instrument was checked before use. K-type thermocouples, with associated conditioners, were also used in this project for temperature measurement. These were a legacy item re-used from previous testing in the laboratory on the Mk.II engine. Whilst pre-calibration by manufacturer is available (RS Pro, nd) it was unknown if this was requested by previous researchers. As a precaution, and to ensure suitability for use an accuracy check was performed to ensure that these already used sensors still read accurately. This was performed in the context of the heat recovery tests as this work was performed before the Mk.III engine tests in the chronology of the project timelines due to the required design and manufacture times of the engine. As a result, two thermocouples were tested to be used for heat exchanger outlet water temperature and condenser water bath temperature. The first thermocouple was accuracy checked against temperatures of 50°C, 60°C, and 70°C to reflect the expected temperatures surrounding the heat exchanger. The second thermocouple was accuracy checked against temperatures of 20°C, 30°C, and 40°C to reflect the expected temperatures in the spray condenser water bath. The check was performed in a tank of water heated to a set temperature by the sous vide heater used to supply

the heated cooling water inlet in the heat recovery experiments. The thermocouples were used to output 10 temperature readings and the average taken to compare against the sous vide heater. A thermometer was also used as a third measurement for confidence. This was repeated three times for each specified temperature and an average taken.

Figure 9-3 shows the thermocouple average values plotted against the heater average values. Full agreement between thermocouples and heater would result in linear trendline gradients of unity. The y-axis error bars are plotted as the precision of the heater (+/- 0.5°C) and the x-axis error bars are plotted as the combined accuracy value for the k-type thermocouple and conditioner as given by the manufacturers (+/- 2.5°C). The former is not considered to represent the whole uncertainty associated with the instrument but is given as an indication without any additional manufacturer data. The trendlines shown in Figure 9-3 show a close match between the average readings from the thermocouple and heater. The average difference between thermocouple 1 and 2 with the heater was -1.2°C and -1.8°C respectively. This is within the tolerance of the manufacturer given accuracy values for the k-type thermocouples with conditioner. The corroboration of results from two instruments within this tolerance limit was considered by the author to justify confidence in the use of those instruments. However, the large x-axis error bars suggest that for future experiments a more accurate temperature measurement instrument should be used, such as PT100 probes. This has already been included as a recommendation in the main thesis body.

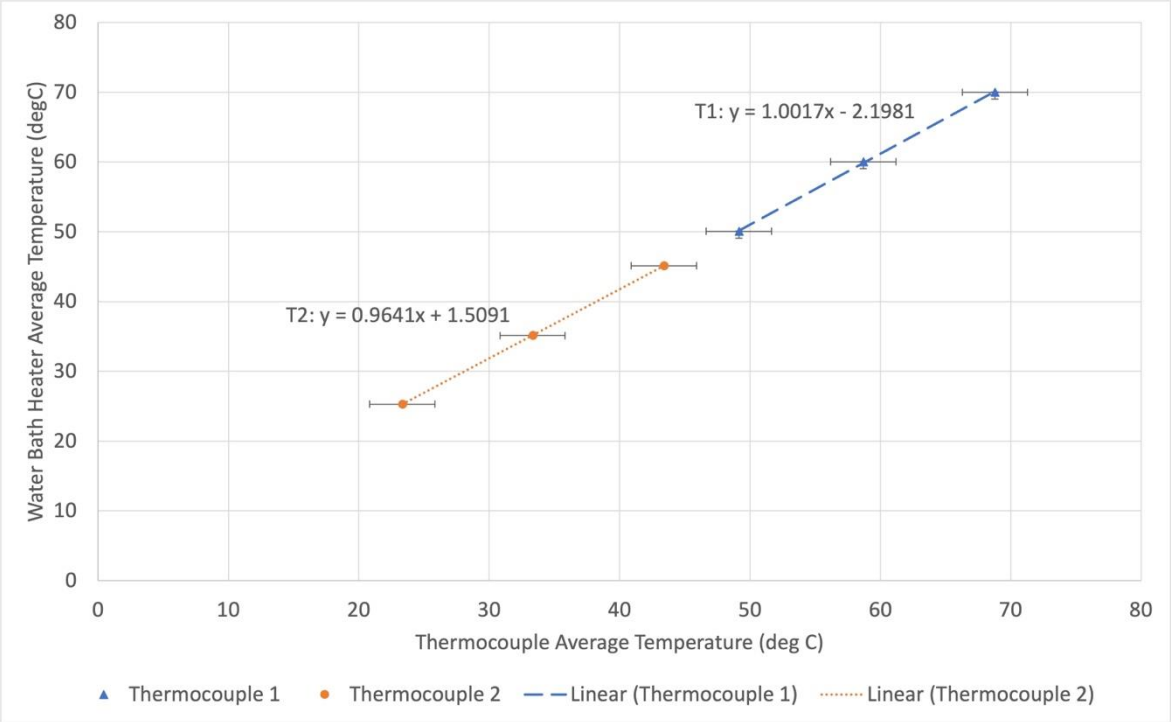

Figure 9-3 Thermocouple accuracy check versus heater readings.

E.1.3 Load Cell Calibration

The load cell used in friction brake tests on the Mk.III engine required calibration in the laboratory. The project used a Sparkfun HX711 load cell amplifier to translate the load cell force reading into a useable signal to be processed by the Arduino microcontroller. To do so, the HX711 Arduino library was used in the engine control code. This allowed for a calibration factor to be defined in the code which was determined in the lab through a series of tests using the Sparkfun HX711 Calibration Arduino script, available online: (Sparkfun, nd). The calibration factor was determined by placing calibrated weights onto the load cell and adjusting the calibration factor to give an accurate reading. This was achieved using an iterative process and a subsequent accuracy check performed. For reference, the calibration factor used in the accuracy check was -433250, as seen in the Mk.III engine code available in this project's data repository.

The accuracy check was performed by systematically placing and removing different mass onto the load cell using calibrated weights. This was performed five times and the average value for each step calculated. The load cell average outputs were then plotted against time to demonstrate accurate measurement against the calibrated weights. The graphical plot is given below in Figure 9-4, showing the measurement of 0.2kg, 0.4kg, and 1kg masses. The test also included zero mass placed on the load cell between each step. These masses were chosen to cover the range expected to be observed during friction brake testing.

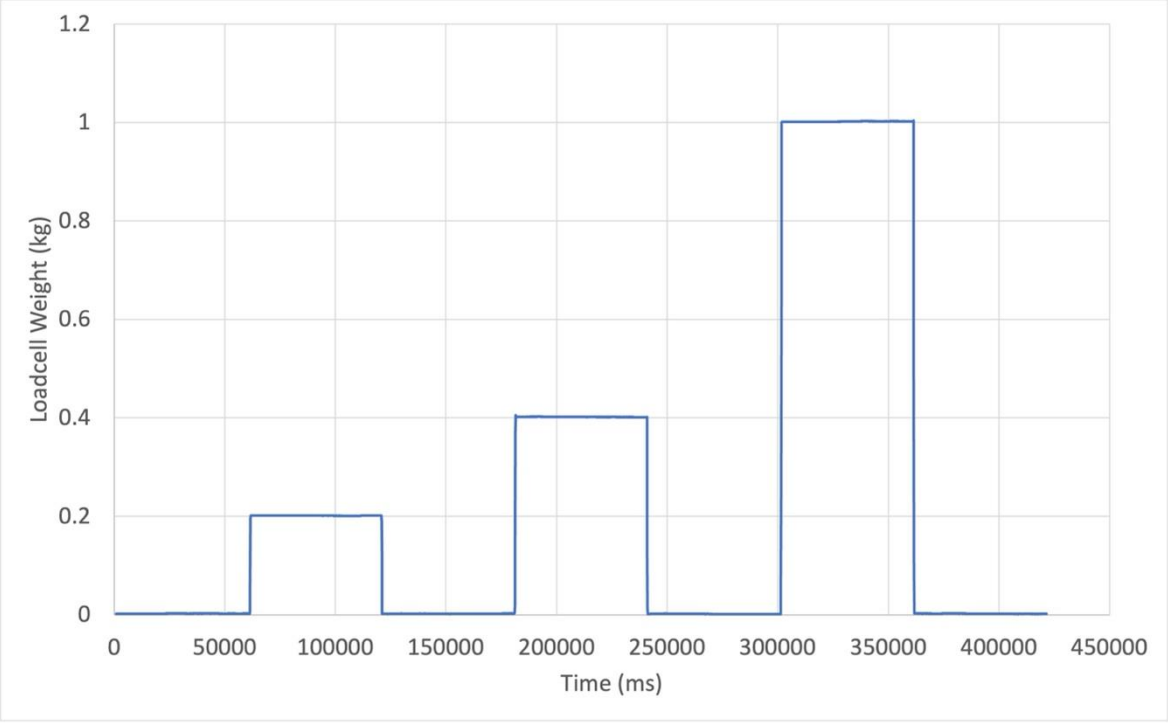

Figure 9-4 Load cell accuracy check following calibration. Checked against calibrated weights at weights of 0kg, 0.2kg, 0.4kg, and 1kg.

The average load cell values had an accuracy of +/- 2 grams. This was unable to be corrected through the calibration factor and therefore a zero-offset was used during Mk.III testing. The raw data from this check is available in the data repository.

E.2 Mk.III Condensing Engine Uncertainty Analysis

The Mk.III condensing engine experiment analysis reported several types of power and efficiency data in the main thesis. Each of these had an associated uncertainty, represented by the error bars on the relevant graphical plots. The total uncertainty was calculated using a method which combined compound uncertainties, presented in the National Physical Laboratory Measurement Good Practice Guide No. 11 (Bell, 2001). The method outlined by Bell (2001) involves collecting an 'uncertainty budget' for each component of a measurement with an uncertainty and converting to a 'standard absolute uncertainty' based on the type of probability distribution. Standard absolute uncertainties, given in the units of the measurement, can then be combined to give an overall standard absolute uncertainty. Where intermediate measurements with a standard absolute uncertainty are used in calculation or standard absolute uncertainties of different units are to be combined, then standard absolute uncertainties are converted to standard relative uncertainties, given as a fractional decimal of the measured value, before being combined. The combination of uncertainties uses the summation of quadrature method. A coverage factor was applied to the final standard uncertainty to give a known confidence range. Each of the steps associated with the uncertainty analysis is given below. This method was applied to each individual data point and therefore uncertainty/error bars for each data value are different. This accounts for the effect of relative (or percentage) errors in absolute values, and the greater impact these have on data points of lower magnitude.

E.2.1 Piston and Engine Power Uncertainty

Piston power was calculated in an iterative procedure by using the measured pressures acting upon the piston and the volume swept to calculate the work done. The engine speed was then used to convert this into a power value. Therefore, the piston power is a function of cylinder pressure, atmospheric pressure, cylinder volume, and engine speed. The values for atmospheric pressure and cylinder volume were fixed and have no associated uncertainty. Therefore, cylinder pressure and engine speed were the measurements with an uncertainty to account for in the uncertainty analysis.

Each of the ten Mk.III engine tests were analysed by calculating the power associated with six pressure profiles chosen during a period of steady operation and an average found. As a result, the

uncertainty associated with each of the six cylinder pressure average values and engine speed average values were accounted for. In this case, the power calculation consisted of two steps, firstly estimating the work done during the downstroke and secondly estimating the work done during the upstroke. Therefore, the uncertainty analysis splits the uncertainty associated with the downstroke cylinder pressure measurements and upstroke cylinder pressure measurements into two distinct parts. The pressure measurements had an associated accuracy and precision uncertainty as well as the uncertainty introduced by the spread of the six average values. The engine speed was calculated by the Arduino microcontroller using the optical sensors as triggers. There is no known accuracy associated with this measurement, but it is acknowledged that the Arduino microcontroller has a clock speed of 16MHz (Arduino, 2021), equivalent to 16 million cycles per second. This is deemed by the author adequately fast for this application, with revolutions taking one to two seconds, and therefore the engine speed is deemed accurate. However, a precision and repeatability uncertainty can be associated to the engine speed. The corresponding uncertainty budget is shown in Table 9-5.

Table 9-5 Uncertainty budget for Mk.III condensing engine power calculations.

Type of Measurement	Source of Uncertainty	Uncertainty Value (+/-)	Probability Density Function	Divisor
Average downstroke pressure measurement	Manufacturer accuracy	0.25%	Normal	1
	Precision	0.005bar	Uniform	$\sqrt{3}$
	Repeatability of measurement (standard deviation)	σ	Normal	$\sqrt{n}$
Average upstroke pressure measurement	Manufacturer accuracy	0.25%	Normal	1
	Precision	0.005bar	Uniform	$\sqrt{3}$
	Repeatability of measurement (standard deviation)	σ	Normal	$\sqrt{n}$
Engine speed	Precision	0.5rpm	Uniform	$\sqrt{3}$
	Repeatability of measurement (standard deviation)	σ	Normal	$\sqrt{n}$

As per the methodology set out by Bell (2001), the first step in the uncertainty analysis was to find all associated standard absolute uncertainties for each type of measurement. A standard absolute uncertainty was calculated for each component by dividing the uncertainty value by the associated

divisor, which was in turn defined by the probability density function associated with the relevant type of measurement. For example, the standard absolute uncertainty associated with the repeatability of measurement is the standard deviation of the data divided by the square root of the number of measurements taken. Likewise, the standard absolute uncertainty for the precision of an instrument is the value of half the width of the graduation divided by the square root of 3, associated with the uniform probability distribution. These functions can be found in literature, eg (Bell, 2001).

$$SU_{abs,repeatability} = \frac{\sigma}{\sqrt{n}}$$

$$SU_{abs,precision} = \frac{Half\ width\ of\ graduation}{\sqrt{3}}$$

Once all standard absolute uncertainties had been calculated for each source of uncertainty in Table 9-5, then a combined standard absolute uncertainty was calculated for each type of measurement. In this case, a combined standard absolute uncertainty was found for the downstroke pressure measurement, upstroke pressure measurement, and engine speed measurement. This was achieved using the summation of quadrature method, shown below.

$$SU_{abs,combined} = \sqrt{{SU_1}^2 + {SU_2}^2 + \cdots}$$

Each combined standard absolute uncertainty associated with each type of measurement was then converted into a standard relative uncertainty by dividing the absolute uncertainty by the average measured value, as shown below. This gave the relative uncertainty as a fractional decimal for each type of measurement.

$$SU_{rel} = \frac{SU_{absolute}}{Average\ Measured\ Value}$$

Once the relative uncertainties associated with downstroke cylinder pressure, upstroke cylinder pressure, and engine speed had all been calculated these were combined using the sum of quadrature method, shown below. The combined relative uncertainty in the piston power value was then converted into the absolute standard uncertainty in the measured piston power by multiplying by the average piston power value.

$$SU_{rel,total} = \sqrt{{SU_{rel,1}}^2 + {SU_{rel,2}}^2 + \cdots}$$

$$SU_{abs,total} = SU_{rel,total} \times (Average\ Measured\ Value)$$

Finally, a coverage factor of k = 2 was also applied to give a confidence interval of 95%, as suggested by the literature.

$$k = 2 \dots Gives\ 95\%\ confidence\ interval$$

The above method was used to find the uncertainty associated with the piston power. As engine power was a theoretical value deemed to be 90% of the piston power, the author designated 90% of the piston power uncertainty to the engine power values. This is equivalent to converting the relative uncertainty associated with power measurement into an absolute uncertainty using the engine power value instead of the piston power value. This analysis can be found in the data files included in this project's data repository.

E.2.2 Friction Brake Uncertainty

The friction brake power was calculated using Equation (4.2), a function of hung weight, the change in load cell reading, the flywheel diameter, and the flywheel speed. The hung weight and load cell reading have associated accuracy, precision, and repeatability uncertainties. The flywheel speed is a function of engine speed. Whilst this does not have a known accuracy, see discussion in the previous section, a repeatability uncertainty can be associated with the spread of data as well as the precision of the reported value. The flywheel diameter is a fixed value without an assigned uncertainty associated with a measurement. The associated uncertainty budget for the friction brake power is given in Table 9-6.

Table 9-6 Uncertainty budget associated with friction brake power uncertainty analysis. (1) RS-Pro 3kg scale has manufacturer accuracy of +/- 0.1kg (RS-Pro, nd). (2) The load cell accuracy is dependent on assembly and was measured during calibration.

Type of Measurement	Source of Uncertainty	Uncertainty Value (+/-)	Probability Density Function	Divisor
Hung weight	Manufacturer accuracy (1)	0.1g	Normal	K = 2
	Precision of scale	0.05g	Uniform	$\sqrt{3}$
	Repeatability of measurement (standard deviation)	σ	Normal	$\sqrt{n}$
Load cell reading	Manufacturer accuracy (2)	2g	Normal	K = 2
	Precision of scale	0.05g	Uniform	$\sqrt{3}$

Type of Measurement	Source of Uncertainty	Uncertainty Value (+/-)	Probability Density Function	Divisor
	Repeatability of measurement (standard deviation)	σ	Normal	$\sqrt{n}$
Flywheel speed	Precision of speed reading	0.5rpm	Uniform	$\sqrt{3}$
	Repeatability of measurement (standard deviation)	σ	Normal	$\sqrt{n}$

The standard absolute uncertainty was calculated for each source of uncertainty and the combined standard absolute uncertainty found for each type of measurement, using the sum of quadrature method. These were converted into a relative uncertainty using the average value associated with each measurement and the relative uncertainties combined to give an overall relative uncertainty, again using the sum of quadrature method. This was converted back into a total absolute standard uncertainty using the average friction brake power value. It is noted that the uncertainty associated with a load cell reading was included twice in the overall uncertainty calculation, accounting for the compound effects of the two load cell readings required to calculate a change in value as required by the calculation of friction brake power. A coverage factor of k = 2 was applied to give a 95% confidence interval.

E.2.3 Thermal Efficiency Uncertainty

The thermal efficiency was calculated as the ratio of useful power output to thermal power input. The useful power output was defined as the engine power, for which the uncertainty had already been calculated. The thermal power input was the summation of the thermal power associated with the working steam and jacket steam requirements. The working steam power requirement was calculated as a function of cylinder volume, steam density, enthalpy, and engine speed. Steam density was a function of measured cylinder downstroke pressure, to calculate the mass of steam required to fill the cylinder volume. Enthalpy was a function of the measured boiler pressure, to calculate the energy required to generate the required steam mass at boiler conditions. The cylinder volume was treated as a constant. Therefore, the uncertainty associated with the working steam power requirement was associated with measured cylinder pressure, measured boiler pressure, and engine speed. Pressure measurements had an associated accuracy, precision, and repeatability (spread) uncertainty. The engine speed had an associated precision and repeatability uncertainty, as explained in previous sections. The steam jacket steam energy requirement was

estimated using a theoretical approach using *Newton's* law of cooling. Whilst this did use measured temperature and pressure data, this was required to give an approximate steam jacket usage value for the minimum case. It was discussed in the main thesis how this method had inherent uncertainty, but it was concluded that the percentage of working steam energy attributed to steam jacket operation was in the expected range, <30%. As this was used as an estimate to improve the accuracy of the reported result the steam jacket steam has not been accounted for in this uncertainty analysis, as the uncertainty involved with the theoretical nature of the estimate could not be accounted for properly in this analysis. This assessment is shown in the uncertainty budget for the thermal power input, given in Table 9-7.

Table 9-7 Uncertainty budget for Mk.III engine thermal power input.

Type of Measurement	Source of Uncertainty	Uncertainty Value (+/-)	Probability Density Function	Divisor
Boiler pressure	Manufacturer accuracy	0.25%	Normal	1
	Precision	0.005bar	Uniform	$\sqrt{3}$
	Repeatability of measurement (standard deviation)	σ	Normal	$\sqrt{n}$
Cylinder downstroke pressure	Manufacturer accuracy	0.25%	Normal	$K = 2$
	Precision	0.005bar	Uniform	$\sqrt{3}$
	Repeatability of measurement (standard deviation)	σ	Normal	$\sqrt{n}$
Engine speed	Precision of speed reading	0.5rpm	Uniform	$\sqrt{3}$
	Repeatability of measurement (standard deviation)	σ	Normal	$\sqrt{n}$

The standard absolute uncertainty associated with each part of each type of measurement was calculated using the methods already described in previous sections. These standard absolute uncertainties were combined using the sum of quadrature and converted into relative uncertainties. The relative uncertainties were combined using the sum of quadrature method, giving a total relative uncertainty associated with the thermal power input.

This value was combined with the already calculated total relative uncertainty associated with the engine power output, using the sum of quadrature method, giving a total relative uncertainty as a

fractional decimal associated with the average thermal efficiency value. This was converted into an absolute standard uncertainty and a coverage factor of *k* = 2 applied to give a 95% confidence interval.

E.2.4 Second Law Efficiency Uncertainty

The second law efficiency was calculated as the ratio of thermal efficiency achieved by the Mk.III engine and the *Carnot* efficiency for the average operation. The uncertainty for the thermal efficiency had already been defined, discussed above. The *Carnot* efficiency is calculated using the heat source and sink temperatures, which as discussed in the main body of thesis are related to the average condenser and maximum cylinder pressure measurements. The uncertainty associated with pressure measurements has already been discussed at length in previous sections. The resulting uncertainty budget is given in Table 9-8.

Table 9-8 Uncertainty budget associated with Carnot efficiency part of second law efficiency uncertainty analysis.

Type of Measurement	Source of Uncertainty	Uncertainty Value (+/-)	Probability Density Function	Divisor
Average condenser pressure	Manufacturer accuracy	0.25%	Normal	1
	Precision	0.005bar	Uniform	$\sqrt{3}$
	Repeatability of measurement (standard deviation)	σ	Normal	$\sqrt{n}$
Maximum cylinder pressure	Manufacturer accuracy	0.25%	Normal	*K* = 2
	Precision	0.005bar	Uniform	$\sqrt{3}$
	Repeatability of measurement (standard deviation)	σ	Normal	$\sqrt{n}$

The standard absolute uncertainty associated with each part of each measurement associated with the *Carnot* efficiency, as given in the uncertainty budget, was calculated using the methods already described in previous sections. These standard absolute uncertainties were combined using the sum of quadrature and converted into relative uncertainties. The relative uncertainties were combined using the sum of quadrature method, giving a total relative uncertainty associated with the average *Carnot* efficiency.

This value was combined with the already calculated total relative uncertainty associated with the average thermal efficiency, using the sum of quadrature method, giving a total relative uncertainty as a fractional decimal associated with the average second law efficiency value. This was converted into an absolute standard uncertainty and a coverage factor of k = 2 applied to give a 95% confidence interval.

E.2.5 Engine Speed Uncertainty

The engine speed for each Mk.III engine test is the average of the six speed values associated with the six pressure profiles used in the power analysis. As discussed previously, the accuracy of the Arduino microcontroller and optical sensor system was unknown and not included in this analysis. Therefore, the uncertainty in the engine speed arises from the precision of the reported value and the spread, or repeatability, in the six speed values. This is reflected in the uncertainty budget given in Table 9-9. Whilst the microcontroller accuracy is unknown, the processing speed was deemed sufficiently high to not introduce error, discussed in a previous section.

Table 9-9 Uncertainty budget associated with reported engine speeds used in Mk.III engine testing analysis.

Source of Uncertainty	Uncertainty Value (+/-)	Probability Density Function	Divisor
Precision	0.5rpm	Uniform	$\sqrt{3}$
Repeatability	σ	Normal	$\sqrt{n}$

The standard absolute uncertainty associated with the precision and repeatability uncertainties were calculated and combined using the sum of quadrature method. As this already had the correct units, the coverage factor of k = 2 was applied directly to this combined value to give a 95% confidence interval.

E.3 Heat Recovery Experiment Uncertainty Analysis

The heat recovery experiment analysis reported pressure data, temperature data, water flow rate data, and heat recovery efficiency data in the main thesis. The total uncertainty associated with these, plotted as error bars on the associated graphs, was calculated using the same method shown earlier in Chapter 9, outlined by the National Physical Laboratory Measurement Good Practice Guide No. 11 (Bell, 2001). This used an uncertainty budget to estimate all standard uncertainties associated with the measurement and combine these using the summation of quadrature method. A coverage factor was applied to the final value to give a confidence interval.

The method used for the heat recovery analysis is described in more detail in the following sub-sections.

E.3.1 Cooling Water Flow Rate Uncertainty

The cooling water flow rate measurement was performed by recording the time taken to fill a 100mL volume and dividing volume by time to give flow rate. This was repeated three times at the start of the experiment and three times at the end of the experiment to account for changes in head in the water tank and therefore subtle changes in flow rate. An average value was taken from the six measurements to give an overall water flow rate for the experiment. An example uncertainty budget for the cooling water flow rate is given in Table 9-10.

Table 9-10 Uncertainty budget for heat recovery cooling water flow rate measurement and calculation. *n* = number of tests.

Type of Measurement	Source of Uncertainty	Uncertainty Value (+/-)	Probability Density Function	Divisor
Volume	Precision of beaker	5 mL	Uniform	$\sqrt{3}$
	Repeatability of measurement (standard deviation)	σ	Normal	$\sqrt{n}$
Time	Precision of stopwatch	0.5 seconds	Uniform	$\sqrt{3}$
	Human reaction -experiment start	0.1 seconds	Normal	1
	Human reaction -experiment end	0.1 seconds	Normal	1
	Repeatability of measurement (standard deviation) – experiment start	σ	Normal	$\sqrt{n}$
	Repeatability of measurement (standard deviation) – experiment end	σ	Normal	$\sqrt{n}$

The precision of the beaker was taken from the graduations on the vessel. The precision of the stopwatch was taken from the display. Repeatability of measurement was calculated as the standard deviation of the measured values. The uncertainty associated with the human reaction time was taken from a published study which found the systematic error, with a normal distribution, due to human reaction to be 0.1 seconds (Faux & Godolphin, 2019). The probability

distributions were estimated for each type of measurement and the associated divisor applied to obtain the standard absolute uncertainty for each source of uncertainty. Standard absolute uncertainty is calculated by dividing the uncertainty value by the associated divisor. For example, the standard absolute uncertainty associated with the repeatability of measurement is the standard deviation divided by the square root of the number of measurements taken. Likewise, the standard absolute uncertainty for the precision of an instrument is the value of half the width of the graduation divided by the square root of 3, associated with the uniform probability distribution.

$$SU_{abs,repeatability} = \frac{\sigma}{\sqrt{n}}$$

$$SU_{abs,precision} = \frac{Half\ width\ of\ graduation}{\sqrt{3}}$$

Once all standard absolute uncertainties had been calculated for each source of uncertainty, then a combined standard absolute uncertainty was calculated for each type of measurement, in this case the volume and time values. This was found using the summation of quadrature method, shown below.

$$SU_{abs,combined} = \sqrt{{SU_1}^2 + {SU_2}^2 + \cdots}$$

Once standard absolute uncertainties for each type of measurement had been calculated, these were converted into relative uncertainties. This was to allow uncertainties of different units to be combined. Standard relative uncertainty was calculated as the standard absolute uncertainty previously estimated divided by the average value for that measurement. For example, the combined standard absolute uncertainty for the volume measurement was divided by the average volume measurement value to give a fractional decimal representing the relative uncertainty.

$$SU_{rel} = \frac{SU_{combined}}{Average\ Measured\ Value}$$

Once standard relative uncertainties had been calculated for both the volume and time measurements these were combined using the summation of quadrature method to give a total standard relative uncertainty. This was then be converted back to a total standard absolute uncertainty in the units associated with the final measurement, mL/s in this case, by multiplying the relative uncertainty by the average cooling water flow rate value.

$$SU_{rel,total} = \sqrt{{SU_{rel,1}}^2 + {SU_{rel,2}}^2 + \cdots}$$

$$SU_{abs,total} = SU_{rel,total} \times (Average\ Measured\ Value)$$

A coverage factor was then applied to give a confidence range. The literature suggests that a coverage factor (k) of 2 gives a standard uncertainty value which gives a 95% confidence that any repeat tests will give a result within the stated range. This was applied to all uncertainty analysis in this thesis.

$$k = 2 \dots Gives\ 95\%\ confidence\ interval$$

The results of this analysis can be found in the data files available in the document repository. Following this analysis, future experiments could be improved by refining the measurement of the cooling water flow rate. It is proposed that the measurement time should be set, and the collected water weighed to give a more accurate measurement reducing the uncertainty associated with this value. This has been included as a recommendation in the main body of this thesis.

E.3.2 Pressure Data Uncertainty

The uncertainty budget for pressure measurements taken during heat recovery analysis are given in Table 9-11. The accuracy of the transducer is given by the manufacturer as +/-0.25%, which is converted to a pressure value based on the average pressure reading taken during testing. The precision was taken from the outputted value. The pulsed nature of the steam means that repeatability of pressure measurements could not be properly accounted for in this analysis. However, it is noted that the uncertainty associated with heat recovery analysis pressure measurements was found to be +/- 0.01bar using this analysis. This supports the variance from known values during the accuracy check, supporting both methods of analysis. This analysis combined standard absolute uncertainties and applied a coverage factor of k = 2 to give the final values for use in the error bars. There was no need to convert to relative uncertainty as all uncertainty values had the same units. Values can be found in the data files stored in the document repository.

Table 9-11 Heat recovery analysis pressure transducer uncertainty budget.

Source of Uncertainty	Uncertainty Value (+/-)	Probability Density Function	Divisor
Manufacturer accuracy	0.25%	Normal	1
Precision	0.005bar	Uniform	$\sqrt{3}$

E.3.3 Temperature Data Uncertainty

The uncertainty budget for temperature measurements taken during heat recovery analysis are given in Table 9-12. The accuracy is taken from the manufacturer stated values for the instruments. As these are given as an absolute value in the units of degrees Celsius, these were assumed to have a coverage factor of k = 2 already applied and were therefore given a divisor of 2. This is typical for stated instrument accuracy values (Bell, 2001). The precision was taken from the outputted values. Temperature values for the heat exchanger outlet water were stable during testing and therefore allowed the standard uncertainty due to the repeatability of the data to also be calculated using standard deviation. This analysis combined standard absolute uncertainties and applied a coverage factor of k = 2 to give the final values for use in the error bars. There was no need to convert to relative uncertainty as all uncertainty values had the same units. Values can be found in the data files stored in the document repository.

Table 9-12 Heat recovery analysis thermocouple uncertainty budget. n = number of measurements.

Source of Uncertainty	Uncertainty Value (+/-)	Probability Density Function	Divisor
Thermocouple accuracy	1.5°C	Normal	2
Conditioner accuracy	2°C	Normal	2
Precision	0.05°C	Uniform	$\sqrt{3}$
Repeatability of measurement (standard deviation)	σ	Normal	$\sqrt{n}$

E.3.4 Heat Recovery Efficiency Data Uncertainty

The heat recovery efficiency values were not directly measured but calculated using water flow rate, pressure, and temperature data recorded during each test. The standard absolute uncertainty associated with each of these has been described above. The standard absolute uncertainty was calculated for the heat recovery efficiency by combining these uncertainties using the appropriate methodology (Bell, 2001). The heat recovery efficiency was calculated as the thermal energy recovered as a percentage of the energy available for recovery. The thermal energy recovered was calculated as a function of the water flow rate and change in water temperature. The energy

available was calculated as a function of the steam flow rate, and therefore as a function of boiler and heat exchanger pressures.

The standard absolute uncertainty in the change in water temperature is a combination of the standard absolute uncertainty in the heat exchanger inlet and outlet temperatures. The outlet temperature standard absolute uncertainty was already calculated according to the method described above. It is important to note that the standard absolute uncertainty already calculated is taken before the coverage factor was applied. The inlet temperature was taken from the sous vide heater. This had not yet had a standard absolute uncertainty associated with it and was calculated using the precision of the instrument as 0.05^{o}C and applying a uniform probability distribution as performed in the above analysis methods. The standard absolute uncertainty in inlet and outlet water temperature was combined using the summation of quadrature method and converted into a relative uncertainty using the average value for the change in water temperature. The standard absolute uncertainty in the cooling water flow rate had also been calculated already, see previous sub-sections. These values were taken prior to the coverage factor being applied and a relative uncertainty found ready for use in later analysis.

The steam flow rate was calculated using *Bernoulli's* equation using boiler and heat exchanger average pressures. Average boiler and heat exchanger pressures were calculated from pressures at the start and end of the pulse. Therefore, the standard absolute uncertainty in pressure measurements already calculated was applied to the start and end of the pulse for both the boiler and heat exchanger and combined using the summation of quadrature method. This was then converted to a relative uncertainty in the pressure difference value between boiler and heat exchanger, as used in the steam flow rate equation.

The final step of this analysis was to combine the relative uncertainties for the change in water temperature, water flow rate, and pressure difference (to drive steam flow) using the summation of quadrature method to give a total relative uncertainty in the final heat recovery efficiency value. This was converted back to a standard absolute uncertainty by multiplying by the average heat recovery efficiency for each test. A coverage factor of k = 2 was then applied to give a confidence interval of 95%. This accounted for all uncertainty in the efficiency value to the best of the author's ability.